Environmental degradation of structural materials in liquid lead- and lead-bismuth eutectic-cooled reactors

Xing Gong, Michael P Short, Thierry Auger, Evangelia Charalampopoulou, Konstantina Lambrinou

Environmental degradation of structural materials in liquid lead- and lead-bismuth eutectic-cooled reactors

Xing Gong [a,*], Michael P. Short [b], Thierry Auger [c], Evangelia Charalampopoulou [d], Konstantina Lambrinou [d,e,*]

[a] *Advanced Nuclear Energy Research Team, Department of Nuclear Science and Technology, College of Physics and Optoelectronic Engineering, Shenzhen University, Shenzhen 518060, China*
[b] *Department of Nuclear Science and Engineering, Massachusetts Institute of Technology (MIT), Cambridge, MA 02139, USA*
[c] *PIMM, Arts et Metiers ParisTech, CNRS, Cnam, HESAM Université, 151 Blvd. de L'Hôpital, 75013 Paris, France*
[d] *Belgian Nuclear Research Centre (SCK CEN), Boeretang 200, 2400 Mol, Belgium*
[e] *School of Computing and Engineering, University of Huddersfield, Queensgate, Huddersfield HD1 3DH, UK*

ARTICLE INFO

Keywords:
Liquid Pb
Liquid LBE
Liquid metal corrosion
Liquid metal embrittlement
Structural materials
Environmental degradation

ABSTRACT

Liquid lead (Pb)- and lead–bismuth eutectic (LBE)-cooled fast neutron reactors (Gen-IV LFRs) are one of the most technologically mature fission reactor technologies, due to their inherent safety, high power density, and ability to burn nuclear waste. Accelerator-driven systems (ADS), in particular, promise to address the issues of long-lived radiotoxic nuclear waste, emerging uranium ore shortages, and the ever-increasing demand for energy. However, the conditional compatibility of conventional structural materials, such as steels, with liquid Pb and liquid LBE is

Abbreviations: ADS, accelerator-driven system; AFA, alumina-forming austenitic (steel); AFM, atomic force microscopy; AuSS, austenitic stainless steel(s); *bcc*, body-centred cubic; BF, bright-field; CCT, centre-cracked tension; CLAM, China low-activation martensitic (steel); COD, crack opening displacement; CSL, coincidence site lattice; CSP, concentrated solar power; CT, compact tension; CW, cold-worked; DBTT, ductile-to-brittle transition temperature; DCT, disc-shaped compact tension; DFT, density functional theory; dpa, displacements per atom; DSA, dynamic strain ageing; EAC, environmentally-assisted cracking; EB, electron beam; EBSD, electron backscatter diffraction; EDS, energy-dispersive X-ray spectroscopy; *fcc*, face-centred cubic; FCG, fatigue crack growth; FFTF, Fast Flux Test Facility; FIB, focused ion beam; F/M, ferritic/martensitic (steel); FP, fission product; GB, grain boundary; GBEM, grain boundary engineered material; GBW, grain boundary wetting; GESA, Gepulste ElektronStrahl Anlage; GSF, generalised stacking fault; HAADF, high-angle annular dark-field; HAZ, heat-affected zone; HEA, high-entropy alloy; HLM, heavy liquid metal; IOZ, internal oxidation zone; LBE, lead-bismuth eutectic; LFR, liquid Pb- or LBE-cooled fast reactor; LLFP, long-lived fission product; LMC, liquid metal corrosion; LME, liquid metal embrittlement; LOC, low oxygen concentration; LOFA, loss-of-flow accident; LOM, light optical microscopy; LPS, liquid phase sintering; LWR, light water reactor; MA, minor actinides; MD, molecular dynamics; MSRE, molten salt reactor experiment; MYRRHA, Multi-purpose hYbrid Research Reactor for High-tech Applications; NITE, nano-infiltration and transient eutectic phase (processing route); NPP, nuclear power plant; ODS, oxide dispersion strengthened; OR, orientation relationship; PLD, pulsed laser deposition; PSB, persistent slip band; PVD, physical vapour deposition; RE, rare-earth; RIS, radiation-induced segregation; RT, room temperature; SA, solution-annealed; SAED, selected area electron diffraction; SEM, scanning electron microscopy; SF, stacking fault; SFR, sodium-cooled fast reactor; SMIE, solid metal-induced embrittlement; SMR, small modular reactor; SMRT, surface mechanical rolling treatment; SPT, small punch test; SSRT, slow strain rate tensile; STEM, scanning transmission electron microscopy; t-EBSD, transmission electron backscatter diffraction; TEM, transmission electron microscopy; TIG, tungsten inert gas; TOF-SIMS, time-of-flight secondary ion mass spectrometry; TWIP, twinning-induced plasticity; UTS, ultimate tensile strength; VHTR, very-high-temperature reactor; XPS, X-ray photoelectron spectroscopy; YAG, yttrium-aluminium garnet.

* Corresponding authors at: Department of Nuclear Science and Technology, College of Physics and Optoelectronic Engineering, Shenzhen University, Shenzhen 518060, China (X. Gong). School of Computing and Engineering, University of Huddersfield, Queensgate, Huddersfield HD1 3DH, UK (K. Lambrinou).

E-mail addresses: gongxing@szu.edu.cn (X. Gong), K.Lambrinou@hud.ac.uk (K. Lambrinou).

still an important concern for the deployment of these advanced nuclear reactor systems, making the environmental degradation of candidate structural and fuel cladding steels the main impediment to the construction of Gen-IV LFRs, including ADS. This article presents a comprehensive review of the current understanding of environmental degradation of materials in contact with liquid Pb and liquid LBE, with a focus on the underlying mechanisms and the factors affecting liquid metal corrosion (LMC) and liquid metal embrittlement (LME), which are the two most important materials degradation effects. Moreover, this article addresses the most promising LMC and LME mitigation approaches, which aim to suppress their adverse influence on materials performance. An outlook of the needed future work in this field is also provided.

1. Introduction

1.1. The demand for economical and clean energy, nuclear safety, and nuclear waste management

The sustainability of our society continues to be challenged by the rapidly increasing demand for energy [1–3]. Although traditional fossil fuels, such as coal, natural gas, and oil, cover most societal energy needs, especially in developing countries [1], their excessive use continues to release large amounts of toxic pollutants and greenhouse gases [4]. This issue is driving the society to seek clean and renewable energy sources – "clean" is self-explanatory (i.e., no or minimal pollutant emission, including CO_2), while "renewable" may or may not include nuclear energy, depending on which type of technology is under consideration, while the socio-political definition of "renewable" refers to either an infinite temporal resource availability in strict terms, or to utilisable resources over timescales relevant to human societies [5]. Traditionally renewable sources of energy, such as solar and wind, are currently preferred and advocated by society at large, particularly after the 2011 Fukushima Daiichi nuclear event in Japan [3]. However, these energy sources have obvious disadvantages, such as power instability, limited capacity factors due to weather dependence and intermittency issues, and prohibitively high costs when accounting for taxpayer and government subsidies [6,7], combined with the need for grid-scalable storage over timescales of both days and months, up to terawatt-hours [8]. By contrast, nuclear power can supply energy that is clean in terms of CO_2 emissions, reliable, and on an enormous baseload scale [9]. In this regard, nuclear energy still holds excellent promise as a major contributor to decarbonise human activities on Earth, even when taking into account the long-term challenges of storing nuclear waste over multi-millennial timescales and preventing rare, yet with severe consequences, nuclear accidents.

Most of today's commercial nuclear power plants (NPPs) use thermal neutron spectra, i.e., neutrons that are mostly at/near room temperature (corresponding energy: 0.025 eV at room temperature, RT). Thermal NPPs covered 10% of the global electricity demand in 2018 [9], with near-zero greenhouse gas emissions, even when accounting for the materials used for their construction, as well as for nuclear fuel production. However, most of these reactors are fuelled with ^{235}U, an isotope only accounting for 0.7% of the total natural uranium (U) existing on Earth. Known, economically recoverable resources of ^{235}U will likely be consumed by the end of this century [10], which means that this class of nuclear reactors is decidedly not renewable. Thermal NPPs also produce significant amounts of high-level radioactive waste, consisting of minor actinides (MA) and long-lived fission products (LLFPs), both of which can remain dangerously radioactive for up to tens of thousands of years [11]. The best current solution to the issue of nuclear waste (though not necessarily a good one, in absolute terms) is its disposal in geological repositories [12]. The problem with nuclear waste stored in geological repositories is that it will take extremely long times for its radiotoxicity to decay down to the level of natural uranium ores [10], leading scientists around the world to question both the short-term safety of such repositories, and the long-term handling of this undesirable for humankind heritage by humankind, tens of thousands of years into the future[1] [13]. This has created serious problems for the public acceptance of nuclear energy, hampering its spread and, by consequence, our collective ability to combat climate change.

By contrast, fast reactors with higher-energy neutron spectra can "breed" the other naturally occurring isotope of uranium, ^{238}U (99.3% abundant), by transforming it into fissile, energetically useful plutonium (Pu) isotope ^{239}Pu [10,11]. This can substantially improve the efficiency of uranium sources, effectively making nuclear power renewable by both making its own fuel and extending available resources for thousands of years. Another advantage is that fast reactors can be fuelled with thorium (Th), which exists in easily recoverable deposits that are three to four times more abundant than the uranium ones; moreover, thorium presents less concerns for the proliferation of nuclear weapons [14]. Compared to today's commercial NPPs outside of Russia, nuclear waste discharged from fast reactors is much lower in volume, and after reprocessing the spent fuel, a so-called "closed fuel cycle" can be achieved where almost nothing is wasted [11,15].

A number of new and innovative reactor concepts could turn this dream into reality. These include fast/epithermal neutron spectrum reactors, such as the PEACER waste-burning liquid metal-cooled design developed at Seoul National University in South Korea [16], and accelerator-driven fast neutron reactors, such as the ADS (accelerator-driven system) MYRRHA (Multi-purpose hYbrid Research Reactor for High-tech Applications) research reactor, currently under development at SCK CEN, Belgium [10]. Such reactor designs can transmute nuclear waste in a much faster and more efficient way, via capture and decays, or nuclear fission reactions. In the case of epithermal spectrum reactors, the neutron spectrum is tuned to match resonances in the capture cross-sections of isotopes

[1] See the documentary "Containment" by P. Galison and R. Moss for a politically neutral discussion of how societies could accomplish this multi-millenial task.

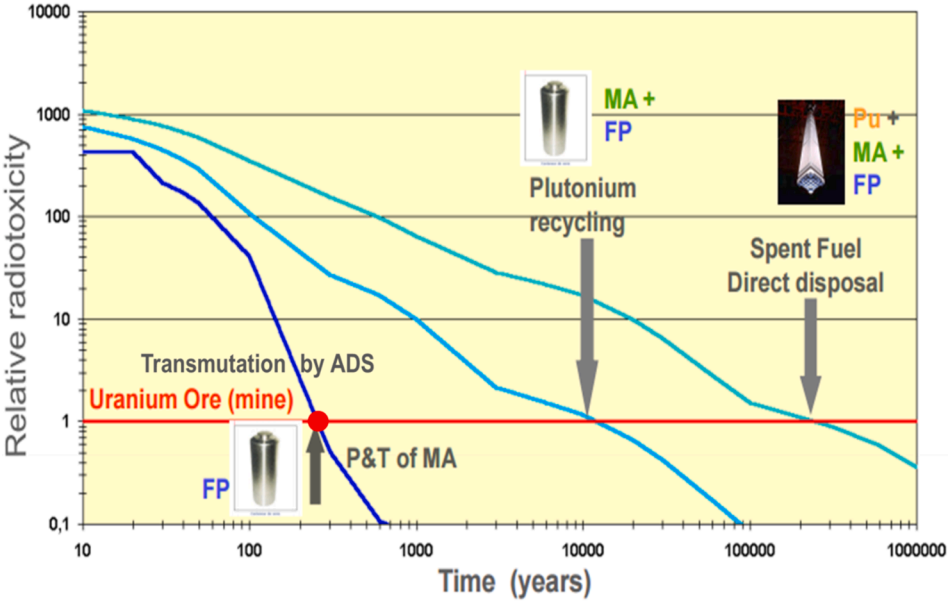

Fig. 1.1. Comparison of nuclear waste radiotoxicity before and after transmutation. MA: minor actinides (Am, Np, Cm); FP: fission products; P&T: partitioning & transmutation; Pu: plutonium. Adapted from [17].

found in long-lived nuclear waste, "burning" them from long-lived (10,000's–100,000's of years) to short-lived (100's of years) waste forms. In the case of ADS designs, a high-intensity proton beam delivered from an accelerator bombards a spallation target (made of a heavy metal in solid or liquid state) in the reactor to generate abundant fast neutrons, which similarly burn nuclear waste isotopes via neutron capture reactions. Both concepts shorten significantly the timescale of radioactive decay (Fig. 1.1). Furthermore, ADS designs, in particular, are inherently safe, as they are typically operated in subcritical mode, where the accelerator is needed to maintain criticality [10]. In case of emergency, the proton accelerator is easily and instantly shut down to terminate the fission reactions. Therefore, fast neutron reactors, including those coupled with a proton accelerator, are promising technologies to cope with the demands for baseload clean energy, minimal to zero nuclear waste production, inherently safe operation, and the ability to burn stored nuclear waste.

1.2. Notable features of liquid Pb- and LBE-cooled fast reactors

Lead-based heavy liquid metals (HLMs), i.e., liquid lead (Pb) and lead–bismuth eutectic (LBE, $Pb_{44.5}Bi_{55.5}$, wt%), are candidate primary coolants and spallation targets for fast neutron reactors and ADS designs [18–22], due to their excellent neutronic, thermo-hydraulic, and thermo-physical properties (Table 1.1). Liquid Pb- and/or LBE-cooled fast reactors (LFRs), including ADS designs, have been selected as one of the six fission reactor concepts in the Generation IV (Gen-IV) Technology Roadmap towards the development of advanced nuclear power [23]. The main advantages of this type of advanced nuclear reactors are listed below:

1. Liquid Pb and LBE exhibit limited neutron moderation and absorption, leading to harder (i.e., higher energy or faster) neutron spectra and more efficient neutron usage [18]. This feature makes reactor designs using liquid Pb and LBE coolants suitable for efficient fuel breeding and nuclear waste transmutation.
2. Liquid Pb and LBE have good heat transfer capability, allowing for a compact core configuration that enables the development of transportable small modular reactors (SMRs) for electricity supply in remote areas [24], smaller communities, and even the potential replacement of large reactor cores while making use of existing nuclear island sites. This enables the production of compact, power-dense cores and numerous designs already exist, such as SVBR [25], SSTAR [26], and PASCAR [27].
3. These two HLMs have high boiling temperatures (>1600 °C, higher than the melting points of steels) and do not undergo strong chemical reactions with air or water [18,20,24], thereby simplifying the nuclear reactor structure and preventing many types of accidents that are inherent in other reactor designs, such as the sodium/air or sodium/water interactions in liquid sodium-cooled fast reactors (SFRs) or high-temperature transients in very high temperature reactors (VHTRs). In addition, decay heat can be removed by natural convection under accidental conditions [18,19]. These characteristics endow Gen-IV LFRs with inherent safety.

Table 1.1
Basic characteristics of select reactor coolants [28].

Coolant	Atomic mass (g/mol)	Relative moderation, accounting for density	Neutron absorption cross-section at 1 MeV (mbarn)	Neutron scattering cross-section at 1 MeV (barn)	Melting point (°C)	Boiling point (°C)	Chemical reactivity with air and water
Pb	207	1	6.001	6.4	327	1737	Inert
LBE	208	0.82	1.492	6.9	125	1670	Inert
Na	23	1.80	0.23	3.2	98	883	Highly reactive
H_2O	18	421	0.1056	3.5	0	100	Inert
D_2O	20	49	0.0002115	2.6	0	100	Inert
He	2	0.27	0.007953	3.7	–	−269	Inert

1.3. Structural material limitations for deployment of Gen-IV LFRs

Candidate structural materials for Gen-IV LFRs must perform reliably in very harsh environments, where material performance can degrade due to radiation-induced damage, liquid metal corrosion (LMC), liquid metal embrittlement (LME), stresses, transmutation, nuclear reactions producing helium gas atoms, and combinations of all the above effects. A major challenge in the deployment of these nuclear systems is that the principal candidate structural materials, including ferritic/martensitic (F/M) steels and austenitic stainless

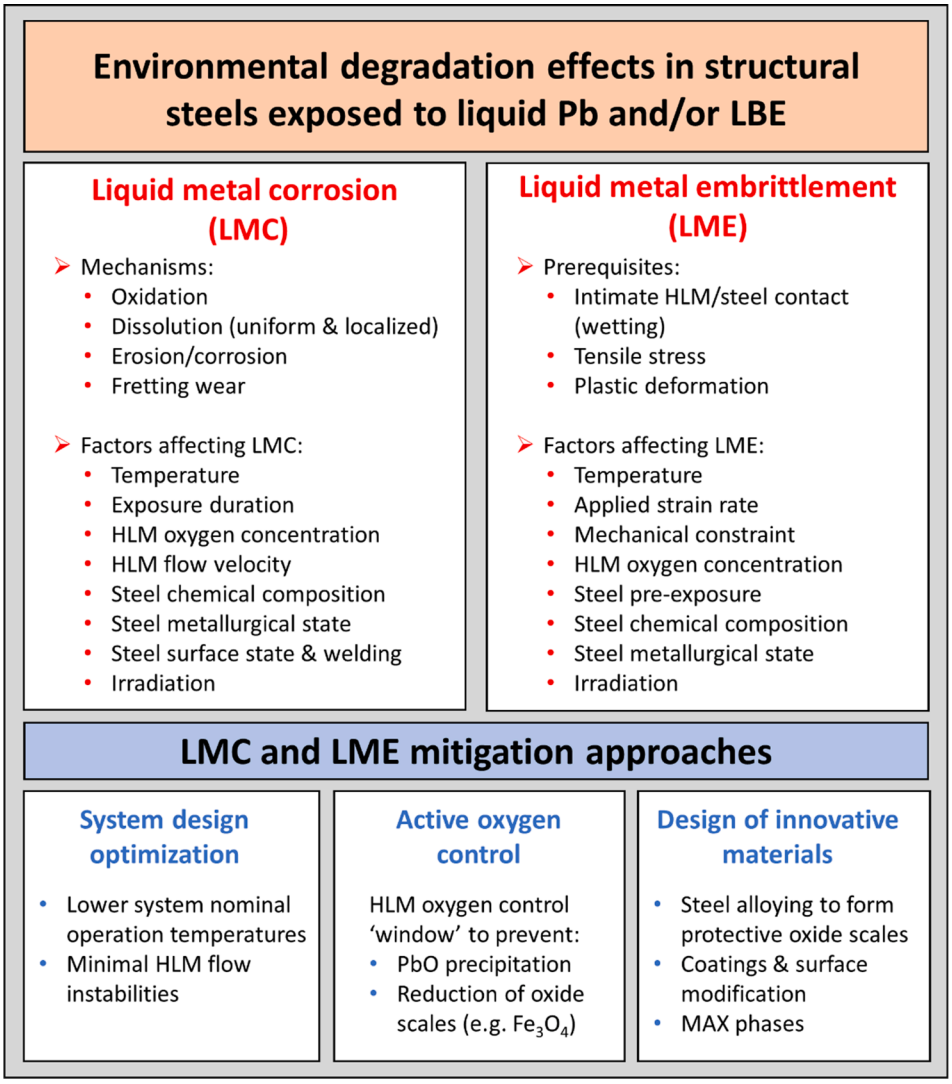

Fig. 1.2. Environmental degradation effects in structural steels exposed to liquid Pb and/or LBE coolants in Gen-IV LFRs, and possible LMC/LME mitigation approaches.

steels (AuSS), are not fully compatible with liquid Pb and/or LBE coolants [29–36], showing severe performance degradation due to LMC and/or LME (Fig. 1.2). LMC and LME are the two most important materials degradation effects resulting from the contact of candidate structural materials, esp. nuclear grade steels, with liquid Pb and/or LBE; therefore, this review article provides an extensive description of the state-of-the-art understanding of both materials degradation effects and an overview of the promising mitigation approaches.

The basic LMC mechanisms include oxidation, dissolution, erosion, and fretting wear, or a combination thereof [29,30,37–39]. Oxidation results in the formation of oxide scales on the material surface, which can either be protective, typically dense and without many defects, or non-protective, rather porous and defective. Thin and dense oxide scales are desirable because they passivate the substrate, protecting it from further corrosion; on the other hand, excessive oxidation causes the formation of prohibitively thick oxides that do not only reduce the component's thermal conductivity due to their insulating capacity (detrimental for fuel cladding and heat exchanger tubes), but may also cause blockage of the primary circuit upon periodic oxide scale spallation (e.g., spallation that occurs spontaneously due to the build-up of internal stresses above a critical oxide scale thickness). In AuSS, dissolution corrosion typically involves the selective loss/leaching of highly soluble steel alloying elements, but might also manifest itself as non-selective leaching depending on the steel chemical composition [40]. This undesirable form of LMC might be locally enhanced (dissolution 'pitting' [40]) and its occurrence is tentatively attributed to the combination of local HLM flow patterns (e.g., eddies), chemical/microstructural inhomogeneities and surface residual stresses of the affected material; dissolution 'pitting' can jeopardise within a short time the integrity of thin-walled components, such as fuel cladding and heat exchanger tubes [40–44]. Erosion is typically caused by fast HLM flow, sites of flow diversion, and the abrasive action of any hard, solid phases entrained within (e.g., spalled oxides, foreign particles of high hardness), and may continuously remove surface oxide scales and dissolution-affected material areas, leading to very high overall corrosion rates. Fretting wear, typically caused by the continuous rubbing of two solid surfaces against each other, can further facilitate dissolution corrosion (in this case, also considered as crevice corrosion, due to the corrosive action of the HLM in a narrow space), thereby adding an aspect of mechanical ablation to a chemically aggressive environment [37–39].

LME involves crack nucleation at the HLM-wetted material surface, followed by fast crack propagation, due to the adsorption of Pb/Bi atoms at advancing crack tips. This effect results in substantial embrittlement (i.e., loss of fracture toughness), reduced fatigue life, and degraded creep properties [36]. When compounded with the effects of neutron irradiation, which typically increases material strength while lowering ductility and fracture toughness (phenomenon known as radiation embrittlement or radiation hardening), the LME effect can become even more pronounced [45].

LMC and LME pose a serious threat to the structural integrity and lifetime of LFR components, impeding the deployment of liquid Pb- and/or LBE-cooled fast reactors. To understand the underlying mechanisms and devise effective mitigation measures, significant research has been conducted with a wide variety of test parameters. When the issues of material degradation in HLM-cooled reactors will have been addressed, no remaining technical challenges that could impede the construction and deployment of Gen-IV LFRs are foreseen.

The objective of the present article is to provide an up-to-date and comprehensive literature review of LMC and LME, the two most important degradation effects of structural nuclear materials in contact with liquid Pb and/or LBE at reactor-relevant conditions, thereby identifying the "state-of-the-art" in this field so as to better target the remaining key problems and find possible solutions. The present review article is organised as follows: first, basic information is provided on representative candidate materials, such as T91 (a F/M steel), 316L (an AuSS), and 15-15Ti (a Ti-AuSS). Second, the mechanisms and key factors affecting the LMC of 316L AuSS and T91 F/M steels, as well as compositionally similar AuSS and F/M steels, are presented, including insights into the effects of irradiation on corrosion from the similar field of corrosion in molten salts. Third, the mechanisms and models of LME in ferritic and F/M steels (e.g., T91) are discussed, and the factors affecting the steel susceptibility to LME are also addressed. Next, the so far developed strategies for the mitigation of environmental degradation effects are summarised, and their advantages/disadvantages are compared. Finally, the conclusions of this review article are presented, including recommendations for future R&D based on the state-of-the-art understanding of the degradation effects in structural materials exposed to liquid Pb and/or LBE, the identified gaps in know-how, and the remaining scientific and technical challenges involved in the development of structural materials suitable for Gen-IV LFRs.

2. Candidate structural materials for Gen-IV LFRs

For the purposes of this review, we focus on candidate structural materials for Gen-IV LFRs that are considered to be "near-term". We deliberately eschew touching upon scientifically advanced, yet technologically immature, alloy concepts, coatings, and surface treatments, unless they are designed to improve the performance of near-term candidate material concepts. Thus, the focus of this chapter is to concisely summarise the main body of knowledge regarding structural materials likely to be used in test and commercial LFRs over the next 10–20 years.

Near-term candidate materials should be either commercially available or almost commercially available, with plenty of available and reliable material property data, in-service experience, and manufacturing technologies to support widespread production. In this case, only qualification of material performance in a representative (industrially relevant) nuclear environment is required, thereby greatly reducing the time and costs necessary for regulatory licensing. Secondary choices include materials with promising properties, but still requiring extensive R&D efforts towards performance qualification. The primary material focal points in the past decades are two families of commercial steels, i.e., F/M steels and AuSS [18]. One of the most intensively investigated F/M steels is the 9Cr-1Mo grade (e.g., T91), while the 316L and 15-15Ti (e.g., DIN 1.4970) grades are among the most thoroughly investigated AuSS for Gen-IV LFRs. Other materials, such as oxide dispersion strengthened (ODS) steels, the MAX ($M_{n+1}AX_n$) phases, SiC_f/SiC (i.e., SiC fibre-reinforced SiC) composites, and refractory metals have some appealing properties, and thus their bulk and/or coating forms have

also been investigated in order to provide a longer-term materials perspective. For the time being, however, F/M steels and AuSS are the two types of structural materials most likely to yield near-term, commercially affordable structural material solutions for Gen-IV LFRs.

In this chapter, the main characteristics of candidate structural materials proposed for use in liquid Pb- or LBE-cooled fast reactors are summarised in terms of their microstructure, chemical composition, and relevant properties. In this and subsequent chapters, reference to materials characterisation techniques is made by employing well-established abbreviations provided in the list of abbreviations at the beginning of this text. Abbreviations appearing in the text are often accompanied by the symbol †.

2.1. Ferritic/martensitic (F/M) steels

F/M steels, particularly 9–12 wt% Cr F/M steels with up to 0.1–0.2 wt% C, have the body-centred cubic (*bcc*) crystal structure and exhibit a good combination of mechanical properties up to elevated temperatures (typically up to 550–610 °C), high thermal conductivity, low thermal expansion, and excellent resistance to radiation embrittlement and void swelling [46–49]. The chemical compositions and microstructures of this type of steels are tailored to enable the formation of austenite during normalisation, followed by the formation of martensite after quenching. To balance strength and fracture toughness, tempering these steels at ~760 °C can transform the martensite to ferrite (also known as "a tempered martensite"), which has superior ductility and fracture toughness. In addition, 9 wt% Cr is generally preferred for nuclear applications, considering that after neutron irradiation, 9Cr F/M steels have the lowest ductile-to-brittle transition temperature (DBTT), as compared to steels alloyed with different Cr contents [46,50] (Fig. 2.1). A higher Cr content increases corrosion resistance, but too much Cr can cause α' phase precipitation [51] or σ-phase embrittlement at higher temperatures, both exacerbated by radiation damage [52], with detrimental effects on the steel ductility and fracture toughness.

One of the most attractive properties of 9Cr F/M steels (modified with the addition of small amounts of V and Nb) is their excellent resistance to void swelling induced by neutron irradiation up to 150–160 displacements per atom (dpa) [46,49], which is conducive to achieving high fuel burn-ups and, thereby, minimising nuclear waste when used as fuel cladding material (Fig. 2.2). Their superior void swelling resistance mainly results from the presence of numerous martensitic lath boundaries decorated with fine carbide and carbonitride particles, and a high density of dislocations, all of which serve as effective sinks for irradiation-induced defects. As an example, Fig. 2.3 shows the microstructure of an as-produced T91 F/M steel. The steel microstructure comprises prior-austenite grains (Fig. 2.3a and Fig. 2.3b), which are formed in the normalisation heat treatment and contain martensitic packets. The packets are filled with blocks of tempered martensitic laths (Fig. 2.3b). The grains or sub-grains mostly exhibit low-angle grain boundaries, GBs (Fig. 2.3c). Fine precipitates are visible at the lath boundaries (Fig. 2.3d). In addition, there are massive dislocation tangles inside the laths (Fig. 2.3e). A schematic illustration of the main microstructural characteristics of this T91 F/M steel is presented in Fig. 2.3f. Other F/M steels have similar microstructures, differing mainly in grain sizes and precipitate distributions.

These steels are somewhat discredited by their long-term creep properties, which ultimately limit their service temperature below 600 °C. Irradiation embrittlement below 400–450 °C may also be a performance-limiting factor [54,55], leaving a rather narrow temperature 'window' suitable for long-term service in reactor. In spite of these concerns, T91 and other F/M steel grades were initially recommended for constructing fuel cladding tubes and other reactor core internals in LFRs and European transmutation systems (e.g., the MYRRHA system), and have, thus, undergone extensive studies of their compatibility with liquid Pb and/or LBE. Table 2.1 summarises the chemical composition of T91 and compositionally similar F/M steels that have been studied for their compatibility with liquid Pb/LBE.

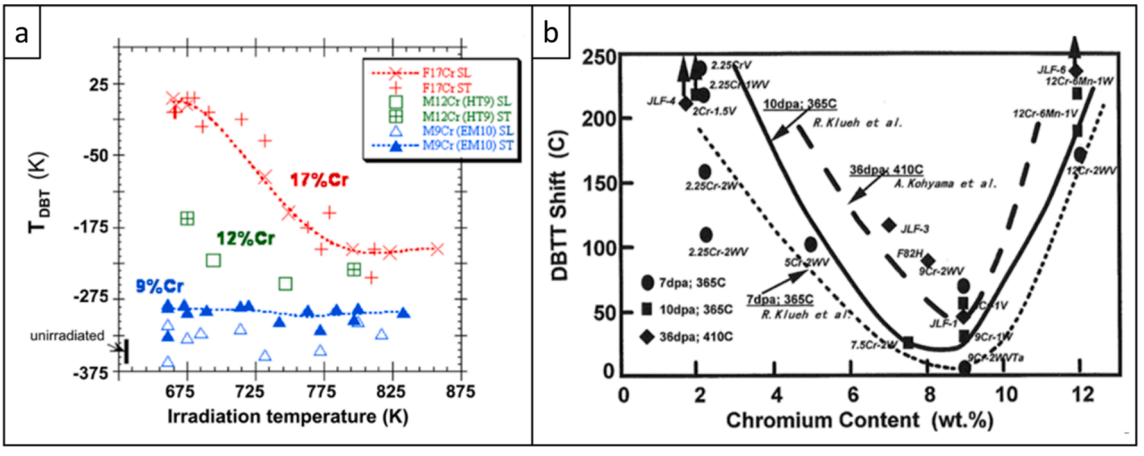

Fig. 2.1. (a) DBTT† of 9Cr, 12Cr, and 17Cr F/M steels after neutron irradiation at different temperatures [46]. (b) DBTT shift of low-activation ferritic steels, as a function of the steel Cr content, after neutron irradiation in the FFTF†. Adapted from [50].

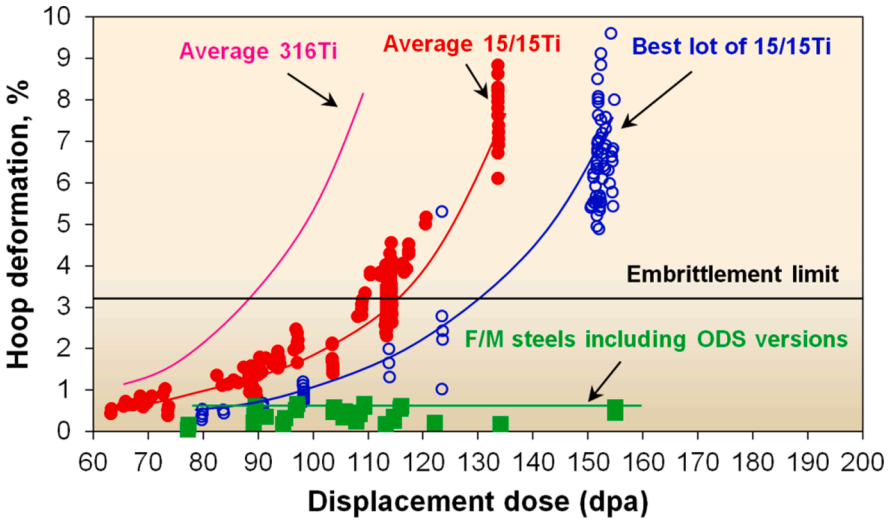

Fig. 2.2. Radiation swelling (hoop) deformation of different grades of AuSS and F/M steels as a function of the irradiation dose (in dpa) at 400–550 °C [46,47].

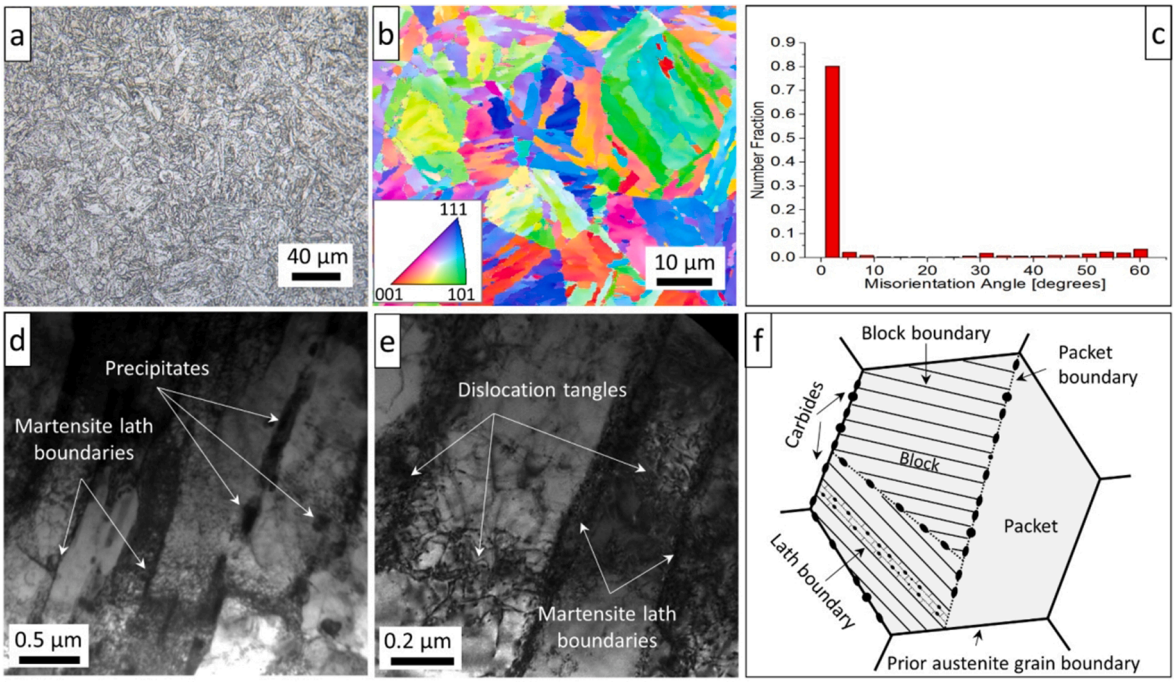

Fig. 2.3. Typical microstructure of a T91 F/M steel: (a) LOM† image; (b) EBSD† grain orientation map; (c) misorientation angles of martensitic laths; (d, e) TEM† bright-field (BF) images; (f) schematic representation of the main microstructural features. Adapted from [53].

2.2. Austenitic stainless steels (AuSS)

316L AuSS have the face-centred cubic (*fcc*) crystal structure and have been used as fuel cladding materials in SFRs†, showing good performance under fast neutron irradiation [56] at the relatively low operation temperatures (350–475 °C) of reactors such as EBR-II. However, their service lifetime was limited by irradiation-induced void swelling at high irradiation doses, leaving little possibility of further extending fuel burn-up. As a consequence, modified versions of the nuclear steel grade AISI 316 have been developed to improve swelling resistance. The main modification is in adjusting their chemical compositions by slightly increasing the Ni to Cr ratio, and by adding small amounts of Si and Ti. These new versions of AuSS are often called "Ti-modified" or "Ti-stabilised" stainless steels. Among them, the most popular ones are the 316Ti grade (e.g., 1.4571 in the German DIN standard, and S31635 in the US UNS

Table 2.1
Nominal chemical composition of grade 91 (T91) and compositionally similar F/M steels (wt%, balance Fe). Slight deviations of the chemical composition of each steel heat from the nominal steel grade composition are not uncommon.

Steel Grade	C	Cr	Ni	Mn	Mo	Si	W	Nb	V	Ta	Ti	Cu	N
E911	0.09–0.13	8.5–9.5	0.1–0.4	0.3–0.6	0.9–1.1	0.1–0.5	0.9–1.1	0.06–0.1	0.18–0.25	–	–	–	–
EM10	0.099	8.97	0.07	0.49	1.06	0.46	<0.002	<0.002	0.013	–	–	–	–
EP-823	0.16	11.70	0.66	0.55	0.74	1.09	0.60	–	0.30	–	–	–	–
EUROFER-97	0.11	8.82	0.02	0.47	<0.001	0.04	1.09	–	0.20	0.13	–	–	–
HT-9	0.17	11.5	0.5	0.6	–	0.4	–	–	–	–	–	–	–
Manet II	0.11	10.3	0.68	0.78	0.61	–	–	0.14	0.2	–	–	–	–
Mod. F82H	0.09	7.8	0.04	0.18	–	0.13	2	<0.01	0.16	–	–	–	–
Optifer IVc	0.56	9.99	–	0.58	–	0.02	0.30	–	0.28	0.02	–	–	–
S2439	0.19	11.58	0.48	0.37	1.03	2.75	0.48	–	0.31	–	–	–	–
S2440	0.19	13.52	0.51	0.38	1.00	4.83	0.45	–	0.31	–	–	–	–
STBA26	–	9	–	–	1	0.2	–				–	–	–
STBA28	–	8.8	–	–	1	0.4	–				–	–	–
T122 (HCM12A)	0.11	10.83	0.39	0.64	0.30	0.27	1.89	0.054	0.19			1.02	0.063
T91	0.10	8.99	0.11	0.38	0.89	0.22	–	0.06	0.21	–	–	–	–
T92	0.11	8.99	0.12	0.43	0.49	0.26	1.75	0.06	0.20	–	–	–	–

Table 2.2
Nominal chemical composition of 304L, 316L, 316Ti, and 15-15Ti AuSS (wt%, balance is Fe). Slight deviations of the chemical composition of each steel heat from the nominal steel grade composition are not uncommon.

Steel Grade	C	Cr	Ni	Mo	Si	Mn	V	Ti	P	S	N	B
304L	0.02	18.5	8.31	0.39	0.49	1.67	–	–	0.026	0.003	0.069	–
316L	0.03	17	10–14	2.0	0.6	1.8	–	–	–	–	–	0.002
316Ti	0.05	16	14	2.5	0.6	1.7	–	0.4	0.03	–	–	–
1.4970	0.1	15	15	1.2	0.4	1.5	–	0.5	–	–	–	0.005
1.4571	0.08	17.5	12	2.0	1.0	2.0	–	0.7	0.045	0.015	–	–
D9	0.052	13.8	15.2	1.50	0.92	1.74	–	0.23	0.003	–	–	–
JPCA	0.06	15	15	2.0	–	–	–	0.25	–	–	–	–
ChS-68	0.05–0.08	15.5–17	14.0–15.5	1.9–2.5	0.3–0.6	1.3–2.0	0.1–0.3	0.2–0.5	<0.02	–	–	0.002–0.005

standard) and the 15-15Ti class (e.g., 1.4970 in the DIN standard, D9 in the UNS standard, JPCA in Japan, and ChS-68 in Russia). Due to their excellent high-temperature creep properties, DIN 1.4970 steels were selected as fuel cladding materials in SFRs, such as the German SNR-300, and the French Phénix & Superphénix [56]. Given the known performance of DIN 1.4970 AuSS under neutron irradiation, this material in a cold-worked state has been chosen as the reference fuel cladding material for the MYRRHA research reactor.

The chemical compositions of the 304L, 316, 316Ti, and 15-15Ti types of AuSS are given in Table 2.2. In the case of the 15-15Ti steels, one may notice that the main alloying elements are Mo, Mn, Si, and Ti. Mo improves the high-temperature mechanical properties, while Si is used to bind vacancies and remove impurities (Bain and Paxton referred to this as steel "killing" by scavenging oxygen [57]). Ti is added to promote the formation of TiC particles. Moreover, some steels of the 15-15Ti type are micro-alloyed with Nb, V, Zr, and Ta, which impart additional phase stability.

These steels are normally subjected to solid solution annealing (SA) at 1010–1120 °C for 0.5–1 h, followed by rapid cooling. The final microstructure of such AuSS is characterised by large, austenitic grains decorated by carbides and annealing twins, as in the example shown in Fig. 2.4a–d. For as-produced 316L steels, lamellae of δ-ferrite enriched in Cr, slightly enriched in Mo, and depleted in Fe and Ni as compared to the steel matrix are also present. Cold working produces a highly dense dislocation network in cold-worked (CW) steels, favouring heterogeneous nucleation of fine intragranular TiC particles in Ti-containing AuSS grades. The interfaces between TiC precipitates and the austenite matrix act as sinks for radiation-induced defects, thereby delaying void swelling (Fig. 2.2). In addition, cold working leads to the formation of numerous slip bands and deformation twins, where the twinning plane is {1 1 1}

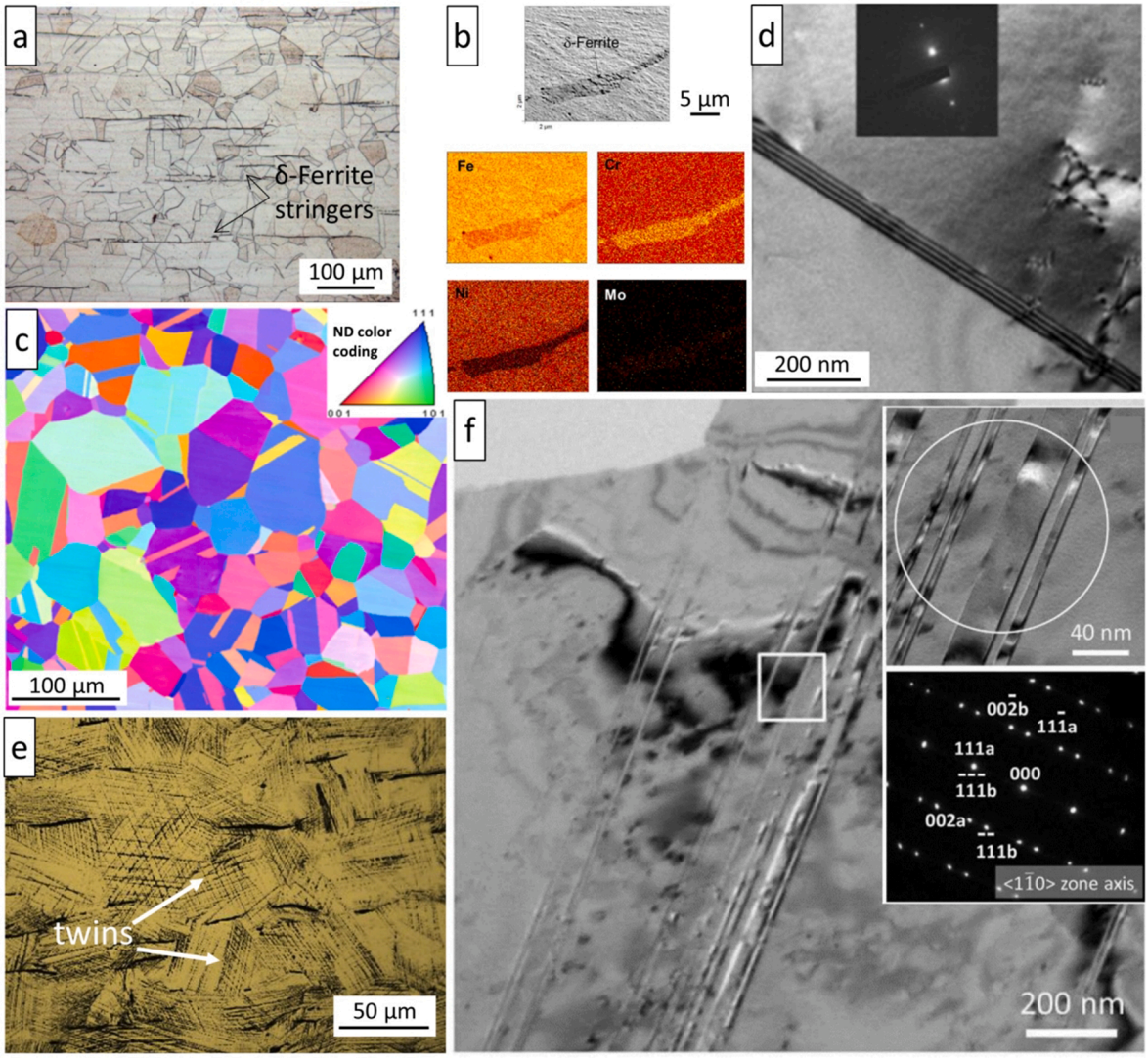

Fig. 2.4. Microstructure of SA† and CW† 316L AuSS. SA 316L: (a) LOM† image of δ-ferrite stringers; (b) EDS† elemental maps of δ-ferrite; (c) EBSD† grain orientation map; (d) TEM† BF image of nano-twins. CW 316L: (e) LOM image of deformation twins; (f) TEM BF images and SAED† pattern of deformation twins. Adapted from [40,58].

(Fig. 2.4e and f). These deformation-induced microstructural features have a strong impact on the corrosion properties of the steels exposed to liquid Pb or LBE, as will be described in detail in Chapter 3.

2.3. Other materials

While the two types of steels reviewed above constitute the bulk of the existing knowledge on the Pb/LBE corrosion resistance of LFR structural materials, we also provide a concise review of many other candidate materials proposed especially in the last two decades as potential improvements.

2.3.1. Oxide dispersion strengthened (ODS) steels

ODS-FeCr steels are defined by their unique microstructure, where nanoscale Y-Ti-O clusters are (ideally) uniformly dispersed in a fine-grained, ferritic (*bcc*) matrix [59]. These oxide nanoclusters are effective obstacles to dislocation motion, improving greatly the steel creep resistance at elevated temperatures when compared to dispersoid-free F/M steels (e.g., T91). Furthermore, the abundant nanoclusters/matrix interfaces provide sinks for radiation-induced defects [60], enhancing the steel resistance to irradiation embrittlement and void swelling, in addition to pinning GBs and maintaining a fine-grained microstructure that is associated with higher strength [61]. In particular, ODS-FeCrAl steels [62] combine the advantages of ODS-FeCr steels with the possibility of forming passivating alumina (Al_2O_3) scales due to the addition of Al; alumina is stable at very low oxygen potentials, hence preventing dissolution corrosion of the bulk steel, and making this steel type a very appealing candidate fuel cladding material for LFRs. Nevertheless, two important challenges associated with the use of ODS-FeCrAl steels are that mature industrial-scale manufacturing methods and joining technologies are not yet widely available. Joining is a particular challenge, as it alters the performance-defining dispersion of fine oxide particles in the steel, even though recent advances in joining technologies, such as friction stir welding, are beginning to show progress [63]. In addition, LME may be a serious issue for this type of *bcc*-structured steels at low temperatures (see Section 5).

2.3.2. Refractory metals

Refractory metals, such as W, Mo, Nb, and Ta, are attractive materials for engineering applications at elevated temperatures, due to their high melting points and excellent strength. These materials have good creep resistance, void swelling resistance, and very low solubility in oxygen-poor liquid Pb and LBE. In this regard, they show potential for future use in LFRs. However, their application in a nuclear system is challenged by their strong susceptibility to low-temperature irradiation embrittlement, weak oxidation resistance (potentially problematic for use in HLMs with high oxygen contents), bad weldability, and manufacturing difficulty [64].

2.3.3. SiC fibre-reinforced SiC matrix composites (SiC_f/SiC)

SiC_f/SiC composites have many appealing properties, such as good radiation tolerance with limited (~1%) radiation swelling up to ~1200 °C [65], high mechanical strength and creep resistance at elevated temperatures, good oxidation resistance, neutron transparency, and good chemical compatibility with both liquid Pb and LBE [31,66], which make these materials good potential candidates suitable for diverse LFR applications. However, specific technical issues render SiC_f/SiC composites a long-term material concept only. For instance, fuel cladding tube hermeticity is not yet fully guaranteed, even though significant progress has been achieved with fuel cladding tube concepts, such as the CEA sandwich design, where a ductile metal liner is deliberately introduced between two SiC_f/SiC composite layers, or highly dense SiC_f/SiC composites produced by liquid phase sintering (LPS), e.g., the nano-infiltration and transient eutectic phase (NITE) process [67]. Due to the brittle nature of monolithic SiC ($K_{Ic} \approx 2.5$–3 MPa·$m^{1/2}$ [68]), the SiC matrix undergoes microcracking at low stress levels, thereby compromising the hermeticity of SiC_f/SiC composites in service. In addition, the persistent lack of mature joining approaches and cost-effective manufacturing technologies, capable of producing SiC_f/SiC composites on an industrial scale, are challenges that must still be addressed.

2.3.4. The MAX ($M_{n+1}AX_n$) phases

The MAX phases are ternary carbides and nitrides described by the general formula $M_{n+1}AX_n$ (n = 1, 2 or 3), where M denotes an early transition metal, A is an element from groups 13–16 in the periodic table of elements, and X is either C or N [69–71]. The MAX phases have an *hcp* nanolayered crystal structure (*$P6_3/mmc$* space group), which is responsible for their unique properties, some characteristic of ceramics and some of metals. Depending on their exact stoichiometry, the MAX phases can exhibit significant thermal stability, high strength, good thermal and electrical conductivity, appealing damage tolerance, low hardness, and machinability comparable to that of graphite. Their properties are primarily defined by the choice of the M, A and X elements, but also by the factor n in the $M_{n+1}AX_n$ formula, giving rise to the 211, 312, and 413 sub-groups of the MAX phase ceramics for n equal to 1, 2, and 3, respectively (Fig. 2.5) [72]. For nuclear applications close to the reactor core (e.g., fuel cladding tube coatings), a crude elemental preselection for candidate MAX phases excludes elements with high neutron cross-sections, such as Hf, Ta, Mo, etc., as the use of MAX phases containing large fractions of such elements might be accompanied by a financially non-viable neutronic penalty. Quite importantly, the possibility of making MAX phase solid solutions by partially substituting the M, A and/or X elements in the $M_{n+1}AX_n$ formula with other elements (e.g., M', A', and/or X') allows the precise tailoring of their properties (phase purity, coefficient of thermal expansion, oxidation/corrosion resistance, radiation response, etc.), so as to meet the property requirements of the end application [73–77].

The LMC resistance of MAX phases compounds was first assessed for Ti_2AlC and Ti_3SiC_2 in contact with static liquid Pb and LBE [78–82], while Utili et al. [80] exposed Ti_3SiC_2 to flowing ($v \approx 1$ m/s) liquid Pb, in order to explore the idea of using such a material for

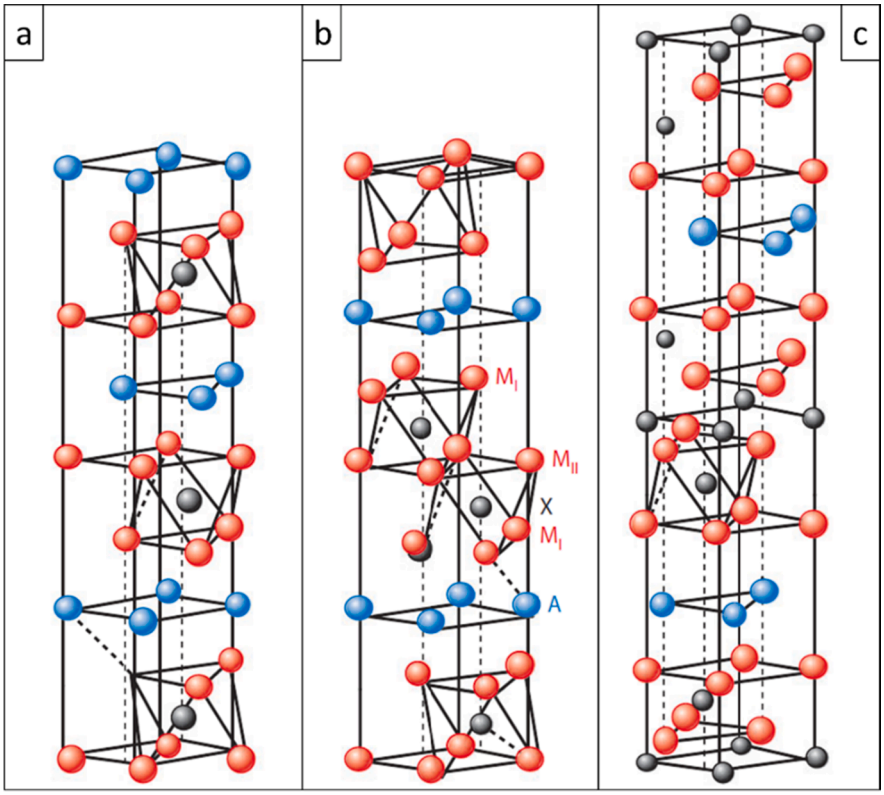

Fig. 2.5. The unit cells of the MAX phases in the (a) 211, (b) 312, and (c) 413 sub-groups of this family of nanolaminated ceramics. Adapted from [72].

the construction of Gen-IV LFR pump impellers. Later, Lapauw et al. [83] exposed a range of MAX phase ceramics for 1000–3500 h at 500 °C to oxygen-poor, static ($C_O \leq 2.2 \times 10^{-10}$ wt%) and fast-flowing ($v \approx 8$ m/s; $C_O \approx 5 \times 10^{-9}$ wt%) liquid LBE, demonstrating that the quasi phase-pure $(Nb,Zr)_4AlC_3$ MAX phase ceramic possessed excellent resistance to both dissolution corrosion and erosion/corrosion (see also Section 5). The relatively low fracture toughness of MAX phase-based ceramics, albeit considerable for ceramic materials, is most likely insufficient for structural applications that would demand their use in a monolithic form; e.g., the highest fracture toughness ever reported for MAX phase ceramics was $K_{IC} \approx 17.9$ MPa·m$^{1/2}$ for highly textured Nb_4AlC_3 [84]. Moreover, the MAX phases are characterised by a quite remarkable neutron radiation tolerance at temperatures >600 °C [85–89], making them appealing for Gen-IV LFRs with nominal operation temperatures higher than 600 °C. Fig. 2.6a shows that GBs in Ti_3SiC_2 neutron-irradiated to 3.4 dpa at 735 °C act as sinks for irradiation-induced defects, establishing large (>1 μm) defect-denuded zones next to

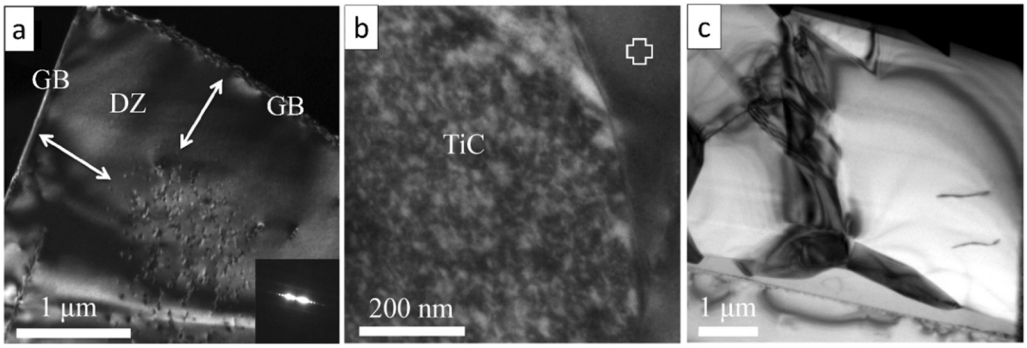

Fig. 2.6. TEM† BF images of Ti_3SiC_2, neutron irradiated to 3.4 dpa at 735 °C (a, b) and 1085 °C (c). (a) Large defect-denuded zones (DZ, arrows) next to GBs suggest that the latter act as sinks for radiation-induced defects, showing the self-healing potential of the MAX phases. (b) The strong mottled contrast indicating radiation damage in the parasitic TiC grain makes a sharp contrast to the defect-free neighbouring Ti_3SiC_2 grain (cross). (c) Defect-free Ti_3SiC_2 grains irradiated at 1085 °C suggest the effective self-healing of radiation-induced defects at elevated temperatures. Adapted from [87].

the GBs, indicative of the self-healing capacity of the MAX phases. Under identical irradiation conditions, grains of parasitic TiC show strong irradiation damage next to defect-free Ti_3SiC_2 grains (Fig. 2.6b). At higher irradiation temperatures (i.e., 1085 °C), Ti_3SiC_2 appeared to be essentially defect-free (Fig. 2.6c). Considering their advantages and disadvantages, the future use of MAX phase ceramics in Gen-IV LFRs is expected to be possible for select applications, such as protective coatings for fuel cladding tubes, pump impeller blades, bearings and bushings, etc. It is also quite clear that the inherent shortcomings of any structural material can, to a certain extent, be circumvented by smart engineering design that exploits the material's strengths and avoids its loading in an unfavourable manner during service in harsh environments [90].

3. Liquid metal corrosion (LMC)

This chapter provides a general phenomenological description of LMC effects in nuclear grade steels, including the main factors affecting the severity of such effects and the basic characteristics of the most important LMC processes expected to occur in Gen-IV LFRs. Particular attention is paid to the LMC effects observed in the F/M steels and AuSS discussed in Chapter 2. A detailed review of the different LMC mechanisms and their main characteristics is provided, followed by a comprehensive review of the key factors affecting the LMC behaviour of the main candidate structural steels for Gen-IV LFRs. The LMC behaviour of other candidate materials, such as oxides and ternary carbides (MAX phases), is addressed in Chapter 5.

3.1. General phenomenological description of LMC

LMC is a potentially severe structural materials degradation effect occurring when such materials are exposed to a HLM coolant, e.g., liquid Pb and/or liquid LBE. The magnitude of the performance degradation of the affected material depends on the extent of physical/chemical interaction at the material/HLM interface [29,30,91]. Thus, factors relating to both materials (typically, steels for LFRs) and HLMs have an impact on the operating LMC processes. These factors include: the steel homogeneity in terms of chemical composition, crystal structure, microstructure, deformation-induced defects, etc.; the HLM concentration of dissolved oxygen, impurities (either dissolved or in the form of solid particles), temperature, and type of flow (laminar, turbulent, eddies); and the duration of the intended component-specific steel/HLM interaction. It is worthwhile mentioning that high HLM flow velocities and turbulent flow reduce the thickness of the fluid boundary layer of quasi-static HLM flow [91], promoting material losses due to flow-assisted LMC effects. Moreover, liquid Pb- and LBE-cooled nuclear systems must be designed to minimise instabilities (eddies) in the HLM flow pattern, as the latter are likely to cause locally enhanced LMC effects.

LMC effects may be divided into uniform and localised [29]. Uniform corrosion is characterised by the uniform steel damage (in terms of thickness of the affected zone and the active corrosion mechanism) across the component surface, while localised corrosion is characterised by the locally enhanced steel damage (e.g., 'pitting'); the latter occurs preferentially at pre-existing steel defects (e.g., grain and twin boundaries), chemical inhomogeneities (e.g., chemical banding), and secondary steel precipitates (e.g., oxides, sulphides, carbides, δ-ferrite in AuSS). For steels in contact with liquid Pb or liquid LBE, the following basic LMC mechanisms may be

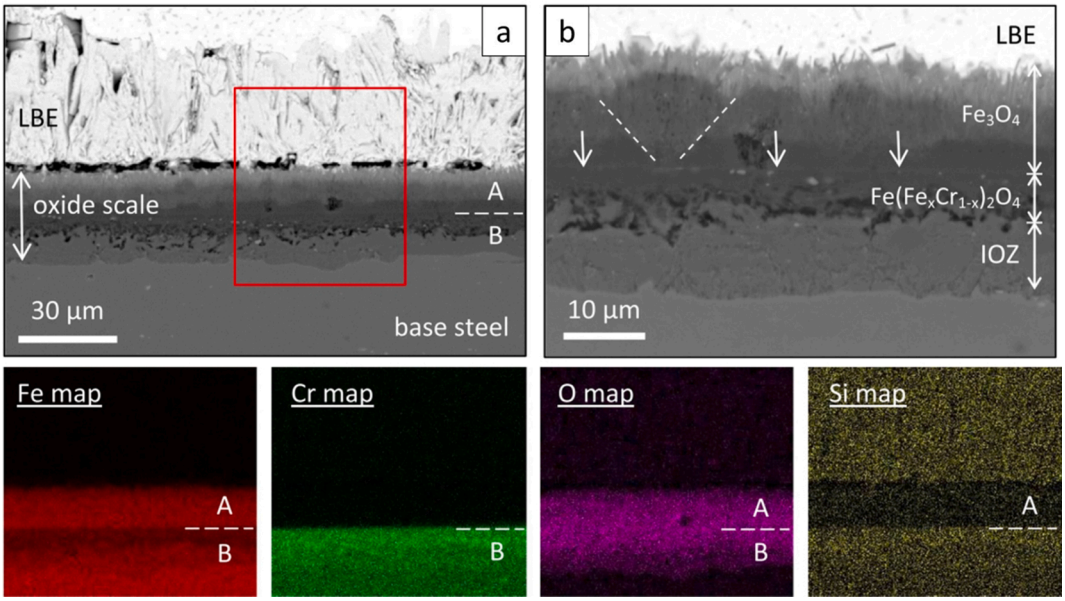

Fig. 3.1. SEM† images of the complex oxide scale on Si-doped EP-823 F/M steel exposed to oxygen-rich, static LBE at 490 °C for 5016 h. The oxide scale consists of magnetite (Fe_3O_4; area A), FeCr-spinel ($Fe(Fe_xCr_{1-x})_2O_4$) & IOZ† (area B). EDS† maps show no Si in magnetite. This oxide scale shows fine porosity at the FeCr-spinel/IOZ interface. Adapted from [92].

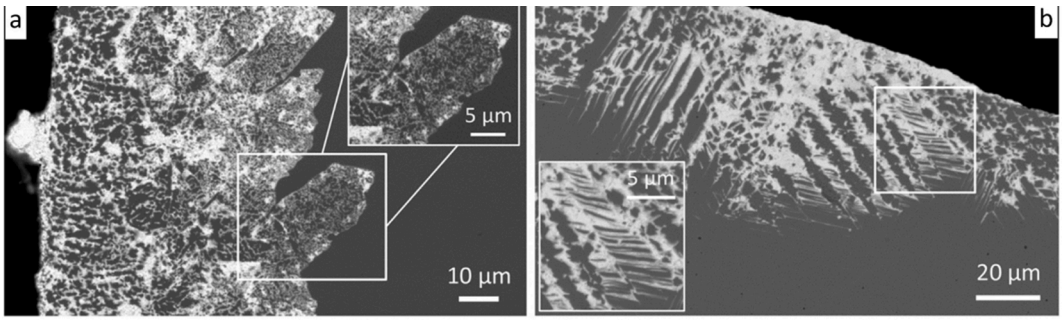

Fig. 3.2. SEM† images of 316L AuSS exposed to oxygen-poor ($C_O < 10^{-8}$ wt%), static LBE at 500 °C: (a) a SA† steel exposed for 3282 h, and (b) a CW† steel exposed for 1000 h. The LBE does not penetrate into the 316L AuSS perpendicularly to the steel surface, but follows preferred ingress paths, such as grain/twin boundaries. Adapted from [40].

distinguished: oxidation, dissolution, and erosion; all mechanisms can be either uniform or localised.

Oxidation occurs when the liquid Pb or LBE contains sufficient dissolved oxygen to cause the *in situ* formation of oxide scales on the steel surface. Scanning electron microscopy (SEM) images of the multi-layered oxide scale found on a Si-doped Russian EP-823 F/M steel (Table 2.1) exposed to static liquid LBE are shown in Fig. 3.1 [92]; EP-823 F/M steels were originally designed for LBE-cooled reactors. When oxide films are thin, dense and defect-free, adherent, resistant to spontaneous spallation, and possess low metal/oxygen diffusivities at reactor-relevant temperatures, they are expected to protect the substrate steel from further LMC attack. However, as oxide scales grow in thickness, heat transfer can be inhibited due to the typically low thermal conductivity of oxides. This is important for reactor components with a heat exchanging function, such as fuel cladding tubes and heat exchanger tubes: fuel cladding tubes must transfer heat from the fuel to the primary coolant, while heat exchanger tubes must do the same from the primary to the secondary coolant. Knowing the oxidation kinetics (as a function of temperature and HLM oxygen concentration) of the steels used to construct such components is important, as the component lifetime is determined by a certain oxide thickness above which heat transfer efficiency is restricted substantially.

When the amount of dissolved oxygen in liquid Pb or LBE is low, the formation of stable and defect-free oxide scales on steel surfaces is inhibited, and dissolution corrosion becomes the predominant LMC process. An example of dissolution corrosion in 316L AuSS (Table 2.2) exposed to liquid LBE is shown in Fig. 3.2 [40]. The severity of dissolution corrosion increases with temperature due to the fact that the solubility of steel alloying elements in the HLM increases with temperature [29,93]. Dissolution corrosion is particularly important for steel alloying elements with high solubilities in liquid Pb or LBE, such as Ni, Mn, and Cr; for example, Ni can be soluble up to 10 at% in liquid LBE at 700 °C [29]. Therefore, all steel grades containing high concentrations of such elements, such as the 316L and 15-15Ti AuSS, are susceptible to dissolution corrosion [40,43,44]. The species that dissolve in the hotter parts of the

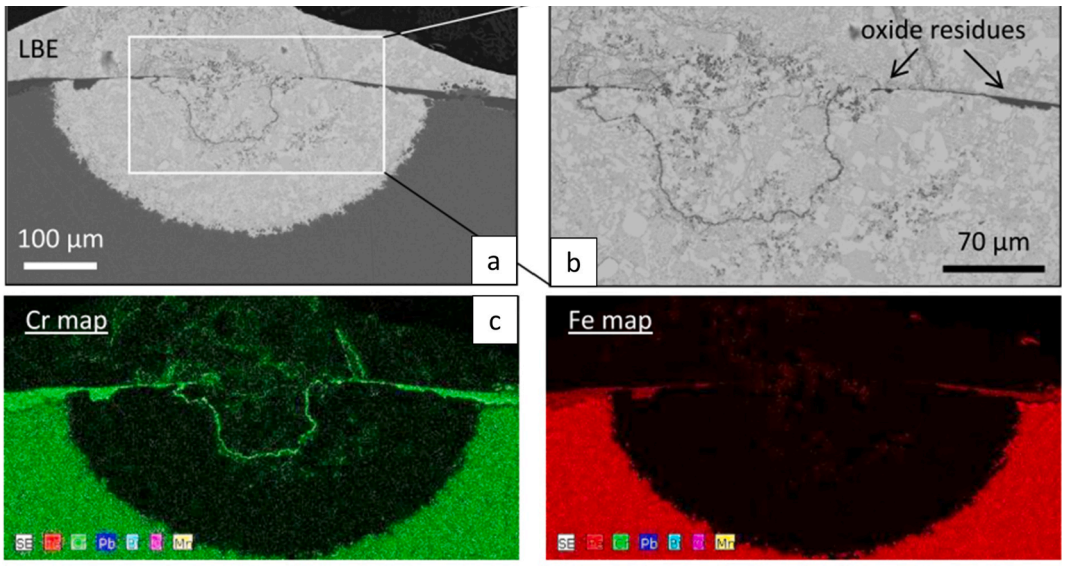

Fig. 3.3. (a-b) SEM† images of a deep (~227 µm) dissolution 'pit' in a EUROFER-97 F/M steel exposed to flowing ($v \approx 1.8$ m/s) LBE with $C_O \approx 2.3 \times 10^{-6}$ wt% at 550 °C for 3000 h. (c) EDS† elemental maps reveal residues of FeCr-spinel oxide scales still covering the largest part of this site of locally enhanced LBE dissolution attack. Adapted from [92].

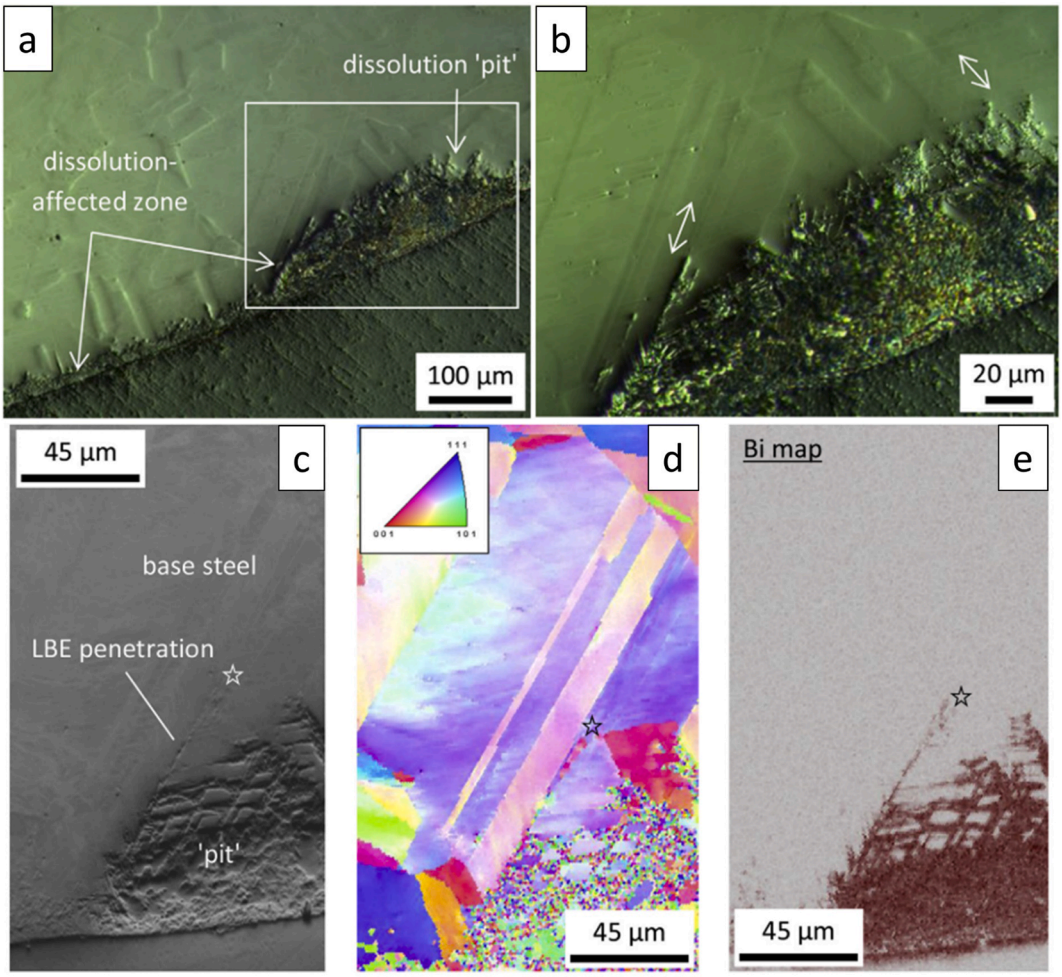

Fig. 3.4. Site of locally enhanced dissolution corrosion ('pit') in a 316L AuSS exposed to oxygen-poor ($C_O < 10^{-8}$ wt%), static LBE at 500 °C for 1000 h. The 'pit' depth exceeds 80 µm, while the depth of dissolution attack in its immediate vicinity is <30 µm. The 'pit' formation is associated with the local convergence of annealing twin boundaries in large steel grains close to the steel surface. (a-b) LOM† images; (c) SEM† image; (d) EBSD† grain orientation map; and (e) EDS† map of the 'pit'. Adapted from [40].

reactor system can precipitate in the colder parts, due to the temperature dependence of elemental solubilities. Moreover, most steel alloying elements that dissolve in the oxygen-containing HLM can oxidise, forming oxide particles that are transported by the HLM flow and may plug narrow flow paths (e.g., in the reactor core or the heat exchangers), jeopardising the safe operation of the nuclear reactor. Flow obstruction due to the plugging of flow paths by the deposition of solid corrosion products caused the failure of the first LBE-cooled USSR nuclear submarine K-27 (also known as the "project 645") in 1968 (this submarine was commissioned in 1963) [94]. Dissolution corrosion is accompanied by HLM ingress into the steel along preferred paths, such as GBs and twin boundaries (Fig. 3.2), leading to the ferritisation of the dissolution-affected zones in AuSS due to the (often selective) leaching of the austenite stabilisers Ni and Mn [40-42]. Preferential LBE penetration into grain/twin boundaries leads to the formation of sharp (notch-like) stress concentrators that facilitate crack nucleation under externally applied loads even in non-irradiated steels [95,96], while the ferritised (*bcc*) zones bear significant risk of LME due to the intimate contact between steel and HLM in these areas [40,41]. The detrimental effect of steel ferritisation is also reflected in the observed degradation of the creep properties of 316L steels exposed to liquid LBE [58]. The synergy of dissolution-induced ferritisation with LME in AuSS is expected to be exacerbated under neutron irradiation, due to the well-known irradiation embrittlement of these steels [97-100] that will ease crack initiation and propagation in the embrittled steel bulk.

In-service (mechanical, chemical) damage of the protective oxide scales or local prevention of their formation (e.g., in areas of low HLM oxygen concentration, such as crevices [92] and/or areas of quasi-static HLM) might lead to locally enhanced dissolution corrosion, known as 'dissolution pitting' [40,43,44,92,101]. Examples of dissolution 'pitting' for EUROFER-97 F/M [92] and 316L AuSS [40] steels exposed to liquid LBE are shown in Fig. 3.3 and Fig. 3.4, respectively. 'Pitting' might also be caused by local disturbances in the HLM flow pattern (e.g., local turbulences known as 'eddies' and/or sites of HLM flow diversion) or steel microstructural features (e.g., local convergence of annealing twin boundaries in coarse-grained steels [40], see for example Fig. 3.4), the accidental presence of which close to the steel surface is accountable for the occurrence of 'pitting'. Non-oxidising steel precipitates (e.

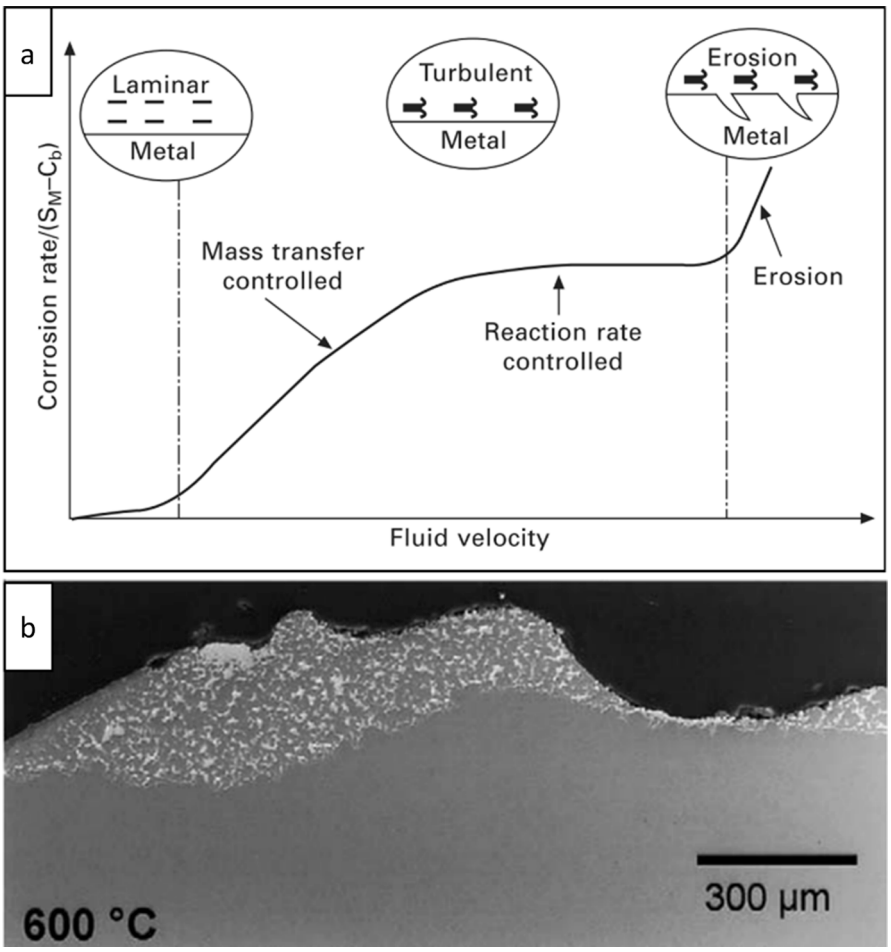

Fig. 3.5. (a) Corrosion mechanisms as a function of the HLM flow velocity [103]; (b) SEM† image of material losses caused by erosion/corrosion in 316L AuSS exposed to flowing LBE ($v \approx 2$ m/s, $C_O \approx 10^{-6}$ wt%) at 600 °C for 2000 h. Adapted from [104].

g., MnS [40]) might also result in 'pitting', not due to their own dissolution in the HLM, but due to the fact that the precipitate/steel matrix interface allows HLM ingress into the steel bulk, thereby attacking the otherwise passivated (i.e., *in situ* surface oxidised) steel surface. The presence of superficial oxide scales [40,92] or the fact that the steel is exposed to adequately oxygenated and flowing HLM (e.g., flowing LBE, $C_O \approx 2.3 \times 10^{-6}$ wt%, $v \approx 1.8$ m/s [92]) cannot prevent the occurrence of dissolution 'pitting'. It has been postulated by Schroer et al. [102] that the presence of defective (i.e., porous or otherwise damaged) oxide scales on the steel surface can promote the development of deep dissolution 'pits', as these oxide scales act as sinks for the inward diffusing oxygen, while allowing the outward diffusion of steel alloying elements and their eventual dissolution in the HLM, thereby maintaining elemental concentration gradients that sustain the further steel dissolution. The same authors suggested that the LBE penetrations become progressively depleted in oxygen as the 'depletion zone' deepens, inhibiting the precipitation of oxides inside this zone and promoting the continued outward diffusion of steel alloying elements, while the oxide scales (or residues thereof) are maintained on the steel surface, despite the unexpectedly deep 'pits' that are present underneath them (Fig. 3.3).

The relative importance of different LMC mechanisms at constant HLM oxygen potential and temperature depends mainly on the HLM flow velocity, v, as illustrated in Fig. 3.5a. At low HLM flow velocities (i.e., laminar flow), the overall corrosion rate is governed by the slow mass transfer of the dissolved species in the HLM boundary layer (i.e., boundary layer adjacent to the steel surface) rather than by the relatively faster dissolution/precipitation reactions at the solid/liquid (i.e., steel/HLM) interface. In this case, the corrosion rate increases with increasing HLM flow velocity. When the HLM flow velocity increases above a certain level, the mass transfer in the HLM boundary layer is accelerated and stops being the rate-controlling process. In this case, the corrosion rate is controlled by the corrosion reactions at the HLM/steel interface, and these are activation-controlled processes independent of the HLM flow velocity. Upon further increase of the HLM flow velocity, erosion and erosion/corrosion (the latter refers to higher HLM temperatures, where the erosive removal of any oxide scales is typically combined with dissolution corrosion of the unprotected steel) become the predominant mechanisms. Erosion may be considered as the mechanical ablation of a steel component exposed to a fast-flowing HLM, and it is often observed when the HLM transports hard solid particles (oxides, carbides) that act abrasively on the steel surface (this is broadly known as "two-phase flow") and at sites of HLM flow diversion or local disturbances in the HLM flow pattern (e.g., 'eddies').

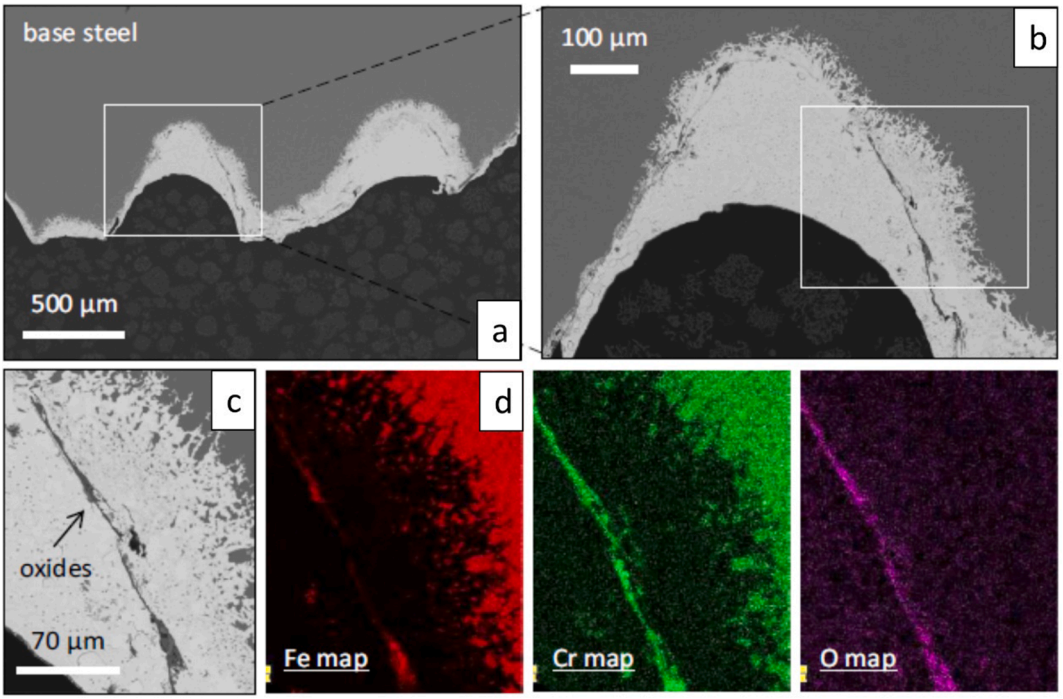

Fig. 3.6. Enhanced local LBE dissolution attack in an ODS-EUROFER-97 ferritic steel exposed to flowing ($v \approx 2$ m/s) LBE with $C_O \approx 1.4–1.6 \times 10^{-6}$ wt% at 550 °C for 5012 h. LBE dissolution attack occurs in the narrow space ('crevice') between the screw threads connecting two cylindrical specimens with each other. (a-c) SEM† images, and (d) EDS† maps of areas of interest. Adapted from [92].

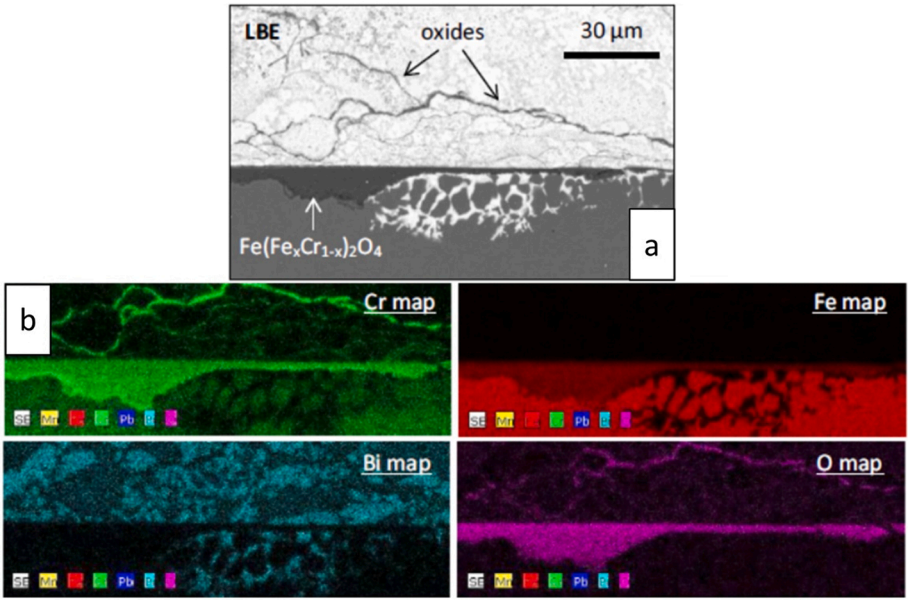

Fig. 3.7. EUROFER-97 F/M steel exposed to flowing ($v \approx 1.8$ m/s) LBE with $C_O \approx 2.3 \times 10^{-6}$ wt% at 550 °C for 3000 h. The FeCr-spinel oxide scale did not prevent the local occurrence of dissolution corrosion; presumably, a defect in the oxide scale allowed the ingress of LBE, which decorated the oxide/steel interface and attacked intergranularly the steel. (a) SEM† image, and (b) EDS† maps of the area of interest. Adapted from [92].

Erosion and erosion/corrosion may lead to severe material losses and possible compromise of the structural integrity of the affected reactor components. An example of material losses caused by erosion/corrosion in 316L AuSS exposed to flowing LBE at 600 °C is shown in Fig. 3.5b. Under certain conditions, bubbles present in the fast-flowing HLM can collapse on the steel surface, creating microjets and locally high stresses, which can destroy that surface within a short period of time [29].

In addition to the basic LMC mechanisms described above, fretting wear is a quite special and important corrosion mechanism responsible for many failures observed in fuel assemblies of commercial NPPs. Fretting wear is also expected to occur in liquid Pb- or LBE-cooled fast reactors, due to the friction between fuel pins and spacer wires in wire-wrapped fuel bundles. This type of corrosion can destabilise protective oxide scales, facilitating steel dissolution attack under crevice corrosion conditions, i.e., in the narrow spaces between spacer wires and fuel pins [37-39]. An example of crevice corrosion observed in an ODS EUROFER-97 ferritic steel exposed to oxygen-containing ($C_O \approx 1.4–1.6 \times 10^{-6}$ wt%), flowing LBE ($v \approx 2$ m/s) at 550 °C for 5012 h is shown in Fig. 3.6 [92].

In reality, one may expect the simultaneous operation of more than one LMC mechanisms, depending on the local exposure conditions (temperature, HLM C_O and flow velocity/pattern) experienced by a specific steel component in service. Fig. 3.7 shows the simultaneous local occurrence of oxidation and dissolution corrosion in a EUROFER-97 F/M steel exposed to oxygen-containing ($C_O \approx 2.3 \times 10^{-6}$ wt%), flowing LBE ($v \approx 1.8$ m/s) at 550 °C for 3000 h [92].

3.2. LMC mechanisms

The principal LMC mechanisms affecting the in-service performance of nuclear steels are oxidation, dissolution, and erosion. Oxidation occurs when a steel is brought into contact with an oxygen-containing HLM; oxidation is a desirable form of corrosion, provided that the oxide scale covering the steel surface is not too thick to degrade the steel thermal conductivity (important for reactor components with a heat exchanging function, such as fuel cladding and heat exchanger tubes) and the oxide scale remains protective throughout the component lifetime, preventing the further HLM attack of the steel bulk. Dissolution corrosion takes place in the absence of oxide scales (e.g., when the HLM oxygen concentration is too low to allow the formation of protective oxide scales, or when the oxide scales are locally damaged), and consists in the solution-based transfer of steel alloying elements into the HLM and the concurrent HLM penetration into the steel bulk. Erosion typically occurs at high HLM flow velocities, at sites of HLM flow diversion, and in cases of two-phase flow (i.e., when hard insoluble particles, such as oxides and carbides, are carried by the HLM flow, acting abrasively on the steel surface), and may lead to severe material losses within rather short timeframes, compromising the structural integrity of the affected component. Due to their frequent in-service occurrence and extensive prior investigations, oxidation and dissolution corrosion will be addressed in detail in Sections 3.2.1 and 3.2.2. Reference will be made to flow-assisted corrosion (e.g., erosion, erosion/corrosion) and fretting wear in Sections 3.2.3 and 3.2.4, respectively.

3.2.1. LMC by oxidation

The presence of an adequate amount (the exact amount is temperature-dependent) of dissolved oxygen in the HLM, C_O, is necessary to form oxide scales – often not fully protective or passivating – on the surface of steels exposed to liquid Pb/LBE. In the case of dissolved water (H_2O) vapour in the HLM, a decomposition reaction takes place, whereupon a temperature-dependent equilibrium is established between water vapour and the corresponding hydrogen (H_2) and oxygen (O_2) decomposition products. The relative amounts of H_2 and O_2 in the HLM can be controlled by the deliberate addition of gaseous H_2 or O_2 to the HLM to render it reducing or oxidising, respectively. This is broadly known as HLM "conditioning" and it is the basic principle of the 'active oxygen control' LMC mitigation approach, which is explained in Section 5.2. The following paragraphs review the thermodynamics of steel oxidation in HLMs, and provide a phenomenological description of oxidation effects in F/M and AuSS structural steels.

3.2.1.1. Thermodynamics of steel oxidation. The oxygen concentration dissolved in liquid Pb or LBE, C_O, is a critical parameter affecting the corrosion behaviour of structural steels, as the formation of passive oxide scales depends strongly on the HLM oxygen potential or the oxygen partial pressure in the gas plenum, which is in thermodynamic equilibrium with the HLM. Fig. 3.8 is a simplified representation of the effect of HLM oxygen concentration on the relative occurrence of dissolution and oxidation in two AuSS tested in flowing liquid Pb at 550 °C for 3000 h [105,106]. This figure shows that dissolution corrosion (named 'liquid metal corrosion') prevails at Pb oxygen concentrations $<10^{-7}$ at.%, while oxidation is the predominant corrosion process at Pb oxygen concentrations $>10^{-6}$ at.%. In the "transition zone" (roughly between 10^{-7} at.% and 10^{-6} at.% oxygen), both oxidation and dissolution are expected, but at a clearly slower corrosion rate (considering the reduced corrosion depth), presenting the possibility of limiting the overall corrosion rates in LFRs by carefully controlling the HLM oxygen potential. Similarly, Klok et al. [107] reported that the onset of dissolution corrosion in a SA 316L AuSS exposed to static liquid LBE at 450 °C for 1000 h occurred in the $C_O \approx 10^{-7}–10^{-6}$ wt% range, while oxidation was the predominant LMC mechanism at $C_O \approx 10^{-5}$ wt%. Moreover, Giuranno et al. [108] reported that the prevailing LMC mechanism in T91 F/M steels exposed to liquid Pb at 550–650 °C for 550 h changed from oxidation in oxygen-saturated HLM to mixed oxidation/dissolution, when the HLM oxygen concentration was reduced to $C_O \approx (9.2 \pm 3.6) \times 10^{-8}$ wt%. All these results indicate the important role of the HLM oxygen concentration in controlling the active corrosion processes.

When the amount of dissolved oxygen in the HLM is sufficient, oxide scales form on the steel surface, ideally shielding the steel bulk from HLM dissolution attack. For a system consisting of a metal (M) that reacts with oxygen (O_2) to form an oxide M_xO_y, the oxidation chemical reaction can be described as follows:

$$\frac{2x}{y}M_{(s)} + O_{2(g)} = \frac{2}{y}M_xO_{y(s)} \tag{3-1}$$

and the equilibrium constant for this reaction is:

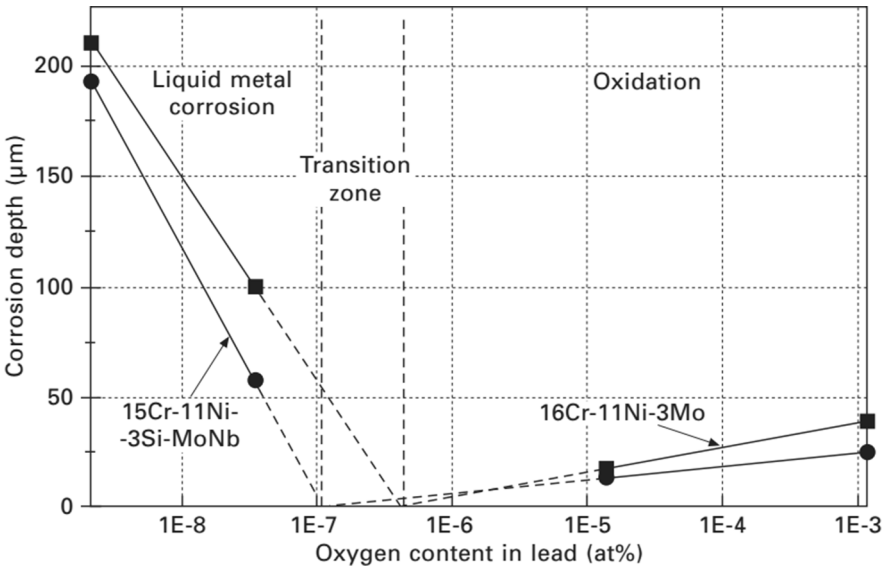

Fig. 3.8. Effect of the dissolved oxygen concentration on the LMC behaviour of two different AuSS exposed to liquid Pb for 3000 h at 550 °C [105,106]. Dissolution corrosion occurs at Pb oxygen concentrations $<10^{-7}$ at%, while oxidation is the prevailing LMC mechanism at Pb oxygen concentrations $>10^{-6}$ at%.

$$K = \frac{a_{M_xO_y}^{2/y}}{a_M^{2x/y} \cdot (P_{O_2}/P^o)} \tag{3-2}$$

where a_M is the activity of the metal ($a_M = 1$, for a standard state), $a_{M_xO_y}$ is the activity of the oxide ($a_{M_xO_y} = 1$, for a standard state), and P_{O_2} is the oxygen partial pressure in the gas plenum above the HLM, which, in turn, determines the HLM dissolved oxygen concentration. P^o is the reference pressure of the chemical potential of gaseous oxygen ($P^o = 1$ bar).

The change in the Gibbs free energy, ΔG, due to metal oxidation can be calculated by the standard Gibbs free energy of oxide formation ($\Delta_f G^o_{M/M_xO_y}$), and the equilibrium constant, K, as follows:

$$\Delta G = \Delta_f G^o_{M/M_xO_y} + RTlnK \tag{3-3}$$

Table 3.1
Thermodynamic data of the standard Gibbs free energy per mol O_2 for the formation of oxides from the main steel alloying elements and liquid Pb/Bi [109].

$\Delta_f G^o_{M/M_xO_y}(kJ \cdot mol^{-1}) = C + D(T/K)$		
	C	D
$\frac{4}{3}Bi(l) + O_2(g) \leftrightarrow \frac{2}{3}(\alpha - Bi_2O_3(s))$	−388.9 (299 ≤ T (°C) ≤ 715)	0.1959
$2Pb(l) + O_2(g) \leftrightarrow 2(\beta - PbO(s))$	−437.96 (339 ≤ T (°C) ≤ 838)	0.19926
$2Ni(s) + O_2(g) \leftrightarrow 2NiO(s)$	−473.75	0.1767
$2Ni(s) + 2Cr_2O_3(s) + O_2(g) \leftrightarrow 2NiCr_2O_4(s)$	−492.26	0.1868
$2Ni(s) + 2(\alpha - Al_2O_3(s)) + O_2(g) \leftrightarrow 2NiAl_2O_4(s)$	−486.53	0.1580
$2Fe(s) + O_2(g) \leftrightarrow 2FeO(s)$	−529.77 (T ≥ 570 °C)	0.1302
$\frac{3}{2}Fe(s) + O_2(g) \leftrightarrow \frac{1}{2}Fe_3O_4(s)$	−549.58 (T ≤ 570 °C)	0.1537
$6FeO(s) + O_2(g) \leftrightarrow 2Fe_3O_4(s)$	−608.94 (T ≥ 570 °C)	0.2241
$2Fe(s) + 2(\alpha - Al_2O_3(s)) + O_2(g) \leftrightarrow 2FeAl_2O_4(s)$	−640.28	0.1495
$2Fe(s) + 2Cr_2O_3(s) + O_2(g) \leftrightarrow 2FeCr_2O_4(s)$	−651.27	0.1495
$\frac{4}{3}Cr(s) + O_2(g) \leftrightarrow \frac{2}{3}Cr_2O_3(s)$	−751.22	0.1700
$Si(s) + O_2(g) \leftrightarrow SiO_2(s)$	−908.28	0.1782
$\frac{4}{3}Al(s) + O_2(g) \leftrightarrow \frac{2}{3}(\alpha - Al_2O_3(s))$	−1118 (200 ≤ T (°C) ≤ 800)	0.2096

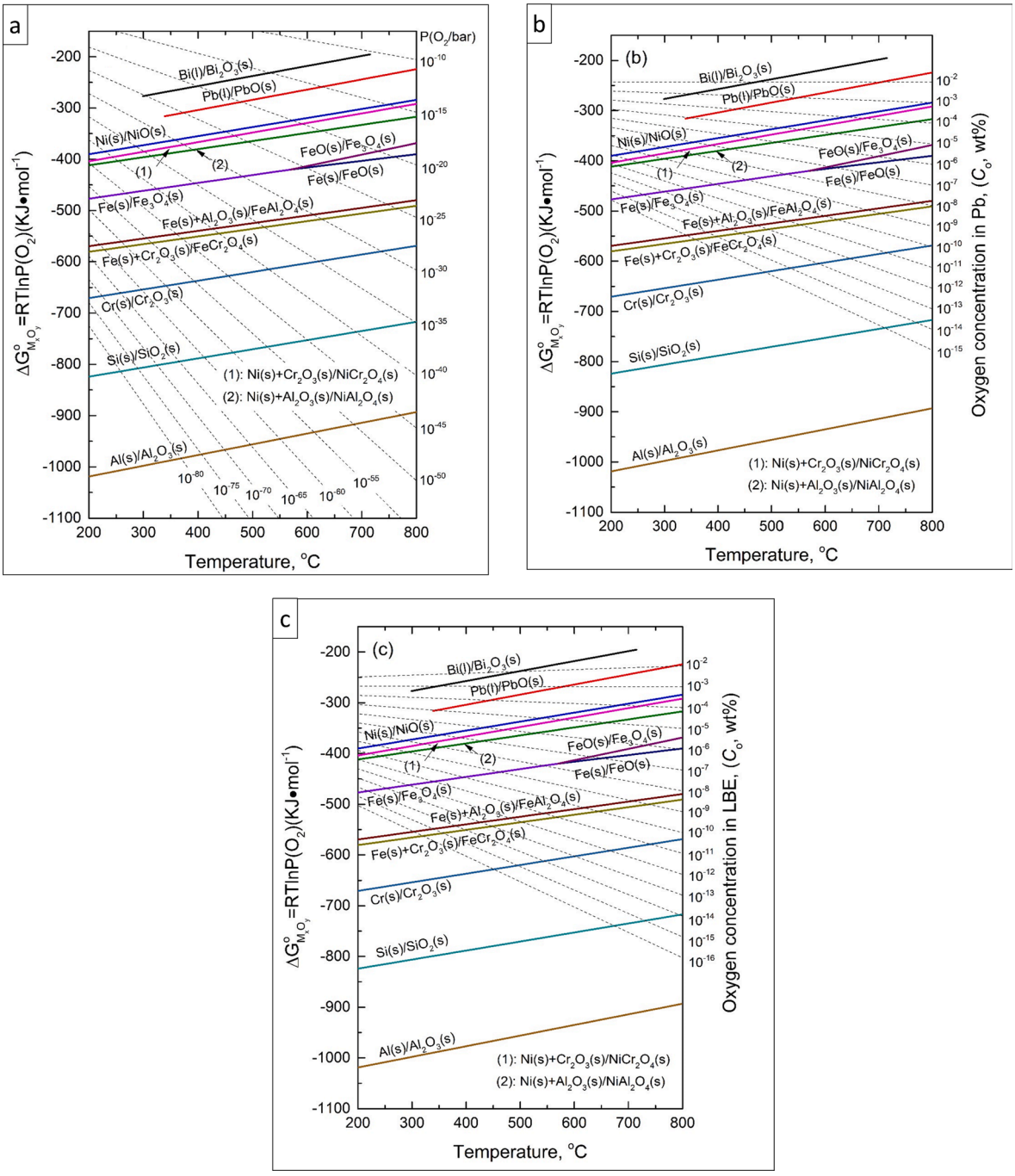

Fig. 3.9. Ellingham diagrams of the standard Gibbs free energy of oxide formation per mol O_2 (left *y*-axis) as a function of: (a) the oxygen partial pressure in the gas plenum above the HLM melt, (b,c) the concentration of dissolved oxygen in liquid Pb and liquid LBE, respectively, (right *y*-axis), and temperature (*x*-axis) for the formation of oxides due to the oxidation of the main steel alloying elements in liquid Pb and LBE. Adapted from [109].

where R is the ideal gas constant (8.3145 J/mol·K) and T is temperature (K). $\Delta_f G^o_{M/M_xO_y}$ is a function of temperature, according to the following expression:

$$\Delta_f G^o_{M/M_xO_y}(kJ \cdot mol^{-1}) = C + D(T/K) \tag{3-4}$$

where C and D are constants. The standard Gibbs free energy of oxide formation due to the reaction between steel alloying elements

and oxygen-containing liquid Pb or LBE has been summarised in Table 3.1 and plotted in Fig. 3.9a. Fig. 3.9a indicates the sequence in oxide formation at a specific temperature: the lower the position of an equilibrium line on the diagram, the easier the formation of the corresponding oxide.

According to the thermodynamic equilibrium criterion, once an oxidation process reaches equilibrium, the change in ΔG is equal to zero. Under this condition, combining Eqs. (3-2) and (3-3) yields the following equations:

$$\Delta_f G^o_{M/M_xO_y} = RTlnP_{O_2} \tag{3-5}$$

or

$$P_{O_2} = exp\frac{\Delta_f G^o_{M/M_xO_y}}{RT} \tag{3-6}$$

Eq. (3-6) indicates the threshold oxygen partial pressure for either oxide formation or dissociation. If the actual oxygen partial pressure is greater than a certain threshold value (the dashed lines plotted in a nomographic scale shown in Fig. 3.9a indicate fixed values of the oxygen partial pressure), the oxide scale corresponding to that threshold value will form. In the opposite case, the oxide is expected to undergo reduction/dissociation. It is worthwhile noting that silica (SiO_2) and alumina (Al_2O_3) have very low standard Gibbs free energies of formation (Table 3.1) and are stable at very low HLM oxygen potentials (Fig. 3.9b and Fig. 3.9c); therefore, they

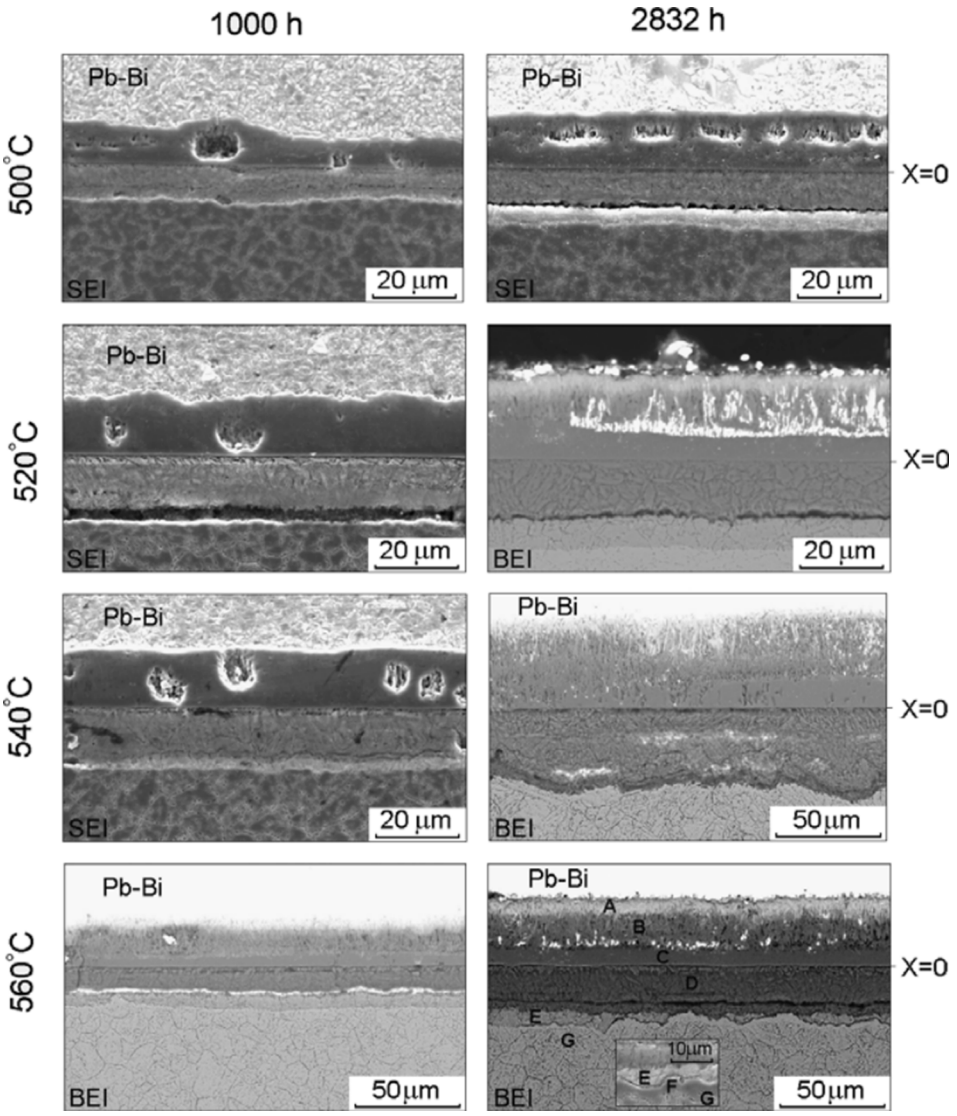

Fig. 3.10. SEM† images of oxide scales formed on T91 F/M steels exposed to oxygen-saturated, static LBE at different temperatures (500–560 °C) and for different durations (1000 h, 2832 h). "X = 0" denotes the initial position of the steel surface [125].

are very effective means of dissolution corrosion mitigation either by their *in situ* formation (e.g., as a result of the exposure of Si- or Al-alloyed steels to oxygen-containing liquid Pb/LBE) or when applied in the form of coatings on the steel surface (see Section 5).

One may use Henry's law (i.e., the relation between oxygen activity, a_o, and HLM oxygen concentration, C_O, can be described by: $a_o = k_H C_o$, where k_H is the Henry constant) and Sieverts' law (i.e., the fact that the HLM oxygen concentration, C_O, is proportional to the square root of the oxygen partial pressure, P_{o_2}, in the gas plenum above the HLM melt, i.e., $\sqrt{P_{O_2}} = kC_o$, where k is the Sieverts' constant) to correlate P_{o_2} (in bar) with C_O (in wt%) dissolved in liquid Pb and liquid LBE. This can yield the following two equations (for more details on the formula derivation, one is recommended to refer to [109]):

$$P_{O_2} = C_o^{\,2} \cdot exp\left\{9.1827 - \frac{29188}{T}\right\} \quad (liquid\ \ Pb) \tag{3-7}$$

$$P_{O_2} = C_o^{\,2} \cdot exp\left\{13.558 - \frac{32005}{T}\right\} \quad (liquid\ \ LBE) \tag{3-8}$$

Combining Eq. (3-6) with Eq. (3-7) or Eq. (3-8) allows plotting of the oxygen concentration dissolved in liquid Pb or LBE in a nomographic scale (right *y*-axis of Figs. 3.9b and c, respectively) as a function of temperature. Since the accurate determination of the oxygen partial pressure in the gas plenum is technically more challenging than the measurement of the HLM oxygen concentration by means of potentiometric oxygen sensors (see Section 5), Figs. 3.9b and c are practically more useful than Fig. 3.9a.

3.2.1.2. Characteristics of steel oxidation. Typically, the oxidation of F/M steels produces a duplex oxide scale structure with an internal oxidation zone (IOZ). The outer oxide scale layer is invariably magnetite (i.e., Fe_3O_4), while the inner oxide scale layer varies, depending on the steel composition (i.e., $Fe(Fe,Cr)_2O_4$ spinel, Cr_2O_3, SiO_2, and/or Al_2O_3). The outer magnetite layer is usually rather porous and will, thus, be infiltrated by the HLM within a certain period of time; in the case of liquid LBE, the HLM penetration appears to be a Pb-based solid solution made of >90 at.% Pb and a small amount of Bi [110]. The inner oxide scale layer is typically more protective than the outer magnetite layer, and its growth into the steel bulk is often preceded by the establishment of an IOZ† at its growth front. The IOZ is usually made of a Cr-based oxide (e.g., Cr_2O_3) that develops preferentially at martensitic lath boundaries [110]. It should be added that it has not yet been clarified whether the inner oxide layer is magnetite (an inverse spinel structure) with dissolved Cr or a Cr-deficient FeCr-spinel ($FeCr_2O_4$). In this review article, FeCr-spinel is used to distinguish the inner oxide scale layer from the outer, Cr-free, magnetite (Fe_3O_4) layer.

In the case the inner oxide scale layer is dense and defect-free, the transport mechanism accounting for the progress of corrosion is the outward metal diffusion and/or the inward oxygen diffusion through the oxide scale. Elemental diffusivity in dense oxide scales is typically ten orders of magnitude slower than in metals at the same temperature [111], effectively stopping corrosion in its tracks. On the other hand, the formation and growth of Cr-rich oxide scales on the steel surface generally give rise to Cr depletion in the steel underneath the oxide scales [112]. This might be problematic when the oxide scales fail locally, since the subsequent Pb/LBE penetration into the oxide scale cracks is likely to reach and affect the Cr-impoverished steel region under the oxide scales, especially when this region is Ni-enriched, since Ni is highly soluble in liquid Pb/LBE. In such cases, one might expect the quick decoration of the oxide/steel interface by the HLM, similar to that shown in Fig. 3.7 for a EUROFER-97 F/M steel exposed to liquid LBE; in the latter case, the decoration of the oxide/steel interface by LBE was not attributed to the Ni enrichment of that interface (EUROFER-97 is Ni-free; see Table 2.1), but to the fine-scale porosity present at that interface due to the counter-diffusion of elements needed for oxide scale growth [92]. Similar effects are expected in steels containing Si and/or Al, as regions depleted in corrosion-resistant elements are invariably observed next to the inner oxide scale layers [113]. In T91 and HT-9 F/M steels exposed to static liquid LBE ($C_O \approx 10^{-6}$ wt%) at 600 °C for 2000 h, a thin Cr-rich oxide was observed to re-form above the Cr-depleted steel region [114].

The oxide scale morphology depends strongly on the steel exposure conditions. As an example, Fig. 3.10 shows the evolution of the oxide scale structure observed on a T91 F/M steel exposed to oxygen-saturated, static LBE at different temperatures (500, 520, 540, and 560 °C) and for different times (1000 and 2832 h). The oxide scales forming on the steel surface typically consisted of an outer magnetite layer and an inner FeCr-spinel layer. After an exposure of 2832 h at 560 °C, the oxide scale showed six distinct zones, marked with the letters A, B, C, D, E, and F in Fig. 3.10. The A and B zones constituted a porous, columnar sub-layer of the multilayered oxide scale. Both zones contained multiple elements, such as Fe, O, Pb, and Bi. X-ray diffraction (XRD) revealed that zone A was composed of plumboferrites, i.e., $PbFe_{12}O_{19}$ and $PbFe_8O_{13}$, while zones B and C were magnetite (Fe_3O_4). Zone B was columnar, while zone C was dense and rather uniform. Zone D was made of FeCr-spinel (i.e., $Fe(Fe,Cr)_2O_4$), the inner boundary of which was marked by a thin porous band. Below the porous band, an IOZ layer formed (letter E). Generally, the growth of the IOZ layer was found to be independent of the total thickness of the three oxide scale sub-layers, and stopped after 2000 h of exposure [115], presumably due to the steel Cr depletion beneath the oxide scale. Layer F, located between the IOZ layer and steel substrate G, was depleted in Cr and O, as compared to the steel G and the IOZ layer E, respectively. It is interesting to note that the oxide sub-layers above and below the initial steel surface (marked by X = 0) were almost symmetrical, suggesting the interdependent development of these sub-layers. When the LBE oxygen concentration approached the level corresponding to the thermodynamic stability of magnetite, a typical duplex oxide scale (i.e., outer Fe_3O_4 & inner $Fe(Fe,Cr)_2O_4$) was observed, however, the plumboferrites disappeared [92,116,117]. These oxidation features described above also characterised other F/M steels containing 8–13 wt% Cr, such as HT-9 or EP-823 [118–124].

In some cases, the compact spinel oxide was penetrated by liquid LBE. Schroer et al. [115] observed the LBE ingress through cracks and open porosity in the FeCr-spinel scale, which resulted in LBE infiltration of that scale. As the steel exposure continued, the IOZ disappeared (Fig. 3.11). Ye et al. [126] emphasised the importance of a Cr-rich IOZ in the oxidation resistance of T91 F/M steels

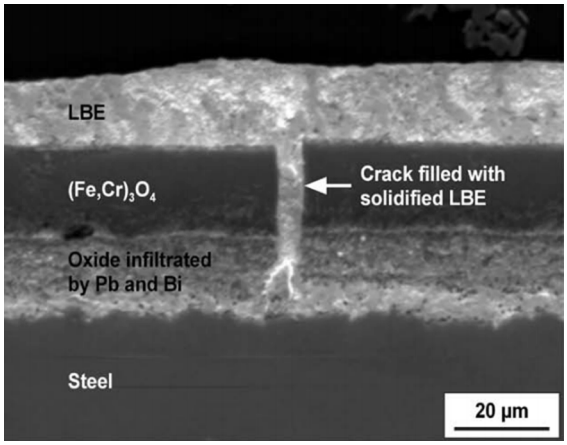

Fig. 3.11. SEM† image of LBE ingress into the spinel oxide scale on a T91 F/M steel after exposure to flowing LBE at 550 °C for 4015 h ($v \approx 2$ m/s; $C_O \approx 1.6 \times 10^{-6}$ wt%) [115].

exposed to oxygen-containing liquid LBE, and suggested methods to rapidly form the Cr-rich oxide scale, which greatly improves the steel oxidation resistance. Such methods include steel cold rolling to produce numerous microstructural defects that act as favourable paths for the outward Cr diffusion.

Hosemann et al. [127] employed atomic force microscopy (AFM) to examine the duplex oxide scale on a HT-9 F/M steel after its exposure for 3000 h at 550 °C to liquid LBE with $C_O \approx 10^{-6}$ wt% (Fig. 3.12). They found that both the magnetite and FeCr-spinel oxide scales had two different microstructures. The outer part of the magnetite layer (outer layer 1) had a columnar grain structure with grains oriented approximately perpendicularly to the steel surface, while the grains in the inner part of the magnetite layer (outer layer 2) were more equiaxed. The GBs of the columnar grains, pore-like defects, and crack-like features in the magnetite layer provided paths of easier LBE ingress. For the FeCr-spinel layer, the region next to the steel substrate was enriched in Cr.

The basic LMC behaviour of ODS-FeCr F/M steels was found very similar to that of conventional chromium (Cr) steels [128–131], however, the finer-grained ODS steels exhibited some differences in their overall corrosion behaviour. Yeliseyeva et al. [128] studied the corrosion behaviour of ODS Fe-9Cr-1.5W and Fe-14Cr-1.5W (Y_2O_3) steels in liquid Pb at 500–650 °C. They found that the fine-grained microstructure facilitated the formation of Cr-based oxide scales in oxygen-containing liquid Pb, due to the more abundant GBs acting as paths for fast Cr diffusion into the growing oxide scale, much like the effect of dislocation networks in cold-rolled F/M steels. Hosemann et al. [132] also observed a similar grain size effect on the corrosion properties of ODS steels exposed to liquid LBE. However, the positive effect of the finer grain size vanished when the ODS steels were exposed to oxygen-depleted liquid Pb. In that case, dissolution corrosion, which started intergranularly and was aided by the numerous GBs, was promoted instead. Moreover, the

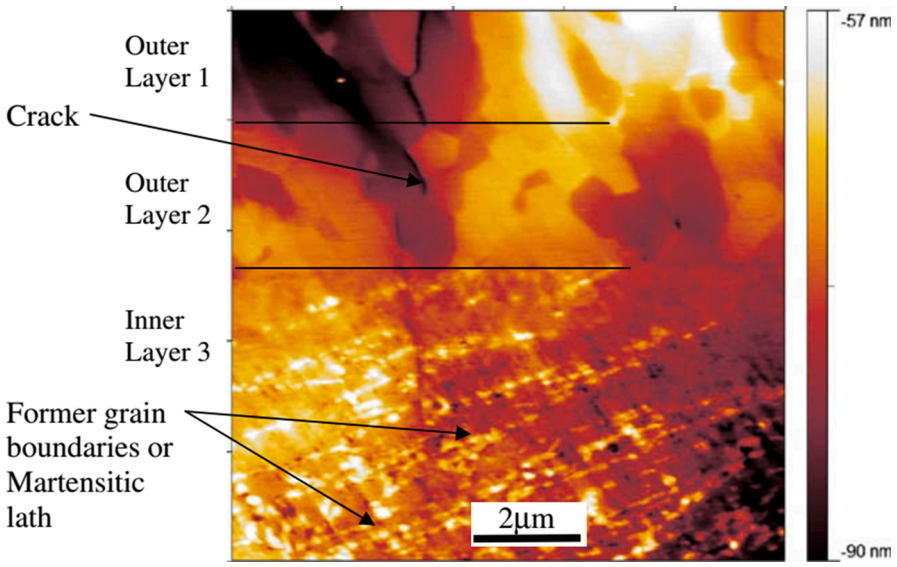

Fig. 3.12. AFM† image of the complex oxide scales formed on an HT-9 F/M steel exposed to liquid LBE with $C_O \approx 10^{-6}$ wt% at 550 °C for 3000 h [127].

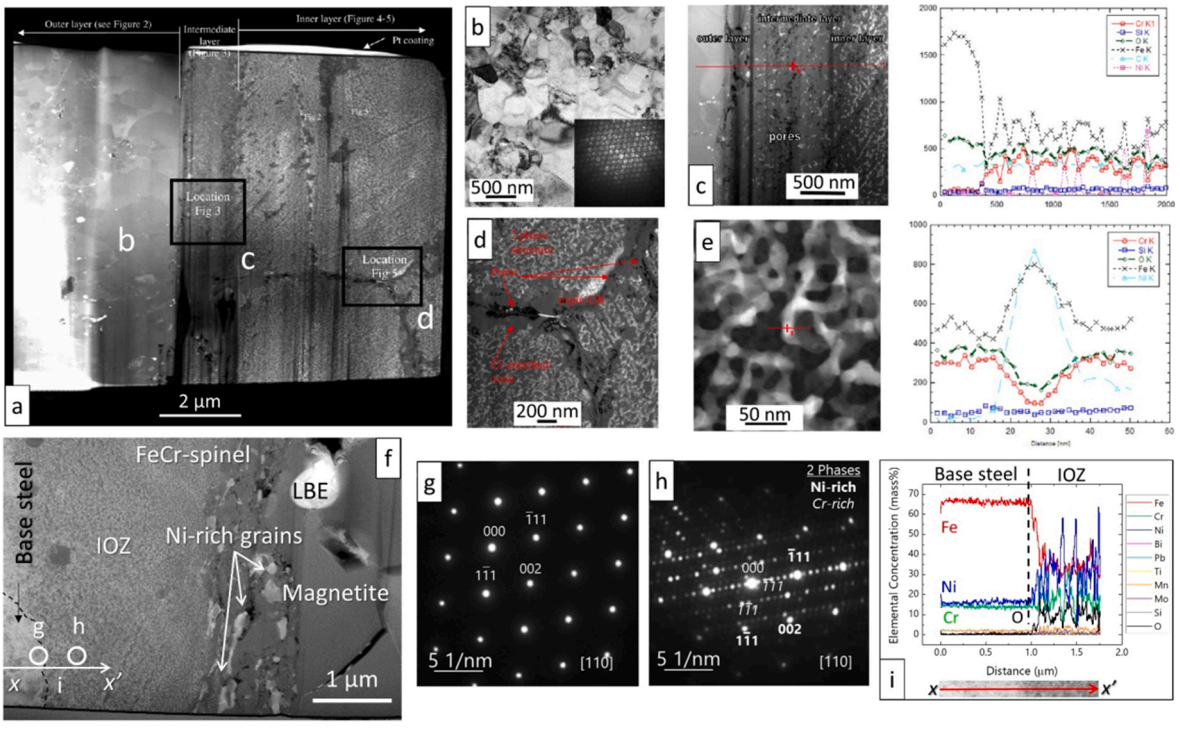

Fig. 3.13. (a) STEM-HAADF† overview of the oxide scales on D9 AuSS. (b) TEM† BF image of the outer oxide and SAED† pattern. (c) STEM† image of the intermediate oxide layer and EDS† line scan. STEM-HAADF images of the two-phase inner oxide layer: (d) overview, and (e) detail with EDS line scan. Test conditions: flowing LBE ($v \approx 2$ m/s), 550 °C, 3000 h, $C_O \approx 3–5 \times 10^{-6}$ wt%. Oxide scales on DIN 1.4970 AuSS exposed at 500 °C, for 1000 h, to static LBE with $C_O \approx 1 \times 10^{-6}$ wt%: (f) STEM-HAADF overview of the oxide scales; SAED patterns of the base steel (g) and the IOZ† (h); (i) STEM-EDS line scan across the base steel and the IOZ. Subfigures (a-e) and (f-i) are adapted from [138] and [142], respectively.

added oxide dispersoids resulted in an increased porosity of the internal oxide scale sub-layer, thereby accelerating oxidation kinetics [129]. The steel extrusion direction was also found to affect the morphology of the formed oxide scales [130].

The oxidation behaviour of AuSS was somewhat different from that of F/M steels [115,133,134]. The oxidation behaviour of this type of steels depended strongly on the exposure temperature. Below 450 °C, a very thin oxide scale formed, consisting of a single FeCr-spinel layer or Cr-based oxide, which was protective. Above 450 °C, the oxide layer evolved into a duplex- or single-layer structure that could prevent dissolution corrosion only temporarily, becoming susceptible to HLM dissolution attack after more prolonged exposures. Above 550 °C, the oxides became permeable to the HLM, losing their protectiveness and leaving the bulk steel exposed to HLM dissolution attack. This was partly attributed to the transformation of magnetite (Fe_3O_4) to wüstite (Fe_xO_{1-x}) at ~570 °C [135], with wüstite being far more porous and brittle than magnetite [136,137].

In-depth characterisation of the oxide scales forming on AuSS was first conducted by Hosemann et al. [138–140]. Their results showed that the oxide scales found on D9 fuel cladding AuSS exposed to LBE were more complicated than expected, and consisted of three different layers, as shown in Fig. 3.13(a-d). The outer layer consisted of ultra-fine, equiaxed Fe_3O_4 grains with a grain size varying between 100 nm and 1 µm. A few LBE inclusions were visible in the outer layer, which was characterised by a sparse overall distribution of pores and other defects. Below the magnetite layer, a 1 µm-thick, porous and Cr-rich spinel layer composed of Fe, Cr, and O (i.e., $Fe_xCr_{3-x}O_4$), with some dispersed Ni-rich phases, was observed. The inner oxide layer was a two-phase structure, consisting of a Cr-enriched phase, which was identified as FeCr-spinel, and a Ni-enriched phase, which was left unidentified in that study. Oxidation of the prior GBs inside the inner oxide layer led to the formation of a ~200 nm-wide Cr-rich phase. The same authors reported even more complicated oxide scales, consisting of four layers, on the surface of 316L AuSS exposed to flowing LBE ($v \approx 2$ m/s, $C_O \approx 10^{-6}$ wt%) at 550 °C for 3000 h [141]. Charalampopoulou et al. [142] elucidated further the structure of the inner oxide layer in a DIN 1.4970 fuel cladding AuSS, a compositionally similar steel to the D9 fuel cladding AuSS. They showed that the formation of the Ni-rich phases resulted from the selective removal of Fe and Cr from the steel matrix, so that the crystallographic orientation of the parent grains was maintained in the IOZ†, see Fig. 3.13(e-g). They observed that the IOZ lacked elemental gradients (Fig. 3.13h), thereby suggesting a spontaneous spinodal decomposition of the steel matrix into a Cr-rich spinel oxide and Ni-rich metallic phases in the IOZ, when the appropriate Fe/Cr/O ratio was locally achieved.

Charalampopoulou et al. [142] found that the oxide types and structures on a DIN 1.4970 fuel cladding AuSS exposed to static liquid LBE ($C_O \approx 10^{-6}$ wt%) for 1000 h also depended on the exposure temperature. Below 475 °C, double-layered oxide scales made of an outer magnetite layer and an inner Fe-Cr-O spinel layer were observed, along with face-centred cubic (*fcc*) Ni-enriched grains at the oxide/steel interface. These Ni-enriched grains were not oxidised and had the same *fcc* structure as the base steel, but with different

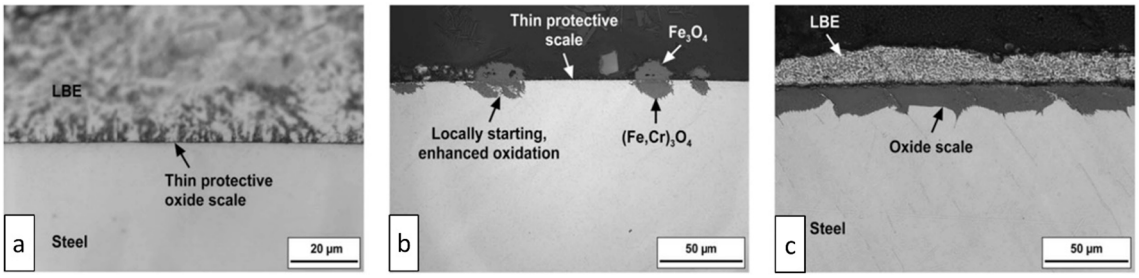

Fig. 3.14. SEM[†] images of oxide scale growth on 316L AuSS exposed to flowing LBE ($v \approx 2$ m/s) with $C_O \approx 1.6 \times 10^{-6}$ wt% at 550 °C for: (a) 503 h, (b) 4015 h, (c) 15,028 h. Adapted from [115].

crystal orientations from that of the grains in the neighbouring steel bulk. Above 475 °C, the formation of a complex triple-layered oxide was observed. The outer double-layered oxides did not change their basic structure, however, the magnetite layer grew thicker, while the FeCr-spinel layer with dispersed Ni-enriched grains became much thinner. At this relatively high temperature, an inner, thick IOZ formed, in addition to the outer duplex oxide scale. It was found that the IOZ consisted of a Ni-rich metallic *fcc* phase and a Cr-enriched (Cr-Fe-O) *fcc* spinel phase, and that both phases had the same crystallographic orientation with the unaffected steel bulk. Moreover, it was observed that the IOZ nucleated along {111} close-packed planes and the GBs of the base steel, which were decorated by a Cr-rich oxide and Ni-rich grains. The growth of the IOZ layer relied on the accelerated diffusion of O and Fe – and the resulting segregation of Cr and Ni – along fast elemental diffusion paths, such as grain and twin boundaries.

The oxidation of AuSS typically occurs more non-uniformly when compared to the oxidation of F/M steels. Fig. 3.14 shows the oxidation process of 316L AuSS exposed at 550 °C for 503 h, 4015 h, and 15,028 h to flowing ($v \approx 2$ m/s) liquid LBE with $C_O \approx 1.6 \times 10^{-6}$ wt%. After a short exposure of 503 h, thin oxides rich in Cr or Si formed on the steel surface. By prolonging the steel exposure to 4015 h, oxidation became non-uniform, with local oxide 'pits' that were partially filled with mixed FeCr-based oxides. As the exposure continued, the 'pits' grew and finally connected to form a continuous oxide scale that grew in thickness up to 20 µm after 4015 h of exposure. Such thick oxides are generally less protective than thin oxide scales. Non-uniform oxidation also manifests itself as preferential steel GB oxidation, whereupon a coarse-grained steel microstructure shows deeper oxide penetrations than a fine-grained microstructure [125]. Moreover, the oxide scales forming on 316L AuSS also depend on the HLM oxygen concentration. Steiner et al. [143] calculated the necessary amount of dissolved oxygen in liquid LBE to grow duplex oxide scales on 316L AuSS, and reported that the LBE oxygen concentration should be higher than $C_O \approx 5 \times 10^{-7}$ wt% in order to develop duplex oxides at 550 °C, otherwise, a single-layer FeCr-based oxide forms.

3.2.1.3. Mechanistic understanding and modelling of oxidation behaviour. Most of the mechanistic understanding and modelling of the oxidation behaviour of steels exposed to liquid Pb/LBE are based on the oxidation mechanisms established for metals exposed to other kinds of oxidising environments, such as steam [144–146], water [147,148], CO_2 [149–151], SO_2 [152], etc., since the oxides formed in the presence of all these oxidants are very similar. In the oxidation mechanisms and models established for these oxidising environments, a so-called "available space model" [144,146,147,152–160] is often adopted as a basis. This model postulates that the outward diffusion of metal cations leads to the formation of an outward growing oxide scale at the interface of the metal/oxidising environment, while generating vacancies at the oxide/metal interface. These vacancies coalesce into micro-cavities that may result in macroscopic porosity, eventually causing oxide scale decohesion. The oxygen species that diffuse through the oxide scales are found at the oxide/metal interface, thus, existing micro/nano-channels are proposed to play the role of oxygen transport paths; these channels can form either by dissociative/perforative growth [149,153,155,157,158] or crack formation due to internal/residual stresses [149,152,158]. The micro/nano-channels connect the cavities with the external oxidising environment, providing paths that allow the oxygen molecules to diffuse inwards and reach the cavities. The oxygen molecules react with the metal at the cavity walls, nucleating the inner oxide until the cavities are filled. This accounts for the discontinuous, nodule-like appearance of the innermost oxide layers

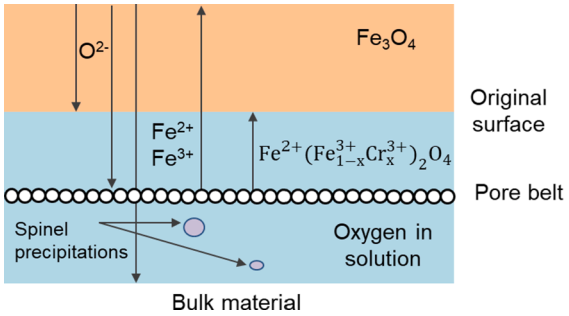

Fig. 3.15. Schematic representation of the oxidation mechanism of Fe-9Cr martensitic steels exposed to liquid Pb. Adapted from [133].

found in many steels exposed to oxygen-containing liquid Pb/LBE. Since the growth of the inner oxide depends on the free spaces produced by the outward diffusion of metal cations, the rate limiting step of the inner oxide growth is the outward metal cation diffusion.

Müller et al. [133] proposed a qualitative mechanism to explain the oxidation process in an Fe-9Cr martensitic steel (i.e., OPTIFER IVc) exposed to liquid Pb ($C_O \approx 8 \times 10^{-6}$ at.%) at 550 °C; the schematic representation of the oxidation mechanism is illustrated in Fig. 3.15. It is assumed that an FeCr-spinel oxide (described by the chemical formula $Fe^{2+}O[Fe^{3+}, Cr^{3+}]_2O_3$) forms first on the steel surface, growing inwards into the steel bulk. Once the spinel forms, Fe cations diffuse through the FeCr-spinel scale from the steel bulk to the surface, where they react with the oxygen dissolved in the HLM to form a magnetite (Fe_3O_4) scale that grows outwards. At the same time, oxygen diffuses inwards through the magnetite scale to react with the steel matrix, thus contributing to the inward growth of the spinel scale. The net diffusion flux of O and Fe ions is responsible for the growth kinetics of the duplex oxide scale made of FeCr-spinel and Fe_3O_4.

Zhang and Li [134] considered that the outer magnetite (Fe_3O_4) scale grows only at the oxide/LBE interface through the outward diffusion of Fe, while the inner FeCr-spinel scale develops at the oxide/steel interface, occupying the space vacated by the Fe outward diffusion. They also argued that a purely parabolic law cannot describe the oxidation kinetics of steels exposed to oxygen-containing LBE, because the removal of the outer magnetite directly in contact with LBE should be considered as well. Therefore, in their model, oxidation is governed by two independent processes, i.e., one is the Fe outward diffusion through the two oxide scales, and the other is mass transfer-controlled corrosion (e.g., erosion, dissolution corrosion) at the outer magnetite/LBE interface. Their oxidation model is built on the basis of Wagner's theory [161], while the effect of mass transfer-controlled corrosion is incorporated using the Tedmon model that was initially developed to describe Cr oxidation at high temperatures, with taking into account oxide vapourisation [162]. The Tedmon model is given below:

$$\frac{d\delta}{dt} = \frac{K_p}{2\delta} - K_r \tag{3-9}$$

where δ is the oxide scale thickness, t is the exposure time, K_p is the oxide parabolic growth rate constant, and K_r is the oxide removal rate constant determined by mass transfer-controlled corrosion.

Finally, the oxidation model proposed by Zhang and Li [134,163] can be expressed by the following approximated equation:

$$\delta = \left(K_p t\right)^{1/2} - \frac{2}{3}K_r t \tag{3-10}$$

The experimental constants of K_p and K_r for different steels exposed to liquid LBE/Pb are summarised in Refs. [30,164]. It can be inferred from this model that the oxide will reach a limiting thickness determined by the ratio of K_p to K_r. Moreover, the rate-controlling step will become elemental diffusion across the inner FeCr-spinel layer after prolonged exposures, since the outer magnetite layer is gradually removed by mass transfer-controlled corrosion, eventually exposing the inner FeCr-spinel layer directly to the HLM. Therefore, this model is applicable for short-term exposures, i.e., prior to the removal of the outer magnetite layer.

In order to predict the long-term oxidation behaviour of steels exposed to liquid LBE, Zhang [165] continued to develop a new oxidation model, in which the change of a duplex oxide scale (i.e., magnetite and FeCr-spinel) to a single-layer oxide scale (i.e., FeCr-spinel) after a long-term exposure was considered, and the growth kinetics of the outer magnetite and inner FeCr-spinel was modelled separately. In the case of the duplex oxide scale, the growth kinetics of the inner FeCr-spinel layer follows a parabolic law, while the growth kinetics of the outer magnetite layer deviates significantly from this particular law. After the magnetite reaches a limiting thickness, it starts to dissolve upon further exposure and the dissolution rate depends on the HLM flow velocity, temperature, and oxygen concentration. The model also suggests that the corrosion rate of HT-9 and T91 steels decreases by about three orders of magnitude after the outer magnetite scale is completely removed by flow-accelerated corrosion [166]. It should be noted, however, that this model does not consider the IOZ, which is often observed after sufficiently long exposures.

Martinelli et al. [167–169] developed a different oxidation model for T91 F/M steels exposed to oxygen-saturated liquid LBE and liquid Bi at 470 °C, based on the following observations and arguments: (a) the oxide thickness data can be fitted using a parabolic law, implying that oxidation is a diffusion-controlled process according to the well-known theory of Wagner [161]. (b) The ^{18}O isotope tracer experiments indicate that the magnetite scale develops at the magnetite/LBE interface, while the FeCr-spinel scale grows at the steel/oxide interface. This implies that oxygen needs to be delivered through both oxides to reach the steel/oxide interface. (c) Oxygen diffusivity in magnetite is too slow to be compared with the growth rate of the spinel oxide scale. Thus, other faster paths must be available for oxygen transport. (d) Pb is found at the steel/spinel interface after exposures to liquid LBE, while Bi is observed at the same interface after exposures to liquid Bi. Given that the oxygen diffusion coefficient in liquid Pb at 470 °C is much larger than that in magnetite (4×10^{-6} $cm^2 \cdot s^{-1}$ *vs.* 3.2×10^{-19} $cm^2 \cdot s^{-1}$), oxygen may diffuse through nano-channels filled with HLM (e.g., Pb) to reach the FeCr-spinel/steel interface. (e) The experimental data indicate that oxygen diffusion in the nano-channels is quite fast, therefore, another rate-limiting step for spinel growth should exist. Finally, the "available space model" was adopted and refined to describe the oxidising scenario of T91 F/M steels exposed to a HLM (Fig. 3.16): the outward diffusion of Fe from the steel matrix to the magnetite/LBE interface leads to magnetite (Fe_3O_4) growth on the steel surface, leaving vacancies at the FeCr-spinel/steel interface. Due to the presence of Cr, most of the vacancies do not annihilate, but combine together to form micro/nano-cavities. Pb nano-channels form above these cavities through the dissociative/perforative growth process [149,153,155,157,158] and oxygen diffuses through the Pb nano-channels to reach the spinel/steel interface. The oxygen arriving at the interface reacts with the steel, forming FeCr-spinel until the existing cavities are filled with that particular oxide. Once the cavities are completely filled, the oxidation reaction pauses until new

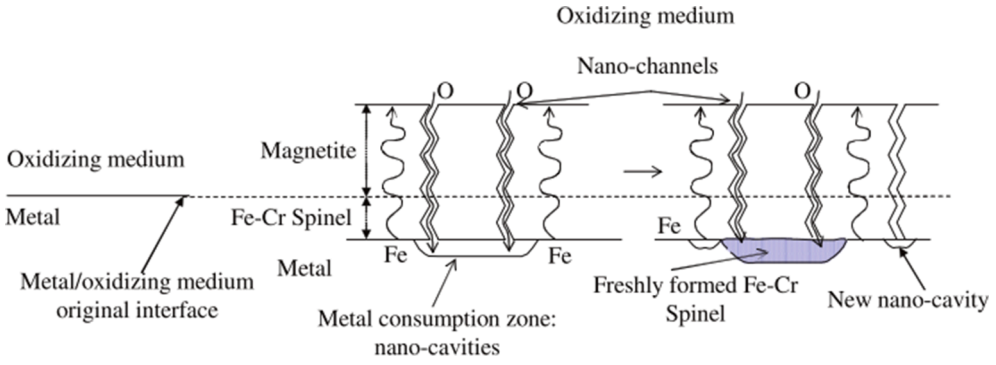

Fig. 3.16. Schematic illustration of the oxidation mechanism of F/M steels based on the "available space model" [168].

cavities are generated by the outward diffusion of Fe. During the entire oxidation process, Cr is considered to be immobile. Thus, the outward Fe diffusion across the oxide scale is the rate-limiting step for FeCr-spinel growth.

Since the growth of both layers in duplex oxide scales is associated with Fe diffusion, the thickness of FeCr-spinel can be derived from that of the magnetite [168,169]:

$$h_{sp} = \frac{C_{Fe}^{mag}}{C_{Fe}^{T91} - C_{Fe}^{sp}} h_{mag} \tag{3-11}$$

where h_{sp} is the FeCr-spinel thickness, C_{Fe}^{mag} is the Fe concentration in magnetite, C_{Fe}^{T91} is the Fe concentration in the T91 F/M steel, C_{Fe}^{sp} is the Fe concentration in the FeCr-spinel oxide, and h_{mag} is the magnetite thickness. The thickness of the magnetite scale is calculated using Wagner's oxidation theory [161]. Finally, Martinelli et al. [169–171] derived the following equation to calculate the thickness of magnetite:

$$h_{mag}^2 = \left[\frac{D_v}{12} ln \left(\frac{1 + 2K_v a_{O_2}^{mag/Pb-Bi^{2/3}}}{1 + 2K_v a_{O_2}^{sp/mag^{2/3}}} \right) - \frac{8}{3} D_I K_I (a_{O_2}^{mag/Pb-Bi^{-2/3}} - a_{O_2}^{sp/mag^{-2/3}}) \right] t \tag{3-12}$$

where D_V is the vacancy diffusion coefficient, K_V is the reaction constant leading to the formation of a vacancy, $a_{O_2}^{mag/Pb-Bi}$ is the oxygen activity at the magnetite/Pb-Bi interface, $a_{O_2}^{sp/Pb-Bi}$ is the oxygen activity at the FeCr-spinel/magnetite interface, D_I is the interstitial

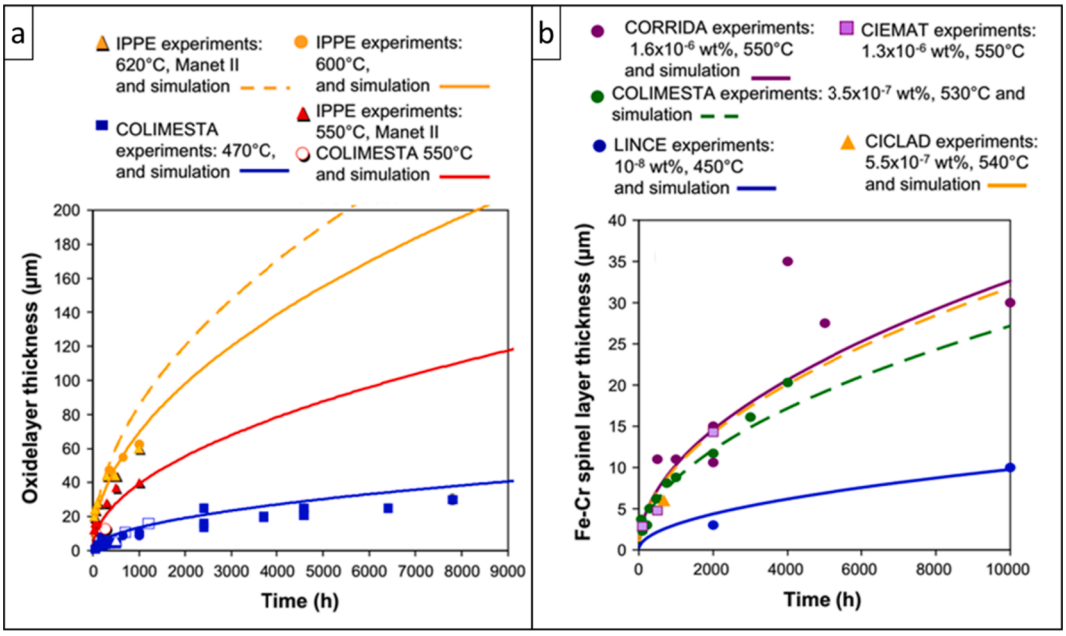

Fig. 3.17. Comparison between the mechanistic model and experimental oxide thickness data for T91 F/M steels exposed to liquid LBE at different temperatures: (a) oxygen-saturated LBE, adapted from [173]; (b) LBE with moderate oxygen concentrations, adapted from [172].

diffusion coefficient, K_I is the reaction constant leading to the formation of an interstitial, and t is the exposure time. The parameters in Eqs. (3-11) and (3-12) can be determined based on literature data as well as by fitting experimental data. More details can be found in Refs. [169–171].

Based on this model, Weisenburger et al. [172] compared the predicted oxide growth kinetics with experimental results obtained from T91 F/M steels exposed to liquid LBE under different conditions. The comparison showed good agreement between the model and experimental data (Fig. 3.17). Long-term exposures to HLMs under diverse conditions are needed, however, to further validate this specific oxidation model.

3.2.2. LMC by dissolution corrosion

Apart from oxidation, dissolution corrosion is an important LMC mechanism that might occur even despite the presence of an oxide scale on the steel surface, for example when the oxide scale is locally defective or when its continuity is breached due to local mechanical and/or chemical damage. Dissolution corrosion can either manifest itself as selective leaching (i.e., the selective transfer of steel alloying elements from the solid steel to the HLM) or as non-selective leaching (i.e., when all steel alloying elements are concurrently dissolved in the HLM). This LMC mechanism is facilitated by the intimate contact between the steel and the HLM (i.e., in the absence of a passivating oxide scale), however, it can also occur by elemental diffusion through a non-protective oxide scale. Dissolution corrosion is promoted when the concentration of dissolved oxygen in the HLM drops below 10^{-7} at.% for most Cr-containing steels, as the formation of a dense, defect-free oxide scale cannot occur sufficiently fast (or at all) to prevent the onset of HLM dissolution attack. The driving force of dissolution corrosion lies primarily in the temperature-dependent differences in the chemical potential of the steel alloying elements between solid steel and HLM; these chemical potential differences are element-specific and HLM-specific (e.g., the solubility of most F/M steel and AuSS alloying elements is 10 times higher in liquid Bi than in liquid Pb, at the same temperature). The dissolution corrosion mechanism is affected by the local temperature and overall system-specific temperature gradients, the HLM dissolved oxygen concentration and gradients thereof, the HLM flow pattern characteristics, the steel chemical composition, microstructure and thermomechanical state, and may become aggravated by radiation-induced effects (e.g., radiation hardening, radiation-induced segregation, enhanced elemental diffusion due to radiation-induced defects) and other materials degradation effects, such as LME. Dissolution corrosion can either be relatively uniform (i.e., the variation of the thickness of the dissolution-affected zone is limited) or locally enhanced; the latter is associated with the formation of highly undesirable dissolution 'pits', which can compromise the structural integrity of thin-walled components (e.g., fuel cladding tubes, heat exchanger tubes) within short periods of time.

3.2.2.1. Characteristics of 'uniform' dissolution corrosion. Dissolution corrosion is driven by the fact that nearly all steel alloying elements have a temperature-dependent, finite solubility in liquid Pb and liquid LBE. Generally, the solubility of both metallic and non-metallic elements in liquid LBE/Pb can be represented by the following equation:

$$logC_s = A_c - B_c/T \tag{3-13}$$

where C_s (wppm) is the solubility limit, T is the temperature (K), and A_c and B_c are thermodynamic constants given in Table 3.2.

Fig. 3.18 shows the solubility limit of the main steel constituents (i.e., Fe, Ni, and Cr) and oxygen as a function of temperature. It can be seen that elemental solubility increases with increasing temperature. Moreover, Ni has a much higher solubility compared to Cr and Fe. For instance, at 600 °C, the solubility of Ni in liquid LBE is as high as 36,674 ppm, as opposed to 23.4 ppm for Cr and 10 ppm for Fe. Since each of the steel alloying elements has a different solubility, selective leaching is likely to take place. The steel alloying elements are more soluble in liquid LBE than in liquid Pb, indicating that LBE is the more corrosive in these two HLMs, while liquid Bi is even more corrosive than LBE. Indeed, it was reported that the corrosiveness of liquid Bi was about 40 times stronger than that of liquid Pb [175]. One consequence of the temperature dependence of elemental solubility is that it establishes mass transfer in non-isothermal nuclear reactor systems, whereupon dissolved species from hotter areas in the nuclear reactor are spontaneously transported to colder areas. The amount of elements that dissolve in the hotter parts of the reactor might exceed their solubility limits in the colder parts of the reactor, causing them to precipitate out of solution [31]; this is particularly true for Fe, which dissolves in massive amounts in the reactor 'hot leg', as almost all components are made of Fe-based alloys, and is expected to precipitate out as Fe-based oxides in the reactor 'cold leg' due to the rather limited solubility of Fe in liquid Pb/LBE (see Fig. 3.18). In a hypothetically isothermal nuclear

Table 3.2
Solubility data of Ni, Fe, Cr, and O in liquid LBE and Pb [29,109,174].

log C_s (wppm) = A_c - B_c/T				
Element	Liquid metal	A_c	B_c	T (K)
Fe	Pb	4.34	3450	673–873
	LBE	6.01	4380	823–1053
Cr	Pb	7.88	6948	600–1517
	LBE	3.98	2280	673–1173
Ni	Pb	5.30	1381	600–1517
	LBE	5.53	843	673–1173
O	Pb	7.21	5100	815–1090
	LBE	6.99	4711	473–773

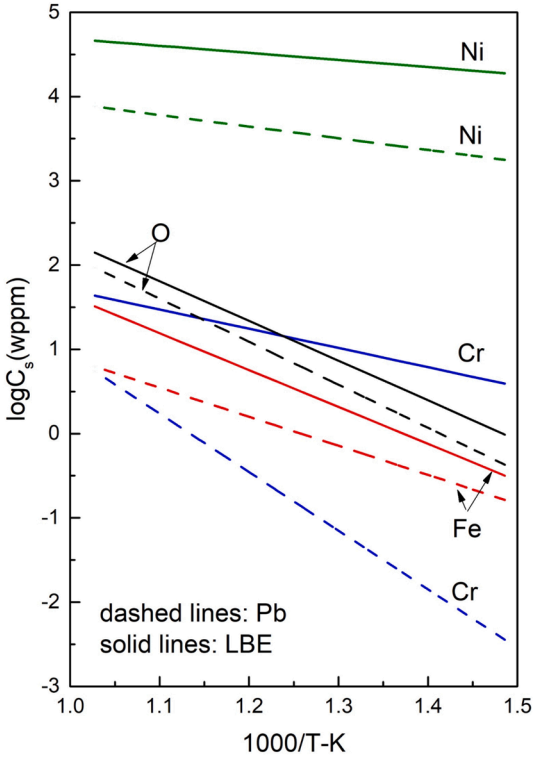

Fig. 3.18. Solubility of Fe, Cr, Ni, and O in liquid Pb and liquid LBE as a function of temperature, adapted from [29].

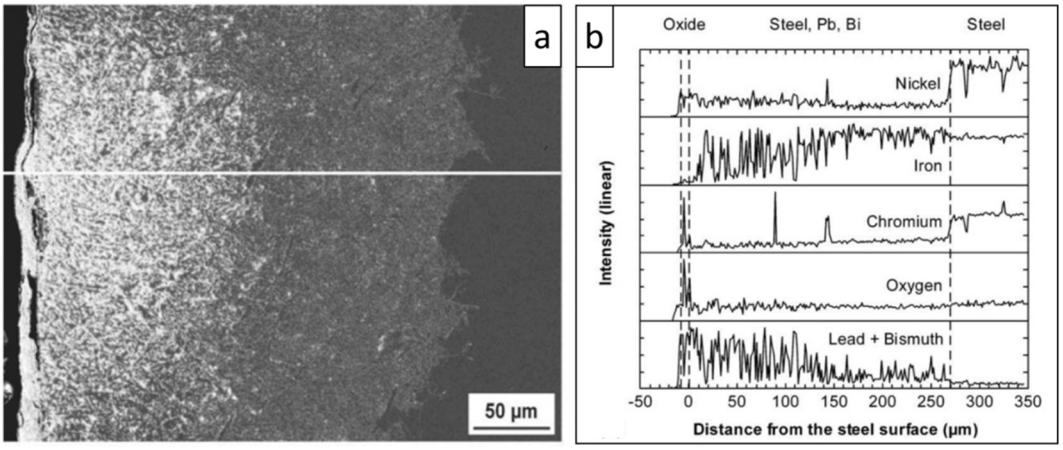

Fig. 3.19. (a) SEM† image of the dissolution-affected zone in 316L AuSS exposed to flowing LBE ($v \approx 2$ m/s, $C_O \approx 1.6 \times 10^{-6}$ wt%) at 550 °C for 7518 h. (b) The EDS† line scan along the white line in (a) reveals the selective leaching of Ni and Cr. Adapted from [115].

reactor system, dissolution corrosion is driven by the difference between the actual concentration of a dissolved element in the HLM and its (temperature-dependent) solubility limit. Because of the high solubility of Ni and Cr in liquid LBE (see Fig. 3.18), it is easy to understand why many studies have reported severe dissolution corrosion damage in 316L and 15-15Ti AuSS [44,93,96,176], as these AuSS contain high amounts of Ni and Cr (see Table 2.2).

Usually, AuSS dissolution starts with the transfer of the highly soluble steel alloying elements Ni, Mn, and Cr into the liquid LBE. The selective leaching of these elements creates empty spaces in the steel, such as vacancies and nano-pores. These empty spaces, which are initially located only underneath the steel surface, become filled by LBE; as the steel dissolution process advances with time, the creation of empty spaces and their subsequent filling with LBE promote the progressive LBE penetration deeper into the steel bulk. Fig. 3.19 provides an example of the macroscopic appearance of selective leaching in 316L AuSS exposed to flowing ($v \approx 2$ m/s) liquid LBE. On the microscopic level, selective leaching proceeds essentially one grain at the time, as shown in Fig. 3.20 for 316L AuSS

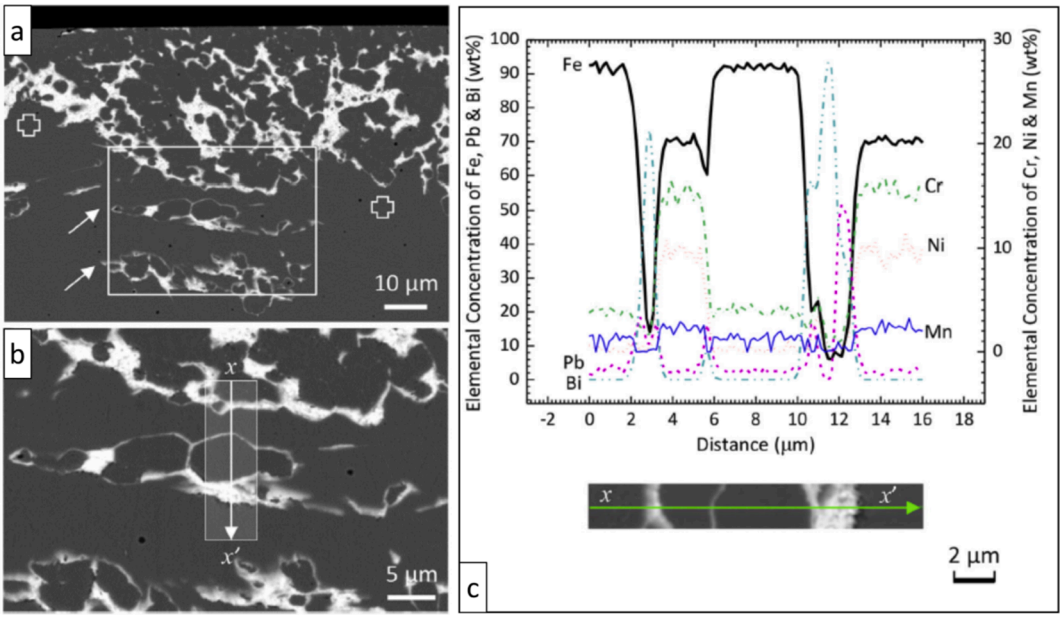

Fig. 3.20. CW 316L AuSS exposed to oxygen-poor ($C_O < 2 \times 10^{-8}$ wt%), static LBE at 500 °C for 3282 h. (a,b) SEM† images of groups of grains ahead of the main dissolution front (crosses), which underwent selective leaching during steel exposure. (c) The EDS† line scan shows selective leaching of Ni, Mn and Cr; Fe enrichment; and Pb/Bi presence at GBs. Adapted from [40].

exposed to static liquid LBE. This happens because selective leaching starts almost invariably with intergranular LBE penetration, as GBs are defect-rich sites that facilitate the LBE ingress when compared to the more defect-free grain bulk. As reported in prior studies on the dissolution corrosion behaviour of 316L AuSS [40,42,177], after its initial intergranular ingress, the LBE continues to penetrate deeper into the steel bulk by using preferred paths, such as GBs, twin boundaries, and interfaces between steel matrix and secondary precipitates (e.g., oxides, sulphides, δ-ferrite). The aspects of dissolution corrosion that relate to the steel microstructure are elaborated in Section 3.3.6. One may point out, however, is that even the so-called 'uniform' dissolution corrosion does not proceed inwards in a straightforward manner (i.e., perpendicular to the surface of the steel component), but it is enabled by the HLM ingress along specific paths in the steel microstructure, which accelerate locally the dissolution corrosion process.

The selective removal of the austenite stabilisers (e.g., Ni and Mn) that are highly soluble in liquid LBE results in the ferritisation of the dissolution-affected zone, i.e., the austenite-to-ferrite (*fcc*-to-*bcc*) phase transformation reported in many studies [40,104,115,178]. The orientation relationship (OR) between pristine austenite (*fcc*) and derivative ferrite (*bcc*) in 316L AuSS (both SA and CW) is dominated by the Pitsch OR model [179]; more discussion on the austenite/ferrite OR in dissolution-induced ferritisation may be found in Section 3.3.6. Selective leaching and ferritisation are promoted by low HLM oxygen concentrations [180], high temperatures [136], or combinations thereof (Fig. 3.21). It should be pointed out that, when the HLM is depleted in oxygen, ferritisation may occur at temperatures as low as 400 °C (Fig. 3.21a), due to the fact that the formation of protective oxide scales is suppressed under such exposure conditions.

Dissolution corrosion was also reported for T91 F/M steels under certain exposure conditions [101,181–183]. For instance, Tsisar et al. [101] observed a maximum (local) dissolution depth of ~190 µm after exposing T91 F/M steels to flowing LBE ($v \approx 2$ m/s, $C_O \approx 10^{-7}$ wt%) at 550 °C for 1007 h. Interestingly, severe dissolution damage with a maximum depth of ~960 µm was observed after exposing such steels to flowing LBE ($v \approx 2$ m/s, $C_O \approx 10^{-7}$ wt%) at 450 °C for 8766 h. This was attributed to the coupling of solution-based corrosion (i.e., dissolution corrosion) with local turbulences in the HLM flow. They also found that the incubation time for dissolution attack depended strongly on the LBE oxygen concentration. When the liquid LBE oxygen concentration decreased from $C_O \approx 10^{-6}$ wt% to $C_O \approx 10^{-7}$ wt%, the incubation time was reduced from 5000–15,000 h to <1000 h at 550 °C, and from >8000 h to 500–5000 h at 450 °C. Other 9Cr F/M steels are also susceptible to dissolution corrosion, as reported in Ref. [181].

3.2.2.2. Modelling of 'uniform' dissolution corrosion. Models describing the 'uniform' dissolution corrosion of Fe-9Cr martensitic steels exposed to liquid LBE were proposed by Balbaud-Célérier et al. [184,185]. They considered two dissolution corrosion scenarios, i.e., a mass transfer-controlled dissolution process at low HLM flow rates, and an activation-controlled dissolution process at higher HLM flow rates. Dissolution corrosion is controlled by three different fluxes, i.e., the dissolution flux corresponding to the dissolution reaction rate, the diffusion flux corresponding to the diffusion of the dissolved iron (Fe) from the steel/LBE interface to the liquid LBE bulk, and the convective flux for flowing liquid LBE.

In the case of low LBE flow rates, the corrosion rate is controlled by mass transfer at the steel/LBE interface and the dissolution rate in this condition can be calculated by the following equation:

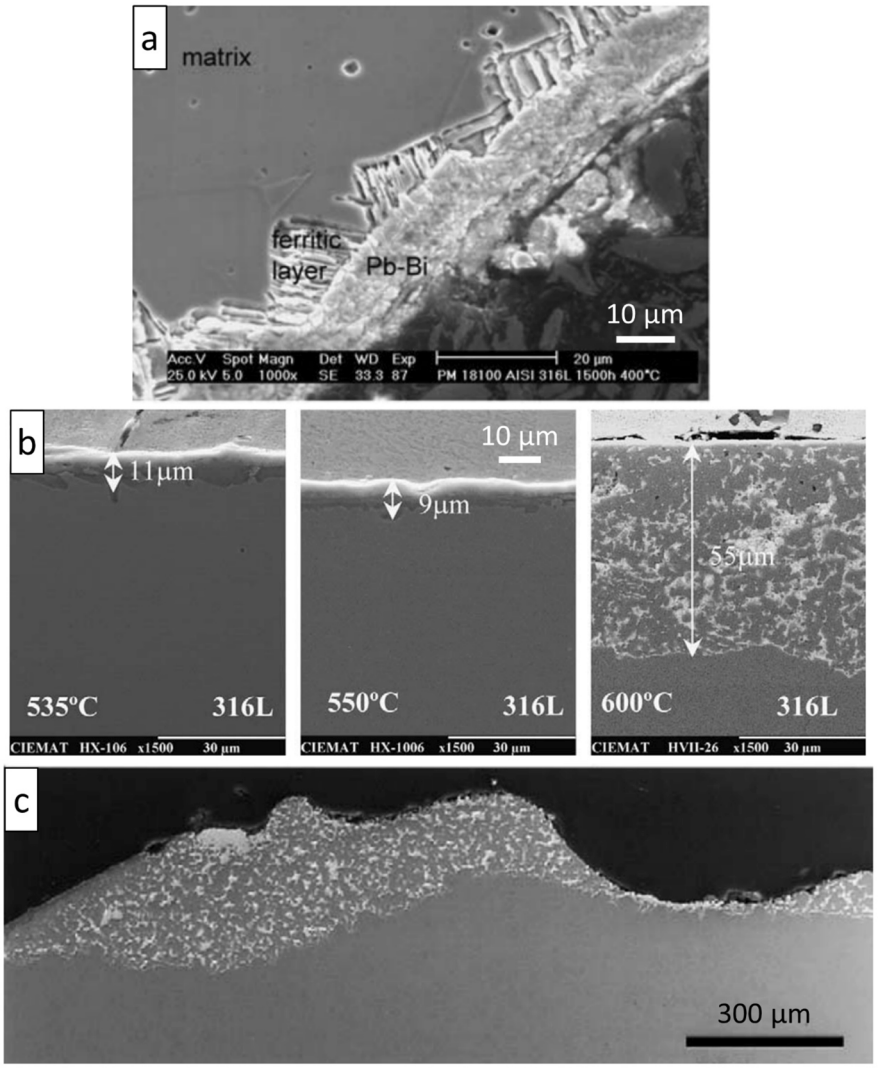

Fig. 3.21. SEM† images of surface ferritisation in 316L AuSS exposed to liquid LBE. Test conditions: (a) 400 °C, 1500 h, flowing LBE ($v \approx 1$ m/s), $C_O \approx 10^{-10}$–10^{-8} wt%; (b) 500 h, 535/550/600 °C, static LBE, $C_O \approx 3$–8×10^{-6} wt%; (c) 600 °C, 2000 h, flowing LBE ($v \approx 2$ m/s), $C_O \approx 1 \times 10^{-6}$ wt%. Adapted from [104,136,180].

$$\frac{1}{S}\frac{\partial m_{Fe}}{\partial t} = K(S_{Fe} - C_b) \tag{3-14}$$

In the case of fast-flowing LBE, the corrosion rate is controlled by the dissolution reaction at the steel/LBE interface, which is an activation-controlled process. In this condition, the dissolution rate is described by the following equation:

$$\frac{1}{S}\frac{\partial m_{Fe}}{\partial t} = k_{pr}(S_{Fe} - C_b) \tag{3-15}$$

where S is the steel/LBE surface area, t is the exposure time, m_{Fe} is the steel weight loss, K is the mass transfer coefficient, k_{pr} is the precipitation rate, S_{Fe} is the Fe solubility limit, and C_b is the Fe concentration in the LBE bulk.

Using these two equations, the ratio of the dissolution corrosion rate (the left hand-side of Eqs. (3-14) and (3-15)) to the difference between the Fe solubility limit and actual Fe concentration in the liquid LBE (i.e., S_{Fe}-C_b) as a function of the angular velocity of steel specimens rotating in LBE (used to simulate flow) can be calculated (see Fig. 3.22). It is shown in Fig. 3.22 that the experimental data do not fit the theory, unless a mass transfer process is accounted for. On the other hand, a better match between theory and experimental data is observed when a mixed control process is considered. Nevertheless, the latter gives rise to a constant precipitation rate, in contrast with a more typical Arrhenius-type rate law. This contradiction may be caused by uncertainties in the physicochemical data used to determine the parameters in Eqs. (3-14) and (3-15).

Recently, Martinelli et al. [186] proposed a new model for the prediction of the dissolution corrosion rate of pure Fe and T91 F/M

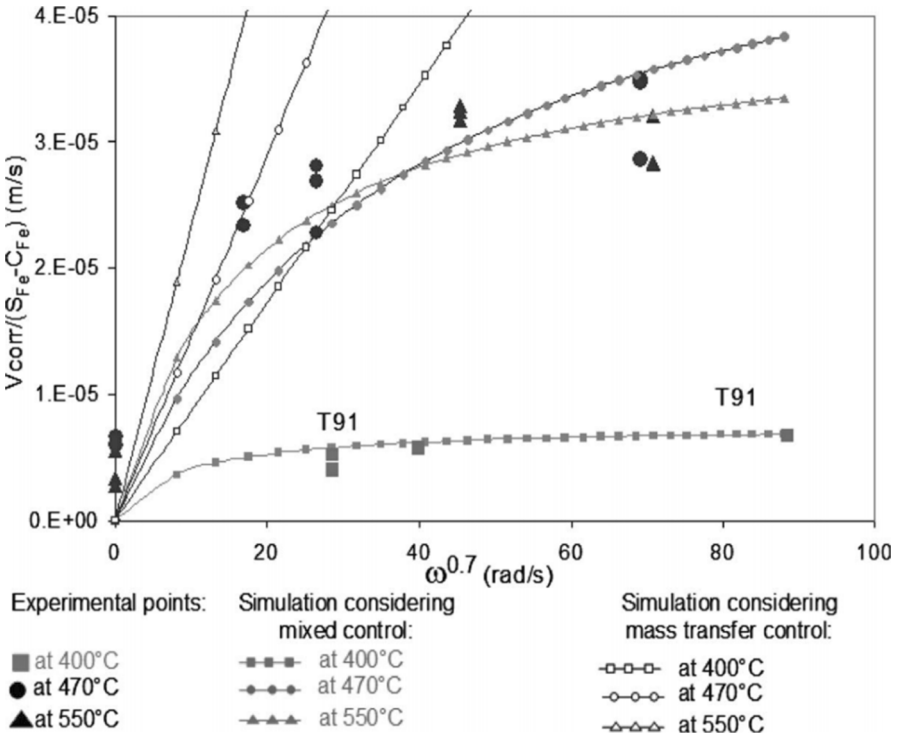

Fig. 3.22. Ratio between the dissolution corrosion rate, V_{corr}, and the (S_{Fe}-C_b) factor as a function of the steel specimen angular velocity, ω, at 400, 470, and 540 °C [185].

steels exposed at 450–550 °C to oxygen-poor ($C_O \approx 3 \times 10^{-15}$–$10^{-8}$ wt%) liquid LBE with variable flow velocity ($v \approx 0$–2.5 m/s). It was found that in static LBE ($v \approx 0$ m/s), the dissolution rate changes linearly with the exposure time, and natural convection is the rate-limiting process. In flowing LBE, the dissolution rates of pure Fe and T91 F/M steels are the same and controlled by both interfacial (dissolution) reaction and diffusion. The following equation was derived to calculate the dissolution corrosion rate (mm/year) of these metallic alloys in the domain of uniform dissolution, upon exposure to flowing LBE and for a pipe geometry:

$$\frac{dh}{dt} = \frac{V^{0.86} Exp\left(-\frac{3540.57}{T}\right)(3.544 \times 10^{-2} T - 303.3)}{-1.22 \times 10^{-4} d_{pipe}^{0.14} \frac{Exp\left(\frac{10484.97}{T}\right)}{(11065 - 1.293T)^{0.53}} + 1.01 \times 10^{-3} V^{0.86}(1.293T - 11065) Exp\left(-\frac{2407.78}{T}\right)} \quad (3\text{-}16)$$

where V is the flow rate (m/s), d_{pipe} is the diameter of the pipe (m), and T is the exposure temperature (K).

3.2.2.3. Locally enhanced dissolution corrosion ('pitting'). Prior studies have reported that 316L AuSS exposed to liquid LBE are susceptible to locally enhanced dissolution corrosion (i.e., dissolution 'pitting') [40,43,102,187]. For example, Martín-Muñoz et al. [187] reported that the exposure of 316L to flowing LBE ($v \approx 1$ m/s) with low oxygen concentration ($C_O \approx 10^{-10}$–10^{-8} wt%) at 452 °C for 5000 h resulted in severe dissolution at a few locations on the steel surface; at these locations of locally enhanced dissolution corrosion damage, the maximum dissolution depth reached 200 μm, while the depth of attack on the rest of the steel surface was ~10 μm. Schroer et al. [102] also observed the enhanced selective leaching of Ni and Cr (followed by Pb/Bi penetration into the steel) at a few sites on the surface of 316L AuSS specimens exposed to flowing LBE ($v \approx 2$ m/s) at 550 °C. The LBE oxygen concentration during these exposures was higher ($C_O \approx 1.6 \times 10^{-6}$ wt%) and more reactor-relevant than in the tests performed by Martín-Muñoz et al. [187]. This indicates that dissolution 'pitting' does not only regard steel exposures to very low LBE oxygen concentrations, but it could possibly compromise steel integrity in conditions expected to occur during the nominal operation of Gen-IV LFRs. The maximum depth of reported localised attack was ~350 μm after 10,021 h at 550 °C, under the aforementioned conditions of LBE oxygen concentration and flow velocity. Quite interestingly, increasing the duration of exposure from 2000 h to >7500 h did not increase the number of 'pits'. This suggests that locally enhanced leaching is somehow linked with the distribution of pre-existing defects in the steel, which make it inherently more susceptible to dissolution corrosion. Considering this a valid assumption, one is obliged to consider that dissolution 'pitting' is a steel-specific degradation effect apart from an effect depending on the exposure conditions (T, HLM C_O, and v). Since the population of steel defects appears to rule to a great extent the distribution of 'pits', one may assume that it is also linked with the steel processing route and it is, thus, not only steel grade-specific, but also steel heat-specific. Links between dissolution corrosion

behaviour and individual steel heats have been established in earlier studies on the 316L AuSS grade [40], emphasising the importance of the steel microstructure and thermomechanical state on the steel dissolution corrosion (detailed analysis in Section 3.3.6). Analogously, the occurrence of dissolution 'pitting' is also expected to be partly affected by the steel processing and the processing-induced population of defects that favour 'pitting'. Fig. 3.4 shows a large (>80 μm deep) 'pit' in a SA 316L AuSS exposed to oxygen-poor ($C_O < 10^{-8}$ wt%), static LBE at 500 °C for 1000 h [40]; the 'pit' growth was attributed to the local convergence of near-surface annealing twins in a coarse-grained, industrial-sized steel heat, thus clearly pointing out the importance of the steel microstructure on dissolution 'pitting'.

Schroer et al. [115] suggested that localised dissolution corrosion might be triggered by near-surface manganese sulphide (MnS) and/or slag inclusions, the size and spatial distribution of which in the steel bulk can be directly linked with the steel processing route. It should be pointed out that such secondary precipitates/inclusions are very often more resistant to HLM dissolution attack than the steel matrix. For instance, δ-ferrite (*bcc*) inclusions in 316L AuSS were reported to be more resistant to LBE dissolution attack than the austenitic (*fcc*) steel matrix [177], presumably due to their lower contents in the highly LBE-soluble Ni and Mn. Lambrinou et al. [40] showed that even though the most common secondary 316L AuSS precipitates (MnS, oxides, δ-ferrite) are insoluble in liquid LBE, the precipitate/steel matrix interfaces are paths for the fast LBE ingress into the steel. Therefore, it is safe to assume that the near-surface presence of large non-oxidising inclusions (e.g., MnS, oxides) will favour dissolution corrosion locally by allowing the LBE penetration into the inclusion/steel matrix interfaces. The role of steel precipitates on dissolution 'pitting' is further addressed in Section 3.3.6.

Zhang et al. [118] reported sites of locally enhanced dissolution corrosion in 316L AuSS exposed to flowing LBE ($v \approx 1.9$ m/s) with $C_O \approx 3–5 \times 10^{-6}$ wt%, after 3000 h at 550 °C. The average depth and width of these localised LMC sites were 120–140 μm and 820 μm, respectively, while the maximum depth of attack was ~220 μm. The rest of the steel surface was covered by a thin (1–4 μm) oxide scale that did not exceed ~10 μm locally. The authors associated the occurrence of localised corrosion with the position of the steel specimens in the forced convection loop: the specimens with severe local LMC damage were probably too close to the test section wall, creating narrow spaces of quasi-static, poorly oxygenated liquid LBE that triggered "slot corrosion" or "crevice corrosion" effects. Schroer et al. [102] proposed the following mechanism for dissolution 'pitting' in 316L AuSS: first, Ni is transferred from the solid steel to the liquid LBE due to its high solubility in the HLM; next, steel depletion in Cr occurs after the dissolution process has advanced to a certain depth. Cr remains in solution only in oxygen-depleted liquid LBE, otherwise, it re-precipitates as a Cr-based oxide (e.g., Cr_2O_3). Once in solution, Cr is transported to the steel surface and is carried away by the HLM flow. Due to its strong affinity to oxygen, the LBE-dissolved Cr contributes to the LBE oxygen depletion close to the steel surface, rendering the LBE that penetrates into the steel later in time and poorer in oxygen, further facilitating the process of selective leaching and locally deepening the LMC attack.

Moreover, Lambrinou et al. [40] observed the formation of dissolution 'pits' in 316L AuSS exposed to oxygen-poor ($C_O < 10^{-8}$ wt %), static LBE at 500 °C (see Fig. 3.4). In that work, the depth of the largest 'pits' in CW 316L AuSS exposed to LBE for 3282 h varied between 250 μm and 350 μm, while the same depth in SA 316L AuSS remained <120 μm, for identical exposure conditions. These findings highlight once more the importance of the steel microstructure and thermomechanical state on the steel dissolution corrosion behaviour and especially the severity of dissolution 'pitting'.

Tsisar et al. [43] compared the maximum depths of dissolution 'pits' observed in different AuSS grades (Fig. 3.23). As may be seen,

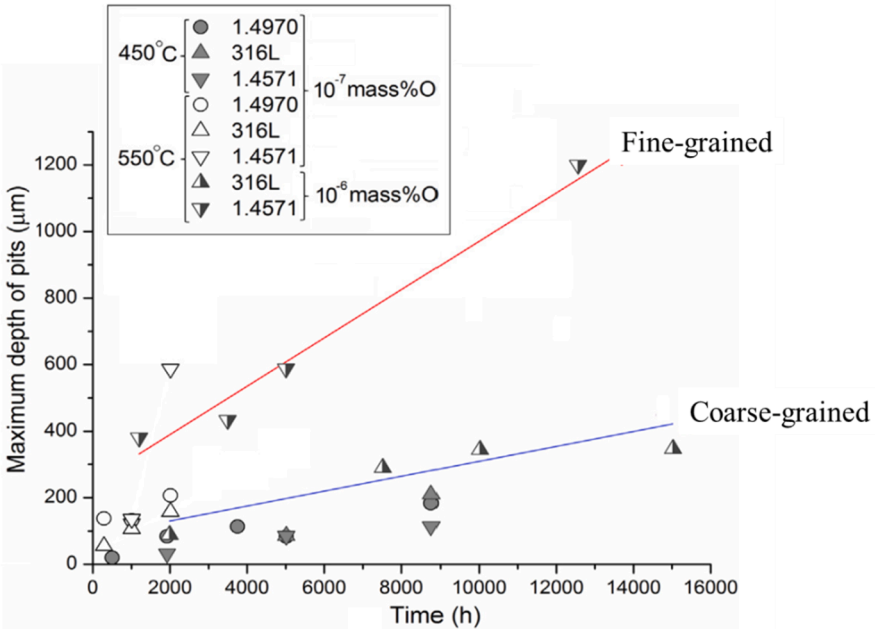

Fig. 3.23. Maximum 'pit' depths observed in 316L, 1.4970 and 1.4571 AuSS exposed to flowing LBE ($v \approx 2$ m/s) under different exposure durations, oxygen concentrations, and temperatures. Adapted from [43].

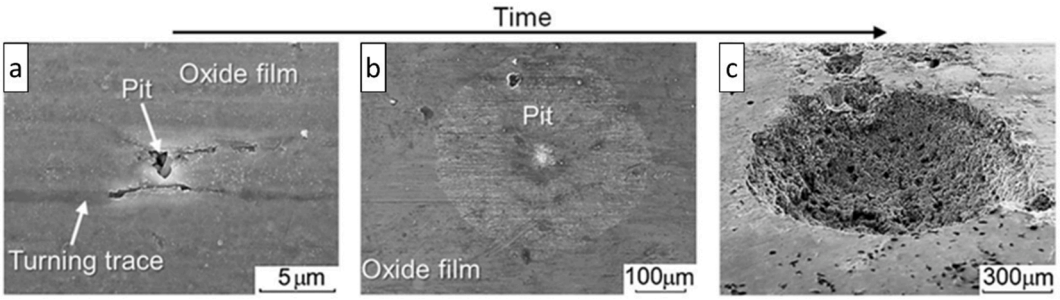

Fig. 3.24. SEM[†] images of the projected growth of 'pits' on the surface of 1.4970 and 1.4571 AuSS exposed to flowing LBE ($v \approx 2$ m/s, $C_O \approx 10^{-7}$ wt %). Adapted from [43].

the depth of the maximum 'pit' found in 1.4571 AuSS exposed to flowing LBE ($v \approx 2$ m/s) at 550 °C for ~12,564 h was ~1200 μm. At the same temperature (i.e., 550 °C), dissolution 'pitting' started faster when the LBE oxygen concentration decreased from $C_O \approx 10^{-6}$ wt% to $C_O \approx 10^{-7}$ wt%, suggesting that the oxide scales (i.e., Cr-based oxides) that formed at the early stages of exposure degraded faster as the LBE oxygen concentration decreased. Fig. 3.23 also indicates that a finer-grained steel microstructure may cause deeper pitting attack. It should be mentioned that the mechanistic understanding and modelling of dissolution 'pitting' are still not available; therefore, a linear empirical relation is used to fit the maximum pit depth data as a function of the steel exposure time, as shown in Fig. 3.23.

Tsisar et al. [43] proposed an evolution process for dissolution 'pitting': first, 'pits' nucleate as small defects in the Cr-based oxide scale, at sites close to turning marks resulting from specimen machining (Fig. 3.24a), followed by the development of a spheroidal 'pitting' zone characterised by the presence of LBE and the steel depletion in Ni (Fig. 3.24b). Finally, the 'pit' volume is eliminated by the LBE flow, leading to the formation of large craters on the steel surface (Fig. 3.24c). This mechanism implies that the occurrence of dissolution 'pitting' is associated with both steel surface and steel bulk, since both surface finish and residual stresses are expected to contribute to the formation of 'pits'. These factors, in conjunction with the local HLM flow conditions, facilitate the local damage of the protective oxide scales, leading to locally enhanced dissolution corrosion damage. Once the oxide scales have been locally damaged, dissolution attack of the steel bulk and uninhibited 'pit' growth continue, due to the fact that the HLM becomes progressively more depleted in oxygen as it penetrates deeper into the steel.

Dissolution 'pitting' seems to affect all AuSS with compositions similar to that of 316L AuSS. Schroer et al. [188] reported the locally enhanced selective leaching of Ni and Cr (accompanied by Pb/Bi penetration into the steel) at a few locations in 1.4571 AuSS tubing used for long times (23,000–29,000 h) in the CORRIDA loop, KIT. The steel exposure conditions were: 550 °C, LBE $C_O \approx 10^{-6}$ wt %, and $v \approx 1.7$ m/s. Many more dissolution 'pits', with a maximum depth of 1 mm, were observed on 1.4571 AuSS specimens tested in the CORRIDA loop for shorter periods of times (<12,564 h), under similar exposure conditions (550 °C, LBE $C_O \approx 10^{-6}$ wt%, and $v \approx 2$ m/s). The difference in the severity of dissolution 'pitting' between loop tubing made of 1.4571 AuSS and corrosion specimens made of the same AuSS was not easy to explain. The authors suggested that the minimisation of LBE turbulence (e.g., by eliminating flow obstacles in the loop ducts or avoiding sites of abrupt flow diversion) might reduce the occurrence of severe localised damage caused by dissolution corrosion. Weisenburger et al. [172] and Balbaud-Célérier et al. [189] also attributed the occurrence of dissolution 'pitting' to the effects of locally turbulent HLM flow.

F/M steels are also not immune to dissolution 'pitting'. Fig. 3.3 shows a deep (~227 μm) 'pit' in a EUROFER-97 F/M steel exposed to flowing LBE ($v \approx 1.8$ m/s) with $C_O \approx 2.3 \times 10^{-6}$ wt% at 550 °C for 3000 h. This 'pit' grew underneath the FeCr-containing oxide scales covering the steel surface; such defective oxides prevent the replenishment of the oxygen content at the LBE penetration fronts, which eventually become totally depleted in oxygen. The complete removal of oxygen from the LBE penetrations in the 'pit' volume prevents the precipitation of Cr-based oxides on the LBE penetration 'walls', which results in the continuous leaching of Cr outwards. The oxide residues on the steel surface tend to capture the steel alloying elements (Cr, Fe) that diffuse outwards as well as the oxygen that tries to diffuse inwards, promoting rather than decelerating the growth of the 'pit'. Locally enhanced dissolution corrosion was reported in 9Cr F/M steels, including the T91, T92, E911, and EUROFER grades with slight differences in chemical composition, e.g., in the Cr and Si contents [101,181,182,190]. Schroer et al. [183] reported very severe localised dissolution corrosion damage (depth: ~1190 μm) in a "T91-B" steel (8.99 wt% Cr) exposed to oxygen-containing ($C_O \approx 1 \times 10^{-7}$ wt%), flowing LBE ($v \approx 2$ m/s) at 400 °C for 13,172 h in the CORRIDA loop (KIT), while a "T91-A" steel with a relatively high Cr content (9.44 wt%) did not suffer such extreme LMC damage under identical exposure conditions. This difference suggests that a higher Cr content in the "T91-A" steel promoted the formation of more stable oxides (e.g., Cr-based oxides), resulting in a better steel resistance to dissolution 'pitting'. Interestingly, under similar exposure conditions, the severe localised dissolution corrosion damage was not observed in T91 (8.99 wt%) F/M steels tested in the CRAFT loop (SCK CEN), after even a longer exposure up to ~20,000 h. This may result from different local flow patterns in the two forced convection loops [190]. In addition to the steel Cr content, the severity of dissolution 'pitting' relies heavily on the test temperature and LBE oxygen content [101]. Upon increasing the exposure temperature from 400 °C to 450 °C, the "T91-B" steel (8.99 wt% Cr) exhibited a local dissolution attack of 960 μm in contact with oxygen-containing ($C_O \approx 1 \times 10^{-7}$ wt%) flowing LBE ($v \approx 2$ m/s) for only 8766 h; a longer exposure time (13,172 h) was required for a similar depth of LBE dissolution attack at 400 °C. The exposure time necessary for significant local dissolution corrosion damage is further shortened when the exposure temperature is elevated to 550 °C.

At this higher temperature, a maximum local dissolution corrosion depth of ~190 μm developed after only 1007 h in contact with flowing liquid LBE. In the case of the EUROFER steel, a maximum local dissolution depth of ~1000 μm was observed after exposure to flowing LBE (v ≈ 2 m/s) with $C_O \approx 1 \times 10^{-7}$ wt% for ~2011 h, while exposure to flowing LBE with $C_O \approx 1 \times 10^{-6}$ wt% for ~3000 h resulted in a much shallower local dissolution depth of ~250 μm [181]. Compared to T92 and E911 F/M steels, the EUROFER F/M steel is more susceptible to dissolution 'pitting' due to its finer-grained microstructure. Moreover, it was shown that lower LBE oxygen concentrations and higher exposure temperatures reduce the incubation time needed to initiate (local) dissolution corrosion damage [181].

3.2.3. *Flow-assisted LMC (erosion/corrosion)*

The effect of the HLM flow on the LMC behaviour of 316L/316 AuSS has been addressed in many studies. For instance, Kondo et al. [191] exposed 316L AuSS to flowing LBE ($v \approx 2$ m/s) for 1000 h at 550 °C. During these exposures, the liquid LBE oxygen concentration was maintained low ($C_O \approx 2 \times 10^{-9}$ wt%), promoting both dissolution corrosion (depth of dissolution attack: ~250 μm) and erosion (erosion depth: ~100 μm). Based on their observations, the authors suggested the following erosion-corrosion mechanism for 316L AuSS exposed to similar conditions: first, steel dissolution occurs, followed by LBE penetration, primarily into the steel GBs. The intergranular LBE dissolution attack weakens the GBs, resulting in the detachment of loose grains (or grain clusters) by hydrodynamic shear forces applied by the LBE flow on the steel surface. The occasional detachment of large grain clusters imparts a jagged appearance to the steel surface, as shown in Fig. 3.25.

Moreover, the stability of oxide scales on T91 F/M steels exposed to flowing LBE with $C_O \approx 10^{-6}$ wt% at 550 °C for 2000 h was negatively affected by erosion [192]. It was reported that the outer magnetite (Fe_3O_4) scale adhered to the whole steel surface at an LBE flow rate of $v \approx 1$ m/s, largely disappeared at $v \approx 2$ m/s, and was completely removed at $v \approx 3$ m/s. The inner FeCr-spinel oxide layer remained intact, even at a flow rate of $v \approx 3$ m/s. A similar erosion/corrosion effect was observed in 410 steels (Fe-12Cr) exposed to oxygen-saturated, flowing LBE at 550 °C for 600 h by Chen et al. [193]. In that study, however, the outer magnetite scale was not removed by the LBE flow for a velocity up to $v \approx 2.98$ m/s. Li et al. [194] observed different types of erosion-induced damage, including crack formation in both the oxide scales and the steel bulk, in T91 F/M steels exposed to fast-flowing ($v \approx 1$–5 m/s), oxygen-saturated liquid LBE, with a flow direction normal to the steel surface, at 400 °C for 1000 h. They also reported that the erosion-induced surface cracking of 304N AuSS, exposed to oxygen-saturated, flowing ($v \approx 1$ m/s) LBE at 400 °C for 1000 h, allowed LBE penetration into the steel bulk, causing dissolution corrosion damage in the sub-surface layer [195].

3.2.4. *Fretting wear*

The operation experience of commercial Gen-II/III light water reactors (LWRs) has demonstrated that fuel assemblies fail predominantly by "fretting wear", i.e., a failure mechanism that is triggered by vibrations caused by the flow of the primary coolant and that affects mainly the contacts between fuel cladding tubes and spacer grids. Due to the acceleration of corrosion processes in the contacts between two metals (i.e., fuel cladding material and spacer grid material), fretting wear is considered a corrosion mechanism with chemical and mechanical aspects. Fretting wear is a degradation mechanism that is expected to affect the performance of Gen-IV LFR fuel assemblies as well. Therefore, Del Giacco et al. [37–39] studied the fretting wear behaviour of T91 F/M steels and 15-15Ti AuSS in comparison with their surface-aluminised counterparts by exposing all steels to liquid Pb with $C_O \approx 10^{-6}$ wt% at 450, 500 and 550 °C. Testing was carried out under a contact load of 15–75 N that was vertically applied to the rubbing surface, an oscillation frequency of 10 Hz, and an oscillatory amplitude of 35–165 μm. Their results showed that material loss rates increased invariably by fretting wear: for example, testing at 450 °C (oscillatory amplitude: 75 μm, contact load: 50 N) resulted in 10% loss of thickness in <1000 h. This was attributed to fretting wear-enhanced dissolution corrosion, as the rubbing of the steel surface against a counter specimen made of the same steel damaged the oxide scales, attacking the steel underneath. Due to its high Ni content, 15-15Ti AuSS

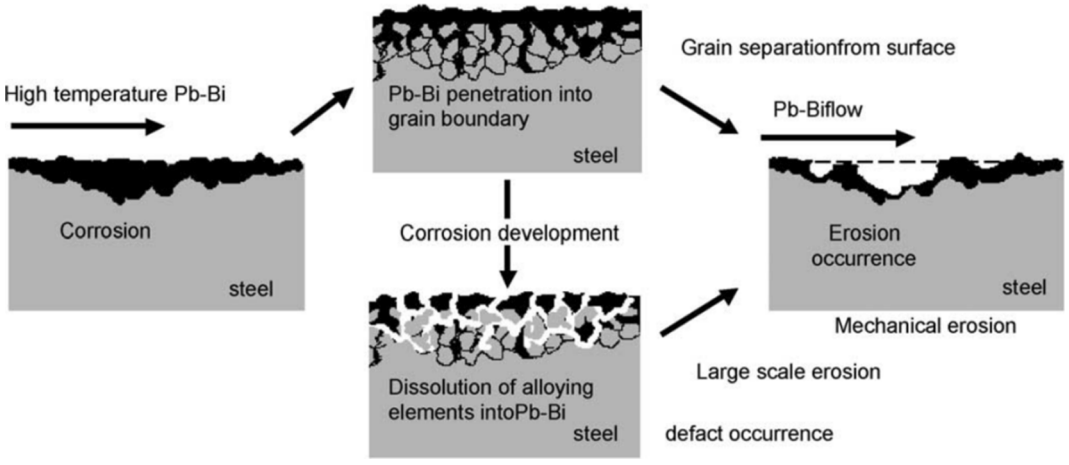

Fig. 3.25. Schematic illustration of an erosion/corrosion mechanism [191].

underwent more severe HLM dissolution attack. Above 500 °C, oxidation-enhanced fretting wear was observed in T91 F/M steels, as these steels form thick oxide scales under similar exposure conditions (see Fig. 3.28); therefore, the continuous formation and mechanical dislodging of oxide scales favoured fretting wear. The work of Del Giacco et al. [37–39] showed that fretting wear can be mitigated by the steel surface alloying with Al, presumably due to the formation of a durable (i.e., wear-resistant) alumina (Al_2O_3) scale on the steel surface. The surface-aluminised T91 F/M steel variant exhibited the best resistance to fretting wear up to 550 °C.

3.3. Factors affecting LMC

This section addresses the factors affecting the LMC behaviour of nuclear grade steels in contact with HLM coolants. These factors may be divided into those extrinsic to the steel, e.g., exposure temperature and duration, HLM oxygen concentration, HLM flow velocity, and those intrinsic to the steel, e.g., steel chemical composition, microstructure and thermomechanical state, surface finish. With respect to the factors that are intrinsic to the steel, the importance of defects (GBs, twins, inclusions) introduced either during steel processing and/or service due to thermomechanical loads and/or neutron irradiation is extensively addressed.

3.3.1. The role of exposure temperature

The influence of the exposure temperature on the LMC behaviour of 316L AuSS and similar steels is shown in Fig. 3.26 for static LBE conditions and Fig. 3.27 for flowing HLM conditions, respectively. As may be seen, irrespective of the presence or absence of HLM flow, increasing the exposure temperature above 400–450 °C promotes all LMC effects (oxidation, uniform and locally enhanced dissolution). Below 450 °C, both oxidation and (uniform/localised) dissolution corrosion become significantly milder, however, locally enhanced dissolution remains a concern even at temperatures <450 °C, as a corrosion depth of ~200 μm has been reported in contact with low-oxygen, static liquid LBE at 400 °C (Fig. 3.26). Moreover, the depth of the corrosion-affected layer can exceed 100 μm within relatively short times (2300–3000 h), when high exposure temperatures (565–570 °C) are combined with low concentrations of dissolved oxygen ($C_O \approx 10^{-11}$ wt%) in the liquid LBE [196].

Regarding the most severe localised dissolution ('pitting') damage, a depth of 620 μm was reported for 40% CW 1.4970 AuSS after ~2200 h in contact with static LBE ($C_O \approx 10^{-8}$ wt%) at 550 °C (see green box in Fig. 3.26). This damage may be attributed to the high density of deformation twins formed during the steel cold deformation; as will be explained in Section 3.3.6, deformation twin boundaries are paths of fast LBE ingress into the steel, hence, the deep dissolution corrosion damage in this case can be justified by the high density of deformation twin boundaries in the bulk of the CW 1.4970 AuSS [197]. In contact with flowing LBE ($v \approx 2$ m/s), severe localised dissolution of ~1200 μm in depth was reported for 1.4571 AuSS exposed for ~12,564 h at 550 °C in contact with moderately oxygenated liquid LBE ($C_O \approx 10^{-6}$ wt%) [43,188]. Disregarding any differences in steel chemical composition (1.4970 *vs.* 1.4571), LBE oxygen concentration ($C_O \approx 10^{-8}$ *vs.* 10^{-6} wt%), and most importantly, exposure duration (2200 h *vs.* 12,564 h), the deep dissolution

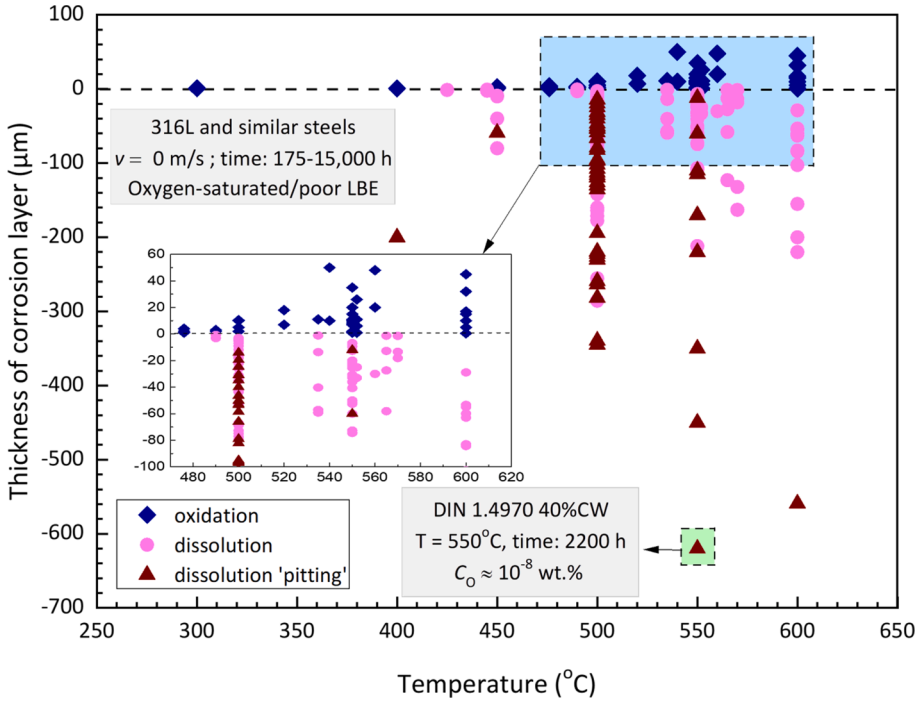

Fig. 3.26. Corrosion layer thickness in 316L AuSS and similar steels (304L, 316Ti, 15-15Ti) exposed to *static* LBE as a function of the exposure temperature. The magnified inset shows data acquired in the 476–600 °C range and corresponding to corrosion layer thicknesses between −100 μm and 60 μm. Data collected from Refs. [40,42,107,116,125,136,177,178,196–213].

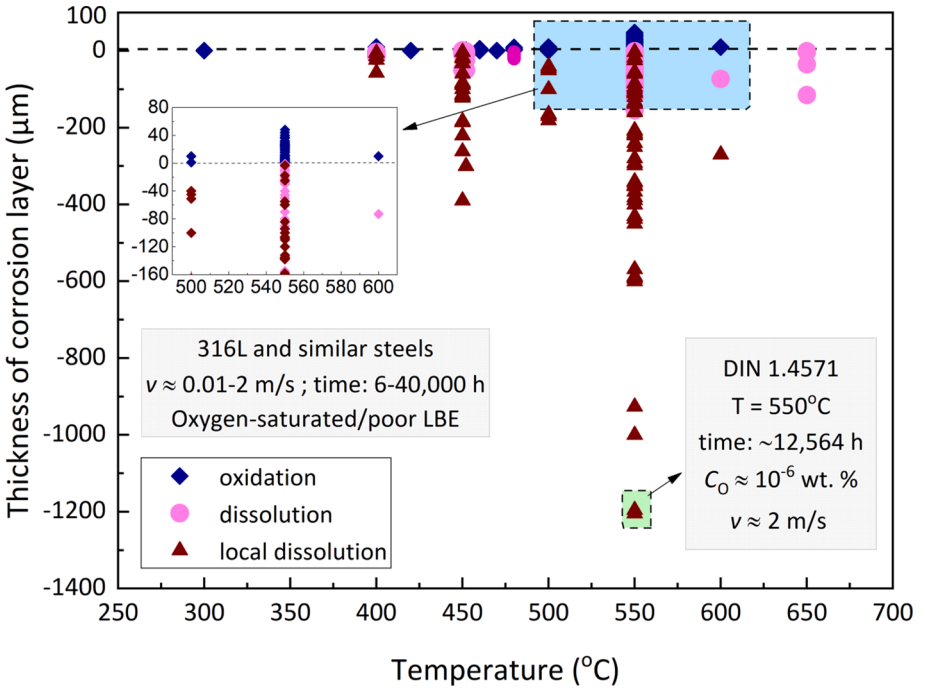

Fig. 3.27. Corrosion layer thickness in 316L AuSS and similar steels (304L, 316Ti, 15-15Ti) exposed to *flowing* HLMs as a function of the exposure temperature. The magnified inset shows data acquired in the 500–600 °C range and corresponding to corrosion layer thicknesses between −160 µm and 80 µm. Data collected from Refs. [43,44,95,96,102,104,106,115,118,141,172,180,187–189,191,214–230].

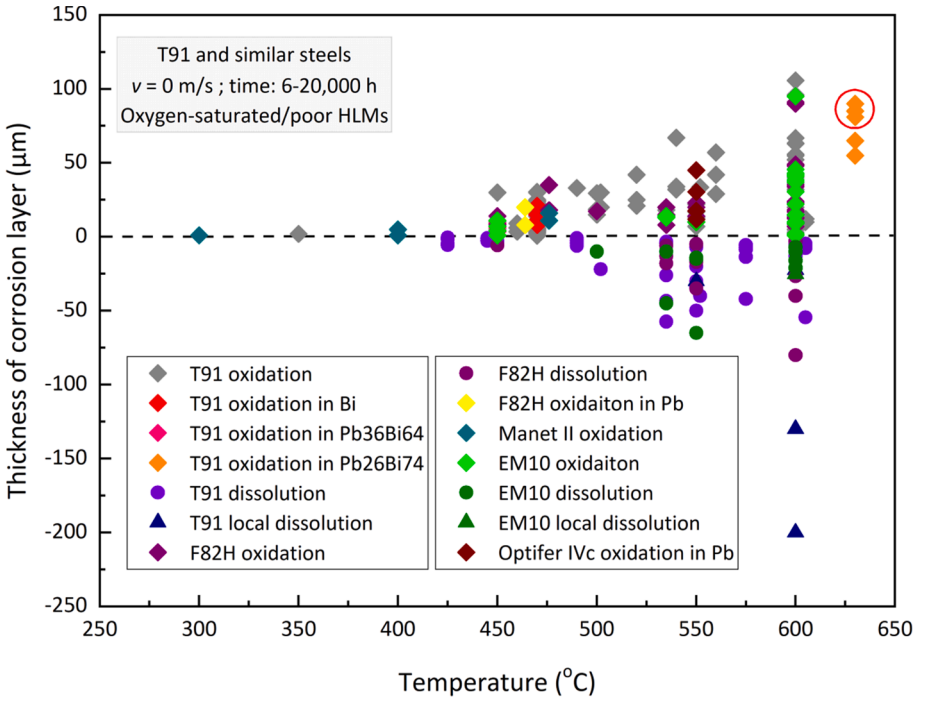

Fig. 3.28. Corrosion layer thickness in T91 F/M and similar steels as a function of the exposure temperature in *static* HLMs. Steel grades: T91, F82H, Manet II, EM10 and Optifer IVc. HLMs: LBE, Pb, Bi, 36Pb-64Bi, 26Pb-74Bi. Data collected from Refs. [92,116,125,133,136,167,169–171,189,196,198,202–205,208–211,231,233–236]. Mechanisms: uniform oxidation (diamonds), uniform dissolution (circles), and locally enhanced dissolution (triangles).

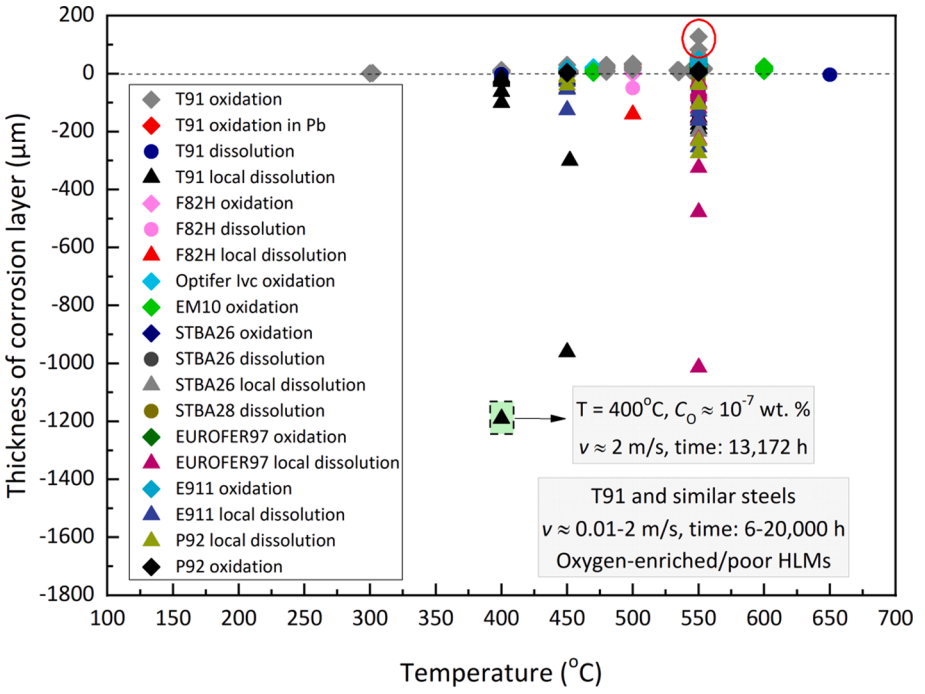

Fig. 3.29. Corrosion layer thickness in T91 F/M and similar steels as a function of the exposure temperature in *flowing* HLMs. Steel grades: T91, F82H, Optifer IVc, EM10, STBA26, STBA28, EUROFER-97, E911 and P92. HLMs: LBE, Pb, Bi, 36Pb-64Bi, 26Pb-74Bi. Data collected from Refs. [92,101,115,117,172,180,181,183,185,187,189–191,215–217,219,225,227,230–232,234,237–240]. Mechanisms: uniform oxidation (diamonds), uniform dissolution (circles), and locally enhanced dissolution (triangles).

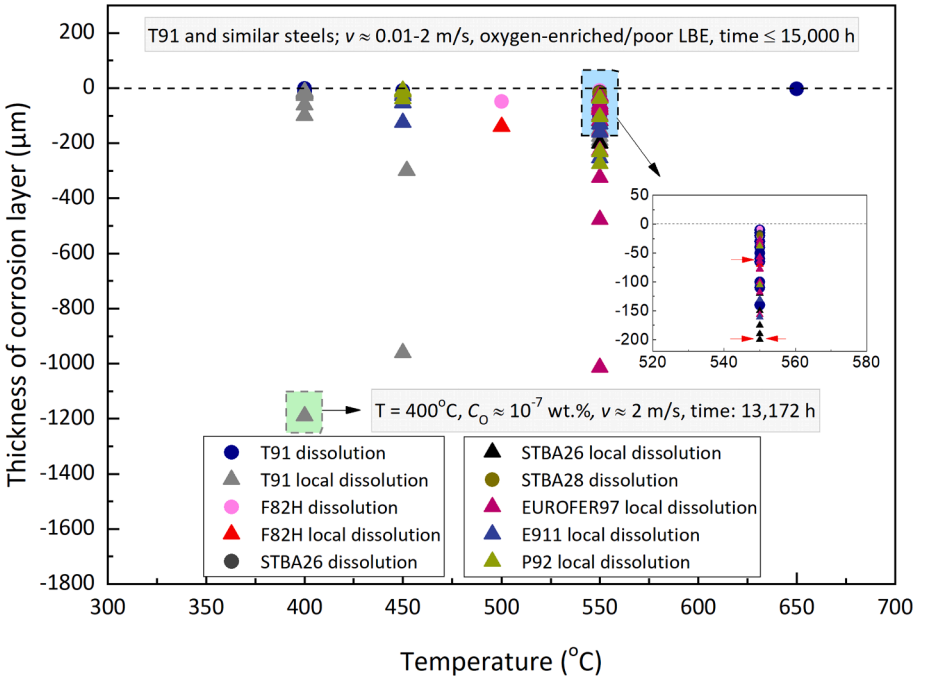

Fig. 3.30. Dissolution depths in T91 F/M and similar steels as a function of the exposure temperature in *flowing* LBE. The magnified inset shows data acquired at 550°C and corresponding to corrosion layer thicknesses between -200 µm and 50 µm. Data collected from Refs. [92,101,117,180,181,183,187,190,191,215–217,225,227,231,232]. Steel grades: T91, F82H, STBA26, STBA28, EUROFER-97, E911 and P92. Mechanisms: uniform dissolution (circles), and locally enhanced dissolution (triangles).

'pitting' depth measured under flowing LBE conditions may partly be attributed to the fact that HLM flow does not allow the establishment of thick diffusion barrier layers at the steel/HLM interface. Such diffusion barrier layers are created by the (temperature-driven) dissolution of steel alloying elements into the HLM, and when they are not removed by the HLM flow (as in the case of static HLMs), they become saturated in dissolved steel alloying species, eventually delaying or stopping the further steel dissolution. The fact that the HLM flow reduces the thickness of the diffusion barrier layers at the steel/HLM interface, thus promoting the further steel dissolution explains the deeper (dissolution) corrosion depths typically observed in flowing LBE conditions (Fig. 3.27) as compared to static LBE conditions (Fig. 3.26).

Compared to static LBE conditions, oxidation of 316L and compositionally similar AuSS may appear less severe in flowing LBE conditions (Fig. 3.27), but this is most likely due to the continuous (partial) removal of the outer oxide scale layer (magnetite) by the HLM flow (erosion effects, see Section 3.2.3), resulting in an overall thinner oxide scale on the steel surface. In ideal conditions, oxide scale formation and removal by the HLM flow happen simultaneously and at such rates that do not allow the steel to ever remain unprotected by a superficial oxide scale. The two competing processes can reach a (temperature-dependent) equilibrium, when the HLM oxygen concentration permits the spontaneous oxide scale restoration while the HLM flow is not so high so as to cause severe material losses and total removal of the near-surface oxidised steel part.

The scatter in the existing corrosion data of grade 91 (T91) and compositionally similar F/M steels as a function of the exposure temperature is shown in Fig. 3.28 for static HLMs and Fig. 3.29 for flowing HLMs. Once more, the choice of the steel grade and/or HLM (Pb or LBE) does not seem to significantly impact the LMC effects, as all exposed steels behave similarly, irrespective of the HLM, at least for the reported exposures. As expected, the data displayed in Figs. 3.28 and 3.29 show that all LMC effects (oxidation, uniform and localised dissolution) on grade 91 and similar steels become aggravated as the exposure temperature increases above 400–450 °C. This indicates that despite the prevailing conviction that T91 and compositionally similar F/M steels are more LMC-resistant than AuSS, these steels demonstrate an enhanced susceptibility to LMC effects in the same temperature range as the AuSS (i.e., >400 °C). Interestingly, the maximum reported oxide scale thicknesses on T91 F/M steels are larger than the same thicknesses on 316L AuSS under static HLM conditions, while the opposite happens for the dissolution-affected zone thicknesses under static HLM conditions, i.e., 316L AuSS show deeper corrosion damage than T91 F/M steels. In simple terms, this means that T91 F/M steels are more prone to oxidation (i.e., the formation of rather thick oxide scales) than 316L AuSS in contact with similarly-oxygenated HLMs, most probably due to the fact that 316L AuSS contain more Cr than T91 F/M steels and this alloying element is characterised by a high affinity to the oxygen dissolved in HLM. On the other hand, 316L AuSS are more susceptible to HLM dissolution attack than T91 F/M steels, especially in oxygen-poor HLMs, due to their higher overall (cumulative) contents in highly soluble steel alloying elements (Ni, Mn and Cr).

In terms of the maximum reported corrosion layer thicknesses in T91 F/M steels under static HLM conditions, the thickest oxide scales (81–90 μm) formed on steels exposed at 630 °C for 300–700 h (red circle in Fig. 3.28) [171], while in flowing HLM conditions, the thickest oxide scales (76–128 μm) resulted from exposures at 550 °C for 10,000–15,000 h (red ellipse in Fig. 3.29) [115]. It is also

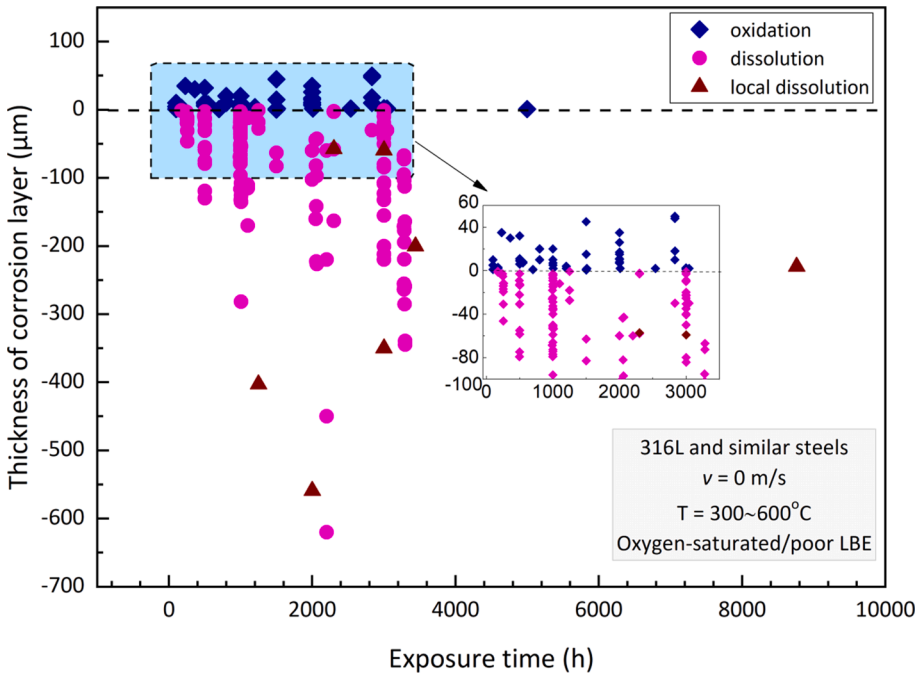

Fig. 3.31. Corrosion layer thickness in 316L AuSS and similar steels as a function of the duration of exposure to *static* LBE. The magnified inset shows the evolution in corrosion layer thickness within the first 3000 h of exposure and for corrosion layer thicknesses between −100 μm and 60 μm. Data collected from Refs. [40,42,107,116,125,136,177,178,196–213].

worthwhile mentioning that locally enhanced dissolution corrosion damage in T91 F/M and similar steels is significantly deeper than uniform dissolution corrosion damage occurring under similar test conditions (Fig. 3.30). Such differences are accentuated in flowing LBE conditions and they might again be associated with the fact that the HLM flow does not allow the establishment of thick diffusion barrier layers at the steel/HLM interface. Hence, when dissolution 'pitting' is favoured (either due to the test conditions or the nature/distribution of dissolution-promoting steel defects), the steel alloying elements dissolved in HLM are quickly removed by the HLM flow from the vicinity of the steel surface, promoting further dissolution attack. A similar trend is observed in 316L and similar AuSS exposed to flowing HLMs (Fig. 3.27).

Examples of the magnitude of differences between uniform and localised dissolution corrosion damage observed in T91 F/M or similar steels exposed to flowing LBE under similar conditions are: (a) uniform dissolution of 65 μm in depth was reported for the exposure of a T91 F/M steel at 550 °C for ~10,000 h to flowing liquid LBE ($v \approx 2$ m/s) with $C_O \approx 5 \times 10^{-7}$–$10^{-5}$ wt% (single red arrow, Fig. 3.30) [231]; (b) locally enhanced dissolution of ~200 μm in depth resulted from exposing T91-A (9.44 wt% Cr) F/M steels at 550 °C for ~15,028 h to flowing LBE ($v \approx 2$ m/s) with $C_O \approx 1.4 \times 10^{-6}$ wt% (two red arrows, Fig. 3.30) [232]; (c) a severe case of dissolution 'pitting' of ~1190 μm was reported for a T91 F/M steel exposed to flowing ($v \approx 2$ m/s) LBE with $C_O \approx 10^{-7}$ wt% at 400 °C for 13,172 h. Such a deep HLM dissolution attack at otherwise moderate exposure conditions (400 °C, $C_O \approx 10^{-7}$ wt%) could be associated with possible local disturbances (e.g., 'eddies') in the HLM flow pattern. The long exposure time (13,172 h) could be partly accountable for the observed deep corrosion damage in the latter case, as other shorter exposures (2011–8766 h, Fig. 3.34) of T91-B (8.99 wt% Cr) and EUROFER F/M steels at 450–550 °C to flowing LBE ($v \approx 2$ m/s) with $C_O \approx 10^{-7}$ wt% resulted in deep (961–1000 μm) dissolution corrosion damage as well [101,181].

It is worthwhile noting that the same depth (~1190 μm) of locally enhanced dissolution corrosion resulted from exposing T91 F/M and 1.4571 AuSS for similar times (13,172 h *vs.* 12,564 h) to flowing LBE ($v \approx 2$ m/s) with comparable oxygen contents ($C_O \approx 10^{-7}$ wt% *vs.* $C_O \approx 10^{-6}$ wt%); however, the T91 F/M steel was exposed to 400 °C (Fig. 3.29 and Fig. 3.30), while the exposure temperature of 1.4571 AuSS was 550 °C (Fig. 3.27). Even if the dissolution 'pitting' damage in the T91 F/M steel was caused by local LBE flow turbulences, one cannot disregard the low-temperature susceptibility of T91 F/M steels to 'pitting' under certain exposure conditions (e.g., 'eddies' in the HLM flow pattern).

3.3.2. The role of exposure duration

The influence of the exposure duration on the LMC behaviour of 316L AuSS and compositionally similar steels is shown in Fig. 3.31 for static LBE conditions and Fig. 3.32 for flowing HLM conditions, respectively. As may be seen, after a certain amount of time (3000–4000 h) that depends on the HLM flow velocity, the oxide scale thickness does not increase further or, at least, not remarkably. On the contrary, prolonging the steel exposure appears to decrease the oxide scale thickness both in static and flowing HLM conditions. The reduction of oxide scale thickness is attributed to the periodic oxide spallation that occurs when the internal stresses built in the

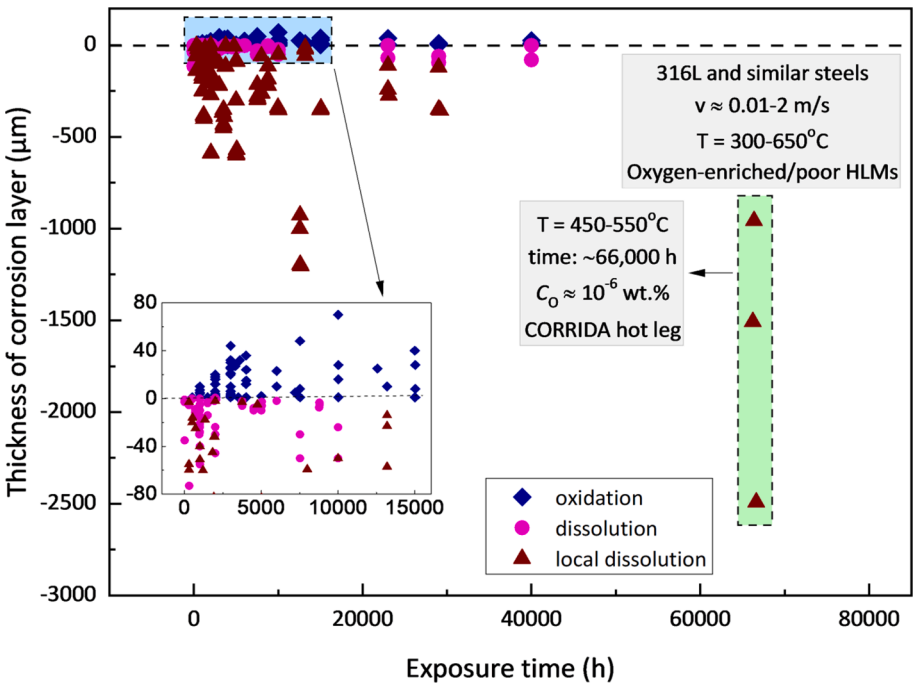

Fig. 3.32. Corrosion layer thickness in 316L AuSS and similar steels as a function of the duration of exposure to *flowing* HLMs. The magnified inset shows the evolution in corrosion layer thickness in the first 15,000 h of exposure and for corrosion layer thicknesses between −80 μm and 80 μm. Data collected from Refs.[43,44,95,96,102,104,106,115,118,141,172,180,187–189,191,214–230].

oxide scale during its growth reach a critical value that is sufficiently high to cause its mechanical failure. Moreover, oxide scale growth is controlled by both inward O diffusion and outward diffusion of steel alloying elements (in particular Fe, as this controls the growth of the outer magnetite layer) through the initially formed oxide scale; the thicker the oxide scale, the more time is needed for the aforementioned interdiffusion of elements, hence, the slower the further oxide scale growth. Therefore, it is not surprising that the oxide scales do not thicken linearly with the exposure duration, as the concurrent effects of oxide spallation (often assisted by the HLM flow) and oxide growth counterbalance each other, forcing the overall oxidation process to enter a steady state.

An interesting issue that merits discussion is the proposed 'maximum allowed oxide scale thickness of 40 μm' [30,118]. This oxide scale thickness is even considered by nuclear system designers as limiting the lifetime of components with a heat exchanging function, such as heat exchanger tubes. The reason for this is that oxide scales act as thermal insulators, therefore, when their thickness exceeds a certain critical value, the oxidised steel can no longer conduct the heat in an efficient manner. This can be a problem for both fuel cladding tubes and heat exchanger tubes. Since fuel assemblies are regularly replaced, this problem is not so critical for fuel cladding tubes; however, for components with a longer lifetime, such as heat exchangers, this might eventually mean the need for replacing the heat exchangers, which is a costly maintenance operation that also interrupts the reactor operation. The herein conducted review of existing LMC data revealed that the oxide scale thickness on 316L AuSS can indeed exceed the proposed limit of 40 μm, depending on the exposure conditions. In static conditions, a maximum oxide scale thickness of 50 μm was reported after exposing 316L AuSS for 2832 h at 540 °C in oxygen-saturated LBE [125]. In flowing conditions, a maximum oxide scale thickness of 48 μm was reported after exposing 316L AuSS for 7518 h at 550 °C to flowing LBE ($v \approx 2$ m/s) with $C_O \approx 1.6 \times 10^{-6}$ wt% [115]. The existing possibility of forming quite thick (>40 μm) oxide scales on 316L (and similar) AuSS within a relatively short period of time (<1 year), even in the presence of HLM flow and in contact with moderately oxygenated HLMs, indicates that a perspective nuclear reactor system must be designed and operated in such a manner, so as to delay or even avoid the replacement of important components with a heat exchanging function.

Contrary to oxidation, dissolution corrosion does not stop after reaching a certain depth and, provided the right conditions, it can continue uninhibitedly until the steel is completely consumed. Dissolution corrosion is favoured by high temperatures (>450 °C, Figs. 3.26 and 3.27) and low HLM oxygen concentrations ($C_O < 10^{-6}$ wt% for static HLMs and $C_O < 5 \times 10^{-6}$ wt% for flowing HLMs, Figs. 3.36 and 3.37). In the absence of oxide scales at the steel/HLM interface, relatively thick (>100 μm) and uniform dissolution-affected zones may be established rather quickly (2000–3000 h) on the steel surface (Figs. 3.31 and 3.32). However, the formation of oxide scales on the steel surface is not sufficient to prevent dissolution corrosion, as local defects in the oxide scales can allow the HLM ingress into the base steel and the development of dissolution 'pits' beneath the oxide scales (see Fig. 3.3). Locally enhanced dissolution corrosion ('pitting') is usually also promoted by the coupled effects of high temperature and low HLM oxygen concentration, reaching large depths of attack (200–620 μm) within short periods of time (1000–3000 h). For example, 316Ti AuSS samples removed from the 'hot leg' of the CORRIDA forced convection loop underwent severe dissolution corrosion damage with a record

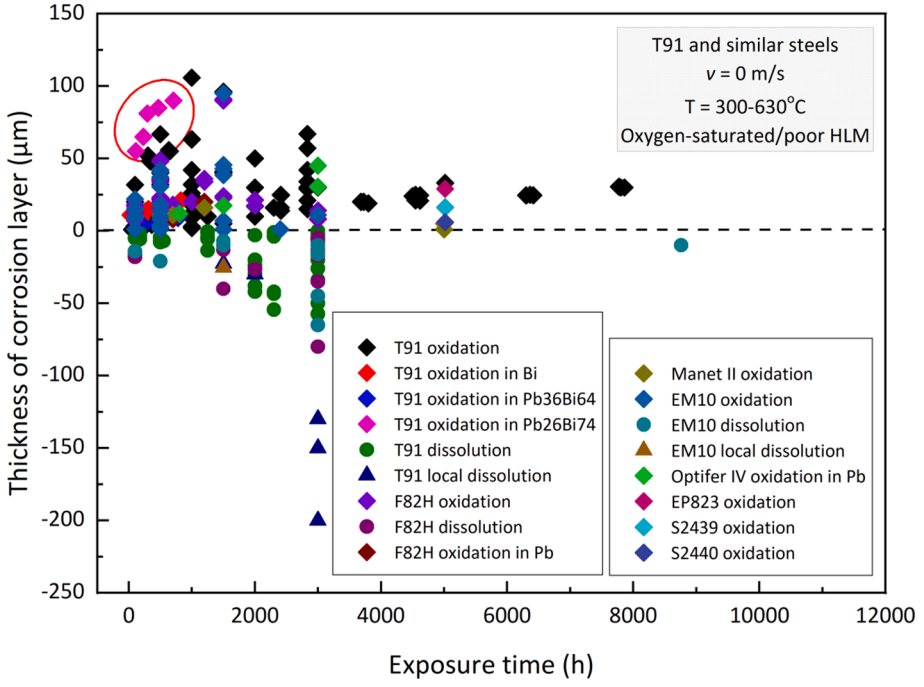

Fig. 3.33. Corrosion layer thickness in T91 F/M and similar steels as a function of the exposure duration in *static* HLMs. Steel grades: T91, F82H, Manet II, EM10, Optifer IVc, EP823, S2439 and S2440. HLMs: LBE, Pb, Bi, 36Pb-64Bi and 26Pb-74Bi. Data collected from Refs. [92,116,125,133,136,167,169–171,189,196,198,202–205,208–211,231,233–236]. Mechanisms: uniform oxidation (diamonds), uniform dissolution (circles), locally enhanced dissolution (triangles).

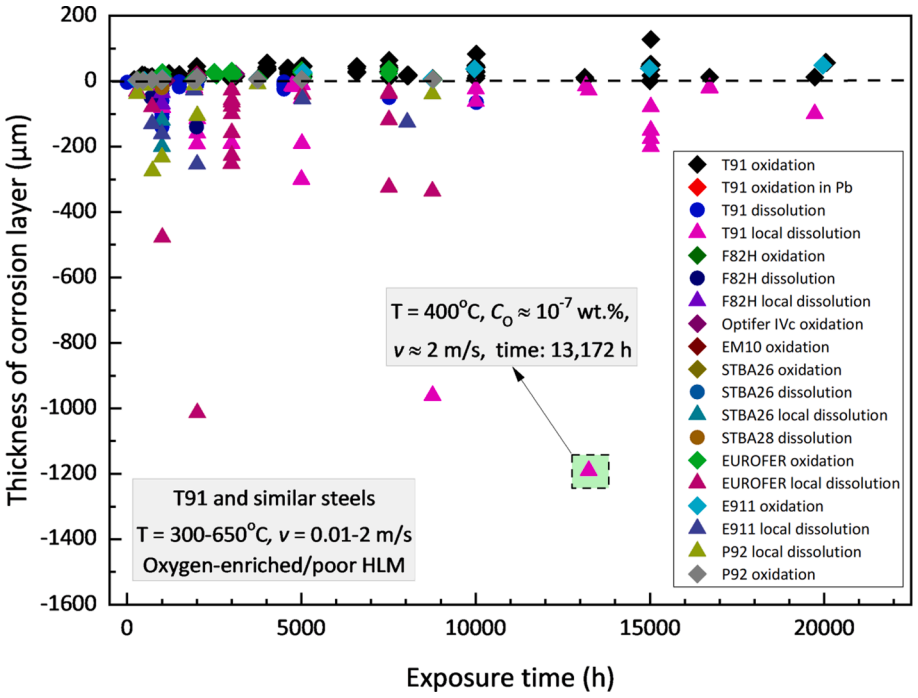

Fig. 3.34. Corrosion layer thickness in T91 F/M and similar steels as a function of the exposure duration in *flowing* HLMs. Steel grades: T91, F82H, Optifer IVc, EM10, STBA26, STBA28, EUROFER-97, E911, and P92. HLMs: LBE, Pb, Bi, 36Pb-64Bi, 26Pb-74Bi. Data collected from Refs. [92,101,115,117,172,180,181,183,185,187,189–191,215–217,219,225,227,230–232,234,237–240]. Mechanisms: uniform oxidation (diamonds), uniform dissolution (circles), locally enhanced dissolution (triangles).

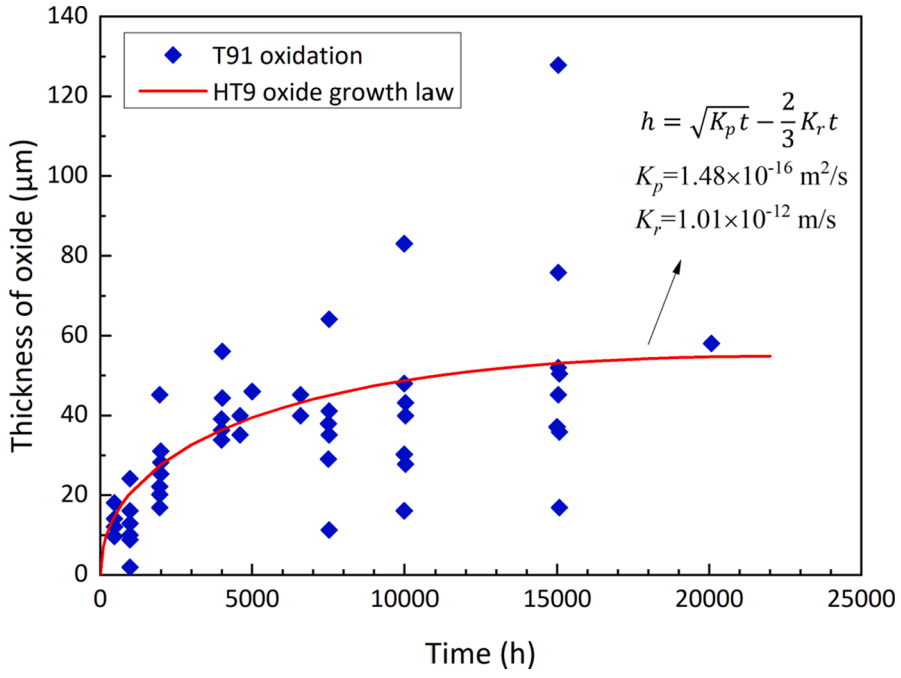

Fig. 3.35. Thickness of oxide scales on T91 F/M steels as a function of exposure duration in *flowing* LBE. All data resulted from steel exposures at 550 °C to oxygen-containing LBE ($C_O \approx 10^{-6}$–10^{-5} wt%). The red curve corresponds to the oxide scale growth law suggested for HT-9 F/M steels by Zhang [30,134]. (For interpretation of the references to colour in this figure legend, the reader is referred to the web version of this article.)

depth of ~2500 μm (Fig. 3.32); these steel samples were exposed to oxygen-containing ($C_O \approx 10^{-6}$ wt%), flowing LBE ($v \approx 2$ m/s) at 450–550 °C for >66,000 h. The fact that dissolution 'pitting' is capable of yielding severe local corrosion damage in relatively short times makes it a real concern for Gen-IV LFRs, as it may lead to the untimely failure of thin-walled components. Understanding the causes of dissolution 'pitting' – these are either associated with steel defects or with weaknesses in the design of the nuclear system – is of paramount importance, as it is impossible to predict the exact locations where 'pits' will form, and it is also technically challenging to detect them.

The scatter in the available LMC data of T91 and similar F/M steels as a function of the exposure duration is shown in Fig. 3.33 for static and Fig. 3.34 for flowing HLMs. As expected, the thickness of the corrosion layer caused either by oxidation, uniform dissolution or locally enhanced dissolution increases with the steel exposure duration. For example, the thickness of the oxide scale on the surface of T91 F/M steels exposed to static 26 %Pb-74 %Bi at 630 °C increased from 55 to 90 μm as the exposure time increased from 110 to 710 h, respectively (red ellipse in Fig. 3.33) [171].

Many studies on the oxidation behaviour of T91 and compositionally similar F/M steels showed that at any moment during the steel exposure, the oxide scale thickness is defined by two competing processes: (a) oxide scale formation (parabolic law), and (b) oxide scale removal by the HLM. The curve corresponding to Eq. (3-10) is plotted in Fig. 3.35 against a set of data resulting from T91 F/M steel exposures to oxygen-containing ($C_O \approx 10^{-6}$–10^{-5} wt%), flowing LBE ($v \approx 2$ m/s) at 550 °C. This figure shows a general agreement between the oxide scale growth curve for HT-9 F/M steels and the available oxidation data for T91 F/M steels, although several data points show deviations from the curve representing the HT-9 oxide growth law. These deviations may be partly attributed to differences in the oxidation behaviour of the two steel grades, but may also stem from the reliability of the values of experimental constants proposed by Zhang [30,134], as the latter were determined based on a limited amount of experimental data.

Under static HLM conditions (Fig. 3.33), localised dissolution became prevalent for T91 and compositionally similar F/M steels after an exposure of 3000 h, yielding the maximum localised dissolution depth of ~200 μm in T91 F/M steels. Moreover, the incubation period needed for visible localised dissolution was much shorter (<1000 h) under flowing HLM conditions (Fig. 3.34). It can also be seen that noticeable, locally enhanced dissolution started within the first 1000 h of exposure, reaching a dissolution depth of ~500 μm in EUROFER steels, while other F/M steels suffered non-negligible localised dissolution as well. The localised dissolution depth in EUROFER F/M steels increased to ~1000 μm after 2011 h of exposure at 550 °C to flowing LBE ($v \approx 2$ m/s, $C_O \approx 10^{-7}$ wt%) (Fig. 3.34). The most severe case of locally enhanced dissolution corrosion of ~1190 μm was reported for T91 F/M steels exposed to oxygen-containing ($C_O \approx 10^{-7}$ wt%), flowing LBE ($v \approx 2$ m/s) at 400 °C for 13,172 h (Fig. 3.34).

3.3.3. *The role of HLM oxygen concentration*

The existing experimental data regarding the effect of the oxygen concentration dissolved in the HLM on the LMC behaviour of

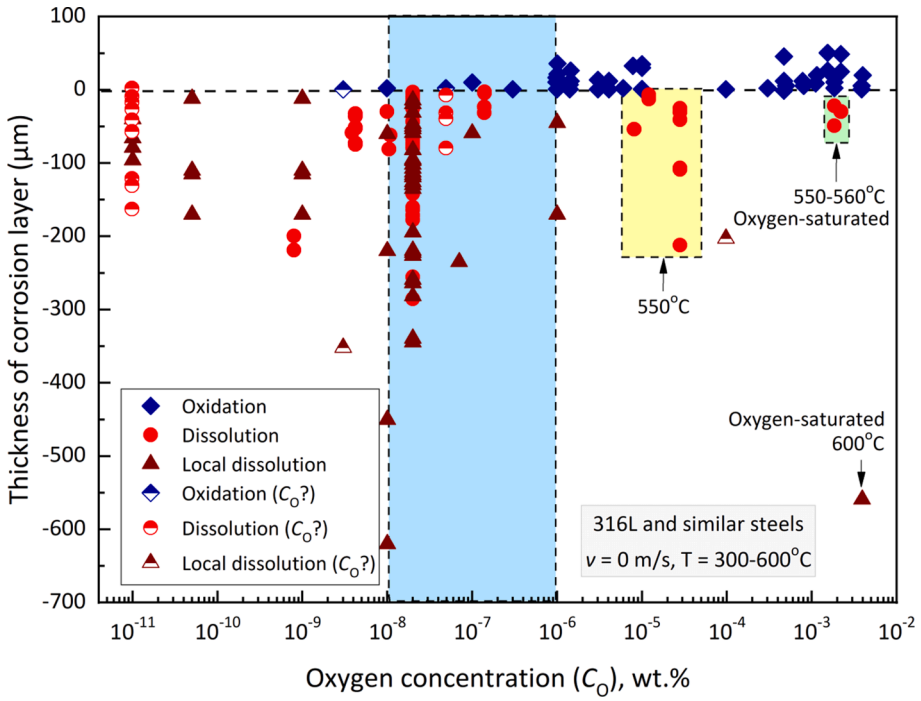

Fig. 3.36. Corrosion layer thickness in 316L AuSS and similar steels (316, 304L) as a function of the oxygen content in *static* LBE. Data points corresponding to uncertain LBE oxygen contents are indicated by special symbols and "C_O?" in the figure legend. Data collected from Refs. [40,42,107,116,125,136,177,178,196–213]. Mechanisms: uniform oxidation (diamonds), uniform dissolution (circles), and locally enhanced dissolution (triangles).

316L AuSS and similar steels exposed to static LBE are compiled in Fig. 3.36. Despite the fact that dissolution is the prevalent LMC mechanism at low HLM oxygen concentrations ($C_O < 10^{-7}$ wt%) and oxidation prevails at high HLM oxygen concentrations ($C_O > 10^{-6}$ wt%), there is a 'transition' range of oxygen concentrations (10^{-8} wt% $< C_O < 10^{-6}$ wt%), where oxidation and dissolution tend to appear concurrently for exposure temperatures lower than 500 °C. In this range, oxidation has also been reported to change into dissolution corrosion after a certain exposure time, a phenomenon that mainly depends on the exact combination of exposure temperature and HLM oxygen concentration. It is obvious that under such exposure conditions, the oxide scales covering the steel surface are rather defective and thus not adequately protective, allowing the HLM penetration into the base steel after some time. As already mentioned, when the HLM reaches the steel bulk, dissolution attack starts underneath the oxide scales. This is an undesirable situation, as the defective oxide scales remaining on the steel surface can neither stop the outward diffusion of steel alloying elements nor the inward diffusion of HLM (Pb/Bi) atoms, often leading to dissolution 'pitting' (see examples in Figs. 3.3 and 3.7).

The dissolution corrosion data in Fig. 3.36 correspond to uniform LBE corrosion, i.e., the thickness of the dissolution-affected zone remains the same over the entire steel surface with few minor fluctuations. The depth of uniform dissolution rarely exceeds 200 μm, except if the LBE oxygen concentration is very low [196,202,205]. Note that both uniform and locally enhanced dissolution can occur even under oxygen-saturated HLM conditions when the exposure temperature exceeds 550 °C. This indicates that at these elevated temperatures, the oxide scales become permeable to the HLM, allowing its penetration into the steel bulk. One of the possible causes of the latter is the known magnetite/wüstite phase transformation at ~570 °C. These observations support the fact that dissolution corrosion, and in particular dissolution 'pitting', are favoured by low HLM oxygen concentrations, high exposure temperatures, or combinations of both.

Fig. 3.37 compiles the existing data relating to the LMC behaviour of 316L AuSS and similar steels exposed to flowing HLMs (Pb, LBE) with various oxygen contents. One may readily observe that oxidation occurs mainly at HLM oxygen concentrations $C_O \geq 10^{-6}$ wt %, while dissolution corrosion becomes progressively more dominant at $C_O \leq 5 \times 10^{-5}$ wt%. Both oxidation and dissolution corrosion operate at intermediate HLM oxygen contents, i.e., 10^{-6} wt% $< C_O < 5 \times 10^{-5}$ wt%, competing against each other. In this HLM oxygen concentration range, the exact exposure conditions (i.e., temperature, duration, HLM flow velocity) will determine which of the two LMC mechanisms is the predominant one. Comparing static HLM data (Fig. 3.36) with flowing HLM data (Fig. 3.37), the HLM oxygen concentration below which dissolution corrosion is predominant at temperatures <550 °C increases from $C_O \approx 10^{-8}$–10^{-7} wt% in static LBE to $C_O \approx 10^{-6}$ wt% in flowing HLMs. This suggests that safeguarding the protectiveness of the oxide scales on the steel surface requires higher HLM oxygen concentrations in flowing HLMs as compared to static HLMs. This could be attributed to the following reasons: (a) oxide scale formation and growth are faster at higher HLM oxygen concentrations, allowing the restoration of oxide scales that are affected by the erosive action of the flowing HLM, and (b) the diffusion barrier layers that are established at the steel/HLM interfaces are thinner under flowing HLM conditions. Such diffusion barrier layers form even when the steels are oxidised, as oxide

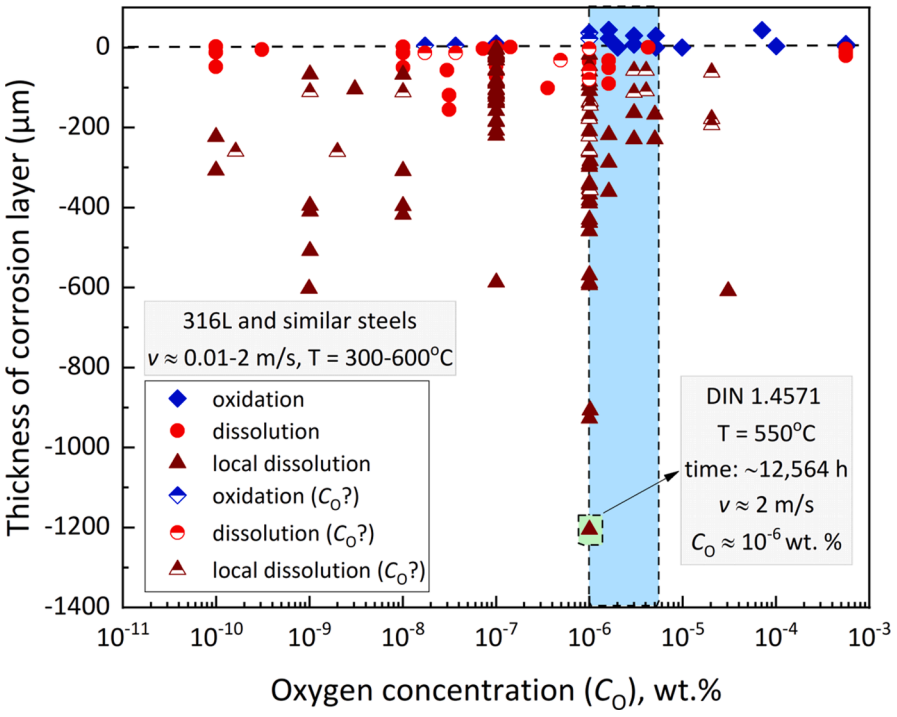

Fig. 3.37. Corrosion layer thickness in 316L AuSS and similar steels (316, 1.4571, 18Cr-10Ni-Ti, 08 × 16H11M3) as a function of the oxygen content in *flowing* HLMs. Data corresponding to uncertain HLM oxygen contents are indicated by special symbols and "C_O?" in the figure legend. Data collected from Refs. [43,44,95,96,102,104,106,115,118,141,172,180,187–189,191,214–230].

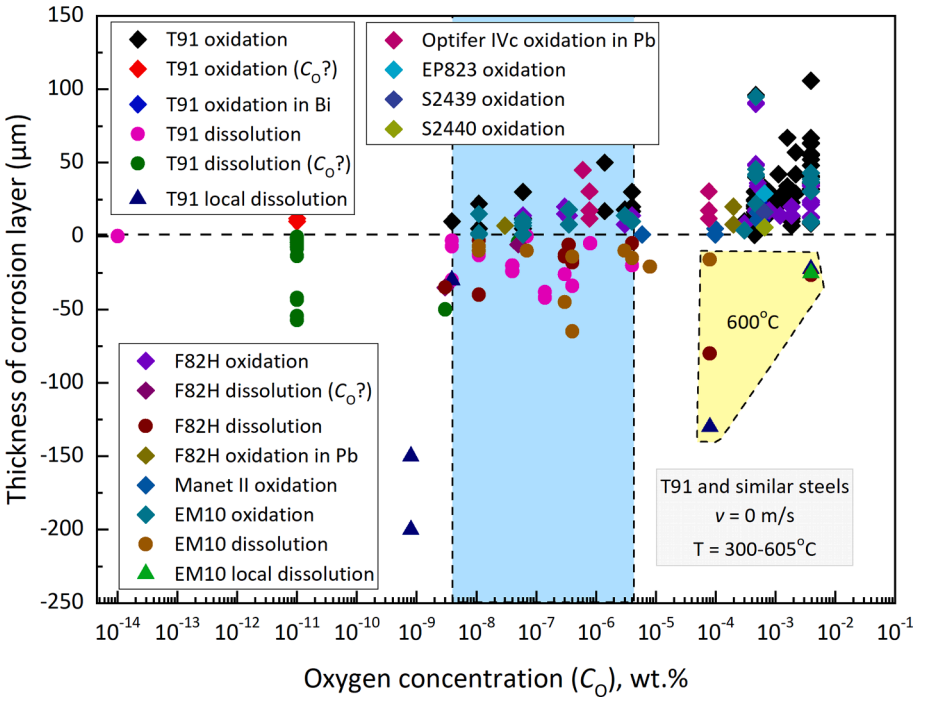

Fig. 3.38. Corrosion layer thickness in T91 and compositionally-similar F/M steels, as a function of the oxygen concentration in *static* HLMs. Steel grades: T91, F82H, Manet II, EM10, Optifer IVc, EP823, S2439 and S2440; HLMs: Pb, LBE, and Bi. Data corresponding to uncertain HLM oxygen contents are indicated by "C_O?" in the figure legend. Data collected from Refs. [92,116,125,133,136,167,169–171,189,196,198,202–205, 208–211,231,233–236]. Mechanisms: uniform oxidation (diamonds), uniform dissolution (circles), and locally enhanced dissolution (triangles).

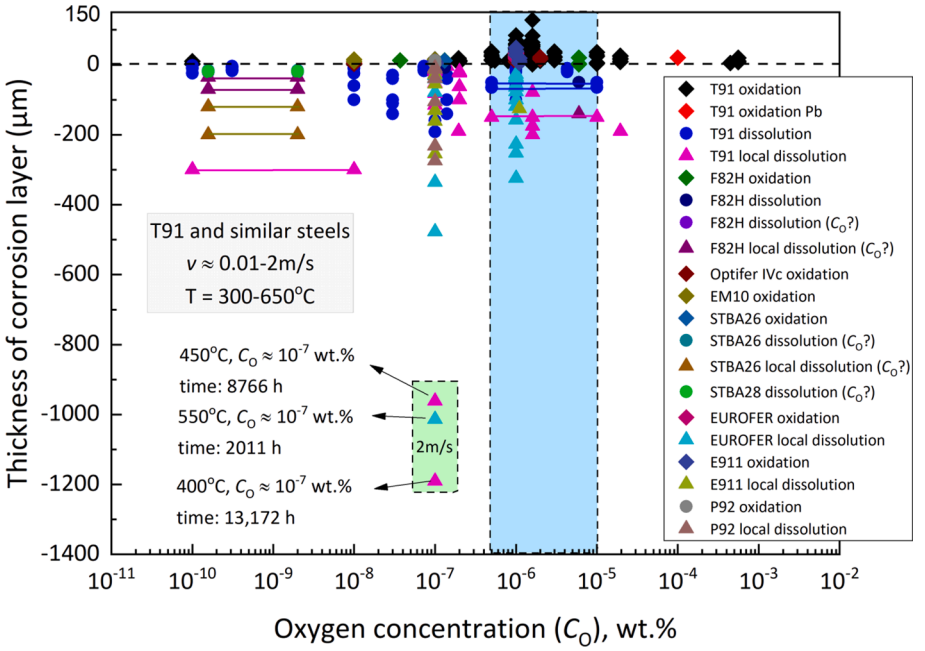

Fig. 3.39. Corrosion layer thickness in T91 and compositionally-similar F/M steels, as a function of the oxygen concentration in *flowing* HLMs. Steel grades: T91, F82H, Optifer IVc, EM10, STBA26, STBA28, EUROFER-97, E911 and P92; HLMs: Pb and LBE. Data corresponding to uncertain HLM oxygen contents are indicated by "C_O?" in the figure legend. The bars indicate cases of localised dissolution resulting from exposures to C_O ranges. Data collected from Refs. [92,101,115,117,172,180,181,183,185,187,189–191,215–217,219,225,227,230–232,234,237–240]. Mechanisms: uniform oxidation (diamonds), uniform dissolution (circles), and locally enhanced dissolution (triangles).

scales might be incapable of fully preventing the interdiffusion of species (i.e., outward diffusion of steel alloying elements, inward diffusion of Pb/Bi). When the diffusion barrier layers at the steel/HLM interfaces are sufficiently thick (e.g., under static HLM conditions), they can delay the further steel dissolution.

Moreover, careful examination of the available LMC data indicates that locally enhanced dissolution corrosion is primarily facilitated by elevated exposure temperatures, especially >550 °C, but it may also occur at lower temperatures (450–460 °C), when the HLM is rather poor in oxygen ($C_O < 10^{-7}$ wt%). Localised corrosion has been attributed to local disturbances in the HLM flow pattern (e.g., HLM flow instabilities, turbulences) in some prior studies [118,172]. Local HLM flow turbulences can cause severe material losses within short periods of time, resulting in deep LMC damage. Also, specific steel microstructural features (e.g., annealing twins in coarse-grained steels; Fig. 3.4) can promote dissolution 'pitting' (see Section 3.3.6). The deepest localised dissolution (~1200 h) was reported for 1.4571 AuSS exposed to moderately oxygenated ($C_O \approx 10^{-6}$ wt%), flowing LBE ($v \approx 2$ m/s) at 550 °C for 12,564 h; in this case, the deep damage can be attributed to the prolonged exposure (12,564 h) at a high temperature (550 °C).

The existing experimental data on T91 and similar F/M steels are compiled as a function of the HLM oxygen concentration in static (Fig. 3.38) and flowing (Fig. 3.39) conditions. All F/M steels showed similar LMC behaviours, which is not surprising considering their similar chemical compositions. Moreover, the LMC behaviours of these steels were comparable, irrespective of the HLMs used for steel exposure. One should point out, however, that the limited availability of experimental data from steel exposures to HLMs other than liquid LBE does not permit confident conclusions with respect to the relative corrosiveness of the employed HLMs.

One should also mention that the confidence in some of the reported LMC data is rather limited, due to the fact that the amount of dissolved oxygen in the HLMs was poorly monitored during the steel exposures. These data points are indicated by "C_O?" in the legends of Figs. 3.36–3.39. Moreover, the data reported in several studies were associated with exposures to rather broad C_O ranges and not to single C_O values (Fig. 3.39). This makes the interpretation of the experimental data very challenging, as it is impossible to correlate the reported LMC results to specific C_O levels in the HLMs. From the pool of data that were acquired from exposures to HLMs with significantly variable C_O levels (e.g., by two orders of magnitude or more), the data that show deep dissolution are connected with lines that extend over the corresponding (reported) C_O range in Fig. 3.39. This gives a more accurate impression of the exposure conditions that may yield dissolution corrosion depths >50 μm, as a result of exposing T91 and similar F/M steels to different HLMs (Pb, LBE).

Despite the uncertainties in the available experimental data, one may identify some general trends in the LMC behaviour of T91 and similar F/M steels as a function of the HLM oxygen concentration, C_O. For example, Fig. 3.38 shows that by increasing the HLM oxygen concentration from $C_O \approx 4 \times 10^{-9}$ wt% to $C_O \approx 4 \times 10^{-3}$ wt%, oxidation is promoted in static HLMs, producing oxide scale thicknesses >100 μm. Even though oxidation is the predominant LMC mechanism at HLM oxygen concentrations $C_O > 10^{-4}$ wt%, dissolution corrosion was also observed at high HLM oxygen concentrations for exposures at 600 °C (see yellow triangular area in Fig. 3.38). This again shows that at such high temperatures, the oxide scales are not adequately protective, allowing the penetration of LBE through the oxide scales and the eventual attack of the base steel. Between $C_O \approx 4 \times 10^{-9}$ wt% and $C_O \approx 4 \times 10^{-6}$ wt%, both oxidation and dissolution can take place, while dissolution corrosion is the predominant LMC mechanism at $C_O < 4 \times 10^{-9}$ wt%. In flowing HLMs (Fig. 3.39), dissolution corrosion (uniform and localised) prevails below $C_O \approx 2 \times 10^{-7}$ wt%, while for HLM oxygen concentrations

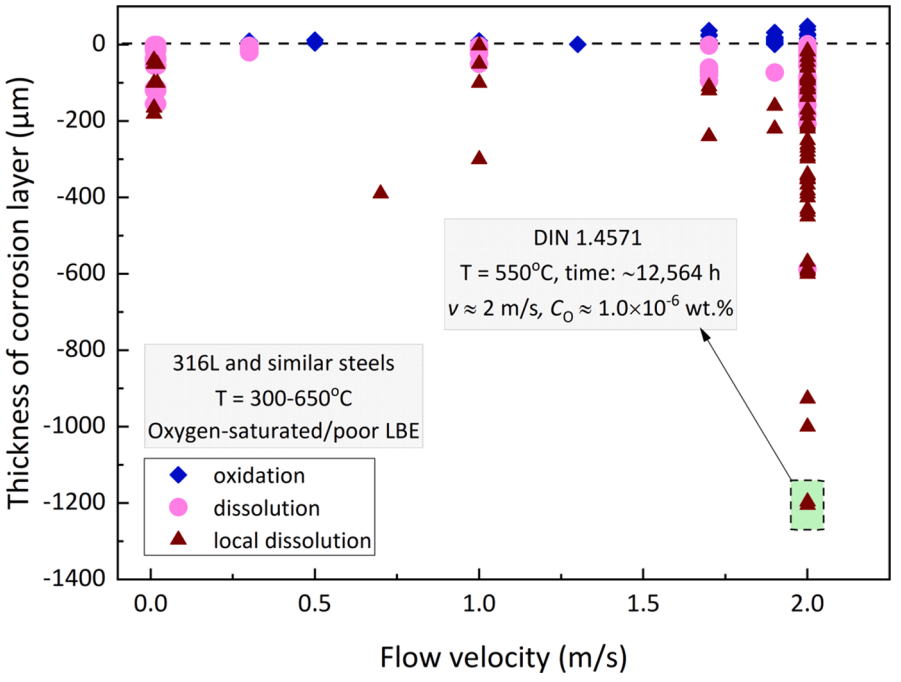

Fig. 3.40. Corrosion layer thickness in 316L AuSS and similar steels as a function of the LBE flow velocity. Data from steel exposures to both static and flowing ($v \approx 0.01$–2 m/s) conditions are included. Data collected from Refs. [40,42,107,116,125,136,177,178,196–213,230].

between $C_O \approx 5 \times 10^{-7}$ wt% and $C_O \approx 1 \times 10^{-5}$ wt%, both oxidation and dissolution corrosion can occur. In particular, deep (961–1190 μm) localised dissolution damage was found after exposures of 2011–13,172 h at 400–550 °C in moderately oxygenated ($C_O \approx 10^{-7}$ wt%), flowing LBE ($v \approx 2$ m/s) (green rectangular area in Fig. 3.39). The fact that deep (~1190 μm) localised dissolution damage can occur even under mild reactor-relevant conditions, i.e., at a low temperature (400 °C) and in contact with moderately oxygenated LBE ($C_O \approx 10^{-7}$ wt%) circulating at a typical flow velocity ($v \approx 2$ m/s), is a concern.

Similar to 316L AuSS, the HLM oxygen concentration below which dissolution corrosion (both uniform and localised) becomes the predominant LMC mechanism in T91 F/M and similar steels shifts to higher values in contact with flowing HLMs ($C_O \approx 5 \times 10^{-7}$ wt%) as compared to static HLMs ($C_O \approx 4 \times 10^{-9}$ wt%). As mentioned earlier, this may be attributed to two reasons: (a) oxide scales are affected by the erosive action of flowing HLMs, requiring higher HLM concentrations to remain protective, and (b) the diffusion barrier layers at the steel/HLM interface are thinner in flowing HLMs, thereby becoming less efficient in preventing the further dissolution of steel alloying elements through the (non-protective) oxide scales on the steel surface.

3.3.4. The role of HLM flow velocity

The influence of HLM flow velocity on the LMC behaviour of 316L and similar AuSS is shown in Fig. 3.40, for both static and flowing HLM conditions. The HLM flow velocity in testing under isothermal static conditions was assumed to be $v \approx 0$ m/s, except for testing under non-isothermal static conditions, where limited HLM movement was caused by thermal convection [201].

As may be observed from Fig. 3.40, both uniform and locally enhanced dissolution occur regardless of the HLM flow velocity. As already mentioned, localised dissolution is promoted by combinations of high exposure temperatures and low HLM oxygen concentrations, and this happens regardless of the precise HLM flow velocity (e.g., for HLM flow velocities in the $v \approx$ 0–1.8 m/s range; Fig. 3.40). This observation corroborates the idea that local disturbances in the HLM flow pattern (e.g., the local occurrence of 'eddies') affect the LMC behaviour of 316/316L AuSS more than the average HLM flow rate for $v \leq 2$ m/s. Nonetheless, the severity of localised dissolution corrosion is associated with the HLM flow velocity, as when this becomes equal to $v \approx 2$ m/s, the depth of localised dissolution damage increases to the maximum depth of ~1200 μm (see green rectangle in Fig. 3.40).

The available LMC data on T91 and similar F/M steels are presented in Fig. 3.41 as a function of the HLM flow velocity; this figure comprises only the data acquired from tests in liquid LBE and Pb. The largest part of the data resulted from exposures to liquid LBE that was either static ($v \approx 0$ m/s) or circulated in a forced convection loop at $v \approx 2$ m/s, while few data points resulted from exposures to liquid LBE flowing at $v \approx 1$ m/s. Based on the data collection in Fig. 3.41, it can be inferred that both uniform and localised dissolution can occur regardless of the HLM flow velocity, however, upon increasing the HLM flow velocity to $v \approx 2$ m/s, locally enhanced dissolution corrosion becomes more severe, resulting in damage depths in the 961–1190 μm range, depending on the exposure temperature and duration. This conclusion is similar to that drawn from the available experimental data on 316L and similar AuSS

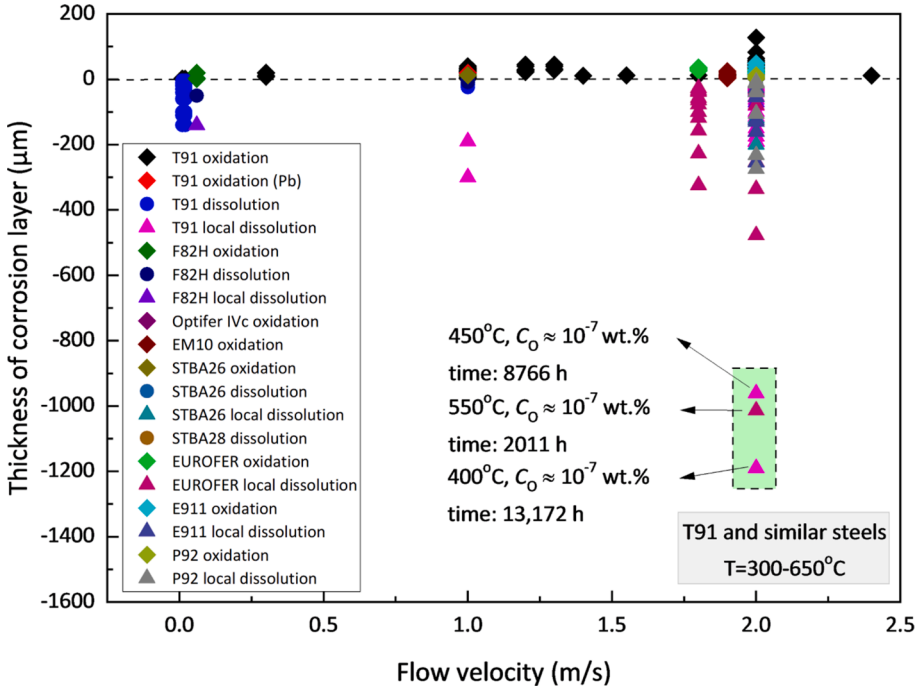

Fig. 3.41. Corrosion layer thickness in T91 and compositionally similar F/M steels (T91, F82H, Optifer IVc, EM10, STBA26, STBA28, EUROFER, E911, and P92) as a function of the HLM flow velocity. Data collected from Refs. [92,101,115,117,172,180,181,183,185,187,189–191,215–217,219,225,227,230–232,234,237–240]. Mechanisms: uniform oxidation (diamonds), uniform dissolution (circles), and locally enhanced dissolution (triangles).

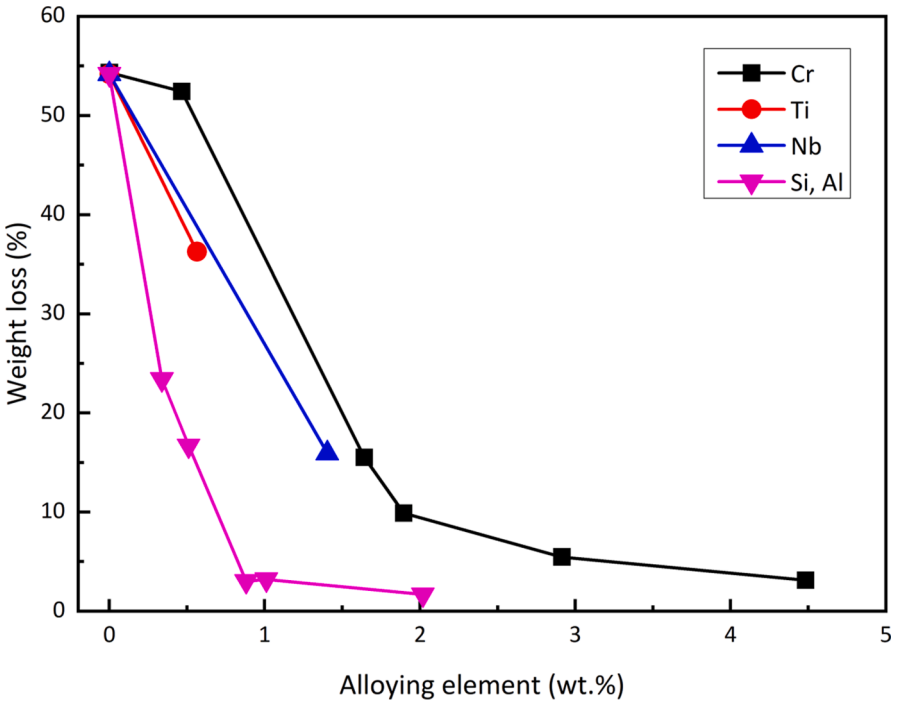

Fig. 3.42. Influence of different steel alloying elements on the LMC resistance of low-alloy steels exposed to flowing LBE ($v \approx 6$ m/s) at 600 °C. Adapted from [106].

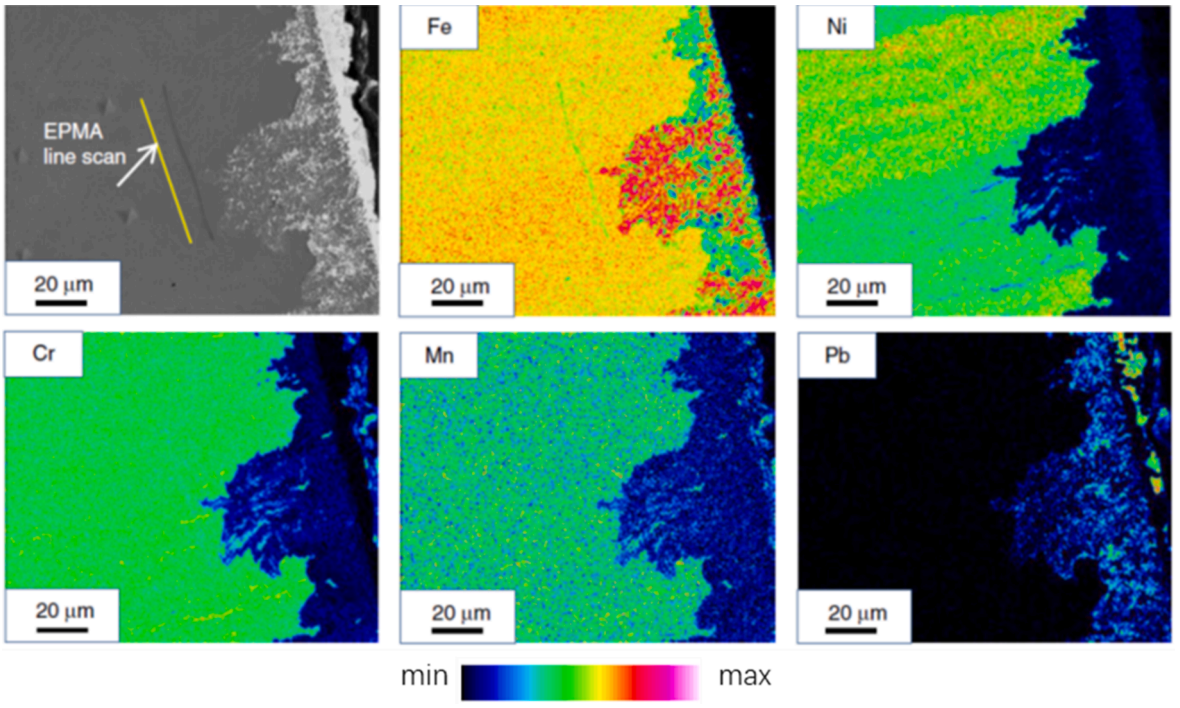

Fig. 3.43. EPMA† elemental maps showing the correlation of chemical bands with the local LBE dissolution attack in a SA 316L AuSS exposed to oxygen-poor ($C_O < 10^{-11}$ wt%), static LBE at 500 °C for 1000 h. Bands poorer in Ni are more attacked than bands richer in Ni. Adapted from [177].

(Fig. 3.40).

3.3.5. *The role of steel chemical composition*

The steel chemical composition is the overarching factor that is intrinsic to the steel and affects greatly its compatibility with a specific HLM coolant. The effect of steel alloying elements, such as Cr, Ti, Nb, Si, and Al, on the LBE corrosion resistance was studied by Gorynin et al. [106] (Fig. 3.42). Fig. 3.42 shows that, increasing the concentration of these elements in low-alloy steels decreases sharply the weight loss in contact with fast-flowing LBE ($v \approx 6$ m/s) at 600 °C. The most effective steel alloying elements against LBE corrosion are Al and Si. More specifically, for Al or Si additions higher than 2 wt%, the steel weight loss is negligible. This section will provide more information on the effect of various steel alloying elements on the steel corrosion behaviour in contact with HLMs.

Nickel (Ni): among the main alloying elements of 316L AuSS and similar steels, Ni has the highest solubility in liquid Pb and LBE, approaching 10 wt% in the latter at 700 °C. Therefore, Ni is the first steel alloying element to dissolve in the HLM, leaving behind micro-cavities in the steel that are subsequently filled with LBE, thereby facilitating the dissolution of other steel alloying elements (e.g., the dissolution of Cr is easier in oxygen-depleted LBE, and LBE becomes progressively depleted in oxygen as it penetrates deeper into the steel). Schroer et al. [102,115] remarked that the formation of a protective Cr- (and Si-rich) oxide scale on the steel surface might result in Ni segregation at the steel/oxide interface. The local damage of this oxide scale is followed by the fast HLM dissolution attack of the Ni-enriched layer and the further attack of the base steel, often leading to the formation of sites of locally enhanced dissolution corrosion.

Klok et al. [177] reported that periodic fluctuations in the chemical composition (esp. in the Ni content) of industrial-sized AuSS heats, a phenomenon known as 'chemical banding', resulted in local disturbances of the dissolution front. This was observed in 60% CW 316L AuSS specimens exposed to oxygen-poor ($C_O < 10^{-11}$ wt%), static liquid LBE for 1000 h at 500 °C. Surprisingly, bands richer in Ni (10.4 wt% Ni) were less attacked by LBE than bands poorer in Ni (8.2 wt% Ni), as shown in Fig. 3.43, despite the fact that Ni is the most soluble in LBE steel alloying element (Fig. 3.18). Chemical banding results from the mechanical alignment (e.g., by means of cold rolling) of steel alloying element segregations stemming from melt solidification. Differences in the relative resistance of the chemical bands to dissolution corrosion were attributed to differences in the distribution of steel defects (e.g., deformation twins) that favour LBE dissolution attack. The latter stem from differences in the Ni content of the chemical bands, as Ni defines band deformability by affecting the steel stacking fault energy (i.e., energy required to form stacking faults that interfere with dislocation motion) in each

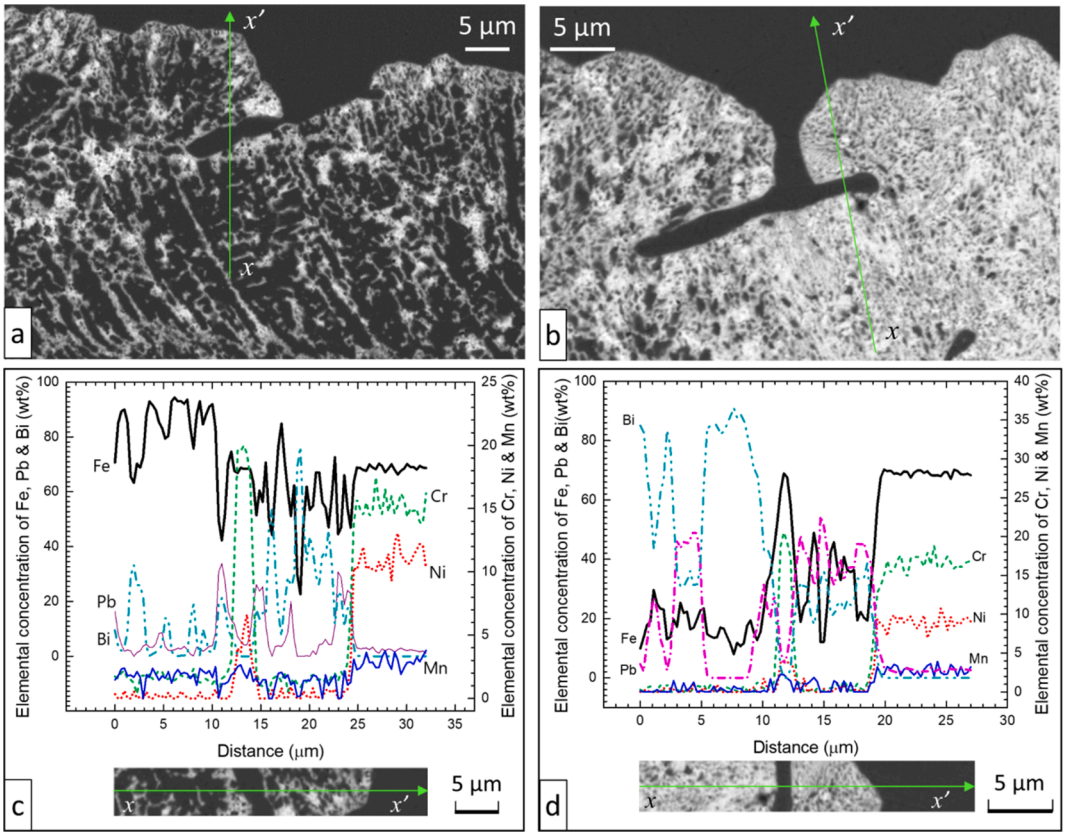

Fig. 3.44. SEM† images and EDS† line scans of the dissolution front in a SA 316L AuSS exposed to oxygen-poor ($C_O < 10^{-8}$ wt%) static LBE at 500 °C for 3282 h: (a,c) selective leaching of Ni, Mn and Cr; (b,d) non-selective leaching of Ni, Mn, Cr and Fe. This steel specimen was fabricated from the same SA 316L AuSS heat showing chemical banding in Fig. 3.43. Adapted from [40].

band. Since Ni increases the stacking fault energy (SFE) of the steel, bands richer in Ni contain less deformation twins, explaining why they suffer less LBE dissolution attack as compared to bands poorer in Ni, which contain more deformation twins. Since chemical banding in industrial-sized steel heats is associated with differences in band deformability and, therefore, in the density of defects that promote dissolution corrosion, it can also change the dissolution corrosion mechanism from selective leaching to non-selective leaching. This is shown in Fig. 3.44 for a SA 316L AuSS exposed to oxygen-poor ($C_O < 10^{-8}$ wt%), static liquid LBE at 500 °C for 3282 h [40]. The dissolution mechanism changed periodically from selective leaching (Fig. 3.44a) to non-selective leaching (Fig. 3.44b) at intervals of ~45 μm, in accordance with the width of the chemical bands in this cold-rolled, industrial-sized steel heat (see also Fig. 3.43). The EDS line scans in Fig. 3.44 show that the Ni content in the bands undergoing selective leaching is slightly higher than 10 wt%, while the Ni content in the bands suffering non-selective leaching is lower than 10 wt%. This suggests that the threshold Ni content of (316L) AuSS, which can change the dissolution corrosion mechanism from selective leaching to non-selective leaching by affecting the steel SFE, is around 10 wt%.

Moreover, the selective leaching of Ni can eventually lead to steel ferritisation, i.e., the austenite-to-ferrite phase transformation, as mentioned earlier. Ferrite is sensitive to LME, therefore, (brittle) crack formation is facilitated in ferritised zones of AuSS that are exposed to liquid Pb/LBE while being subjected to external mechanical loads. The combined effect of steel ferritisation caused by the selective leaching of Ni with the plastic strain-induced martensite phase transformation on the LME susceptibility of AuSS will be discussed in more detail in Section 4.5.

Chromium (Cr): Cr has also a relatively high solubility in liquid Pb and LBE as compared to Fe, Mo, or Si, thus contributing to the susceptibility of 316L AuSS and similar steels to dissolution corrosion in contact with these two HLMs (Fig. 3.18). First, it is important to note that the types of oxide scales formed on steels in air depend on their Cr content. For Cr < 2 wt%, Fe-based oxides are formed; for Cr ≈ 9 wt%, duplex Fe-based and FeCr-based oxides are formed; for Cr ≈ 16 wt%, pitting corrosion and duplex Fe-based and FeCr-based oxides are observed, and for Cr > 28 wt%, Cr-based oxides are formed [228]. The oxidation behaviour of steels in liquid Pb and LBE is similar to their behaviour in air, thus the Cr content of both AuSS and 9Cr F/M steels favours the formation of duplex magnetite (outer) and FeCr-spinel (inner) oxide scales. Usually, Cr- and Si-rich oxides are more protective than Fe-based ones; however, the efficiency of an oxide scale as metal diffusion barrier depends on its density and lack of defects, which in turn depend on both test temperature and HLM oxygen concentration. One might expect that steel exposures to high HLM oxygen concentrations promote the formation of thick, defect-rich oxide scales, as steel oxidation under such conditions (especially at high temperatures) proceeds fast, therefore, the probability of forming perfect (i.e., defect-free, dense) oxide scales is low. On the other hand, steel exposures to moderate conditions (i.e., moderate HLM oxygen concentrations and exposure temperatures) are expected to (slowly) form dense and defect-poor oxide scales that are more protective than their thicker and less dense counterparts. Moreover, the high Cr contents of T91 F/M and ODS ferritic steels result in the formation of more protective Cr-based oxide scales as compared to steels with lower Cr contents. The better protectiveness of Cr-based oxide scales is reflected in the longer incubation times needed for the onset of dissolution corrosion [101,225,241].

Manganese (Mn): the effect of Mn on the steel LMC behaviour has not yet been systematically investigated. As pointed out by Yamaki et al. [178], the solubility of Mn in liquid LBE is very high (2.3 wt% at 500 °C), making it comparable to the solubility of Ni (2.7 wt% at 500 °C). Interestingly, Johnson et al. [242] reported that the concentration of Mn tended to increase at the GBs of D9 steels during exposure to liquid LBE ($C_O \approx 3–5 \times 10^{-6}$ wt%, $v \approx 1.9$ m/s) at 550 °C for 1000–3000 h. Combining this information with the fact that dissolution corrosion in 316/316L AuSS starts invariably by the HLM penetration into the steel GBs (where Cr also tends to segregate), one may assume that Mn facilitates the onset of dissolution corrosion; of course, this hypothesis must be further confirmed experimentally. Another contribution of Mn to the susceptibility of 316L/316L AuSS to dissolution corrosion, possibly in terms of dissolution 'pitting', is via the formation of MnS precipitates, as suggested by Schroer et al. [115]. As discussed in Section 3.2.2.3, the presence of (sizeable) MnS precipitates close to the steel surface enables the HLM ingress into the steel bulk via the steel/MnS precipitate interfaces [40].

Molybdenum (Mo): Soler et al. [210] partly attributed the difference in the LMC behaviour of 304L and 316L AuSS to the presence of Mo in the latter (2.0–3.0 wt%). They found that the exposure of 316L AuSS to well-oxygenated ($C_O \approx 4.7 \times 10^{-4}–2 \times 10^{-3}$ wt%) static liquid LBE at 600 °C for ≤1500 h resulted in the formation of a duplex magnetite/FeCr-spinel oxide scale. Elemental analysis of the duplex oxide scale revealed the segregation of Mo in the inner FeCr-spinel layer; in fact, Mo appears to promote the formation of duplex magnetite/FeCr-spinel oxide scales. On the other hand, exposing 304L AuSS to the same conditions resulted in the formation of a thin chromia (Cr_2O_3) scale on the steel surface. One should mention, however, that 304L AuSS are richer in Cr (18–20 wt% Cr) than 316L AuSS (16–18 wt% Cr), a fact that might partly explain the formation of chromia on 304L as opposed to the formation of FeCr-spinel on 316L. The LMC resistance of both AuSS was found to be satisfactory at these exposure conditions [210]. The segregation of Mo in the porous, rather thick (~30 μm) oxide scale formed on 316L AuSS exposed for 959 h at 550 °C to flowing ($v \approx 2$ m/s) LBE with an oxygen concentration of $C_O \approx 5 \times 10^{-7}$ wt% was reported by Takahashi et al. [224]. Ilinčev et al. [223] reported that Mo impedes the passivation of 316L AuSS, which may dissolve at a rate of 1000–2000 μm/year when not passivated. In their study, 304, 304L, and 316 AuSS were exposed for 1000 h at 500 °C to slow-flowing ($v \approx 1–2$ cm/s) LBE with two different oxygen concentrations, i.e., $C_O \approx 3–4 \times 10^{-6}$ wt% and $\sim 2 \times 10^{-5}$ wt%. They found that the dissolution rate of mechanically ground 316 AuSS was about 400–1600 μm/year, while that of ground 304/304L AuSS was <400 μm/year under both exposure conditions. If this difference is indeed attributed to the presence of Mo in 316L AuSS, then it may be suggested that Mo has an adverse effect on the steel LMC resistance. In fact, the effect of Mo depends on the HLM oxygen concentration. For instance, Mo proved to be highly LMC-resistant in contact with static liquid LBE ($C_O \approx 5 \times 10^{-6}$ wt%) at 700 °C for 1000 h [82], presumably due to its very low solubility in low-oxygen HLMs (e.g., <1 ppm in liquid Pb at 700 °C [243]) that does not really drive its dissolution in HLMs. By contrast, Mo underwent severe oxidation when exposed to oxygen-saturated liquid LBE after only 100 h at 600 °C [244].

Silicon (Si): numerous studies have reported that the addition of Si to the steel improves the LMC resistance of both 316 and similar AuSS [188,202,207,245], as well as ferritic steels [92,111,245–249]. For example, Kurata and Saito [202] reported the better resistance of Si-containing 316L AuSS (2.43 wt% Si in Si-316SS *vs*. 0.69 wt% Si in 316L) to dissolution corrosion when compared to normal 316L AuSS. By exposing both steels to oxygen-saturated, static liquid LBE at 550 °C for 3000 h, the authors found that the uniform ferritisation depth in 316L AuSS was ~100 μm, while the ferritisation of Si-316L AuSS was very sparse and localised. Also, Kurata and Futakawa [207] reported that the LMC resistance of 18Cr-20Ni-5Si steels was better than that of 316L AuSS (0.69 wt% Si) exposed to oxygen-saturated, static liquid LBE for 3000 h at 550 °C. They found that a highly protective, Si-rich (probably SiO_2) oxide scale formed upon the outward diffusion of Ni and Cr, protecting the steel from LBE dissolution attack.

For 9Cr-1.5Si ferritic steels, it was reported that the addition of Si resulted in much thinner and more protective oxide scales when compared to traditional 9Cr steels with a typical Si content after exposure to static liquid LBE ($C_O \approx 2.5 \times 10^{-5}$ wt%) at 550 °C for 1372 h. However, the favourable effect of the 1.5 wt% Si addition became insignificant at 550 °C when the LBE oxygen concentration decreased to $C_O \approx 4.4 \times 10^{-8}$ wt% [245]. The same phenomenon was also observed in 316 AuSS doped with 2.4 wt% Si [245]. The experimental results of 10Cr-2Si steels exposed to flowing ($v \approx 1$ m/s) LBE with $C_O \approx 10^{-8}$ wt% or $C_O \approx 10^{-6}$ wt% at 550 °C for 3116 h showed that the produced oxide scales were mostly detached, and only a thin Cr- or Cr/Si-rich oxide scale remained adherent to the steel surface [250]. Studies on the LMC behaviour of the Russian steel EP-823 (12Cr-2Si) exposed to flowing ($v \approx 2$ m/s), oxygen-containing liquid LBE ($C_O \approx 1–2 \times 10^{-6}$ wt%) at 470 °C showed that thinner duplex oxide scales with Si enriched inner layers (i.e., FeCr-spinel) covered the whole surface, in comparison to other similar F/M steels [238], whereas an increase in the exposure temperature to 550 °C led to the formation of a single-layer scale and the absence of the outer magnetite layer [199,238]. The LMC behaviour of EP-823 F/M steels is different in contact with static liquid LBE. It was reported that an IOZ† was formed after exposing such steels to oxygen-saturated static LBE at 490 °C for 5000 h, in addition to the formation of the typical duplex oxide scales [92]. The IOZ layer was found to be evident in the first 1000 h of the exposure to liquid Pb at 550 °C. Extending the exposure time for another 1000–2000 h led to the disappearance of the IOZ layer, while the material loss under these exposure conditions for such steels was larger than that for similar steels doped with only 0.5 wt% Si [122]. Particularly, increasing the exposure temperature to 650 °C, severe oxidation occurred in 100 h, leading to the formation of very thick and porous oxides with a thickness of ~500 μm [123]. Compared to T91 F/M steels, the oxide scales formed on EP-823 F/M steels after their exposure to oxygen-saturated, static liquid LBE at 550 °C for 1500 h were found to be harder and stiffer, resulting in higher susceptibility to cracking [251]. Schroer et al. [247] studied the LMC behaviour of 9Cr-3Si steels 1.4718 (X45CrSi9-3) exposed to flowing ($v \approx 2$ m/s) liquid LBE with $C_O \approx 10^{-7}$ wt% and $C_O \approx 10^{-6}$ wt% at 450 °C and 550 °C for 8000 h. They observed improvement of the steel LMC resistance at 450 °C in contact with moderately oxygenated ($C_O \approx 10^{-6}$ wt%) liquid LBE, whereas the benefits from Si doping became unclear at 550 °C, and even an adverse effect was found in high-oxygen liquid LBE at that temperature. Moreover, it should be pointed out that, despite the beneficial effect of Si addition under specific exposure conditions, the ductility and fracture toughness of Si-enriched steels are deteriorated and this type of steels is highly susceptible to LME [251] as well as radiation embrittlement [252].

Titanium (Ti): the role of Ti additions on the LMC behaviour of 316/316L AuSS is not completely clear. It has been reported that Ti-containing steels were subjected to deep localised corrosion under flowing HLM conditions for no clear reason [44]. On the other hand, Ilinčev et al. [223] reported that 321 AuSS (06Cr18Ni10Ti) proved to be resistant to dissolution corrosion when exposed for 1000 h at 500 °C to slow-flowing ($v \approx 1–2$ cm/s) liquid LBE with $C_O \approx 3–4 \times 10^{-6}$ wt%, irrespective of the steel surface condition. The satisfactory LMC resistance of these Ti-containing AuSS was attributed to the formation of a protective Ti-rich oxide scale, possibly rutile (TiO_2), on the steel surface. Rutile oxide scales have shown to be very resilient to LBE dissolution attack for other Ti-containing materials, such as Ti-based MAX phases. For example, Heinzel et al. [79] observed thin (≤ 1 μm) rutile scales on the surface of Ti_3SiC_2 MAX phase-based ceramics exposed to low-oxygen ($C_O \approx 10^{-8}$ wt%), static liquid LBE at 650 °C for 3000 h. These oxide scales were protective under the aggressive exposure conditions, preventing the occurrence of dissolution corrosion damage or other chemical interactions with liquid LBE.

Aluminium (Al): adding Al to steels can form passivating alumina (Al_2O_3) scales that remain stable at very low oxygen potentials (see Fig. 3.9). For this reason, Al is an important steel alloying element that is used to develop alumina-forming LMC-resistant materials, either in the bulk form or in the form of coatings on commercial steels. The bulk materials include alumina-forming ferritic alloys (e.g., FeCrAl alloys), alumina-forming austenitic (AFA) stainless steels, and alumina-forming high-entropy alloys (HEAs) that typically consist of at least five equimolar principal elements. A detailed review of the role of Al on the steel LMC behaviour will be given in Chapter 5.

3.3.6. The role of steel microstructure and thermomechanical state

The microstructure (grain size distribution, texture) and defects (GBs, annealing and deformation twins, secondary precipitates) are important factors that are intrinsic to the steel and affect its LMC behaviour in contact with a specific HLM coolant. The steel thermomechanical state (e.g., degree of cold working), microstructure and defects created during the various stages of steel manufacture affect all LMC mechanisms and especially dissolution corrosion (uniform and locally enhanced). Due to the possible detrimental effects of dissolution corrosion on the reliable steel performance, especially for thin-walled reactor components, this section will address extensively all steel microstructural aspects that are associated with this particular LMC mechanism. As already mentioned in Section 3.1, dissolution corrosion in 316L AuSS and similar steels progresses by the HLM ingress into preferred paths, such as GBs and twin boundaries, resulting in the ferritisation of the dissolution-affected zones due to the (often selective) leaching of the austenite stabilisers, i.e., Ni and Mn.

The strong interplay between the steel microstructure and the dissolution corrosion process (see Fig. 3.2) shows the need to understand all processes responsible for the creation of microstructural defects favouring dissolution corrosion. The most important one

of these processes is cold working, which is unavoidable to a certain extent for specific components, such as fuel cladding tubes, as it improves the steel strength and enhances its resistance to neutron irradiation-induced void swelling and creep. However, cold working affects greatly the steel LMC behaviour, due to the fact that it modifies certain aspects of the steel microstructure (grain size distribution, annealing/deformation twins, distribution and orientation of precipitates, texture) which in turn alter the steel susceptibility to LMC [42,177,253]. First, the effect of cold working on the LMC behaviour of 316/316L AuSS has been associated with deformation-induced grain refinement. Johnson et al. [228] reported the following effects of cold rolling on the oxidation behaviour of 316/316L AuSS: (a) grain refinement, (b) increased surface roughness (rolling marks), and (c) creation of a highly deformed layer close to the steel surface. In their study, solution-annealed (grain size: ~40 μm) and cold-rolled (grain size: ~10 μm) 316/316L AuSS were exposed to flowing ($v \approx 1.9$ m/s) liquid LBE with $C_O \approx 3–5 \times 10^{-6}$ wt% for 3000 h at 550 °C. The authors suggested that finer grain sizes in cold-

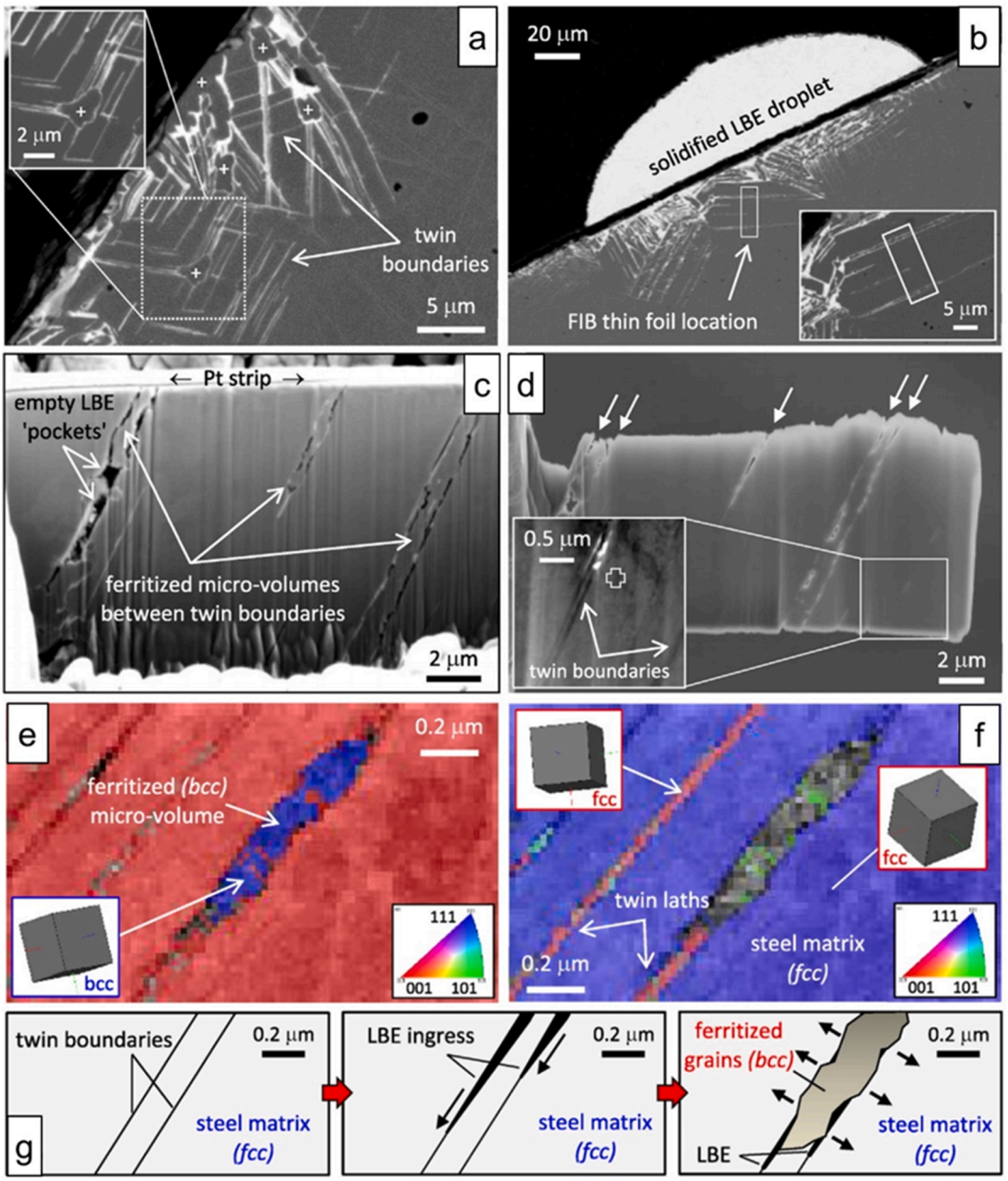

Fig. 3.45. CW 316L AuSS exposed to oxygen-poor ($C_O < 10^{-8}$ wt%), static liquid LBE at 450 °C for 1000 h. SEM† images of: (a) LBE ingress into deformation twin boundaries; (b) location of FIB† thin foil extraction; (c) ferritised steel micro-volumes between twin boundaries; (d) FIB thin foil showing twin boundaries decorated by LBE. (e-f) t-EBSD† phase maps showing ferritised (*bcc*) micro-volumes in an *fcc* steel matrix, and twin boundaries. (g) Schematic illustration of accelerated LBE ingress into twin boundaries, and ferritisation of steel micro-volumes between twin boundaries. Adapted from [41].

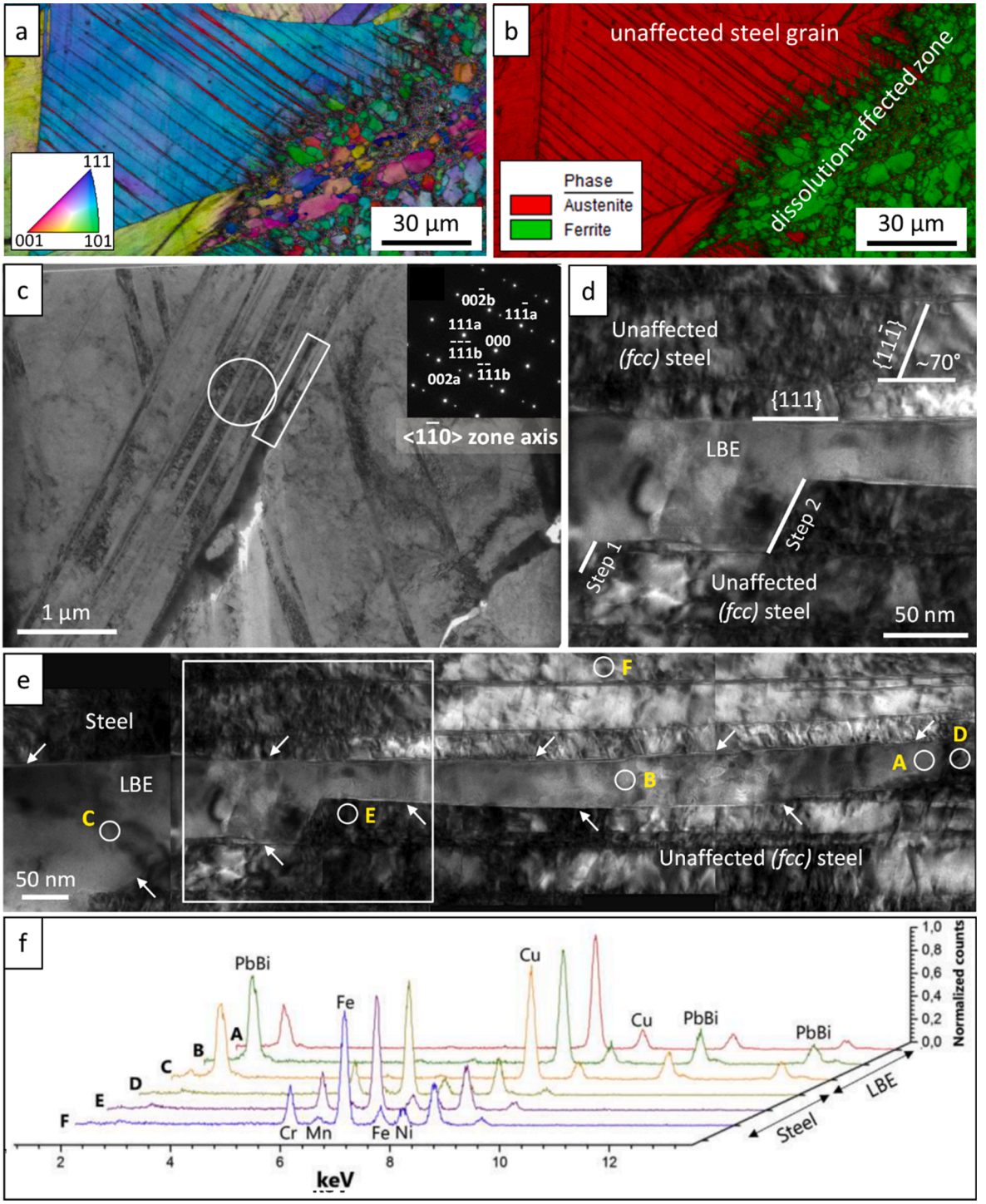

Fig. 3.46. CW 316L AuSS exposed to oxygen-poor ($C_O < 10^{-8}$ wt%), static liquid LBE at 500 °C for 1000 h. (a) EBSD† grain orientation map showing LBE penetration along closely-spaced striations in an austenitic grain. (b) EBSD phase map showing that the dissolution-affected zone is ferritic and the unaffected grains austenitic. (c) TEM† BF image and SAED† pattern of deformation twins along the ⟨1 1 0⟩ zone axis. (d-e) TEM BF images of the stepwise removal of steel layers during LBE penetration. (f) EDS† point analyses of LBE penetration (A, B, C) and steel matrix (D, E, F). Adapted from [40].

rolled 316/316L AuSS improved the steel LMC resistance for the following possible reasons: (a) GBs provided paths of rapid diffusion of Cr atoms to the steel surface, thus enabling the formation of highly-protective chromia (Cr_2O_3) scales; and (b) chromia nucleated mostly at GBs, growing laterally to form continuous oxide scales. These authors argued that GBs provide paths of faster diffusion of Cr atoms than the grain bulk; once available at the steel surface, Cr atoms form highly protective Cr_2O_3 scales, the formation of which would have otherwise been suppressed in favour of less protective Fe-based and FeCr-based oxide scales. Hence, fine-grained 316/316L AuSS are more likely to form continuous, protective oxide scales than coarse-grained steels when exposed to adequately oxygenated HLMs. The authors suggested that the other two cold rolling effects, i.e., the increased surface roughness and the highly deformed sub-surface layer, might have also improved the steel LMC resistance because the surface roughness could 'anchor' the chromia scale more efficiently against thermomechanical degradation and spallation, while the deformed sub-surface steel layer might form a metastable oxide scale that can eventually transform to a protective oxide scale. Soler et al. [210] also observed very thin (0.5 μm) chromia scales on CW 304L AuSS exposed to static liquid LBE with $C_O \approx 4.7 \times 10^{-4}$–$2 \times 10^{-3}$ wt% for $\leq$ 1500 h at 600 °C, in contrast to a 45-μm thick duplex oxide layer under the same testing conditions. They attributed this difference in steel oxidation behaviour to the formation of a disordered sub-surface steel layer (induced by CW) that enabled the rapid Cr diffusion to the steel surface, followed by the formation of a protective chromia scale.

However, contradictory findings have been reported by some researchers with respect to the effect of cold working on the steel LMC resistance. For instance, Kurata [213] reported a detrimental effect of cold working on the LMC resistance of 316 and JPCA (15Cr–15Ni–Ti) AuSS exposed to static LBE ($C_O \approx 4.2 \times 10^{-9}$ wt%) at 550 °C for 1000–3000 h. They found that cold working accelerated the formation of double-layer oxide scales, even though their thickness was increased only slightly, presumably due to the low LBE oxygen concentration. Moreover, the depth of ferritisation was found to increase by a factor of two in CW steels as compared to SA steels, a fact that was attributed by these authors to the increased dislocation density resulting from cold working. Several studies have shown that deformation twin boundaries and slip planes in CW AuSS promote HLM dissolution attack, presumably due to dislocation pile-ups at these sites in the steel bulk [40–42,177,212,229,254]. Klok et al. [177] reported that the maximum dissolution depth in 316L AuSS exposed to oxygen-depleted ($C_O < 10^{-11}$ wt%) static liquid LBE at 500 °C for 1000 h increased from 40 μm in non-deformed steels to 96 μm in 60% CW steels; the increase in LBE dissolution corrosion depth due to cold working was attributed to formation of deformation twins in the steel bulk. A similar effect was also reported by Tsisar et al. in CW 15-15Ti AuSS [197]. Moreover, Klok et al. [42] reported that decreasing the steel deformation temperature from 150 °C to −150 °C increased the maximum dissolution depth in the CW 316L AuSS from 25 μm to 53 μm, due to the increased deformation twin density in the steel specimen deformed at lower temperature.

Cold working also affects severely the oxidation behaviour of T91 and Si-enriched F/M steels [255,256]. Dong et al. [255] reported that cold rolling decreased the oxide scale thickness on T91 F/M steels exposed to oxygen-saturated static liquid LBE at 450 °C and 550 °C for 2000 h. The authors attributed this phenomenon to the rapid diffusion of Cr to the steel surface and the subsequent formation of thinner, more protective chromia scales. In that study, the numerous non-equilibrium GBs and migrating dislocations produced by cold rolling acted as fast diffusion paths for Cr, which also resulted in the formation of a continuous Cr-rich band next to the inner oxide scale adjacent to the IOZ. Dong et al. [256] also studied the effect of steel deformation (by tension or compression) on the oxidation behaviour of Si-enriched F/M steels (nominal steel composition: Fe-0.14C-1.26Si-1.65Mn-9.94Cr-1.72W-0.2V-0.15Ta; all in wt%) before exposing these steels to oxygen-saturated static liquid LBE at 550 °C for different durations. They found that the thickness of the oxide scale did not change by the steel pre-deformation treatment, however, the IOZ disappeared locally and the inner FeCr-spinel oxide layer became thinner. These changes in the oxide scale morphology were associated with the formation of a Cr-rich belt of uneven thickness within the inner FeCr-spinel layer. The presence of the Cr-rich band was associated with steel pre-deformation, which induced the formation of massive dislocations and non-equilibrium GBs enhancing the outward diffusion of Cr and the oxidation of the Cr-rich GB phase $M_{23}C_6$. In addition to the effect of steel pre-deformation, *in situ* bending stresses were also found to affect the oxidation behaviour of T91 F/M steels. Liu et al. [257] observed that the growth rates of the magnetite and FeCr-spinel oxide layers were accelerated at the tensile side of the *C*-ring specimens exposed to oxygen-saturated, static LBE at 480 °C. In addition, steel loss due to the formation of duplex oxide scales increased rapidly when the bending stress exceeded 300 MPa, indicating that applying a tensile stress transformed the inner FeCr-spinel scale to the outer magnetite scale. This was attributed to the stress-induced increase in the density of cavities or other defects (e.g., microcracks) in the spinel scale. Their results also suggested that the effect of applied stresses on the oxidation behaviour of T91 F/M steels should not be neglected, as stresses are almost invariably present during reactor operation.

Grain boundaries: dissolution corrosion in 316L AuSS and similar steels starts almost invariably intergranularly (see Fig. 3.20). This is not surprising considering that GBs are two-dimensional defects characterised by many imperfections (dislocations, point defects, small voids, impurity segregations) that favour the LBE penetration into the steel. The faster LBE ingress into GBs is not only attributed to the higher density of defects as compared to the grain bulk, but also to the GB enrichment in steel alloying elements that are highly soluble in the HLM, such as Cr that precipitates in the form of Cr-based carbides upon high-temperature annealing [258]. The high solubility of Cr in both liquid Pb and liquid LBE (Fig. 3.18) contributes to the faster HLM dissolution attack of GBs, especially when the steel is in contact with oxygen-poor HLMs, as at higher HLM oxygen concentrations, the removal of Cr might be delayed due to the formation of chromia (Fig. 3.9). The combination of low HLM oxygen concentrations and high exposure temperatures leads to the concurrent intergranular and transgranular LBE dissolution attack of the exposed steel [196]. Lambrinou et al. [40] observed that CW 316L AuSS with a finer grain size were more susceptible to dissolution corrosion than similar steels with a coarser grain size when exposed to oxygen-poor ($C_O < 10^{-8}$ wt%) static liquid LBE at 500 °C for 253–3282 h. Typically, cold working produces finer-grained steels, hence, one might expect that very fine-grained steels are highly susceptible to dissolution corrosion; even if that seems to be a reasonable assumption, one should also consider that high degrees of cold working are not only responsible for steel grain refinement,

but for high densities of defects (e.g., deformation twins) promoting HLM dissolution attack. It must also be mentioned that dissolution 'pitting' has been reported as a result of converging annealing twin boundaries in large (>170 μm) grains close to the surface of 316L AuSS (see Fig. 3.4) [40]. These findings suggest the possible existence of an optimum grain size distribution and type/density of defects (e.g., annealing/deformation twins) favouring dissolution corrosion that must be identified for all candidate 316L or similar structural AuSS prior to their use in reactor. Such considerations are very important during steel manufacturing, so as to produce AuSS with tailored microstructures that are suitable for the construction of Gen-IV LFRs.

Twin boundaries: as already mentioned, annealing/deformation twin boundaries are paths of fast HLM penetration into CW AuSS, presumably due to the dislocation pile-ups in the steel matrix close to these two-dimensional defects. Twin boundaries can provide very deep LBE penetrations into the steel bulk that reach a few hundred micrometres [40–44], as shown in Fig. 3.4. In-depth investigations of the effect of twin boundaries on the dissolution corrosion behaviour of 316L AuSS have been carried out by Hosemann et al. [41], Lambrinou et al. [40], and Klok et al. [42,177]. Hosemann et al. [41] and Lambrinou et al. [40] showed that deformation twins with a $\{1\ 1\ 1\}$ twinning plane typical for *fcc* metals promote the LBE ingress into the steel, facilitating the selective leaching of the steel alloying elements (Ni, Mn, Cr) that are highly soluble in LBE. Hosemann et al. [41] used transmission EBSD (t-EBSD) to demonstrate the ferritisation (i.e., the *fcc*-to-*bcc* phase transformation) of twin lath micro-volumes between successive twin boundaries in a CW 316L AuSS exposed to oxygen-poor ($C_O < 10^{-8}$ wt%), static LBE at 450 °C for 1000 h (Fig. 3.45). Possible volumetric changes in the ferritised micro-volumes between twin boundaries (either expansion due to the *fcc*-to-*bcc* phase transformation [41], or shrinkage due to the loss of steel alloying elements caused by selective leaching [42]) 'open' the twin boundaries, facilitating the further LBE ingress along these boundaries.

Lambrinou et al. [40] showed by transmission electron microscopy (TEM) that LBE penetrations along deformation twin boundaries in CW 316L AuSS dissolved the steel in a stepwise manner (Fig. 3.46e). The steps of steel removal occurred at $\{1\ 1\ \bar{1}\}$ close-packed planes, i.e., at typical slip planes in *fcc* metals that are observed at a 70° angle with the $\{1\ 1\ 1\}$ twinning plane and the twin deformation boundary in Fig. 3.46 [40].

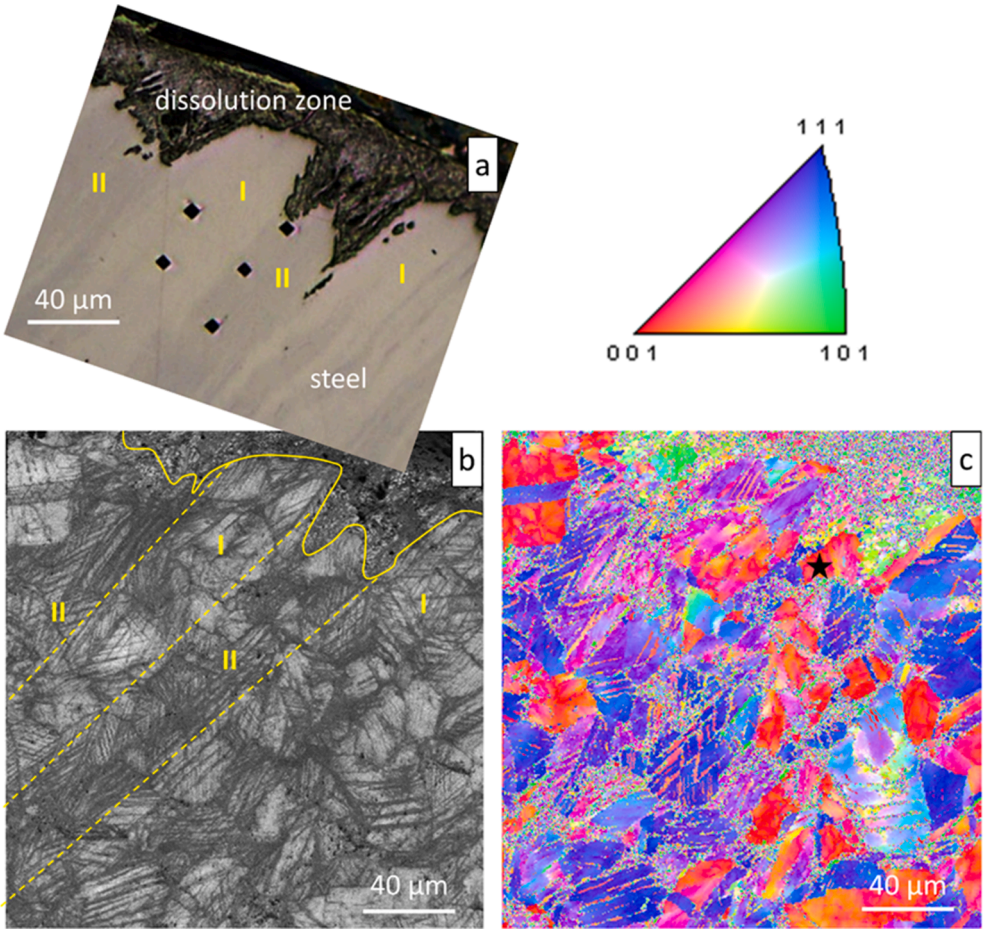

Fig. 3.47. (a) LOM† image of 60% CW 316L AuSS exposed to oxygen-poor ($C_O < 10^{-11}$ wt%), static LBE at 500 °C for 1000 h: I – bands with higher Ni content, II – bands with lower Ni content. (b-c) EBSD† analysis shows that the segregation of defects is higher in the bands with lower Ni content. Adapted from [42].

As mentioned earlier, increasing the degree of cold working increases the density of deformation twins, thereby intensifying the severity of dissolution corrosion damage; this has been demonstrated for CW 316L AuSS, where the maximum depth of LBE dissolution attack increased with the degree of cold working in steels with 0%, 20%, 40% and 60% of cold deformation [177]. Moreover, the density of deformation twins – and, accordingly, the severity of dissolution corrosion damage – increases as the steel deformation temperature decreases for the same degree of steel cold working. This was demonstrated for CW 316L AuSS deformed at −150 °C, 25 °C and 150 °C, where the maximum dissolution depth doubled when the steel deformation temperature decreased from 150 °C to −150 °C [42]. As reported by Klok et al. [177], periodic steel chemical inhomogeneities (phenomenon commonly referred to as 'chemical banding'), esp. with respect to the Ni content in steels, in industrial-sized 316L AuSS heats also affected the local density of deformation twins, which was directly reflected in the local advancement of the dissolution front. Prior studies have provided adequate experimental evidence of the effect of twin spatial distribution, orientation, and interconnectivity on the dissolution corrosion behaviour of 316L AuSS [40,42,177]. Last, but not least, the non-favourable orientation with respect to the steel surface of annealing twins in coarse-grained steels can cause dissolution 'pitting', as shown in Fig. 3.4 [40].

Texture: no systematic study has yet been performed on the effect of texture on the steel dissolution corrosion behaviour. Only Klok et al. [42] identified a tentative relation between the grain crystallographic orientation and its susceptibility to LBE dissolution attack. More specifically, it was found that grains with their ⟨1 1 1⟩ orientation parallel to the direction of tensile loading in CW 316L AuSS are more susceptible to dissolution corrosion, due to the fact that this orientation is more prone to twinning. This is shown in Fig. 3.47, where one may observe the undulations of the dissolution front in 60% CW 316L AuSS exposed to oxygen-poor ($C_O < 10^{-11}$ wt%), static liquid LBE at 500 °C for 1000 h. These undulations were caused by 'chemical banding' (i.e., fluctuations in the Ni content in steels), where the Ni-poorer bands are more attacked by LBE due to the higher density of deformation-induced defects, while the Ni-richer bands are less attacked by LBE due to a lower defect density. At the dissolution front of one of the Ni-poorer bands, one may identify a less LBE-attacked grain with the ⟨0 0 1⟩ orientation; this grain is probably less attacked since it contains less deformation-induced defects, presumably due to the fact that twinning is not favoured in this crystallographic orientation. It is well known that cold working of 316L and similar AuSS typically results in mixed [1 1 1] and [0 0 1] textures. Mixed textures are only able to affect the steel dissolution behaviour locally, as shown in Fig. 3.47. However, knowing the susceptibility of certain grain crystallographic orientations to dissolution corrosion might aid in further refining the steel manufacturing process to limit dissolution corrosion to the extent possible; this is especially important for structural components that are expected to undergo in-service (possibly local) plastic deformation under thermomechanical loading.

Another aspect of the dissolution corrosion behaviour of austenitic stainless steels that is indirectly associated with the steel texture is the orientation relationship (OR) between the original austenite (*fcc*) and the derivative ferrite (*bcc*) phases involved in dissolution corrosion-induced steel ferritisation. Charalampopoulou et al. [179] were the first to determine the OR between austenite (γ, *fcc*) and

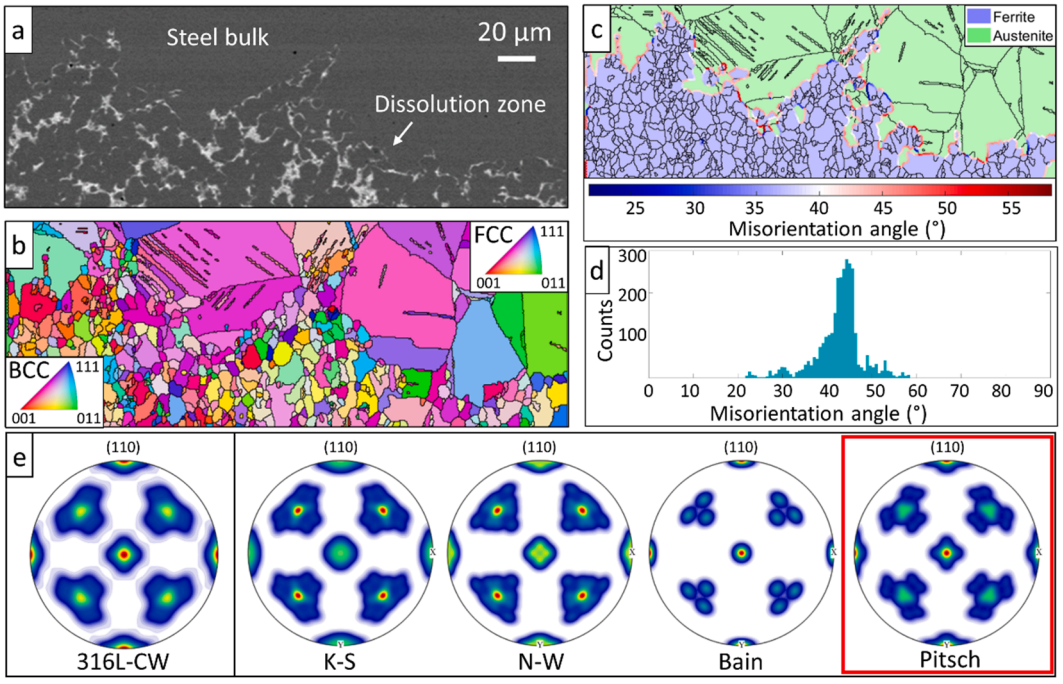

Fig. 3.48. (a) SEM† image of the ferritised dissolution-affected zone in a CW 316L AuSS exposed to oxygen-poor ($C_O \approx 10^{-9}$ wt%), static LBE at 550 °C for 1000 h. (b) EBSD† orientation map with inverse pole figure colour maps for *fcc* and *bcc* phases. (c) EBSD phase map of the γ/α interface misorientation boundary. (d) Misorientation angle distribution at the γ/α interface boundary. (e) Estimated *iso*-density pole figures from experimental data and theoretical OR models in the (1 1 0) plane of the CW 316L AuSS. Adapted from [179].

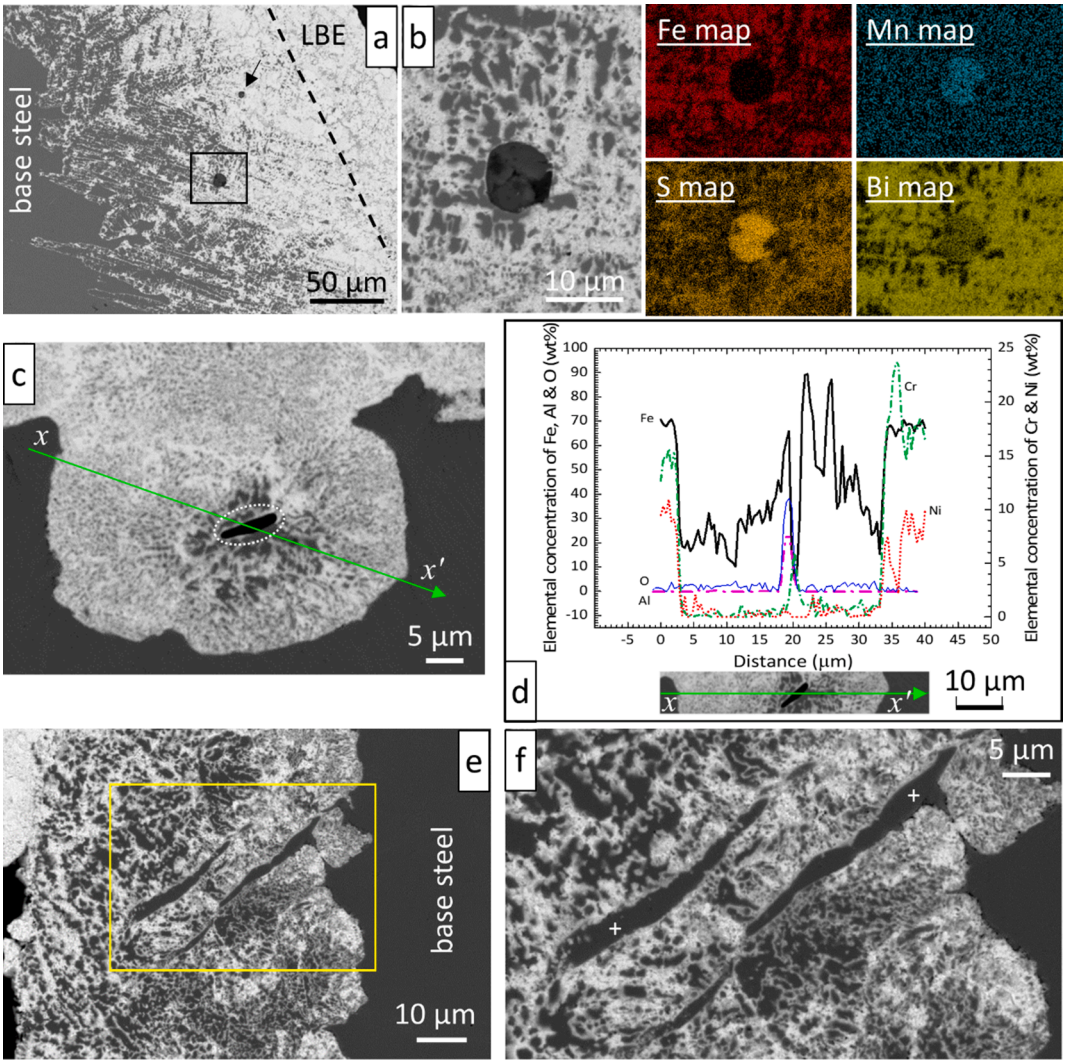

Fig. 3.49. SEM† images of precipitates in 316L AuSS exposed to oxygen-poor ($C_O < 10^{-8}$ wt%), static liquid LBE at 500 °C for 3282 h: (a-b) MnS precipitates in CW 316L AuSS; (c-d) Al-rich oxide inclusion with corresponding EDS† line scan, and (e-f) δ-ferrite stringers (crosses) in SA 316L AuSS. Adapted from [40].

ferrite (α, *bcc*) involved in the ferritisation (i.e., γ → α phase transformation) of SA & CW 316L AuSS exposed to oxygen-poor ($C_O \approx 10^{-9}$ wt%), static liquid LBE at 550 °C for 1000 h. Typically, *fcc*-to-*bcc* phase transformations in AuSS are best described by the Kurdjumov-Sachs (K-S) and Nishiyama-Wassermann (N-W) OR models. However, Charalampopoulou et al. [179] revealed that the loss of steel alloying elements due to LBE dissolution attack, and the presence of liquid LBE at the ferritisation (dissolution) front result in the relaxation of the fundamental lattice distortions occurring at the ferrite nucleation stage, therefore, the *fcc*-to-*bcc* phase transformation in SA & CW 316L AuSS was found to be best described by the Pitsch OR model (Fig. 3.48).

Steel precipitates: as already mentioned, the interfaces between secondary precipitates/inclusions and steel matrix are preferred paths of HLM ingress into 316L and similar AuSS under exposure conditions favouring dissolution corrosion. Lambrinou et al. [40] showed that the interfaces between the 316L AuSS steel matrix and typical precipitates/inclusions (MnS, oxides, δ-ferrite) are paths of fast LBE ingress into the steel, even when these precipitates/inclusions are insoluble or very slowly dissolving in liquid LBE (see Fig. 3.49). Therefore, the presence of large non-oxidising inclusions (e.g., MnS, oxides) intercepting the steel surface will allow the LBE ingress into the inclusion/steel matrix interfaces, thereby triggering the occurrence of dissolution corrosion at the exact locations of these steel inclusions. It is also quite reasonable to assume that elongated precipitates/inclusions, such as δ-ferrite and oxide stringers that form during the rolling of industrial-sized steel heats, could lead to dissolution 'pitting', as the interfaces of such inclusions with the steel matrix will allow the fast penetration of the HLM deep into the steel bulk. Even when the steel is completely covered by a protective oxide scale except from the locations of non-oxidising inclusions, the onset of dissolution corrosion at these sites is likely to lead to dissolution 'pitting' for reasons similar to those causing dissolution 'pitting' in the vicinity of local oxide scale defects (see Figs. 3.3 and 3.7).

3.3.7. The role of steel surface state and welding

Ilinčev et al. [223] reported significant discrepancies in the LMC behaviour of 304 and 316 AuSS with three different surface conditions, i.e., ground, passivated, and as-produced. These steels were exposed to slow-flowing ($v \approx 1$–2 cm/s) liquid LBE for 1000 h at 500 °C and in two distinct LBE oxygen concentrations (i.e., $C_O \approx 3$–4×10^{-6} wt% and $C_O \approx 2 \times 10^{-5}$ wt%). Under these exposure conditions, the ground steels corroded much faster than the passivated ones, and, for the ground 316L AuSS, the dissolution corrosion rate was 400–600 μm/year. It was emphasised by authors that the steel surface condition was important at the early stages of exposure, and passivation was an effective measure to improve the steel LMC resistance. Similar results regarding the influence of passivation were also reported by Doubková et al. [227]. Tsisar et al. [229] reported that 15-15Ti AuSS specimens with a polished surface were more sensitive to dissolution corrosion. However, contradictory results were reported by Martín-Muñoz et al. [209], who showed that 316L AuSS and T91 F/M steel specimens with different surface finishes (as-machined; ground; ground and polished; electropolished) exhibited comparable uniform dissolution corrosion damage, alongside a porous Ni/Cr-depleted oxide scale, when exposed to oxygen-containing ($C_O \approx 1.4 \times 10^{-7}$ wt%), static liquid LBE at 552 °C for 2000 h.

In general, welds were reported to exhibit similar liquid Pb/LBE LMC behaviours with the base metals, regardless of the used welding methods [209,259,260]. Kikuchi et al. [259] compared the LMC behaviours of parent and electron beam (EB) welds of F82H F/M steels and JPCA AuSS exposed to flowing ($v \approx 0.4$–0.6 m/s) liquid LBE with $C_O \approx 2$–4×10^{-5} wt% at 450 °C and 550 °C for 500–3000 h. It was found that the EB welds showed similar oxidation behaviours as the parent steels, i.e., the oxide scales on the F82H F/M steel and its welds consisted of an outer magnetite (Fe_3O_4) layer and an inner spinel ($FeCr_2O_4$) layer with an oxygen diffusion layer underneath, while the corrosion layers on the JPCA AuSS and its welds included a magnetite (Fe_3O_4) oxide scale and pitting. Martín-Muñoz et al. [209] studied the effects of tungsten inert gas (TIG) welds and surface finishing (as-received; ground; ground and polished; electropolished) on the LMC behaviour of 316L AuSS and T91 F/M steels exposed to static liquid LBE with two different oxygen concentrations ($C_O \approx 10^{-6}$ wt% and $C_O \approx 10^{-8}$ wt%) at 500 °C and 550 °C for 100–2000 h. They concluded that the surface finish had no pronounced effect on the LMC behaviours of these steels and their welds. The LMC properties of similar T91/T91 welds were the same as those of the parent F/M steels, while the dissimilar 316L/T91 welds showed dissolution corrosion damage in the seam area, which might be associated with a 309S alloy electrode that was used to weld the dissimilar metals. More recently, Heinzel et al. [260] studied the LMC behaviour of different F/M steel welds in contact with liquid Pb: T91 steel welds were obtained by friction stir welding and electromagnetic pulse welding, while 14Cr ODS steel welds were obtained by explosive welding. All welds were exposed to liquid Pb with $C_O \approx 10^{-6}$ wt% at 550 °C for 2131 h, and the obtained results showed no obvious differences in dissolution and oxidation behaviour for both welds and base metals. On the contrary, Mustari et al. [261,262] found that the fusion zone of welds prepared by TIG, yttrium–aluminium-garnet (YAG) or EB welding had much thicker oxide scales than the base metal (HCM12A F/M steel) exposed to liquid LBE with $C_O \approx 4.7 \times 10^{-6}$ wt% or $C_O \approx 7 \times 10^{-7}$ wt% at 600 °C and 650 °C for 500 h. This observation is in accordance with the results reported by Wang et al. [263]. Moreover, Chen et al. [264–266] reported that both the TIG weld and base metal of a China Low Activation Martensitic (CLAM) steel exposed to oxygen-saturated, static or flowing ($v \approx 1.7$–2.98 m/s) liquid LBE at 500 °C and 550 °C for 200–1500 h showed similar corrosion modes, but the weld was less resistant to erosion as compared to the base metal. Differences in the steel and weld oxidation behaviour may result from microstructural differences between welds and base metals, such as differences in grain size distribution and secondary precipitates. Therefore, it is important to use an appropriate post-weld heat treatment to homogenise the weld microstructure [267]. For instance, tempering the weld of the CLAM steel at 760 °C for 1 h was found to effectively reduce the oxidation kinetics in contact with liquid LBE [265].

Even though most of the studies showed that there were no large differences in the LMC corrosion behaviours of base steels and their welds, the susceptibility of welds to LME was reported to be significantly enhanced, a problem that will be extensively addressed in Chapter 4.

3.3.8. The role of irradiation

Liquid metal corrosion is not the only materials degradation effect of importance for Gen-IV LFRs, as nuclear grade steels will also be subjected during service to neutron irradiation, which is responsible for displacement damage, microstructural changes (e.g., radiation-induced segregation, RIS), and deterioration of mechanical properties (e.g., radiation embrittlement, radiation creep). Since radiation-induced microstructural and compositional modifications can have a non-negligible effect on the steel LMC behaviour, the interplay of LMC and neutron irradiation is an important challenge associated with the deployment of Gen-IV LFRs. Moreover, the effect of irradiation on the corrosiveness of each HLM coolant is largely unknown; however, recent studies on similar materials in molten salts have shown some unexpected and interesting results [268].

The neutron irradiation of T91 F/M steels, 316L and 15-15Ti AuSS, performed in the Russian BOR-60 reactor up to 9.1 dpa at 350 °C in contact with oxygen-saturated, static liquid LBE, did not produce severe LMC damage in the irradiated steels [18]. Similarly, the MEGAPIE samples of T91 F/M steels and 316L AuSS irradiated to 6–7 dpa at 300–340 °C for 4 months in liquid LBE did not result in significant LMC damage in the steels [18]. These results suggest that at the selected steel test conditions, the LMC effects were not aggravated by neutron irradiation, presumably due to the low exposure temperatures.

Ion irradiation has been tentatively used as a surrogate for neutron irradiation, since ion irradiation can induce irradiation damage in an accelerated manner, and under the right conditions, it can simulate neutron irradiation-induced defect microstructures, at least qualitatively [269]. In situ proton irradiation/corrosion tests (with 5.5 MeV protons, up to a damage dose of 22 dpa) performed by Frazer et al. [120] resulted in the enhanced oxidation of HT-9 F/M steel in contact with static liquid LBE ($C_O \approx 2 \times 10^{-6}$ wt%) at 420–450 °C for 80 h. They found that the HT-9 F/M steel was covered by duplex oxide scales, consisting of outer magnetite and inner FeCr-spinel layers, which were thicker in the areas that were both irradiated and exposed to liquid LBE than in the areas that were only exposed to liquid LBE. Similar results were also reported by Lillard et al. [270] and Yao et al. [271]. In addition to enhanced oxidation,

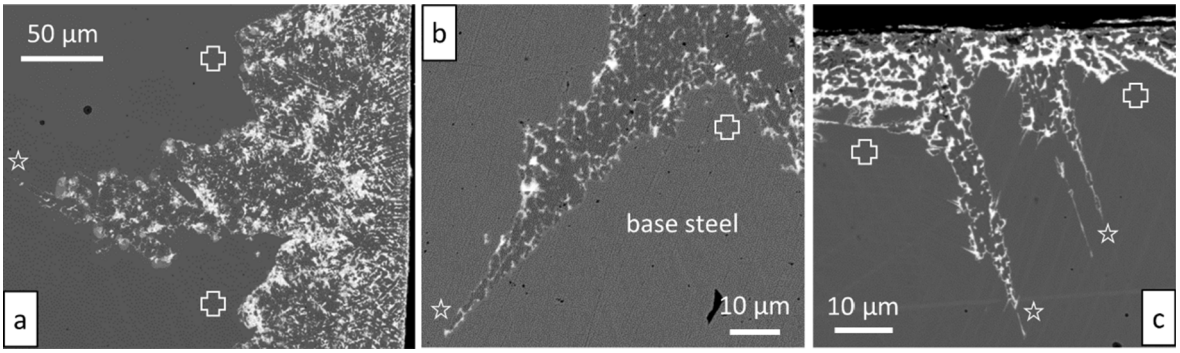

Fig. 3.50. SEM† images of sharp protrusions of the dissolution front in CW 316L AuSS exposed to oxygen-poor ($C_O < 10^{-8}$ wt%) static LBE at 500 °C for (a) 3282 h, (b) 2055 h, and (c) 501 h. Adapted from [40].

Li et al. [272] reported that 4H-SiC was subjected to enhanced dissolution corrosion in oxygen-saturated LBE at 550 °C for 167 h of exposure, after irradiation up to 1.6 dpa at RT with 880 keV Si^{5+} ions.

A new theory and supportive evidence of radiation-decelerated corrosion effects have recently emerged. Radiation is known to accelerate corrosion in LWR-relevant conditions [273], as confirmed by the use of both ions [274] and neutrons [275]. Also, corrosion effects in molten salts were accelerated under electron irradiation [276] and helium ion irradiation [277], even though the damage induced by such irradiations was quite different from damage induced by neutrons. On the other hand, the Molten Salt Reactor Experiment (MSRE) conducted in the 1960s by the Oak Ridge National Laboratory (ORNL), USA, showed surprisingly low corrosion rates for the exposed materials, such as Ni-based alloys [278]. The underlying irradiation/corrosion synergies were not fully explored, until the resurgence of molten salt reactor (MSR) R&D activities in the past ten years. A recent facility built by Zhou et al. [279] has shown that when selective leaching is the prevalent corrosion mechanism, proton irradiation (which is the best surrogate for neutron irradiation) decelerates molten salt corrosion of Ni-Cr binary alloys [268]. The proposed theory is that radiation-induced defects favour the outward diffusion of both Ni (noble in fluoride salts) and Cr (susceptible to dissolution), enriching the alloy surface in the more noble Ni and slowing down corrosion in this case. If this theory is indeed valid, a similar mechanism of radiation-decelerated corrosion may be active for steels in contact with liquid Pb/LBE/Bi at oxygen potentials that are too low to form passivating oxides. In other words, after the initial (selective) loss of the steel alloying elements that are highly soluble in the HLM, the increased subsurface concentration in less soluble steel alloying elements will eventually decelerate LMC under neutron irradiation. Confirming this hypothesis would be promising for Gen-IV LFRs, while the out-of-pile testing of steels in low-oxygen HLM conditions becomes the more conservative tests to determine LMC rates for such conditions. Of course, one should also establish whether the overall steel LMC rates under low-oxygen conditions are acceptable and whether the reactor operation in low-oxygen HLM conditions is safe considering other materials degradation effects (e.g., irradiation hardening, LME) and their synergies with LMC. For example, it is known that the dissolution front in AuSS is often characterised by the formation of sharp local protuberances as those shown in Fig. 3.50 for CW 316L AuSS exposed to oxygen-poor ($C_O < 10^{-8}$ wt%), static LBE at 500 °C for 501–3282 h [40]. The high stress intensity established in the immediate vicinity of such protuberances, due to the steel ferritisation and LBE penetration, might make them act as internal steel 'notches'. These 'notches' could cause crack nucleation in irradiated 316L AuSS that have become notch-sensitive due to irradiation embrittlement [97–100]. Once cracks nucleate in embrittled 316L AuSS, they are expected to propagate easily, leading to the premature failure of thin-walled components (e.g., fuel cladding tubes, heat exchanger tubes) [40].

3.4. Chapter summary

This chapter reviews the current understanding of the LMC mechanisms (i.e., oxidation, dissolution, erosion) that affect the performance of both AuSS and F/M steels in contact with liquid Pb/LBE. At a given temperature, steel oxidation is promoted when the oxygen concentration dissolved in HLM exceeds a certain (temperature- and HLM-specific) level, while dissolution corrosion occurs below that level of HLM oxygen concentration or at locations where the protective oxide scales covering the steel surface are defective and/or mechanically damaged. The overall LMC behaviour of a specific steel in contact with a specific HLM is also affected by the HLM flow velocity, as high flow velocities might result in severe material losses due to erosion and erosion/corrosion effects. LMC effects can either be uniform or localised; the latter can be caused by inhomogeneities in the steel microstructure and/or chemistry, as well as by a local disturbance in the exposure conditions (e.g., HLM oxygen concentration, HLM flow pattern). The most deleterious mode of LMC at reasonable HLM flow velocities (i.e., $v \approx 1$–2 m/s) is dissolution 'pitting' (i.e., locally enhanced dissolution corrosion), which might occur under a defective oxide scale even at high HLM oxygen potentials and in the presence of HLM flow. The difficulty in predicting the occurrence of dissolution 'pitting' might result in a compromise of the structural integrity of thin-walled components in rather short periods of time. The kinetics of dissolution 'pitting' has not yet been studied systematically, and since 'pitting' is a complex phenomenon affected by many factors (e.g., steel microstructure and chemistry, local failure of oxide scales, local HLM flow pattern), this is a topic for further in-depth investigation due to its practical importance.

The synergy between LMC and irradiation is a largely unexplored domain, which must be investigated and understood before the

confident deployment of Gen-IV LFRs. If the irradiation-decelerated corrosion of steels and Ni-based alloys observed in molten salts occurs also in HLMs (still to be demonstrated by dedicated experiments), this might enable the safe operation of Gen-IV LFRs in lower HLM oxygen concentrations than those currently foreseen based on experimental data collected from non-irradiated steels. If irradiation improves the resistance of steels to dissolution corrosion, this will also limit crevice corrosion and/or dissolution 'pitting' effects in Gen-IV LFRs. Last, but not least, one should not disregard the potential synergy between dissolution corrosion (esp., the dissolution corrosion-induced ferritisation of AuSS), liquid metal embrittlement (LME), and irradiation hardening of AuSS (see also Section 4).

4. Liquid metal embrittlement (LME)

The first discovery of LME can probably be traced back to 1914, when Huntington reported the first LME case, in which intergranular cracking was observed when β-brass with 2 %Al was exposed to mercury (Hg) [280]. Since then, extensive investigations have been performed to reveal the mechanisms of this important materials degradation phenomenon [281–283]. It has been found that a wide range of solid metal/liquid metal couples can suffer from LME [284], leading to reductions in ductility (ability to deform plastically without fracturing) and toughness (ability to resist fracture) of solid metals when brought in contact with certain liquid metals. LME, which occurs at the atomic scale, can be influenced by several mesoscale effects, such as corrosion by the liquid metal or the thermodynamic evolution of the system in the case of miscibility between the solid and liquid metals. At the same time, it can proceed via competing processes, such as the plastic deformation of the solid metal. Thus, it is difficult in macroscopic experiments to connect directly with the underlying mechanism at the crack tip, where LME occurs. Particularly, the LME features characterising one solid metal/liquid metal couple cannot be fully generalised to describe other couples. Therefore, even though a large number of important results had been collected from many other solid metal/liquid metal couples, the couples of T91 F/M steels, 316L & 15-15Ti AuSS, and similar steels with liquid LBE and/or Pb have received great attention in the past two decades in order to investigate their LME susceptibility and characteristics. The in-depth investigation of this effect has been driven by the need for materials qualification and nuclear safety evaluation of advanced Gen-IV LFRs, including ADS.

In this chapter, a comprehensive review of LME in these technologically important solid metal/liquid metal couples will be presented, updating the previous review by Kamdar [282] with the current state-of-the-art. Special attention will be given to the parametric effects and mechanistic understanding of crack initiation and propagation in T91/HLM couples, considering that these exhibit severe LME and are good systems to discuss the LME mechanism. Prior to reviewing LME in steel/HLM couples, it is necessary to first give a general phenomenological description of LME based on past experimental studies of various liquid metal/solid metal couples, including typical materials degradation features, prerequisites/criteria for LME occurrence, and major affecting parameters. Following this part, a summary of the phenomenology of LME in steels is given from an historical perspective. Then, several promising LME mechanisms and models that have been widely used to analyse the LME features of the steels/HLM couples are also described. Moreover, new developments in atomic-scale understanding of the LME mechanisms of the Al/liquid Ga and other interesting couples studied in the past ten to twenty years are also briefly summarised. All this information is an important reference for understanding the LME mechanisms of steel/HLM couples that are relevant to nuclear safety. Lastly, some remaining issues are discussed at the end of this chapter.

4.1. General phenomenological description of LME

LME refers to the transition from a normally ductile fracture of metallic materials via void nucleation, growth and coalescence to a brittle fracture induced by straining the solid in contact with a liquid metal. The brittle nature of fracture is to be understood as a cleavage, or an interfacial fracture mode (e.g., along GBs, interphase boundaries, precipitates/steel matrix interfaces, or in weakened crystal directions), or at least a premature fracture instead of the expected ductile fracture. The effects of LME on the mechanical properties of the affected metallic material include loss of ductility and/or loss of ultimate tensile strength (but not yield strength), loss of fatigue resistance, as well as loss of toughness upon testing in a liquid metal environment. LME is considered to be a special subset of environmentally-assisted cracking (EAC), which is initiated at the solid/liquid interface with crack nucleation on the surface of the solid metal, followed by crack propagation into the solid metal bulk, with the liquid constantly supplied at the crack tip via capillarity. In a general case, the LME fracture process occurs within such a time scale that it does not obviously modify the chemical or structural properties of the bulk of the solid metal. LME is thus considered to be a surface phenomenon [285]. LME-induced cracks can propagate critically or sub-critically so that, in the latter case, they compete with other processes that can occur in the material in the course of straining (e.g., ductile fracture, diffusion, corrosion by liquid metal impurities, etc.). The LME phenomenon has some typical characteristics that distinguish it from stress corrosion cracking or hydrogen embrittlement. Most of the LME cases as a result of tensile loading report that when LME occurs, the tensile behaviour of the solid metal is changed, as manifested by a reduction in total elongation, but its yield strength is not [286]. There is a threshold stress or a threshold strain prior to the onset of cracking.

Not all solid/liquid couples are subjected to LME; this materials degradation effect concerns mostly low melting point liquid metals (i.e., Hg, Ga and its alloys, Bi, Pb and its alloys, Na and its alloys, Li and its alloys, Sn, Zn, In, Tl, Cd, Te, Sb, and Cs). Nevertheless, some high-temperature embrittlement cases are also known with liquid zinc (Zn) in contact with Fe-based materials, as reported in [287–289]. Some systems are also immune to LME. For instance, pure Ni can be severely embrittled by liquid lithium (Li), but is not susceptible to embrittlement induced by other liquid alkali metals [285,290]. T91 F/M steels have a similar LME selectivity. It is found that crack initiation in these steels depends upon the liquid metal types (LME sensitivity: LBE > Bi > Pb) [291]. Because of this apparent selectivity of sensitive couples (also called "LME specificity") and given its potential for unpredictable and catastrophic

component failure, an LME sensitivity assessment is crucial for every new couple.

Many factors can affect the severity of LME for a given solid metal. It is useful to separate the effects of liquid metal adsorption on the mechanical properties of a solid metal into three main groups: (I) factors related to the atomic interactions driving the intrinsic sensitivity to LME (i.e., crystallographic structure or chemical composition of both the solid and liquid metals); (II) factors related to the microstructure and metallurgy of the solid metal (i.e., presence and type of GBs, phase distribution in the solid, wettability and its dependence on superficial oxide scales); (III) "kinetic" factors related to the conditions of plastic deformation, fracture, and interactions with corrosion (i.e., temperature, strain rate $\dot{\varepsilon}$, pre-exposure). Specific expressions of these factors include: chemical alloying of both metals, grain size of the solid metal, stress level and pre-exposure (factor types I & II), temperature and strain rate (factor type III). The reactivity at the interfaces between a liquid metal and a solid metal could be modified by adding some soluble elements into the liquid, which results in either a decrease or an increase of the LME susceptibility [283]. Particularly, limited mutual solubility at the solid metal/liquid metal interface facilitates LME, while it is restricted when interfacial intermetallics form (a process that competes with LME and can be seen as a shield against it) [292,293]. Changes of the solid metal chemical composition can also influence its embrittlement tendency, for example, when a solid metal is strengthened by certain alloying elements, its LME susceptibility typically increases. An enhanced LME by solid solution strengthening appears to be closely associated with a reduced number of slip systems or restricted dislocation cross-slip [294,295].

Type I factors describe the intrinsic sensitivity to LME, for which a thorough theory is still lacking, while type II and III factors encompass all the variability in the LME phenomenology relating to materials and testing conditions. One key step is to establish the LME case as an intrinsic possibility (i.e., a type I factor), then understanding its variability by determining the boundaries for LME occurrence from type II and type III factors.

Some basic physicochemical and mechanical prerequisites must be satisfied for LME to occur [36,282,283,286,296–302]. For instance, the surface must be oxide-free or oxides must be damaged to enable intimate contact (i.e., wetting) between liquid metal and solid metal. In the case of a crack initiation-controlled process, the surface condition is crucial to determine LME susceptibility, considering that the surface can be corroded to form 'pits' serving as stress concentrators, and surface oxides can also be damaged or eliminated to improve wettability. Therefore, pre-exposure (esp. to a liquid metal with low oxygen concentration) for some time prior to loading facilitates the occurrence of LME [303]. Reaching a threshold stress or critical stress intensity factor at the crack tip is another important prerequisite for the occurrence of LME [282]. Residual stresses, dislocation obstacles, and stress concentrators favour the fulfilment of this criterion, thereby enhancing LME susceptibility. A certain amount of plastic deformation of the solid metal is also generally required for LME.

One of the requirements often quoted for LME is the absence of intermetallic compounds in the phase diagram, which is associated with a low solubility of the liquid chemical species in the solid metal [282]. This rule, however, should be taken with a grain of salt, as counterexamples abound. One example is the sizeable solubility of gallium (Ga) in solid Al (reaching 8 at.% at RT[†]), which represents the canonical LME system. Another example is the iron/tin (Fe/Sn) system, which has several intermetallic phases (FeSn, $FeSn_2$) at intermediate temperatures, while being one of the first known LME couples [304]. Such rules should only serve as a guideline, indicating that LME must be considered as a possibility for a given couple. Their non-observance does not exclude the possibility of LME in other test conditions.

LME susceptibility is also temperature-dependent. The influence of temperature is generally assessed based on tensile elongation data, and is typically characterised by a phenomenon called the "ductility trough". This means that the tensile elongation of a solid metal first decreases with increasing temperature, then reaches a plateau where elongation is temperature-independent, followed by an increase in elongation with a further increase in temperature. In other words, LME occurs only within a certain temperature range, i.e., in the plateau region [286]. This interesting phenomenon was tentatively attributed to a restricted supply rate of liquid metal to the crack tip at low temperatures [305] and crack tip blunting induced by ductility recovery at high temperatures [282]. In addition, the reduced LME effect at high temperatures may also be linked to the desorption of liquid metal atoms [306]. It should be noted that LME occurring just above the melting point of the liquid metal was also observed [306]. The effect of applied strain rate was linked to the transport of the embrittling liquid metal to the crack tip, which is a rate-controlling process [307]. At lower strain rates, stress relaxation at the crack tip favours the reduction of stress intensity. Higher strain rates or loading speeds do not facilitate the occurrence of LME, as an intimate contact of liquid and solid metal must be maintained at the crack tip, and this is more difficult at higher strain rates due to the finite speed of liquid metal transport to the crack tip. In addition, the shape of the "ductility trough" can be affected by the strain rate. For the Zn/liquid indium (In) couple [307], decreasing the applied strain rate shifted the upper boundary of the "ductility trough" towards the low temperature domain, and the plateau region of strongest LME became narrow and even disappeared.

LME-induced fracture is usually intergranular for polycrystals [308]. In this case, the chemical properties of GBs (e.g., elemental segregation [309–313]) are important to determine LME severity. Transgranular cleavage fracture has also been observed in some cases [308,314]. Even single crystals can suffer from transgranular LME along certain crystal directions [308]. Given the major role of intergranular cracking in LME, it is important to subdivide the LME cases into the following two categories: (a) the category of GB wetting (GBW), where LME does not require an externally applied stress, and (b) the standard LME phenomenon, where spontaneous GBW does not occur and brittle cracking occurs upon mechanical loading. GBW prototypal cases, such as Al/Ga or copper/bismuth (Cu/Bi), can be described as the result of a low solid/liquid surface energy (γ_{SL}) relative to the GB interface energy (γ_{GB}). In the case where $2\gamma_{SL} > \gamma_{GB}$, the replacement of a GB by a liquid film is not energetically favourable, therefore, an energy barrier for cracking exists (Fig. 4.1). It is then the role of strain (elastic or plastic) to overcome that energy barrier. The LME of steels in contact with most liquid metals, including lead (Pb) or lead alloys, falls into the second subcategory, because no spontaneous GBW is observed. If $2\gamma_{SL} < \gamma_{GB}$, then spontaneous GB penetration is energetically favourable, leading to the replacement of the GB by a liquid film (also

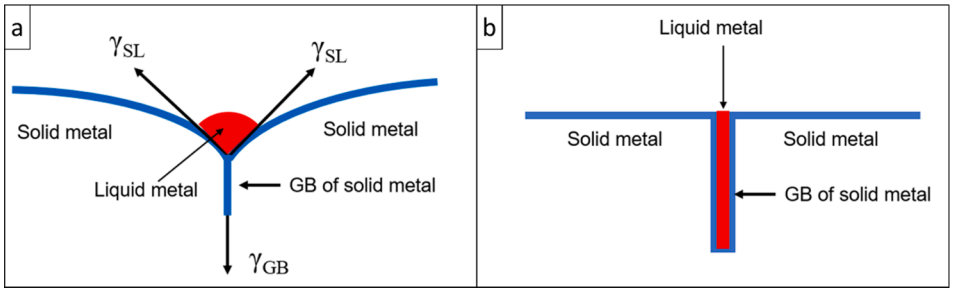

Fig. 4.1. GBW[†] at the interface between a liquid metal and a solid metal: (a) $2\gamma_{SL} > \gamma_{GB}$; (b) $2\gamma_{SL} < \gamma_{GB}$.

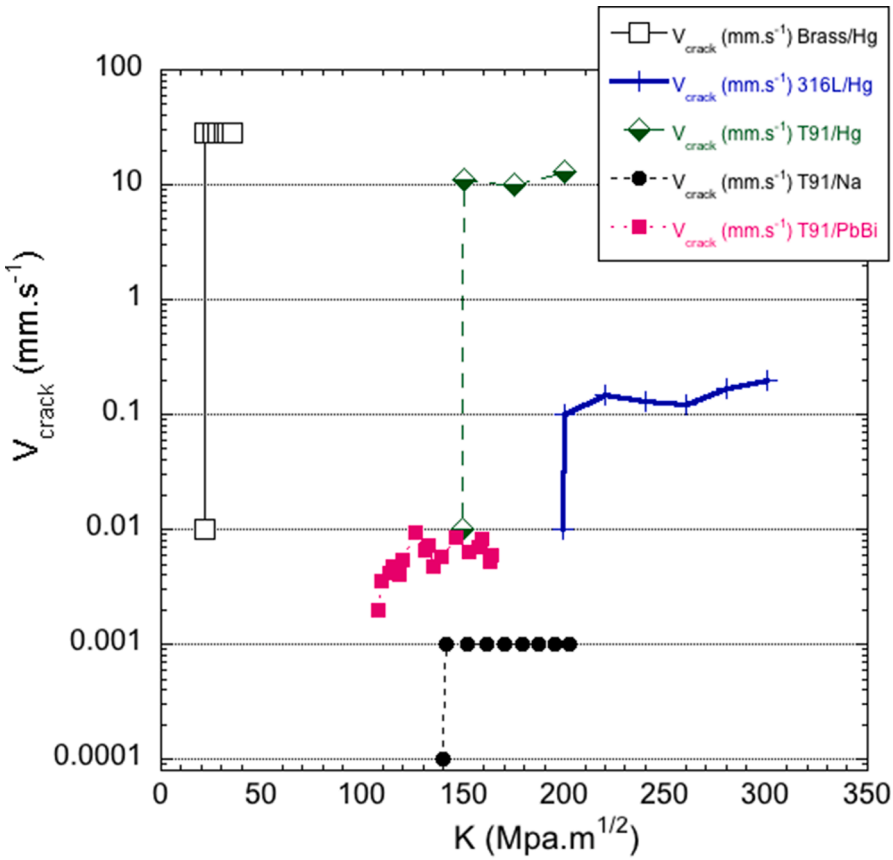

Fig. 4.2. Crack growth rate *vs.* stress intensity factor in various solid/liquid metal couples.

called 'GB complexions').

LME occurs in a temperature domain ranging from the melting point of the liquid metal (or liquid alloy) to a certain recovery temperature. It is also possible to observe embrittlement at temperatures below the melting point. This phenomenon is referred to as solid metal-induced embrittlement (SMIE), but it will not be covered in this review, as it is inapplicable to Pb/LBE/Bi couples in actual Gen-IV LFRs. Still, it is worthwhile mentioning that there is evidence of the involvement of surface diffusion in the SMIE transport mechanism [315].

The engineering task of giving an estimate of the safety margins relative to LME (maximum load and maximum admissible deformation) before using any structural material in contact with a liquid metal is of the utmost importance and can be carried out by tensile and fatigue testing, and fracture mechanics experiments. LME crack propagation rates can span over many orders of magnitude, depending on the system and the loading parameters. Fig. 4.2 shows accumulated crack propagation rate data as a function of the stress intensity factor in various systems, showing the wide span of possible crack growth rates. Brass tested at RT in contact with Hg in a Centre-Cracked in Tension (CCT) specimen geometry can reach over 10 mm·s^{-1}, while the crack rate for T91 F/M steels in contact with liquid sodium (Na) saturates at just 1 μm·s^{-1}.

With respect to other examples, the crack growth rate reached up to ten millimetres per second for the Al alloy 7075-T651, several

tens of millimetre per second for a Ti alloy (Ti-8Al-1Mo-1 V), but was much lower for a high-strength steel (D6aC) tested in liquid Hg [316]. Moreover, a crack propagation rate faster than 1 mm/s in the Al/Ga couple was observed by Kolman [317]. However, there is an upper limit to the crack propagation rate, and after a certain stress intensity factor is reached, the crack growth rate is found to be independent of the stress intensity factor [292,316]. In some cases, prior to fast crack propagation, a long incubation time was required, which might be related to the failure of oxide scales by localised deformation [316,318] or liquid metal diffusion along GBs [298,318].

The challenge in predicting LME for a given solid metal/liquid metal couple (factor type I), explaining its variability relative to the material's properties (factors II) and their kinetics (factor III) remains a formidable one.

4.2. Steel LME phenomenology with liquid Pb and Bi

Considering the lack of intermetallic phases in the Fe/Pb, Fe/Bi, Cr/Pb, and Cr/Bi systems, pure iron (Fe) and steels at least satisfy one of the criteria indicating potential susceptibility to LME. However, establishing the intrinsic susceptibility to LME for these systems was slow to uncover. The awareness of the potential effect of these two liquid metals on the steel mechanical properties arose when a small addition of Pb was found to have a significant impact on the steel's machinability. A significant reduction in energy consumption for machining can be obtained with the addition of traces of this element, while retaining similar RT† mechanical properties [319]. The benefit with respect to machining, however, came with a major drawback, when using the material at temperatures above 300 °C. Swinden reported in 1943, in a comprehensive study that leaded Mn-Mo steels that were heat treated to reach an ultimate tensile strength (UTS) between 760 and 900 MPa (En 16 type steels: 0.36C-1.43Mn-0.43Mo-0.19Pb) showed less ductility and a pronounced drop in reduction of fracture area after tensile testing than non-leaded steels (Fig. 4.3) within the 300–550 °C range [320]. It was also reported in the discussion of this study by Wragge that similar findings characterised the performance of a leaded carbon steel (S.A.E. 1020 steel) and a leaded manganese steel (S.A.E. × 1314 steel) with a much lower UTS† (413 MPa).

The role of LME in this process is to reduce the energy consumption during steel machining, achieved by local adiabatic heating that is produced by high-speed machining and can melt Pb inclusions [321]. This effect of steel embrittlement by Pb addition on steels became widely acknowledged also in the former Soviet Union after the work of Potak and Shcheglakov [322], who investigated the free machining of low-alloy steels.

Being able to draw a parallel between internally induced embrittlement and LME requires one to show that embrittlement can also be triggered by an external source of liquid metal, yielding essentially the same results in terms of sensitivity and dependence on kinetic factors. The first LME results on steels in contact with liquid Bi and liquid LBE were obtained on a heat-resistant alloy (30KhGSA steel) tested at 500 °C by Kishkin and Nikolenko in 1956 in the former Soviet Union [323]. The embrittlement effect of liquid Bi/LBE was clearly seen during tensile testing of smooth 30KhGSA steel specimens exposed to these two HLMs (Fig. 4.4).

Despite of these preliminary results, the concern that LME may occur in liquid Pb, Bi, and LBE was not clearly recognised for some time. Rostoker was still reporting in his review published in 1960 that the steel/Pb and steel/Bi couples were non-embrittling systems, based on data collected by means of bending tests used for screening material mechanical properties [296]. Similar negative results by tensile testing at 300 °C were obtained more than ten years later by Radeker who carried out the tests in liquid Bi at 300 °C and in liquid Pb-20Bi alloy at 300 °C and 400 °C on several low-alloy and heat-resistant steels (Armco iron, St.35, 15Mo3, 17CuNiMo4) [324]. This illustrates the somewhat difficult conditions to obtain reliable estimates of the LME sensitivity in uncontrolled experimental conditions. LME of steels in HLMs was finally shown in 1964 by Andreev on a quenched and tempered 40KhNMA steel tested with a Pb coating (deposited as molten metal) [325]. LME was observed during tensile testing between the melting point of Pb and 450 °C (depending on the strain rate). The first observation of mechanical degradation during fatigue testing of a steel (40Kh steel) in liquid LBE at 500 °C was found in the work of Chaevskii et al. [326]. Similar results were also quickly demonstrated for this steel in pure

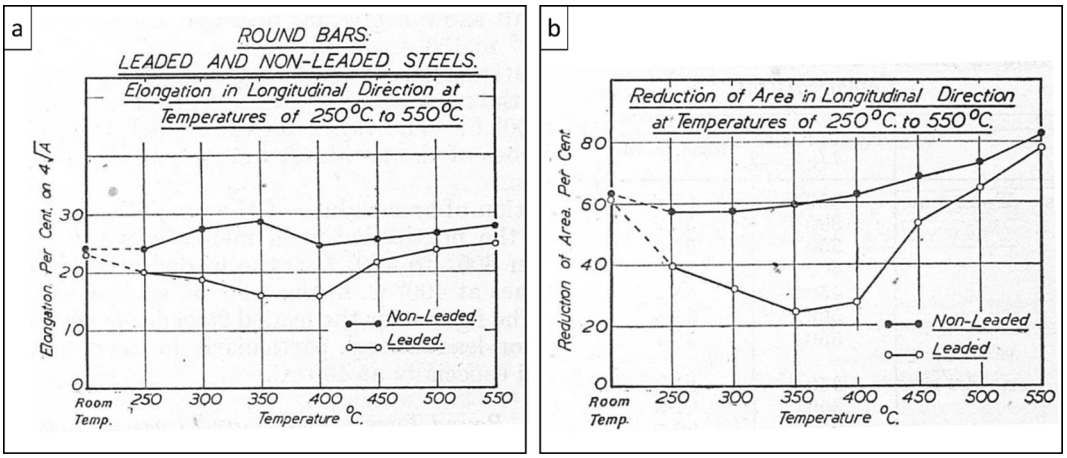

Fig. 4.3. Elongation and reduction of area of leaded and non-leaded Mn-Mo steels at different test temperatures. Adapted from [320].

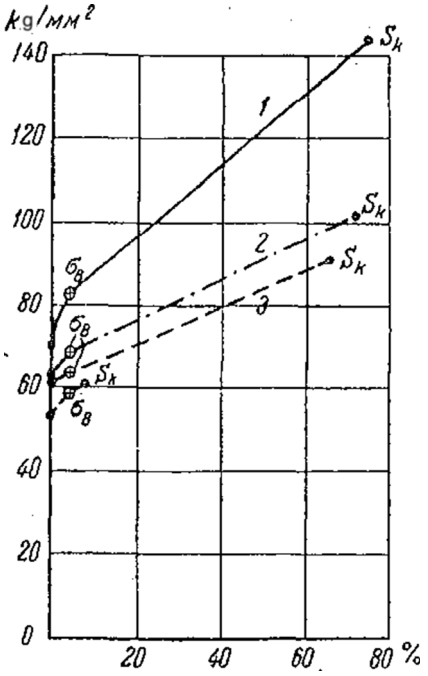

Fig. 4.4. Stress–strain curves for a 30KhGSA steel after tempering in air (1), liquid Bi (2), liquid LBE, (3) and liquid Pb-Sn alloy (4) at 500 °C [323].

liquid Pb and pure liquid Bi [327]. The case of intrinsic LME susceptibility for both Fe/Pb and Fe/Bi couples (factor type I) was, however, still not fully recognised, even in the Soviet Union, as may be seen in the review published in 1966 by Shchukin and Yushchenko [328], while the LME of low-alloy steels was acknowledged. In this respect, the LME sensitivity of steels was still considered a special case, because of the variability in the material's mechanical and metallurgical states (factor type II).

A major shift in the perception of the problem arose starting from the mid-sixties with several works in Japan and in the US, but particularly in the former Soviet Union. The potential issue of LME of steels became widely acknowledged and it became the subject of dedicated studies. The research efforts at that time were mostly divided between a Soviet school (disciples of the academician Rebinder) and studies in the USA, mostly under the direction of Prof. Breyer at Illinois Institute of Technology.

In the former Soviet Union, the subject of embrittlement of steels by soldered LBE was investigated further probably in the context of developing LBE-cooled nuclear submarines. The fatigue resistance of several carbon steels (St35, St45, & St50) was reported to be strongly reduced in rotating bending and torsion between 200 °C and 500 °C [329]. Chaevskii and Bichuya subsequently studied the effects of applied strain rate and LBE oxygen concentration on the LME of St50 steels at 400 °C [330,331]. The protective role of oxygen against the steel mechanical degradation due to the action of the HLM was evidenced. The notion that re-oxidation of the steel can happen at low strain rates (the occurrence of which would protect the steel from LME) was put forth.

The behaviour of several low-alloy steels was then studied by the different groups looking at this problem in the Soviet Union. Notably, the behaviour of the 12KhM pearlitic steel (0.16C-1Cr-0.5Mo-0.5Mn-0.24Si) in liquid LBE was evaluated by tensile testing and shown to be sensitive to LME between 200 °C and 500 °C [332]. The importance of the steel surface state (rough, mirror polished, or pre-tinned) was then noted, and the process of pre-tinning was found to impart maximum sensitivity to LME. At about the same time, a significant decrease in fatigue strength at 470 °C and 550 °C was also reported for LBE pre-tinned 15KhS1MFB steel [333]. These papers were very influential for the LME of T91 F/M steels, since they gave hints about the strong influence of surface preparation on crack initiation or, in other words, on the importance of LBE wetting.

In Japan, Tanaka and Furukawa studied a mild/low-carbon steel (SS41-0.2C-0.49Mn-0.24Si) and reported an LME effect in liquid Pb, during tensile testing of notched specimens at 350 °C and 460 °C with a ductile recovery at 550 °C [334]. Testing smooth specimens in liquid Bi showed that this environment induced LME at 350 °C and 460 °C, while the test results in liquid Pb showed no LME [334,335]. In rotating bending fatigue tests, an extensive study on both notched and un-notched specimens showed a significant reduction in lifetime in contact with liquid Pb (quantified as an environmental factor of the order of 0.6) at all tested temperatures (350, 460, and 550 °C), but only for notched specimens [335–337]. The effect was not sensitive to the holding time before testing [337], and the fracture mode was mainly intergranular [335]. The study was extended to a ferritic steel (SUH2-0.38C, 13.3Cr, 2.22Si, 0.44Mn) and a 18–8 (grade 304) AuSS in liquid Pb. It was found that this liquid metal at 460 °C and 550 °C induced a reduction in the fatigue lifetime of smooth SUH2 steel specimens, while it increased the lifetime of the 304 AuSS [337].

In the USA, Mostovoy and Breyer showed that leaded 4145 high-strength steels (0.46C-0.87Mn-0.98Cr-0.15Ni-0.15Mo-0.3Pb) were susceptible to internal Pb-induced embrittlement at 200–450 °C [338]. The degree of embrittlement was correlated with the hardening achieved by heat treatment, whereupon the highest strength steels had no remaining ductility. The fracture mode was characterised as being intergranular and associated with MnS inclusions surrounded by an envelope of liquid Pb [339]. They reached the conclusion

that the steel composition was not of major importance [340], nor was the internal Pb content [341].

The results of an investigation of solid metal-induced embrittlement by soldered Bi at 20–271 °C on 4140 low-alloy steels revealed no effect due to the exfoliation of the solid deposit. On the other hand, soldered Pb embrittled the steel above 200 °C [342]. Therefore, the temperature range for embrittlement is similar for both internal (i.e., for a leaded steel, as described earlier) and external (i.e., pre-tinning the steel surface with Pb) Pb wetting. Another type of steel (AISI 3340) was soon found to be susceptible to LME by Pb soldering [343].

The next important piece of work was a detailed study of the temperature and strain rate dependence of the LME recovery temperature of leaded 4145 steels [344]. It was shown that the recovery temperature (T_r) *vs.* strain rate ($\dot{\varepsilon}$) curve obeys a thermally activated correlation, which was rationalised by the requirement at recovery to reach a critical mobile dislocation density:

$$\frac{1}{T_r} = A - B\log\dot{\varepsilon} \quad \text{with A and B constants} \tag{4-1}$$

This could indicate that in many systems, including steels, LME competes with plasticity and ductile fracture. The temperature dependence of the recovery temperature was also found to follow a similar correlation with St.3sp steels in liquid metals [345]. On the other hand, a study of the effect of Pb alloying in 4140 steels showed that this recovery temperature could be raised significantly in tests with soldered Pb alloys (up to 150 °C with a Pb-25Bi alloy as compared to pure Pb) [346]. Similar results were already known for 414X type steels with antimony (Sb) impurities [341,347] and for AISI 4340 steels embrittled by a Pb alloy [348]. It is, therefore, difficult to draw a definite relationship between kinetic factors in the recovery domain, if some impurities can have such a large effect. A compilation of these data from Refs. [325,344,345] is shown in Fig. 4.5. While the thermal activation correlation is clearly seen across several systems, as evidenced by the linear slope of the $1/T - \log\dot{\varepsilon}$ graph, it is impossible to unambiguously link the activation energy with a specific process. Several processes could be active (e.g., corrosion by impurities, diffusion processes taking place simultaneously, etc.). The steel grain size was also a factor affecting the recovery temperature, making it difficult to give a generic mechanistic explanation.

The LME occurrences reviewed so far have been found in systems involving carbon and low-alloy, high-strength steels. The question of addressing the type I factor (LME selectivity) remained largely unanswered until the work of Popovich and Dmukhovskaya [349]. They tried to address the Fe system using Armco iron (0.037C) in contact with various liquid metals, and found that liquid Bi (Fig. 4.6) [349], liquid LBE, and liquid Pb [350] would induce LME in Armco iron. The question addressed in that work was whether

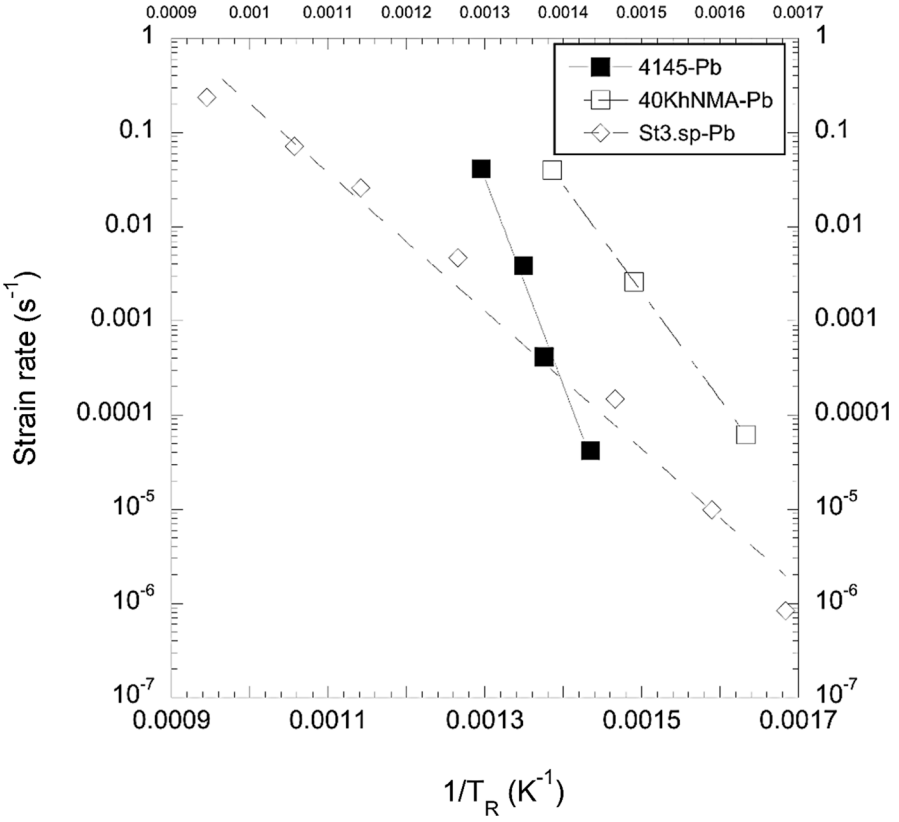

Fig. 4.5. Strain rate *vs.* critical recovery temperature correlation plot. Data compiled from Refs. [325,344,345].

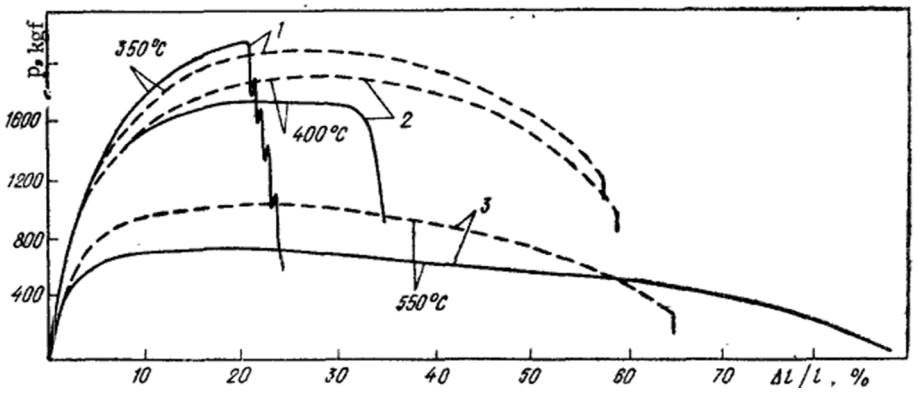

Fig. 4.6. Tensile load–strain diagrams of Armco iron specimens tested in liquid Bi (continuous lines) and vacuum (dashed lines) at 350 °C (1), 400 °C (2), and 550 °C (3) [349].

the Fe/Pb and Fe/Bi systems are intrinsically susceptible to LME during tensile testing.

It was first demonstrated that in the 300–400 °C range, Armco iron in contact with liquid Bi failed mainly in a brittle, and intergranular manner [351]. Liquid Pb was revealed to be a more difficult medium to wet the surface of Fe during testing than liquid Bi or liquid LBE (NB: these tests were initially carried out in air, so that the liquid metal/solid metal interface was susceptible to re-oxidation). Finer-grained materials were observed to be less susceptible to LME than coarse-grained materials [352]. The recovery temperature was shown to depend not only on the applied strain rate, as it did in carbon steels [353], but also on the formation of new phases at the liquid metal/solid metal interfaces, such as $PbFe_3O_4$ in liquid Pb or $BiFeO_4$ in liquid Bi [354]. An iron nitride was also thought to have formed, based on XRD† analysis [354]. The variation of the recovery temperature was then attributed to the different interfaces formed *in situ* during the exposure of iron to the liquid metal. The essential role of stress concentration (for example, via a notch) was uncovered with Armco iron in contact with liquid LBE, as this enabled the clear elucidation of LME over a broad temperature range (200–500 °C) for notched cylindrical specimens [355]. Preliminary analyses of a few failed samples of Chromesco 3 (a 2.25Cr steel) in liquid Pb at 325 °C and 335 °C were published by Broc et al. [356]. While interesting, because the material was clearly intended for nuclear applications, this work was not continued.

As shown by this survey, the main body of the preliminary work on LME dealt with high-strength carbon steels and low-alloy steels, while only a few studies were dedicated to other classes of steels, such as AuSS or ferritic steels. The main ones were carried out at rather high temperatures (500 °C or 600 °C) on the corrosion-fatigue interaction in 4Kh13 or 1Kh19N9T steels (the latter is essentially 304 AuSS) exposed to liquid LBE [329,357–359]. Corrosion affected the fatigue properties of pre-tinned steel samples at these high temperatures by significantly reducing the steel lifetime under rotating bending or cyclic loading. This behaviour does not strictly meet the criteria of an LME behaviour, but it represents a coupling between creep and corrosion.

The LME case of high-alloy steels (F/M type) was first investigated by Abramov et al. in 1992, under torsion testing of ferritic Fe-12Cr-Mo steels in liquid Pb [360]. A limited degradation of mechanical properties was observed on tempered steels in the 400–500 °C range. On the other hand, a strong property degradation was observed on hardened steels (no tempering heat treatment) in the 300–600 °C range, with a cleavage-like fracture surface. Pre-tinning of the samples with liquid Pb was employed in this study to ensure that Pb was wetting the sample surfaces. This work aimed at studying the LME susceptibility of simulated welded materials, indicating that LME is more pronounced in such microstructures (type II factor).

In summary, at the outset of this review, after several decades of work in many laboratories, the occurrence of LME in several carbon steels, low-alloy steels, and pure Fe has been experimentally confirmed. The behaviour of a ferritic steel (Fe12Cr) had also been investigated in liquid LBE in a single study to date, with limited effects except in the case of a hardening tempering heat treatment. There were, therefore, no publicly available data on 9Cr martensitic steels. The case of AuSS (of the 304 type) had been investigated mainly in liquid LBE at relatively high temperatures in the context of corrosion-induced material degradation.

4.3. Mechanisms and models for LME

LME is a complex phenomenon, a unified explanation of which is still missing, especially on the atomic scale. In spite of this fact, several promising mechanisms or models have been proposed in the period between the 1960s and the 1980s that can complementarily cover most of the LME cases. These mechanisms and models have been extensively discussed in the LME studies of steel/HLM couples, and they include reduction in surface energy [296], adsorption-induced reduction in cohesion [361,362], adsorption-enhanced dislocation emission [285,363–365], localised plasticity and GB penetration [366], stress-assisted dissolution [367,368], GB penetration via atomic diffusion [298], and enhanced work hardening [369]. Recent advances in understanding the LME effect are mainly concentrated on GB embrittlement caused by liquid metals, which is an important reference to facilitate the understanding of the LME effect in the steel/liquid Pb and steel/LBE couples, and thus it will be summarised in a later section.

In the following subsections, the main ideas, strong points and weaknesses of the mechanisms attempting to explain LME will be briefly described and compared. The latest developments in exploring LME are also presented.

4.3.1. Reduction in surface energy

The mechanism that refers to the reduction in surface energy is based on the combination of the Rebinder effect [370] and Griffith fracture theory. The Rebinder effect states that the surface free energy of a solid metal decreases due to the adsorption of liquid metal atoms. The Griffith theory considers an energy balance in a purely elastic solid, i.e., the stored elastic strain energy during fracture is completely transferred to surface energy due to newly formed fresh surfaces by cleavage, as shown below:

$$\sigma_a = \sqrt{\frac{2E\gamma_{sl}}{\pi a}} \tag{4-2}$$

where σ_a is the applied stress, E is the Young's modulus of the solid, γ_{sl} is the specific surface energy at the liquid/solid metal interface, and a is the half-length of an internal, pre-existing crack (Fig. 4.7). It can be inferred from Eq. (4-2) that the stress required for fracture is lowered by the reduced γ_{sl} resulting from the adsorption of a foreign liquid metal species. This represents a necessary condition for brittle fracture.

In a real situation, crack propagation accompanies plastic deformation, thus one part of the elastic strain energy is stored in the plastic zone in the vicinity of the crack tip. This requires rewriting Eq. (4-2) by adding a plastic strain energy term, γ_p, as follows:

$$\sigma_a = \sqrt{\frac{2E(\gamma_e + \gamma_p)}{\pi a}} \tag{4-3}$$

This mechanism has been widely accepted, as it can qualitatively explain the LME phenomenon very well. But it is limited to a thermodynamic approach and is difficult to use for a quantitative assessment of the effects of various material parameters on the surface energy. Nevertheless, an estimate of surface energy reduction can be given in the case of the Fe/Pb couple. Measuring the surface energy of a heterogeneous solid/liquid interface can be conventionally carried out by two approaches.

The first uses the wettability of a surface by the liquid metal. The energetics of the wettability of a surface is a balance equation between γ_{sl} – the solid/liquid interface energy, γ_{lv} – the liquid/vapour interface energy, and γ_{sv} – the solid/vapour interface energy. The liquid/vapour interface energy, γ_{lv}, is well known experimentally and is measured, for example, by the sessile drop technique. The solid/vapour interface energy, γ_{sv}, depends on the adsorption energy and the coverage rate Θ ($\Theta = \frac{\Gamma}{\Gamma_t}$ is the ratio of the number of occupied sites to the number of available sites) and it is described by the expression: $\gamma_{SV}(\Theta) = \gamma_0 - \frac{\Theta \cdot |E_{ads}|}{a^2}$ (in J/m^2), where a^2 is the unit adsorption surface correlated with Θ. At the thermodynamic equilibrium, the sign of the following balance equation gives the wettability trend (i.e., the total wetting *vs.* the partial wetting):

$$S = \gamma_{sl} + \gamma_{lv} - \gamma_{sv} \tag{4-4}$$

For the total wetting case ($S < 0$), one can only deduce an upper bound for the solid/liquid surface energy, γ_{sl}. For the partial wetting case ($S > 0$), the Young's equilibrium equation applies at the triple line and, in principle, a measurement of the wetting angle, θ, imposes an additional constraint on all terms:

$$\gamma_{sl} = \gamma_{sv} - \gamma_{lv} cos\theta \tag{4-5}$$

While the wetting angle can be fairly well measured ($\theta = 50^{\circ}$, for the Fe/Pb couple [371,372]), the adsorption energies and the coverage Θ are not known *a priori* and can vary depending on the thermodynamic conditions, making a direct measurement of the solid/liquid interface energy, γ_{sl}, problematic in many cases.

The second possibility is the use of the equilibrium wetting angle (φ) at a GB in the case of an internal interface (similar to that

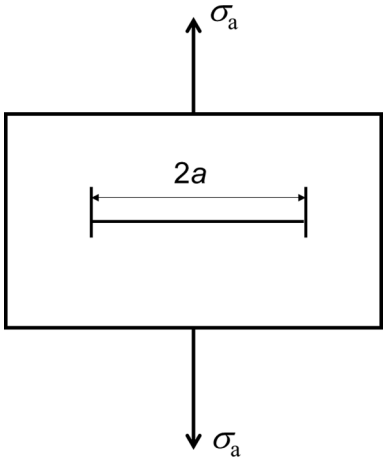

Fig. 4.7. Typical geometry used to describe the reduction in surface energy mechanism of LME, where a solid sheet containing a flat crack with a length of $2a$ is remotely loaded by a stress σ_a.

obtained in leaded steels, for example). The balance equation at equilibrium then reads:

$$\gamma_{gb} = 2\gamma_{sl}cos(\frac{\varphi}{2}) \tag{4-6}$$

Therefore, a direct measurement of this wetting angle and the GB surface energy, γ_{gb}, allows the extraction of the solid/liquid interface energy, γ_{sl}, on the assumption that no segregation at GBs could modify their surface energy. In the case of Fe, the GB surface energy can be measured by means of a 'zero creep experiment', combined with a measurement of the dihedral angle at the base of thermally etched GB grooves [373]. The experimentally determined value of the GB surface energy of iron is: $\gamma_{gb} = 0.985\ J{\cdot}m^{-2}$. On the other hand, the wetting angle at a GB of annealed, mechanically alloyed and sintered Fe-Pb powders was measured to be: $\varphi = 135^{\circ} \pm 10^{\circ}$ [374]. The calculated estimate of the solid/liquid interface energy is then in the order of $\gamma_{sl} = 1.28\ J{\cdot}m^{-2}$, i.e., it has suffered a reduction by a factor of two (49%) as compared with the measured surface energy of Fe, $\gamma_s = 2.52\ J{\cdot}m^{-2}$ [373]. Therefore, Griffith's brittle fracture theory predicts a lowering of the critical fracture stress for cleavage by a factor of about $1/\sqrt{2}$.

4.3.2. Adsorption-induced reduction in cohesion

The adsorption-induced reduction in cohesion model is a further development of the reduction in surface energy mechanism. This model postulates that adsorption of liquid metal atoms leads to the weakening of interatomic bonds at the crack tip [361,362]. This assumption has been proven by surface science observations [375]. The basic idea of this model is schematically illustrated in Fig. 4.8. As shown in Fig. 4.8a, when the crack tip is loaded, two competing scenarios could occur. First, crack extension may start by successively breaking the interatomic bonds on the plane that is loaded with the maximum tensile stress. Second, dislocation glide may be activated at slip planes, blunting the crack tip. Fig. 4.8b indicates that the potential energy of the bond A-A_o at the crack tip, U(a), and the stress imposed on the bond, σ(a), depend on interatomic distance, a. The σ(a) curve is approximated to be one-half of a sine wave. a_o and σ_m denote the initial equilibrium interatomic distance and the maximum stress necessary to break the bond, respectively. Assuming that the work necessary to break the atomic bond A-A_o is equal to the surface energy resulting from the formation of fresh fracture surfaces, then, σ_m can be described by:

$$\sigma_m = \left(\frac{E\gamma_o}{a_o}\right)^{1/2} \tag{4-7}$$

where E and γ_o denote the Young's modulus and surface free energy, respectively. In the case of a flat crack with a length c in a thin sheet loaded remotely by a tensile stress σ_a, the maximum stress σ_c at the crack tip can be calculated by the following equation based on Griffith's theory:

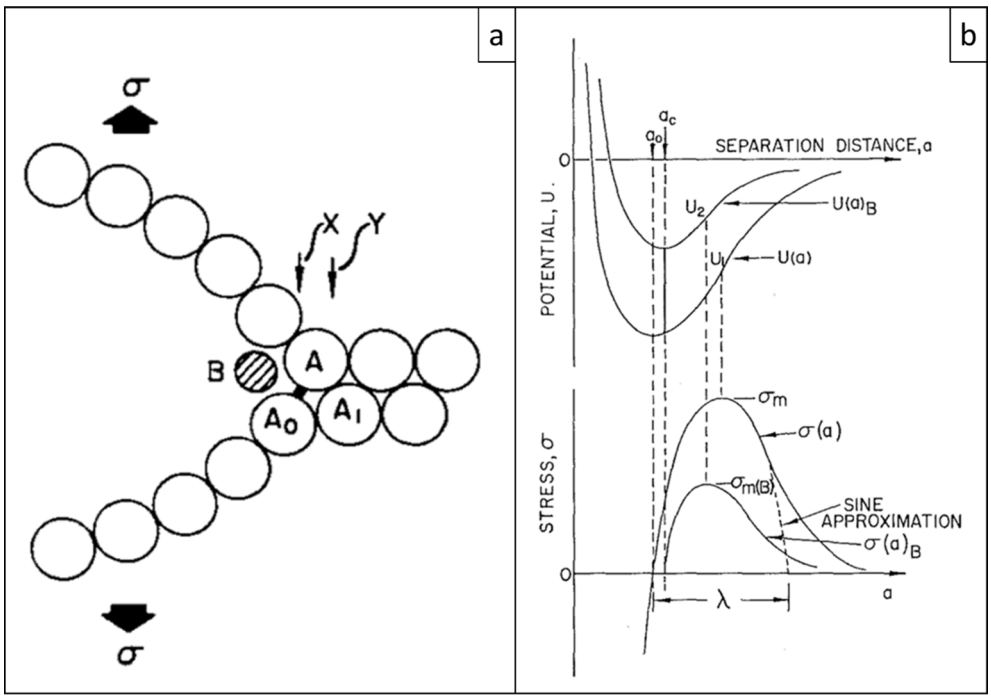

Fig. 4.8. Schematic illustration of the adsorption-induced reduction in cohesion model. (a) Atomic-scale process leading to the reduction of cohesion by breaking A-A_0 atomic bonds. (b) Schematic of the reduction in the magnitude of the interatomic potential and the associated, lowered stress required to overcome this potential energy barrier. Adapted from [362].

$$\sigma_c = 2\sigma_a\left(\frac{c}{R}\right)^{1/2} \tag{4-8}$$

where R is the radius of the crack tip. In the case of an atomically sharp crack, $R = a_o$, combining Eqs. (4-7) and (4-8) results in an expression to calculate the stress needed to propagate the crack as follows:

$$\sigma_p = \left(\frac{E\gamma_0}{4c}\right)^{1/2} \tag{4-9}$$

In reality, a crack is always plastically blunted to some extent. Assuming that the crack radius increases from a_o to a_p due to plasticity around the crack tip, and $a_p/a_o = \rho$ (ρ is a dimensionless ratio depending on the magnitude of plastic relaxation at the crack tip), then it can be derived from Eqs. (4-8) and (4-9) that:

$$\sigma_p(blunted) = \left(\frac{E}{4c}\cdot\rho\cdot\gamma_o\right)^{1/2} \tag{4-10}$$

As a result, the energy required to propagate a blunted crack is $\rho{\cdot}\gamma_o$. In addition, it is assumed that the adsorption of a foreign atom B at the crack tip gives rise to electronic rearrangements that, in turn, decrease the bonding strength of the A-A_o pair of atoms (Fig. 4.8a). Because of the adsorption-induced weakening effect, the potential curve $U(a)$ in Fig. 4.8b moves to $U(a)_B$, while the stress imposed on the bond shifts from $\sigma(a)$ to $\sigma(a)_B$. Therefore, crack extension takes place via decohesion of the A-A_o bond at the stress level of $\sigma_{m\text{-}X}$, followed by the adsorption of the embrittling atoms on the newly formed surfaces to repeat the same process described above.

This model indicates that the intimate contact of the liquid metal with the crack tip on the atomic scale is mandatory to trigger LME. Therefore, the crack extension rate depends on the transport velocity of the liquid metal to the crack tip. In addition, the influence of the adsorbed embrittling atoms should be limited to surface layers with a thickness of a few unit cell lengths due to electron screening effects. However, the presence of liquid metal atoms at the crack tip does not necessarily cause interatomic bond weakening, as intermetallic compounds could form, or elemental diffusion could produce a solid solution [281]. For example, liquid metal/solid metal couples, such as Al, Ni, Ti, and Fe alloys exposed to liquid Hg, show high sub-critical cracking rates, low mutual solubility, and no formation of intermetallic compounds. In these couples, the LME effect could be attributed to the mechanism of adsorption-induced reduction in cohesion [285]. Since adsorption is critical to determine the LME crack propagation rate, influential factors, such as

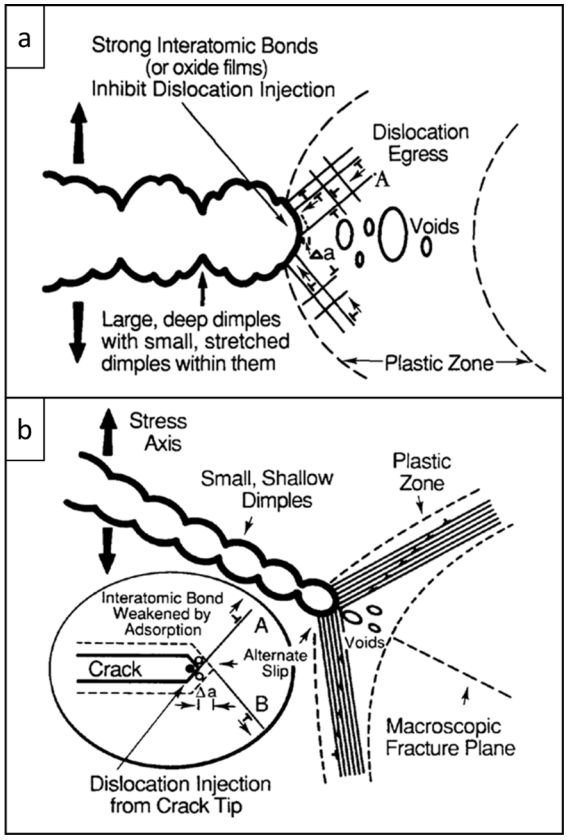

Fig. 4.9. Schematic illustration of the mechanism of adsorption-enhanced dislocation emission in: (a) an inert and (b) a liquid metal environment. Adapted from [365].

temperature, stress/strain, and chemical composition, must be thoroughly understood in order to properly simulate the adsorption process. Unfortunately, direct measurements to substantiate this interatomic bonding weakening mechanism are lacking.

4.3.3. Adsorption-enhanced dislocation emission

The adsorption-enhanced dislocation emission mechanism was developed by Lynch [285,363–365], based on the extensive fractographic characterisation of various liquid metal/solid metal couples. This mechanism was proposed to explain the presence of microvoids and dimples on fracture surfaces affected by LME. It is assumed by this mechanism that the shear strength of interatomic bonds around the crack tip is reduced by the adsorption of liquid metal atoms. This weakening effect promotes the emission of dislocations at the crack tip, therefore, crack propagation is controlled by localised plasticity and void growth/coalescence (see Fig. 4.9).

In an inert environment, strong plastic deformation involving massive dislocation activities occurs around the crack tip. A small fraction of the dislocations generate a short crack extension, while most of them lead to crack tip blunting and plastic strain in the plastic zone. Meanwhile, void nucleation occurs at microstructural discontinuities in the plastic zone. As the voids grow, they coalesce and combine with the crack front to advance the crack (Fig. 4.9a). Consequently, the fracture surface is typically dimpled.

By contrast, in a liquid metal environment (Fig. 4.9b), dislocation emission at the crack tip is facilitated, presumably because adsorption of liquid metal atoms induces weakening of the interatomic shear strength of a few atomic layers in the vicinity of the crack tip. The enhanced emission of dislocations results in crack advancement rather than crack tip blunting by promoting a higher rate of void nucleation ahead of the crack tip. Therefore, a limited plastic strain is available in the plastic zone, the voids cannot grow in size, and the fracture surface is characterised by much smaller dimples as compared to failure in an inert environment.

Even though this mechanism was proposed based on the observations of voids on fracture surfaces, it has often been challenged by the cases where voids could not be observed, even at very high magnifications [281]. Nevertheless, this mechanism seems to be supported by molecular dynamics (MD) simulations of the Al/liquid Ga couple [376–378]. The simulation results showed that the presence of liquid Ga led to rapid Ga penetration into the steel bulk by promoting the nucleation of dislocations at GBs intersecting the steel surface; after their nucleation, the dislocations would climb down along the GB surfaces and into the steel bulk. In addition, Keller and Gordon [318] found that the incubation period prior to the rupture for the Al 7075-T651/liquid Hg couple under a constant static load was likely associated with the coupled effects of adsorption-enhanced dislocation emission and stress-assisted dissolution mechanisms.

At the fundamental level, this scenario can be tested using the approach of Peierls-Nabarro complemented by the influence of the surface energy induced by the emission of a free dislocation [379]. The key aspect of this approach is to use the concept of generalised stacking fault (GSF) to account for the lattice friction for dislocation emission by the crack tip, as introduced by Rice in 1992 [380]. In counting the surface influence, one has to add the energy cost of a surface step created by dislocation emission and the attractive force induced by the presence of a surface [379]. The inclusion of a surface energy term was shown to be key to reconcile threshold stress intensity factors of dislocation emission at the crack tip, as extracted by MD modelling compared with a continuum approach based on that of Peierls-Nabarro [381]. In the setting introduced by Schoeck [379], one looks variationally for an equilibrium using the following equation:

$$\Delta G_T = E_0 - \int_0^\infty \tau_K(x)u(x)dx + \frac{1}{2}\int_0^\infty \tau_D(x)u(x)dx + \int_0^\infty \gamma(u_K(x)+u(x))dx + u(0)\gamma_{SL} \tag{4-11}$$

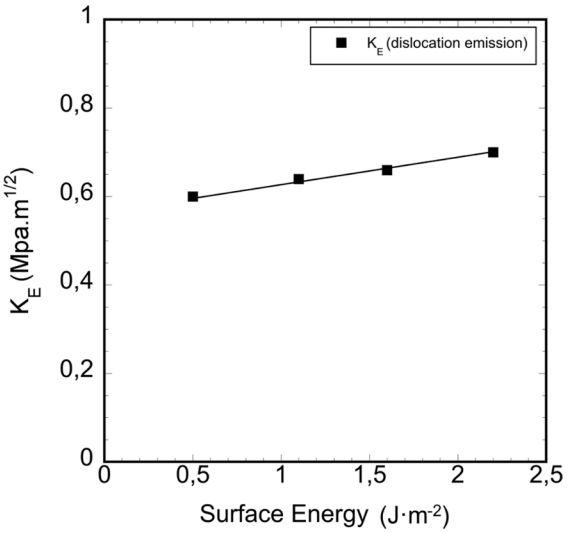

Fig. 4.10. Critical stress intensity factor for dislocation emission at a crack tip for iron (Fe) as a function of surface energy.

where E_0 is the self-energy of the dislocation core, $u(x)$ is the displacement field, $\tau_K = \frac{K}{\sqrt{2\pi x}}$ is the stress field at the crack tip, τ_D is the stress image field, and $\gamma(u(x).)$ is the GSF function. Whenever the equilibrium is not reached (i.e., when a stable solution is not found), then a dislocation is emitted to relax the built-up stress. Using this approach, the critical stress intensity factor for dislocation emission in mode II shear clearly depends linearly on the surface energy, as can be seen in Fig. 4.10.

Therefore, lowering the surface energy by adsorption induces a reduction of the critical stress intensity factor for dislocation emission at the crack tip, as advocated by the dislocation emission scenario (or the HELP mechanism in the context of hydrogen embrittlement [285]).

4.3.4. Localised plasticity and GB penetration mechanism

This mechanism was proposed on the basis of experimental observations upon the liquid Hg/CuAl couple that was fractured in an intergranular way with a faceted and featureless fracture surface [366]. It was stated in this mechanism that LME was caused by the strong interactions between dislocation pileups formed during localised plastic flow and liquid metal embrittling atoms that diffused a certain distance along GBs in the vicinity of the crack tip. The interactions led to GB weakening, so that the crack preferentially propagated in an intergranular manner. Therefore, the crack propagation rate relied on the atomic diffusion rate along GBs. However, as mentioned earlier, LME-induced crack growth can be very fast, up to tens of mm/sec. It is, thus, doubtful that atomic diffusion could be comparable with the fast crack propagation rate observed in many liquid meal/solid metal couples.

4.3.5. Stress-assisted dissolution model

This model was originally proposed by Robertson [367], and modified later by Glickman [368] (then labelled "a dissolution-condensation model") to predict crack growth kinetics. There are three basic assumptions made in Robertson's model: first, the crack is perfectly filled with liquid metal and there are no barriers available inside the crack to obstruct the solid from dissolving into the liquid. As a result, a chemical potential gradient is created by the stress distribution around the crack tip, leading to a diffusion flux directed from the solid to the liquid. Second, the dissolution rate of a solid metal or alloy ingredients is largely enhanced by stresses. The dissolved species then deposit or condense at stress-free surfaces behind the crack tip, where the chemical potential is seemingly higher. Last, the stress distribution ahead of a blunted crack tip is calculated by elastic stress analysis. Based on these assumptions, an equation can be derived to calculate the crack growth rate (da/dt), as given below [367]:

$$\frac{da}{dt} = \left(\frac{C_o D \Omega^2 \gamma}{kT}\right) \frac{1}{\rho^2} \left(\frac{2a\sigma_a^2}{E\gamma} - 1\right) \tag{4-12}$$

where C_o is the equilibrium concentration of the solid metal in the liquid metal per unit volume, D is the diffusion coefficient of the solid metal atoms in the liquid metal, Ω is the atomic volume of the solid metal atoms, γ is the solid/liquid interfacial energy, ρ is the crack tip radius, a is the half length of the crack, σ_a is the remotely applied stress, E is Young's modulus, k is Boltzmann's constant, and T is the temperature.

This model has not been widely accepted, due to some limitations. For instance, a high solubility of the solid metal in the liquid metal would reduce the sharpness of the crack tip, suppressing crack propagation, rather than causing severe embrittlement, as assumed by the model. In addition, the solubility of the solid metal in the liquid metal should not be influenced by stresses. In particular, the small space inside the crack would easily render the liquid metal saturated with the solid metal, so that the dissolution rate should not be affected solely by the stresses at the crack tip. In addition, Lynch [285] argued that if the stress-assisted dissolution

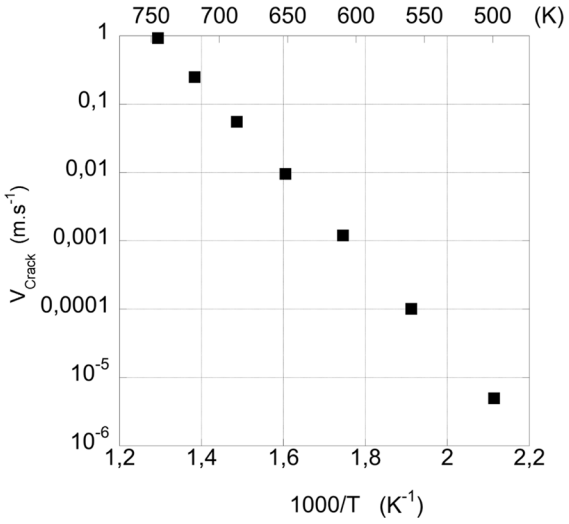

Fig. 4.11. Maximum predicted crack growth rate for the Fe/LBE couple, using the stress-assisted dissolution model.

model is valid, any role of dissolution can be discounted for LME, since it cannot occur in solid metal or metal vapour environments, where embrittlement of solid metals could happen via surface diffusion. Nam et al. [377] rejected this model, as their simulations showed that the LME susceptibility did not depend upon the concentration of Al in liquid Ga.

However, one merit of that approach is that Eq. (4-12) defines a maximum crack extension rate as a function of temperature, which could then be compared with experimentally measured ones by neglecting the second term on the right side of Eq. (4-12). This can be calculated using:

(1) the solubility of Fe (C_s) in liquid LBE [29]:

$$\log C_s(\mathrm{T,K}) = 6.01 - \frac{4380}{\mathrm{T}} \quad (\mathrm{wppm}) \tag{4-13}$$

(2) the diffusion coefficient (D) of Fe in liquid Pb/LBE [29]:

$$D(\mathrm{T,K}) = 4.9 \times 10^{-7} \exp\left(-\frac{44100 \pm 6300}{\mathrm{RT}}\right) \quad (\mathrm{m^2/s}) \tag{4-14}$$

Additionally, the following parameters are used: E = 194 GPa, $\rho = 0.384$ nm, $\Omega = 1.16968 \times 10^{-29}$ $\mathrm{m^3/at}$, $a = 1$ cm, and $\sigma_a = 1$ GPa. Then, the maximum crack growth rate in the case of the Fe/LBE couple can be calculated, as shown in Fig. 4.11.

4.3.6. GB Penetration via atomic diffusion

The GB penetration via atomic diffusion mechanism was developed by Gordon and An [298], based on experimental observations of delayed failure in the 4140 steel/liquid In couple under tensile load below the steel yield strength. This mechanism postulates that liquid metal atoms must diffuse along the GBs of the solid metal to reach a critical depth and concentration. As a result, a crack can nucleate at the GB after an incubation period, and the atomic diffusion process is stress-assisted. The liquid metal ingress into the steel bulk involves atomic diffusion, which is a thermally-activated, rate-controlling process. The corresponding crack nucleation time (t_n) required to form a liquid metal penetration zone depends on:

$$t_n \sim \ exp\left(\frac{\Delta G_s}{RT}\right) exp\left(\frac{\Delta G_d}{RT}\right) \tag{4-15}$$

where ΔG_S is the activation energy required for the liquid metal atoms to transition from the adsorbed state to the diffusion state on the steel surface, and ΔG_d is the activation energy for atomic diffusion along GBs.

This mechanism explains well the delayed failure phenomenon, but it does not clarify whether crack propagation depends on the atomic diffusion-induced formation of penetration zones as well. Despite this argument, GB diffusion has indeed also been observed in many other liquid metal/solid metal couples (e.g., Al/Ga, Ni/Bi, Cu/Bi, Cu/Hg) during the crack propagation process. The liquid metal forms a nanoscale liquid film or a secondary phase with a thickness of 1–3 atomic layers at GBs, leading to intergranular cracking under low stresses. However, the liquid films or secondary phases that are present in cracks may not necessarily result from GB diffusion. Instead, adsorption-induced intergranular cracking may be accountable for them, as the liquid metal could be sucked into cracks via capillary forces [285].

4.3.7. Enhanced work hardening mechanism

The enhanced work hardening mechanism was proposed by Dmukhovskaya and Popovich [369]. Similar to the main assumption in Lynch's mechanism, this mechanism postulates that adsorption of embrittling liquid metal atoms at the crack tip reduces the interatomic shear strength, so that dislocation emission at the crack tip is remarkably enhanced. However, this particular mechanism differs, in the sense that it assumes that the enhanced dislocation emission results in work hardening of the steel layers around the crack tip (Fig. 4.12). Moreover, it also assumes that the adsorbed embrittling species can activate new slip systems, further enhancing plastic flow and work hardening. As a consequence, cracks nucleate at dislocation pileups and other stress concentrators, followed by fast crack propagation through the hardened steel layers.

4.3.8. New understandings of LME in the past two decades

In the past ten to twenty years, new understandings of the LME phenomenon have been achieved by coupling multiscale modelling, simulations, and advanced experimental studies of GB embrittlement of solid metal/liquid metal couples including, Al/Ga, galvanised steel/Zn, Ni/Bi, Cu/Bi, steel/Na, steel/Pb and steel/LBE. Instead of going into too much detail, a nice review of which is given in Ref. [284], this subsection will only give a brief summary of the new insights into these LME couples, except for the steel/Pb and steel/LBE systems, which are the main focus of the present article. Thus, these two couples will be reviewed in detail in Sections 4.5 and 4.6.

The Al/Ga couple appears to be the most extensively investigated system, because it exhibits a severe LME effect characterised by fast GB penetration and debonding. Multiscale modelling and simulation efforts have been attempted to examine the LME effect of this couple on the nanometre and atomic scales. The results are very intriguing and have brought new insights, even though a gap in understanding still exists between atomic-scale modelling and macroscopic experimental observations. For instance, it was found that liquid Ga affected not only vacancy/void nucleation in solid Al, but also dislocation behaviour. The presence of Ga atoms at Al GBs triggers the formation of vacancies/voids [310,382,383] or is responsible for volumetric changes that ultimately develop into crack

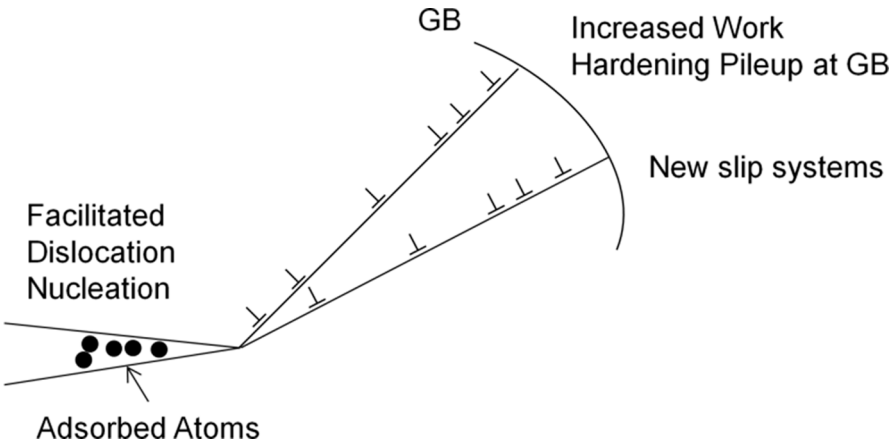

Fig. 4.12. Schematic illustration of the enhanced work hardening model, whereby the greatly enhanced emission of dislocations (effectively leading to the local crack tip work hardening) facilitated by the adsorbed liquid metal atoms increases significantly the crack growth rate.

initiation sites [384]. On the other hand, MD simulations indicated that the presence of liquid Ga facilitated dislocation nucleation at GBs of solid Al [376–378,385]. This finding seems to strongly support the adsorption-enhanced dislocation emission mechanism proposed by Lynch, as described earlier. It was also revealed that multiple parameters, such as stress, GB type, grain size, and temperature, all affected the LME kinetics. Advanced experimental studies based on TEM and non-destructive synchrotron radiation *in situ* observations have also greatly improved the understanding of LME of the Al/Ga couple. It was shown that the Ga penetration rate governed the crack propagation rate, which was favoured along high-angle GBs compared to low-angle ones [386,387]. The thickening of the Ga penetration layer at the Al GBs was associated with the GB angle, and stress was a key prerequisite for the formation of the nanoscale Ga penetration layer [388–392]. It was proposed to consider the penetration layer as a new phase, with a different structure and properties when compared to the solid metal [393]. Crack propagation was controlled by the mechanical properties of the solid metal instead of the GB properties, an assumption contradicting the generally accepted idea that GB properties should play the decisive role in liquid metal penetration [310,378,386,394,395]. Moreover, Glickman [396] proposed that local plasticity enhanced GB grooving might be a governing LME mechanism.

The LME phenomenon in Zn-galvanised steels (e.g., stainless steels, dual-phase steels, high-Mn twinning-induced plasticity steels) is of practical importance, because these steels could suffer LME-induced failure during industrial hot processes (e.g., hot-dip galvanizing, welding, hot stamping, etc.) or fire accidents [397,398]. Under these circumstances, the corrosion-inhibiting Zn coating can melt and trigger LME of the steel substrate. Extensive investigations have been performed to examine the LME characteristics of such couples [287–289,399–416]. The main findings showed that the dominant fracture mode was Zn penetration along austenite GBs and/or twin boundaries, forming liquid metal films and causing both the formation of Zn-rich intermetallic compounds and phase transformations [399,408,411,413,415,416]. The penetration of Zn into austenite GBs was stress-assisted, and a threshold stress was required for LME to occur [413,414]. The Zn concentration at GBs was critical for embrittlement [407]. Beal et al. [287–289] found that the embrittlement of twinning-induced plasticity (TWIP) steels exposed to liquid Zn occurred only within a specific temperature range, depending on the applied strain rate. LME in galvanised steels generally involves higher temperatures, which distinguishes this case from many other solid/liquid metal couples. This may be due to the relatively high melting point of Zn (419.5 °C). As a result, atomic diffusion and transport of the embrittling liquid metal atoms were observed to be greatly enhanced. Kang et al. [408] stated that the LME mechanism might be controlled by stress-assisted diffusion and/or mass transport along GBs. LME caused by liquid Zn did not only affect the austenite phase, but also the ferrite phase was sensitive to liquid Zn-induced embrittlement, while differences in the initial steel microstructure, such as the presence of retained austenite, did not impact strongly the steel susceptibility to LME [407,417,418]. Razmpoosh et al. [419] found that liquid Zn penetrated selectively into random high-angle GBs in 304 AuSS. In addition, segregation of Cr and other impurities at GBs might promote the occurrence of LME at random high-angle GBs in 304 AuSS exposed to liquid Zn [420]. An increase in the amount of coincidence site lattice (CSL) GBs improved the resistance of 304 AuSS to the LME effect [421]. Based on density functional theory (DFT) calculations, Bauer et al. [422] found that GBs were destabilised by Zn wetting and whether GBs were more vulnerable to LME or not relied on the operative mechanism and the Zn concentration levels. Moreover, DFT simulations performed by Scheiber et al. [423] also showed that an increase in the Al and/or Si content in the pure iron (Fe) reduced the concentration of Zn in both the GBs and surface of Fe, thereby attenuating the LME effect caused by liquid Zn. It must be pointed out that DFT calculations have also shown that tellurium (Te) bonds with GB atoms and induces GB expansion in Ni-based alloys, leading to far easier GB decohesion [424]. This has significant implications for molten salt-fuelled fission reactors, as despite the fact that the coolant is not a liquid metal, Te forms as a fission product that could induce LME in certain reactor components.

Experimental and simulation studies of Ni/Bi and Cu/Bi couples mostly focused on the existing forms of the liquid metal atoms at the GBs of the solid metal, as well as their effect on the GB properties of the solid metals. Most of the results showed that the adsorbed embrittling atoms reacted with solid metal atoms at GBs, forming a thin film the thickness of which varied from a monoatomic layer to

a nanometres-thick, and even a microns-thick multilayered film. The presence of such thin films led to drastic changes in atomic order, electronic state, faceting, and cohesion of the GBs in the solid metals [395,425–431]. The interactions could proceed in the form of atomic substitution [432,433] and/or nucleating vacancies/voids [310,382,383]. Other interesting statements that have so far been made include the conclusion of Klinger and Rabkin [434] that a liquid metal might be able to embrittle any solid metal as long as their mutual solubility was limited. Moreover, Schweinfest et al. [435] stated that GB embrittlement of Cu by Bi segregation was attributed to an atomic size effect rather than an electronic effect, whereby the large Bi atoms occupied the space of Cu atoms and weakened the GBs. They also stated that this mechanism was valid for all systems with oversized impurities. Also, Yu et al. [436] discovered that Bi segregation led to reconstruction of the GBs in solid Ni, forming ordered superstructures.

The LME susceptibility of AuSS (e.g., 304, 316L, 15-15Ti), ferritic and F/M steels (e.g., T91, ODS steels) exposed to liquid Na was experimentally studied in view of the perspective deployment of Gen-IV SFRs. The relevant findings showed that T91 F/M steels hardened by tempering at relatively low temperatures were embrittled by liquid Na [437]. Multiple parameters, such as the oxygen concentration dissolved in liquid Na, pre-exposure time, and pre-exposure temperature, all affected wettability (a prerequisite for LME), indicating that T91 F/M steels in their standard tempering metallurgical state are also affected by LME [438]. With the exception of 14Cr ODS steels, which showed a pronounced LME effect, the 9Cr and 18Cr ODS steels did not exhibit evident signs of LME after short-term exposures to liquid Na [439]. By contrast, AuSS were observed to be much less sensitive to LME in contact with liquid Na, even though a small amount of intergranular and/or cleavage fracture features were occasionally observed [439–443]. Interestingly, the plastic straining-induced phase transformation of austenite (γ, *fcc*) to ferrite (α, *bcc*) increased the susceptibility of AuSS to LME caused by liquid Na, as reported by Barkia et al. [441,443]. This suggests that differences in the LME susceptibilities of ferritic, F/M steels and AuSS may be primarily associated with their different crystal lattices (i.e., *fcc vs. bcc* steels).

4.4. The role of surface state on LME of 9Cr steels (wettability criterion)

The steel surface state (e.g., the presence of native oxides that formed in air at RT, surface flaws, roughness, notches, etc.) has a strong impact on the LME susceptibility of T91 F/M steels in contact with liquid Pb/LBE [216,444–448]. The main difference between 9Cr steels and carbon or low-alloy steels stems from the significant steel Cr content that promotes the formation of duplex oxide scales in contact with liquid Pb, Bi, or LBE. The inner oxide is an FeCr-spinel ($FeCr_2O_4$), and the outer oxide is chromia (Cr_2O_3) or magnetite (Fe_3O_4). This brings a major difference to the interface wettability by liquid Pb and/or LBE. The native oxides prevent the contact of the base steel with the HLM and its wetting by it. If the oxide scales can remain intact during mechanical loading of the steel, LME is not expected to occur. The observed high contact angles (>90°, indicating poor wettability) of liquid Pb/LBE on T91 F/M steels or 316L AuSS is due to the presence of their native oxide films [116,449–451]. The wettability of solid Fe by liquid Pb has been studied thoroughly in reducing conditions (typically, achieved by a H_2-rich cover gas) and the wetting angle has been measured to be in the order of 50° [371,372]. The Fe/Pb system is, therefore, in a partial wetting condition, and possibly, in a pseudo-partial wetting condition (i.e., a condition where a thin liquid metal film at the GB of a solid metal coexists with a droplet of the liquid metal, and their interfaces have a non-zero dihedral/contact angle [452]), instead of constituting a total wetting system (i.e., a condition with a zero dihedral/contact angle). Steel alloying by Cr is not expected to change this situation for an Fe-Cr/Pb solid/liquid interface in the absence of oxide scales. In practice, this requires the reduction of the native Cr oxide (Cr_2O_3), however, this oxide is much harder to reduce due to its higher formation enthalpy, while it has been found that liquid LBE is in a non-wetting state with respect to this oxide [453]. This state is maintained for short-term exposures, unless the steel is brought to high temperatures, where the formation of ternary phases cannot be excluded and reactive wetting may occur [454,455]. Therefore, in the case of high-Cr steels, one faces a challenge with respect to the assessment of LME, because one cannot exclude the chemical evolution of the solid/liquid interface and the possible degradation of the native oxide. Surface flaws, roughness, and notches created during steel manufacturing and/or machining generally act as stress concentrators or incipient cracks, thereby damaging the native oxides and compromising the oxide scale protectiveness, easing the occurrence of LME.

The LME susceptibility of Fe-9Cr-1Mo F/M steels has been rather tricky to prove. The main issue was that the wettability of this class of F/M steels was not a concern in preliminary searches for LME sensitivity. The first report regarding LME of T91 F/M steels in liquid Pb was given by Legris et al. [456] and Nicaise et al. [457]. They used a hardening heat treatment by tempering the T91 F/M steel at lower temperature (500 °C instead of 760 °C). This increased the steel hardness by almost a factor of two, changed the carbide distribution from interlath to intralath, and altered the dislocation density [458,459]. The tempering heat treatment also aimed at simulating the mechanical hardening induced by the low-temperature (<400 °C) irradiation of Fe-9Cr alloys. LME was then observed in notched specimens with this metallurgical condition, thereby reproducing the findings by Abramov et al. in an Fe-13Cr alloy [360]. More importantly, steel specimens subjected to a normal (750 °C) tempering heat treatment did not exhibit LME; it should be noted that this statement is generally true for monotonic tensile tests, but LME can also occur during small punch tests (SPT) under very low strain rates, as will be described in Section 4.6.2. The same finding was reported by Glasbrenner et al. for T91 F/M steel specimens tested in bending in liquid Bi and liquid LBE [460]. The LME effect after pre-exposure to static liquid LBE was also reported for the standard steel tempering heat treatment [461]. Therefore, it was difficult to classify this LME case, and a consensus on its relevance was never reached, due to the fact that the steel was in an unconventional metallurgical state (i.e., a factor of type II rather than an intrinsic, type I, sensitivity).

This came soon in stark contrast with two findings from corrosion experiments in flowing liquid LBE (in a forced convection loop) corrosion experiments. The used strategy was to pre-expose the steel samples in flowing liquid LBE coupled with testing in a tensile machine. The tested steels were Manet II (a closely related steel, containing 10% Cr and 0.5% Mo) and T91, both after a normal tempering treatment [216,462]. The two steels were found to be sensitive to LME in liquid LBE at 300 °C after 2 h of pre-exposure for

Manet II [462], and at 400 °C after 1500 h of pre-exposure for T91 [216]. Similar results were also reported on normally tempered EUROFER-97 steels tested at 400 °C after 4500 h of pre-exposure in flowing LBE [463]. This way of testing is very cumbersome, requiring large facilities with potentially long waiting times between different test batches.

Auger et al. [444,445] prepared specimens without any native oxide films (the native oxide removal was confirmed by Auger/XPS spectroscopy) by using argon (Ar) ion sputtering in ultrahigh vacuum, followed by physical vapour deposition (PVD) of thin LBE layers to create a direct contact with the steel substrate. The specimens were subjected to tensile tests in liquid LBE at 340 °C, and the results showed brittle fracture with abundant small cracks in the necking region. Intimate steel/HLM contact could also be achieved using soft soldering fluxes [444,464]. This clarified the intrinsic sensitivity of T91 F/M steels to LME by showing that the only criterion that explains the difference in its sensitivity is linked with the quality of direct steel/HLM contact during testing. Auger et al. [465] claimed that the chemical composition of the oxide scales could also play an important role in crack initiation. Different oxides have either different mechanical properties or different HLM wettabilities, leading to different sensitivities to crack initiation [121,251,465]. The fact that interfaces can be prepared by physical or chemical means indicated that a reproducible study of LME is possible if one adopts a strategy to prepare the interface that warrants reproducible conditions favourable to crack initiation.

This has led to two types of mechanical test strategies in liquid LBE: the first is the so-called pre-conditioning or pre-wetting operating procedure. The other relies on the evolution of the steel/HLM interface due to corrosion in an oxygen-reducing condition. Uncontrolled surface conditions with the frequent presence of native oxides might be responsible for the large observed scatter in steel fracture toughness data reported by different researchers [466–471]. It was found that when the specimen was pre-cracked in air, the fracture toughness of T91 F/M steels was weakly influenced by LBE, while an up to 80% reduction in the fracture toughness of these steels was observed in the case of pre-cracking in liquid LBE or pre-wetting the notch with liquid LBE. The promoted LME susceptibility of high-strength 4340 and 2.25Cr steels by fatigue pre-cracking in liquid Pb was also reported by Kamdar long time ago [472]. This might indicate that the surfaces of the crack walls formed during steel specimen pre-cracking were oxidised even at RT, forming native oxides that prevented the intimate contact between liquid LBE and the crack tip during mechanical testing. One may keep in mind that liquid metals, such as LBE, possess a quite high surface tension, imposing further requirements on surface cleanliness to ensure wetting. By contrast, pre-cracking in liquid LBE generates a crack tip that is in good contact with the liquid LBE, so that LME is facilitated.

The difference between plane strain [466–468,470,471] and plane stress [469] test conditions for fracture mechanics tests is also very evident. Generally, the LME susceptibility is greater under plane strain conditions than under plane stress conditions. Enhanced LME was observed in several studies [446–448,464,473], due to the presence of steel surface flaws and notches. This can be ascribed to the fact that stress concentrations at surface flaws and notches facilitate the failure of the superficial oxides. All these studies demonstrate that once a correct procedure is established to ensure crack initiation, reproducible results can indeed be obtained. It is worthwhile mentioning that the native oxides may not be so fragile, as a couple of studies showed that LME did not occur due to the successful protection by oxides under elastic bending stresses [474,475]. Several studies reporting no LME susceptibility are indicative of the experimental difficulty in achieving wetting or the ability of the native oxides to protect the steel from LME.

In summary, it has become very clear that the T91/LBE couple is an intrinsically embrittling couple with typical characteristics of LME (susceptibility to LME type I factor), provided one ensures proper wetting of the steel by LBE prior to tensile testing. Similar requirements hold also for fatigue testing, where a surface treatment or pre-cracking in the HLM is key for a correct assessment.

4.5. LME of AuSS exposed to liquid Pb/LBE

The LME susceptibility of AuSS, such as 316L, 15-15Ti, and their Si-enriched versions, has been evaluated by testing their tensile properties, fatigue life, and fracture toughness in contact with liquid Pb/LBE under different experimental conditions [36,45,58,476–482]. Most of the results showed that, irrespective of testing temperature, HLM oxygen concentration, steel cold working, pre-exposure, neutron irradiation, etc., the mechanical properties of the AuSS were either unaffected or only slightly affected by the HLM, indicating weak susceptibility of these steels to LME by liquid Pb/LBE. However, the creep resistance of 15-15Ti AuSS was reported to be remarkably reduced [483]. This was not considered a result of LME, but it was attributed to stress-enhanced dissolution corrosion and localised intergranular cracking. The testing parameters and main results are summarised in detail in Table 4.1.

Under tensile loading in liquid LBE, most AuSS showed no sign of LME, as the total elongation and fracture modes showed no obvious differences with those obtained in air or an inert environment (Fig. 4.13). The fracture surfaces in nearly all cases were dominated by typical dimple-like features (Fig. 4.14), indicative of ductile failure and absence of LME.

However, a mild degradation effect was observed in AuSS under cyclic loading in liquid Pb/LBE. For instance, Kalkhof and Grosse [477] reported that 316L AuSS were subjected to fatigue life reduction by a factor of 2–3 at high strain amplitudes in the presence of liquid LBE at 260 °C, while the fatigue life at low strain amplitudes was comparable with that in air at the same temperature. Gorse et al. [36] reported that the effect of LBE on the low-cycle fatigue of 316L AuSS at 300 °C, 450 °C, and 500 °C was weak, but a small life reduction was observed when the total strain range was >0.6%. They also checked the effects of holding time and pre-creep (pre-corrosion) treatment on the fatigue properties of 316L AuSS, observing a negligible effect of liquid LBE. This indicated that 316L AuSS were not sensitive to surface defects caused by pre-corrosion. Moreover, Yaskiv and Fedirko [481] also observed slightly degraded fatigue properties of an Fe-18Cr-10Ni AuSS exposed to liquid Pb at 350 °C. It should be noted, however, that a much stronger effect was observed by Chocholousek et al. [58], based on fatigue crack growth rate tests (da/dN) at 300 °C. Their results showed that the fatigue crack propagation rate in 316L AuSS was a factor of 5 higher in contact with liquid LBE as compared to air, and that a low LBE oxygen concentration promoted significantly the crack propagation. However, it is still unclear whether this material degradation effect under the cyclic loading is directly associated with LME.

Barkia et al. [441,443] emphasised that the phase transformation of austenite (γ, *fcc*) to ferrite (α, *bcc*) and the formation of

Table 4.1
Effect of liquid Pb/LBE on the mechanical properties of AuSS under different loading conditions.

Material	Test	Specimen shape & surface condition	Heat treatment & metallurgical state & irradiated state	Pre-exposure conditions	HLM	C_O in HLM	Temperature (°C)	Loading conditions (Strain/loading rate)	Remarks	Refs.
316L	Tensile	CCT[†]; mechanically polished & electropolished	Annealed	LBE pre-wetted notch with a soft soldering flux	LBE	Low-oxygen LBE (conditioned with flowing He + 4 % H_2)	160	$6.67 \times 10^{-8} - 6.67 \times 10^{-3}$ m/s	Embrittlement effect not pronounced; the fracture surface was dominated by intense shear decohesion	[478]
316L	Tensile	Cylindrical	SA[†] at 1050–1100 °C; neutron-irradiated to 9.1 dpa	Pre-exposure to low-oxygen LBE at 450 °C for 20 h	LBE	Oxygen saturation	350	$\dot{\varepsilon} \approx 5 \times 10^{-5}$ s^{-1}	Irradiated 316L not susceptible to LME; all fracture surfaces showed dimples	[45]
316L, Si-enriched AuSS (A078, 2442, L413)	Tensile	Cylindrical & surface-untreated	SA[†] at 1050–1100 °C	No pre-exposure	LBE	Low-oxygen LBE (conditioned with flowing Ar + 5 % H_2)	350	$\dot{\varepsilon} \approx 10^{-6}$–$10^{-3}$ s^{-1}	316L AuSS: no sign of LME, unchanged elongation and fracture surface with dimples; A078 AuSS: LME observed; 2442 & L413 Si-enriched AuSS: no LME	[476]
15-15Ti	Tensile	Flat tapered specimens; polished to 1 μm finish	SA[†]	LBE pre-exposure at 300 °C for 1 h	LBE	$C_O \approx 1 \times 10^{-6}$, 1×10^{-8}, 1×10^{-12} wt%	300	2×10^{-8} m/s	No obvious difference in crack initiation behaviour regardless of exposure environment (LBE or air); no LME observed	[480]
316L	Low-cycle fatigue	Cylindrical bar; mechanically polished	Unknown	Unknown	LBE	No oxygen control	260	Strain-controlled (unknown waveform); strain ratio R = -1; $f = 1$ or 0.1 Hz; $\varepsilon_a \approx$ 0.2–1.0%	316L fatigue life: slightly affected by LBE at the strain amplitudes (ε_a) > 0.5%	[477]
316L	Low-cycle fatigue	Cylindrical-bar; mechanically polished	Unknown	Unknown	LBE	Oxygen saturation	300, 450, 550	Strain controlled; R = -1 (triangular waveform); $\dot{\varepsilon} \approx 4 \times 10^{-3}$ s^{-1}	Slightly detrimental effect observed at total strain ranges > 0.6%; pre-creep in oxygen-saturated LBE under constant stress of 240–260 MPa for 2–4 weeks did not affect the LBE fatigue life at 300 °C; pre-exposure to low-oxygen LBE or oxygen-saturated LBE did not affect the fatigue life	[36]
316L	Creep-fatigue	Cylindrical bar; mechanically polished	Unknown	Unknown	LBE	Oxygen saturation	300	Strain controlled; R = -1; $\dot{\varepsilon} \approx 4 \times 10^{-3}$ s^{-1}; 10 min hold in tension (trapezoidal waveform)	Creep-fatigue life at total strain range of 1.2%: comparable with low-cycle fatigue life at identical testing conditions	[36]
316L	Low- cycle fatigue	Cylindrical; electropolished	SA[†] at 1050 °C & water quenched	Pre-exposure to low-oxygen LBE ($C_O \approx 10^{-11}$ wt%) at 500 °C for 1000 h	LBE	Oxygen saturation	300	Strain controlled (triangular waveform); R = -1; $\dot{\varepsilon} \approx 4 \times 10^{-3}$ s^{-1}	316L fatigue life slightly affected by LBE at relatively high total strain ranges (~1%); nearly no effect at relatively low total strain ranges (~0.3%); pre-exposure to low-oxygen LBE caused surface defects due to LMC[†], but did not degrade the fatigue life noticeably	[482]

Table 4.1 (*continued*)

Material	Test	Specimen shape & surface condition	Heat treatment & metallurgical state & irradiated state	Pre-exposure conditions	HLM	C_O in HLM	Temperature (°C)	Loading conditions (Strain/loading rate)	Remarks	Refs.
Fe18Cr10Ni AuSS	Low- cycle fatigue (cyclic bending)	Mechanically polished	Annealed at 1050°C for 30 min	Surface blanched with liquid Pb and LBE to improve wetting	Pb	Oxygen partial pressure $< 5 \times 10^{-3}$ mm Hg	350	Strain-controlled mode	Fe18Cr10Ni AuSS: slightly degraded by liquid Pb at 350 °C	[481]
316L	FCG† rate	1/2CT† specimens	SA† at 1050–1100 °C	Pre-cracking in air or LBE at 350 °C	LBE	$C_O \approx 5 \times 10^{-11}$–$2 \times 10^{-5}$ wt%	300	Two loading rates: 0.2 mm/min & 0.02 mm/min; f = 0.125 Hz; plane-strain; R = 0.1	FCG† rate in LBE 5 × faster than in air; extensometer not used to measure COD†, measurements corrected afterwards	[58]
316L	Fracture toughness	DCT† specimens; pre-cracking in air	SA† at 1050–1100 °C & water quenched	No pre-exposure	LBE	Oxygen saturation	200, 300	0.25 mm/min	Plane-strain fracture toughness: slightly reduced; fracture surface: dominated by ductile features (e.g., dimples)	[479]
15-15Ti	Creep	Cylindrical; not polished	SA† at 1120 °C for 1 h & fast cooling in water	Pre-exposure for 6 h at each creep testing temperature	LBE	Variable C_O: from oxygen saturation to oxygen-poor conditions	550, 600	Constant load: 300 MPa	Secondary creep rate in LBE at 550 °C & 600 °C was 56× & 6 × higher than in air, reducing drastically creep life; uniform dissolution corrosion and local intergranular cracking were responsible for the weaker creep resistance	[483]

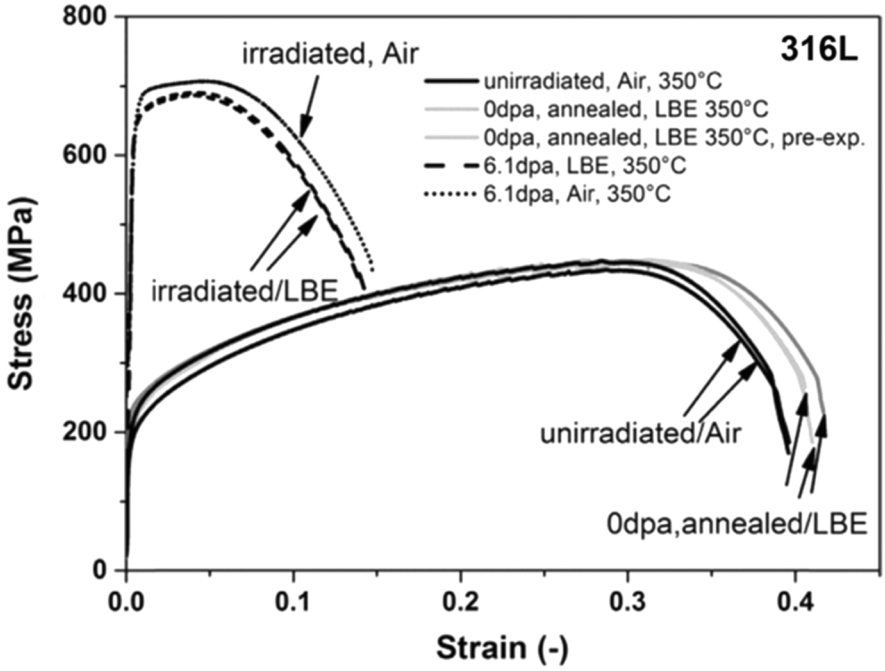

Fig. 4.13. Tensile stress–strain curves of irradiated and non-irradiated 316L AuSS tested in different environments. "Pre-exp." means LBE pre-exposure at 450 °C for 20 h [45].

numerous deformation twins enhanced the occurrence of LME, especially at the steel GBs, in AuSS exposed to liquid Na. The ferrite phase is believed to be susceptible to LME in contact with liquid Pb or LBE, as LME is often observed in T91 F/M steels in an (annealed) ferritic structure. Ferritisation may be induced in AuSS by plasticity at crack tips. In addition, ferritisation of AuSS is observed in dissolution corrosion-affected zones, where the austenite-stabilising steel alloying elements (Ni and Mn) are selectively leached by liquid LBE, resulting in the formation of ferrite, as described in Chapter 3. In this regard, dissolution corrosion-induced ferritisation might be a potentially important cause of LME in AuSS, therefore, special attention must be paid to the possible occurrence of LME when dissolution corrosion-affected steel areas are mechanically loaded at relatively low temperatures (i.e., around 350 °C). The severity of the synergy of dissolution corrosion and LME is expected to be increased in a neutron environment, due to irradiation embrittlement. Interestingly, LME of AuSS exposed to other liquid metals, such as Ga [484], Hg [469,485–490], and Na [439–443], was also demonstrated to be mild, regardless of the load type, even though both intergranular and transgranular brittle failure features were occasionally observed on the fracture surfaces. Despite this weak LME effect, one should be cautious when asserting that AuSS are immune to LME, prior to fully understanding this materials degradation mechanism. The sensitivity of irradiated AuSS has not been assessed yet in an extensive and systematic manner.

When compared to AuSS, the LME effect is much stronger in F/M steels. The LME of F/M steels will be described in detail in Section 4.6, with a focus on the parametric effects and mechanistic understanding of crack initiation and propagation during LME.

4.6. Factors affecting the LME of F/M steels in liquid Pb/LBE

Due to the specificity of each liquid metal environment, a variety of factors (metallurgical, mechanical, chemical) can influence the LME susceptibility of F/M steels in contact with liquid Pb or LBE [36]. These factors can be classified into the following three categories: the first category is associated with the intrinsic steel sensitivity (factor type I), which, in turn, depends critically on the wettability or surface state [257,447,475,491–493] and steel pre-exposure [494,495]. The second category relates to the dependence on the steel metallurgical state [458,471] and its alteration under irradiation [45,493,496–498]. The third category ("kinetic" factors) includes the temperature [447,457,458,471,493,494,499–501], the applied strain/loading rate [306,478,493,494,501–503], and, to some extent, the HLM oxygen concentration [493,502,504]. The mechanical testing standard used to investigate LME until the 1990s has almost exclusively focused on either tensile testing or fatigue testing. Several techniques have been recently developed to complement the set of available mechanical tests: for example, fracture mechanics type tests were explicitly developed for the opaque and conductive HLM medium, which usually prevents the use of conventional techniques to monitor crack growth [469,484]. A mechanical extensometer was developed to directly measure the strain at the gauge length of a specimen submersed in liquid LBE, allowing for more accurate fatigue tests [505]. This technique was later extended to monitor the pre-crack length in liquid LBE so as to obtain reliable fracture toughness data. The CCT† geometry has been developed for fracture mechanics type studies of thin steel sheets in the plane-stress condition. For thicker reactor components, the conventional CT† specimen geometry has been used in conjunction with specific pre-conditioning procedures (i.e., pre-cracking in liquid LBE), due to the otherwise difficult task in wetting the crack tip of

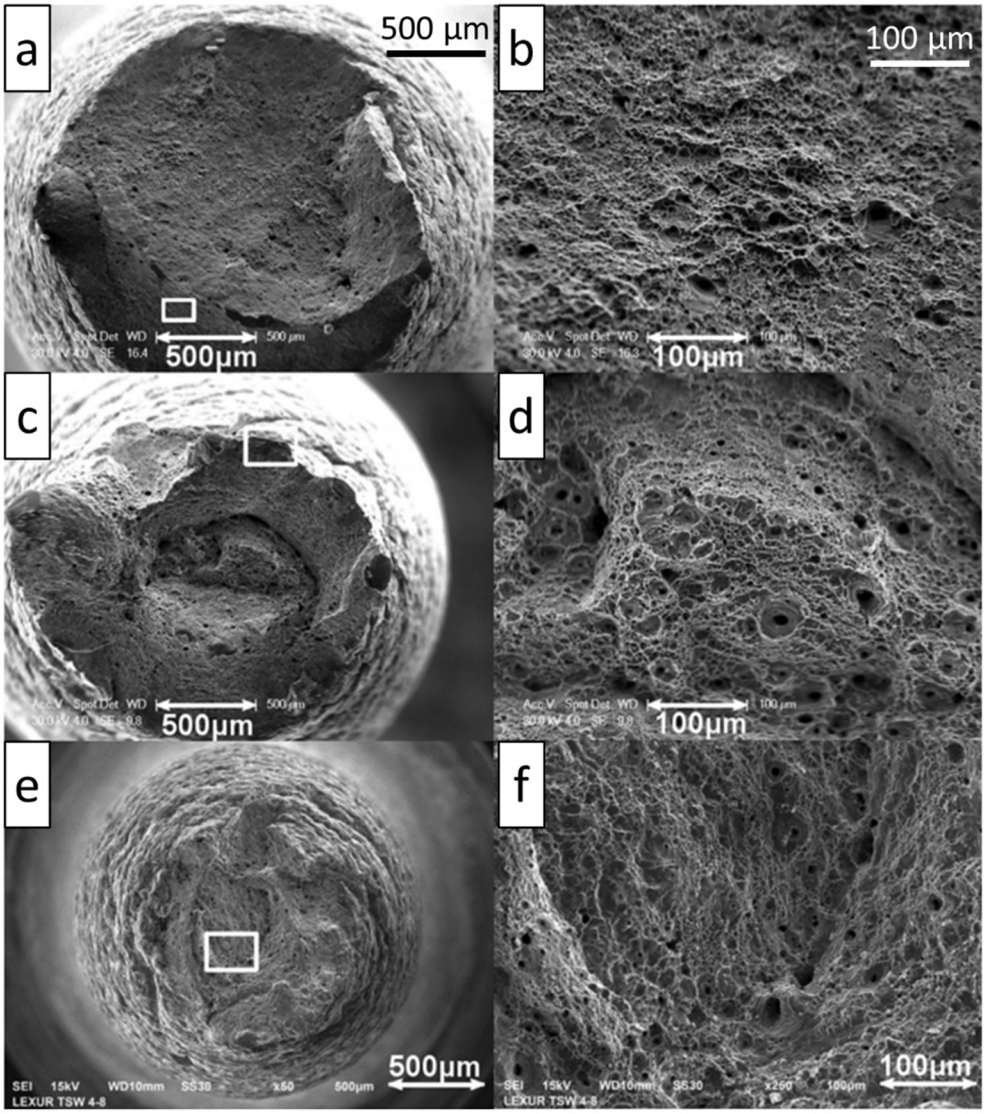

Fig. 4.14. Fracture surfaces of irradiated (a-d) and non-irradiated (e,f) 316L AuSS tested in air (a,b) and liquid LBE (c-f) at 350 °C. Adapted from [45].

a fatigue-induced crack [470]. The miniaturised SPT has been adapted to study LME [506]; this test is particularly sensitive to the surface state [465], and could be adapted to study the LME sensitivity of irradiated samples. The SPT for LME studies is designed in such a manner that the bottom side of a thin disc specimen is loaded via a pushing rod, while the upper side is in contact with liquid LBE.

In the past two decades, extensive experimental investigations have been carried out to understand the effects of a wide spectrum of parameters on tensile [464,507], fatigue [53,481,500,502,505,508–510], fracture toughness [467,468], creep [511–518], and creep-fatigue properties [231,495] of T91 F/M and similar steels exposed to liquid Pb/LBE. This subsection reviews the LME characteristics of T91 (and similar) F/M steels and their welds in contact with liquid Pb/LBE, attempting to unveil the underlying mechanisms that affect crack initiation and propagation upon the LME of these steels. Table 4.2 summarises the experimental conditions and most important findings.

4.6.1. The role of temperature

The temperature effect on the LME sensitivity of T91 F/M steels exposed to liquid Pb/LBE has been investigated by means of tensile tests, fatigue tests, SPT†, etc. The tensile and fatigue tests showed a strong dependence of the LME severity on temperature, known as the so-called "ductility trough" in terms of total elongation [447,458,471], or "fatigue endurance trough" in terms of low-cycle fatigue life [500]. According to its definition, the "trough" indicates that the LME severity is highest within a (system-specific) intermediate temperature range, while LME is absent or weak at both lower and higher temperatures. Depending on the loading condition and steel

Table 4.2
Effect of liquid Pb/LBE on the mechanical properties of ferritic steels & their welds under different loading conditions.

Material	Test	Specimen shape, surface condition	Heat treatment and metallurgical state; irradiated state	Pre-exposure conditions	HLM	C_O in HLM	Temperature (°C)	Loading conditions (Strain rate/loading rate)	Remarks	Refs.
T91	Tensile	Smooth cylindrical; notched	normalised: 1050 °C, 1 h & tempered: 750 °C, 1 h; normalised: 1050 °C, 1 h & tempered: 500 °C, 1 h (hardened)	No pre-wetting	Pb	Oxygen saturation	260, 350	$\dot{\varepsilon} \approx 10^{-4}$ s^{-1}	The notched & hardened specimens showed enhanced LME with transgranular fracture features	[456,519]
T91	Tensile	Smooth cylindrical; notched	normalised: 1050 °C, 1 h & tempered: 750 °C, 1 h; normalised: 1050 °C, 1 h & tempered: 700 °C, 1 h (hardened); normalised: 1050 °C, 1 h & tempered: 500 °C, 24 h (hardened)	No pre-wetting	Pb	Oxygen saturation	350–500	$\dot{\varepsilon} \approx 10^{-4}$ s^{-1}	LME was observed in specimens subjected to tempering/ hardening & notching; "ductility trough" with the lowest elongation at 350 °C and ductility recovery at 450 °C	[457]
T91	Tensile	Smooth cylindrical; surface oxides removed by ion beam sputtering	normalised: 1050 °C, 1 h & tempered: 750 °C, 1 h	Direct contact of steel surface with LBE via vapour deposition or soft soldering fluxes	LBE	LBE conditioned by flowing He, but the C_O was not monitored	340	$\dot{\varepsilon} \approx 10^{-4}$ s^{-1}	The direct steel/LBE contact promoted the occurrence of LME	[444,445]
T91	Tensile	Cylindrical; notched	normalised: 1050 °C, 1 h & tempered: 750 °C, 1 h	LBE pre-exposure at 150–650 °C for 12 h	LBE	Low-oxygen LBE (conditioned with flowing He + 4 %H_2)	300, 350, 400	Loading speed ≈ 10^{-5}–10^{-2} mm/s	LME was observed on notched specimens; in contact with oxygen-poor LBE (LBE conditioned by hydrogenated He), LME was most severe; LBE pre-exposure at 600 and 650 °C facilitated wetting	[461]
T91	Tensile	CCT; plane-stress; mechanically polished & electropolished; no pre-cracking	normalised: 1050 °C & tempered: 750 °C	Notch pre-wetted with LBE by means of a soft soldering flux used to remove the native oxides	LBE	Low-oxygen LBE (conditioned with flowing He + 4 %H_2)	160, 250, 350	$\dot{\varepsilon} \approx 6.67 \times 10^{-7}$–$6.67 \times 10^{-3}$ s^{-1}	Maximum brittle crack propagation rate decreased with increasing temperature; stress-assisted dissolution model & thermally-activated ductility recovery mechanism failed to explain the results; adsorption-induced reduction in surface energy	[306]

(*continued on next page*)

Table 4.2 (*continued*)

Material	Test	Specimen shape, surface condition	Heat treatment and metallurgical state; irradiated state	Pre-exposure conditions	HLM	C_O in HLM	Temperature (°C)	Loading conditions (Strain rate/loading rate)	Remarks	Refs.
									mechanism may be valid	
T91	Tensile	CCT; mechanically polished & electropolished	normalised: 1050 °C & tempered: 750 °C	Notch pre-wetted with LBE by means of a soft soldering flux used to remove the native oxides	LBE	Low-oxygen LBE (conditioned with flowing He + 4 %H_2)	160	$6.67 \times 10^{-8} - 6.67 \times 10^{-3}$ m/s	LME susceptibility depended on the loading rate & ductility recovery occurred at high loading rates	[478]
T91	Cyclic & tensile	Round compact test	normalised: 1050 °C & tempered: 770 °C, 45 min	Pre-exposure to flowing LBE ($v \approx 1$ cm/s), $C_O < 10^{-6}$ wt %, 500 °C, 1000 h	LBE	Low-oxygen LBE (conditioned with flowing He + 5 %H_2)	300	First cyclically loaded, followed by tensile loading	Specimens subjected to LBE pre-exposure showed 30 × faster crack propagation rate than in air	[520]
T91	Tensile	Dog-bone shaped flat; electropolished	normalised: 1040 °C, 1 h & tempered: 760 °C, 1 h	LBE pre-exposure for 12 h at each tensile testing temperature	LBE	Oxygen saturation	150–500	$\dot{\varepsilon} \approx 10^{-5}$ s^{-1}	T91 susceptible to LME at 300–425 °C; LME occurred after necking; surface cracks or flaws promoted LME	[447]
T91	Tensile	Cylindrical; surface ground	normalised: 1050 °C, 1 mm/min & tempered: 770 °C, 45 min	Unknown	LBE	Low-oxygen LBE (conditioned with flowing Ar + 5 %H_2)	300, 500	$\dot{\varepsilon} \approx 10^{-4}$ s^{-1} & $\dot{\varepsilon} \approx 10^{-6}$ s^{-1}	T91 sensitive to environmentally-assisted cracking at 300 °C, typical LME-induced brittle features on the fracture surface; at higher strain rates, more brittle cracks were observed	[499]
Manet II	Tensile	Standard flat specimens	normalised: 1075 °C, 30 min & tempered: 750 °C, 2 h	No pre-exposure	Flowing LBE ($v \approx 1$ m/s)	No oxygen control	180, 200, 250, 300	10^{-4} mm/s	Loss of ductility observed at 250 °C & 300 °C	[462]
T91	Tensile	Flat; mechanically polished	normalised: 1050 °C/ 1040 °C/1040 °C, 1 h & tempered: 760 °C/ 600 °C/500 °C, 2 h	Unknown	LBE	< 50 wppm	150–500	$\dot{\varepsilon} \approx 10^{-5}$ s^{-1}	The effect of temperature on steel tensile elongation in contact with LBE was characterised by a "ductility trough"; as the tempering temperature decreased, the "ductility trough" became wider and deeper, indicating a stronger LME effect; the harder the steel, the more severe the LME	[458]

(*continued on next page*)

Table 4.2 (*continued*)

Material	Test	Specimen shape, surface condition	Heat treatment and metallurgical state; irradiated state	Pre-exposure conditions	HLM	C_O in HLM	Temperature (°C)	Loading conditions (Strain rate/loading rate)	Remarks	Refs.
T91, F82H	Tensile	Dog-bone shaped flat; surface ground	T91: normalised 1040 °C, 1 h & tempered 760 °C, 1 h; F82H: normalised 1040 °C, 38 min & tempered 750 °C, 1 h	Unknown	LBE	< 1 wppm	150–500	$\dot{\varepsilon} \approx 10^{-5}\ s^{-1}$	Irradiated to 20 dpa with mixed spectrum of neutrons & protons; irradiation-enhanced LME, substantial loss of elongation down to 2–3%	[497]
T91	Tensile	Cylindrical samples; unpolished	normalised: 1040 °C, 1 h & tempered: 760 °C, 1 h	Some specimens were pre-exposed to LBE at 450 °C for 4000 h	LBE	Low-oxygen LBE (conditioned with flowing Ar + 5 %H_2)	150–450	$\dot{\varepsilon} \approx 10^{-6}$–$10^{-3}\ s^{-1}$	LME was absent in most of the cases, which might be associated with poor oxygen control; surface defects induced by LMC decreased the steel total elongation	[494]
T91, EUROFER-97	Tensile	Cylindrical samples; unpolished	T91: normalised at 1040 °C, 1 h & tempered at 760 °C, 1 h; EUROFER-97: normalised at 979 °C, 1 h and 51 min & tempered at 739 °C, 3 h and 42 min	Pre-exposure to LBE in some tests	LBE	Low-oxygen LBE (conditioned with flowing Ar + 5 %H_2)	150–450	$\dot{\varepsilon} \approx 10^{-6}$–$10^{-3}\ s^{-1}$	Due to the protective native oxides, no LME was observed in a wide range of testing conditions, including neutron irradiation; pre-exposure and surface stress raisers increased the LME susceptibility	[493]
T91/316L & T91/T91 welds	Tensile	Cylindrical	Welds prepared by TIG† & EB† welding	Pre-exposed to low-oxygen LBE	LBE	Low-oxygen LBE (conditioned by a reducing gas)	350	$\dot{\varepsilon} \approx 5 \times 10^{-6}\ s^{-1}$	The welds were highly susceptible to LME; the TIG welds were more susceptible to LME than the EB welds	[521,522]
T91, T91-Si, EP-823, S2439 (2.75Si), S2440 (4.83Si)	Tensile	Cylindrical; specimen surface in most of the cases untreated	T91: normalised at 1040 °C, 60 min & tempered at 760 °C, 60 min; T91-Si: normalised at 1050 °C, 30 min & tempered at 750 °C, 30 min; EP-823: normalised at 1010 °C, 60 min & tempered at 620 °C, 75 min; S2439: normalised at 1050 °C, 60 min & tempered at 760 °C, 60 min; S2440: normalised at 1050 °C, 60 min &	Unknown	LBE	Low-oxygen LBE (conditioned with flowing Ar + 5 %H_2)	150–450	$\dot{\varepsilon} \approx 5 \times 10^{-7}$–$1 \times 10^{-3}\ s^{-1}$	Compared to T91, Si-enriched steels were more susceptible to LME; all steels showed a "ductility trough" in contact with LBE	[251,523]

Table 4.2 (*continued*)

Material	Test	Specimen shape, surface condition	Heat treatment and metallurgical state; irradiated state	Pre-exposure conditions	HLM	C_O in HLM	Temperature (°C)	Loading conditions (Strain rate/loading rate)	Remarks	Refs.
			tempered at 760 °C, 60 min							
SIMP[†] steel	Tensile	Cylindrical; mechanically polished	normalised: 1050 °C, 30 min & tempered: 500 °C, 90 min	Unknown	LBE	< 1 ppm at 250 °C	200–500	$\dot{\varepsilon} \approx 1.25 \times 10^{-4}$–$1.25 \times 10^{-3}$ s^{-1}	"Ductility trough" between 200 and 450 °C, where LME was most severe	[501]
T91	Tensile	Notched; smooth surface	normalised: 1050 °C, 15 min & tempered: 770 °C, 45 min	Surface treated with chemical flux to remove native oxides, followed by hot dipping in liquid Pb to improve wetting	Pb	$C_O \approx 10^{-5}$ wt% at 450 °C, $C_O \approx 10^{-7}$ wt % at 350 °C (calculated)	350–450	$\dot{\varepsilon} \approx 10^{-8}$–$10^{-2}$ s^{-1}	No LME was observed in smooth specimens, while notched specimens were affected by LME; the serrations in the stress–strain curves of notched specimens affected by LME were attributed to the combined effects of dynamic strain ageing (DSA[†]) and creep	[464]
T91	Tensile	Cylindrical; notched	normalised: 1050 °C, 15 min & tempered: 770 °C, 45 min	Pre-exposure to low-oxygen LBE at 450 °C for 24 h	LBE	Low-oxygen LBE ($C_O \approx 8 \times 10^{-11}$ wt%)	350	$\dot{\varepsilon} \approx 2 \times 10^{-6}$ s^{-1}	Fatigue striation-like markings observed on the fracture surface, indicating intermittent crack propagation in contact with LBE; this feature was associated with both LME and the compliance of the tensile machine	[473]
T91	Tensile	Cylindrical	T91: austenitised at 1050 °C for 1 min/mm & tempered at 770 °C for 3 min/mm; neutron-irradiated to 9.1 dpa	Pre-exposure to low-oxygen LBE at 450 °C for 20 h	LBE	Oxygen saturation	350	$\dot{\varepsilon} \approx 5 \times 10^{-5}$ s^{-1}	T91 susceptibility to LME in contact with LBE was intensified by neutron irradiation; the fracture surface was characterised by quasi-cleavage features	[45]
T91	Tensile	Cylindrical gauge (mechanically polished before irradiation);	normalised: 1100 °C, 15 min & tempered: 770 °C, 45 min	Unknown	LBE	Low-oxygen LBE (conditioned with flowing Ar + H_2)	300	$\dot{\varepsilon} \approx 5 \times 10^{-5}$ s^{-1}	T91 susceptibility to LME in contact with liquid LBE was intensified by neutron irradiation (irradiated at 300 °C;	[496]

(*continued on next page*)

Table 4.2 (*continued*)

Material	Test	Specimen shape, surface condition	Heat treatment and metallurgical state; irradiated state	Pre-exposure conditions	HLM	C_O in HLM	Temperature (°C)	Loading conditions (Strain rate/loading rate)	Remarks	Refs.
		rectangular gauge							max. dose: 2.5 dpa) or the combination of neutron and proton irradiation (irradiated at 250–350 °C, dose: 0.8–3.9 dpa)	
T91	Tensile	Flat tapered specimens; polished	normalised: 1150 °C, 15 min & tempered: 770 °C, 45 min	Unknown	LBE	$C_O \approx 3 \times 10^{-7}$–$6 \times 10^{-6}$ wt%	300	$\dot{\varepsilon} \approx 10^{-2}$, 10^{-4}, 10^{-6} s^{-1}	LME cracks initiated at plastically-strained regions; 1.3% plastic strain and stress close to UTS† required to initiate a crack in contact with LBE; the threshold stress for crack initiation in air was 10% higher than that in LBE, and it decreased with increasing strain rate	[503]
T91	Tensile	Cylindrical and notched; surface treated with flux followed by Pb immersion at 450 °C to grow surface deposits	normalised: 1050 °C, 15 min & annealed: 770 °C, 45 min	Test started 20 h after reaching the targeted temperature	Pb	$C_O \approx 1 \times 10^{-11}$–$1 \times 10^{-7}$ wt%	300, 350, 400, 450	$\dot{\varepsilon} \approx 10^{-4}$ s^{-1} & $\dot{\varepsilon} \approx 10^{-6}$ s^{-1}	LME observed at 350 °C and 400 °C, but not at 450 °C; the most severe LME effect occurred at 350 °C; the LME crack growth rate at 350 °C was in the order of 10^{-6} m/s; SMIE† might occur at 300 °C	[448]
T91	Tensile; Three-point bending	Flat tapered and three-point bending specimens; one flat tapered specimen polished, all others ground	normalised: 1150 °C, 15 min & annealed: 770 °C, 45 min	Unknown	Pb	$C_O \approx 10^{-7}$–10^{-6} wt%	400	2×10^{-8}–2×10^{-4} m/s	The oxide layer remained intact even when the applied stress in a static mode was as high as 110% of the yield strength; the LME crack initiation necessitated the following conditions: T = 350–400 °C, stress > 680 MPa, plastic strain > 5%, and variable strain rate: $\dot{\varepsilon} \approx 10^{-4}$–$10^{-6}$ s^{-1}	[524]

Table 4.2 (*continued*)

Material	Test	Specimen shape, surface condition	Heat treatment and metallurgical state; irradiated state	Pre-exposure conditions	HLM	C_O in HLM	Temperature (°C)	Loading conditions (Strain rate/loading rate)	Remarks	Refs.
GESA†-treated/ untreated 9Cr-ODS†, 12Cr-ODS, 14Cr-ODS	Tensile	Cylindrical; unknown surface state	Unknown	Pre-exposure to low-oxygen LBE at 450 °C for at least 20 h	LBE	Low oxygen LBE	300, 350, 450	$\dot{\varepsilon} \approx 5 \times 10^{-5}$–$2.8 \times 10^{-4}$ s^{-1}	ODS steels are susceptible to LME regardless of the GESA† treatment; the GESA† process possibly enhanced LME susceptibility; 14Cr-ODS had the least LME susceptibility	[525]
Fe-13Cr martensitic steel	Tensile	Flat specimen; mechanically polished	Annealed: 1050 °C, 30 min	The steel surface was covered by Pb or LBE prior to testing	Pb, LBE	Oxygen partial pressure $< 5 \times 10^{-3}$ mm Hg	350–600	$\dot{\varepsilon} \approx 5 \times 10^{-4}$ s^{-1}	UTS† decreased by 10–20% compared to that in vacuum; steel susceptible to LME at 350–450 °C; LME was more severe in contact with LBE than Pb; the elongation reduction in liquid Pb was about 11% at 450℃, in contrast to 30% in liquid LBE at 350–400 °C	[510]
T91	SPT†	Thin disc specimens; first mechanically polished, then electropolished	All normalised at 1050 °C for 1 h & tempered for 1 h at 750 °C, 700 °C, 650 °C, 600 °C, or 500 °C	Unknown	LBE	No oxygen control	300	0.5 mm/min	Steel hardened by tempering at 500 °C and 600 °C showed most severe LME, evidenced by brittle fracture features and reduction in mechanical properties; increasing the tempering temperature to 750 °C, the brittle fracture became ductile	[526]
T91	SPT†	Thin disc specimens; mechanically polished	normalised: 1050 °C, 1 h & tempered: 750 °C, 1 h	Unknown	LBE	Oxygen saturation & low-oxygen	200–450	0.0005–0.5 mm/min	Low strain rate (loading speed), high temperature, and low oxygen concentration promoted LME; the strain rate was the most critical parameter in	[504,527]

Table 4.2 (*continued*)

Material	Test	Specimen shape, surface condition	Heat treatment and metallurgical state; irradiated state	Pre-exposure conditions	HLM	C_O in HLM	Temperature (°C)	Loading conditions (Strain rate/loading rate)	Remarks	Refs.
									determining the susceptibility of T91 to LME	
T91/316L welds	SPT[†]	Thin disc specimens; first mechanically polished, then electropolished	Welds prepared by EB welding; heat treatments: 316L: SA[†] at 1050 °C for 1 h T91: normalised at 1050 °C & tempered at 750 °C for 1 h	Unknown	LBE	No oxygen control	300, 380	0.5 mm/min	Reduction in ductility and formation of brittle cracks were observed in the welds tested in LBE	[528]
T91	SPT[†]	Flat discs	normalised: 1050 °C, 7 h & tempered: 750 °C	Native oxides first removed by ion beam etching, followed by re-oxidation for different times in an oxidising environment	LBE	Unknown	250, 300	Unknown	Some specimens were coated with LBE to achieve direct contact; apart from the direct contact, the type of oxide scales also affected greatly the steel susceptibility to LME, as different oxides had different wetting and diffusivity properties	[465]
T91	Three-point bending	Mechanically polished	All normalised at 1040 °C for 1 h; Tempering: 750 °C, 2 h; 600 °C, 2 h; 500 °C, 2 h	Unknown	LBE	< 1 wppm	200, 300, 400, 500	–	Steel subjected to tempering at the lowest temperature (500 °C) showed the most severe LME; steel *J*-values decreased by 20–50% in contact with liquid LBE as compared to air	[471]
T91	Creep	Cylindrical; ground	normalised: 1050 °C, 30 min & tempered: 770 °C, 1 h	LBE pre-exposure at 500 °C for 100 h	Flowing LBE ($v \approx 0.5$ m/s)	$C_O \approx 10^{-6}$ wt%	500	Uniaxial tensile loading	Compared to specimens tested in air, the creep strain rate of specimens tested in LBE increased by a factor of 53 & the creep lifetime decreased by a factor of 30–90	[515]
FeCrAlY-coated T91	Creep	Cylindrical; untreated surface	T91: normalised at 1050 °C, 30 min & tempered at 770 °C, 1 h	Unknown	Flowing LBE ($v \approx 0.5$ m/s)	$C_O \approx 10^{-6}$ wt%	500, 550	Uniaxial tensile loading	Due to the protection provided by the coating, no changes were observed in the creep properties of the T91 steel in	[513]

Table 4.2 (*continued*)

Material	Test	Specimen shape, surface condition	Heat treatment and metallurgical state; irradiated state	Pre-exposure conditions	HLM	C_O in HLM	Temperature (°C)	Loading conditions (Strain rate/loading rate)	Remarks	Refs.
									contact with liquid LBE	
T91	Creep	Mechanically polished	normalised: 1040 °C, 1 h & tempered: 760 °C, 1 h	LBE pre-exposure at 650 °C for 200 h	Pb	$C_O \approx 10^{-6}$ wt%	650	Uniaxial stress: 100–200 MPa	The creep properties of the T91 steel were not changed in liquid Pb; no dissolution corrosion and Pb penetration was observed	[512]
T92	Creep	Cylindrical	Normalised: 1060 °C, 1 h & tempered: 770 °C, 2 h	No pre-exposure	Pb	$C_O \approx 6 \times 10^{-7}$–$1.7 \times 10^{-6}$ wt%	650	Uniaxial stress: 75–325 MPa	The effect of liquid Pb on the creep properties of T92 was negligible	[514]
T91, T92, 9Cr-ODS, 14Cr-ODS, 12Cr-ODS	Creep	Cylindrical specimens; mechanically polished	T91: normalised at 1040 °C, 1 h & tempered at 760 °C, 1 h; P92: normalised at 1060 °C, 1 h & tempered at 770 °C, 2 h	No pre-exposure	Pb	$C_O \approx 10^{-6}$ wt%	650	Uniaxial stresses: 75–400 MPa	The creep properties of the 9Cr-ODS and 14Cr-ODS steels were slightly affected by liquid Pb	[511,516]
Manet II	Low-cycle fatigue	Cylindrical bar; mechanically polished	Unknown	Unknown	LBE	No oxygen control	260	Strain controlled; R = -1, f = 1 or 0.1 Hz	The fatigue life of Manet II in contact with LBE was reduced by 7 × in the worst case, as compared with that in air; only one crack formed along the length of the specimen, contrary to numerous cracks formed in the specimen tested in air	[477]
T91	Low-cycle fatigue	Cylindrical; electropolished	normalised: 1050 °C & tempered: 750 °C, 60 min	Unknown	LBE	No oxygen control	300	Strain controlled mode; R = -1, $\dot{\varepsilon} \approx 4 \times 10^{-3}$ s^{-1}	The fatigue life of T91 was remarkably reduced by LME; the fatigue crack propagation rate was highly accelerated; the fracture surface after testing in LBE was flat, while an inclination was seen in the specimen tested in air; much less cracks formed in LBE than in air; the results indicated that	[509,529]

(*continued on next page*)

Table 4.2 (*continued*)

Material	Test	Specimen shape, surface condition	Heat treatment and metallurgical state; irradiated state	Pre-exposure conditions	HLM	C_O in HLM	Temperature (°C)	Loading conditions (Strain rate/loading rate)	Remarks	Refs.
									LME modified the fatigue crack initiation mechanism	
T91	Low-cycle fatigue, creep-fatigue	Cylindrical; electropolished	Normalised: 1050 °C & tempered: 750 °C, 60 min	Pre-exposure to low-oxygen LBE at 600 °C for 613 h; Pre-exposure to oxygen-saturated LBE at 470 °C for 502 h	LBE	Oxygen saturation & low-oxygen LBE	300	Strain controlled mode; R = -1, $\dot{\varepsilon} \approx 4 \times 10^{-3}$ s^{-1}; 10 min tension hold for some tests	Pre-exposure to oxygen-rich LBE formed protective oxide scales, which did not affect the fatigue life; pre-exposure to low-oxygen LBE resulted in dissolution corrosion, which facilitated fatigue crack initiation; introducing 10 min tension hold deteriorated the fatigue resistance of T91 in contact with LBE	[482,495]
FeCrAlY-coated T91	Low-cycle fatigue	Cylindrical; unknown surface condition	normalised: 1050 °C & tempered: 770 °C	Pre-exposed to flowing ($v \approx 1.3$ m/s) LBE ($C_O \approx 10^{-6}$ wt%) at 550 °C for 100 h	LBE	No oxygen control	550	Strain controlled mode; R = -1, $f = 0.5$ Hz	Due to the protection by the FeCrAlY coating, no change in the fatigue life of the T91 steel in contact with liquid LBE was observed	[530]
Fe-13Cr martensitic steel	Low-cycle fatigue, cyclic bending	Flat specimens; polished	annealed: 1050 °C, 30 min	The surface was covered by Pb and LBE prior to fatigue testing	Pb, LBE	Oxygen partial pressure $< 5 \times 10^{-3}$ mm Hg.	200, 300, 350, 450	Strain controlled mode; $f = 0.5$ Hz	The fatigue life reduced substantially in the presence of both HLMs; the maximum life reduction could be two orders of magnitude lower than the one in vacuum; LBE-induced LME was more severe than that caused by liquid Pb	[510]
T91	Low-cycle fatigue	Cylindrical; mechanically polished	LBE pre-exposure at 400 °C for 20–24 h	LBE pre-exposure at 400 °C for 20–24 h	LBE	Oxygen saturation, moderate-oxygen LBE & low-oxygen LBE	350	Strain controlled mode; R = -1; $\dot{\varepsilon} \approx 6.2 \times 10^{-6}$–$4.5 \times 10^{-3}$ s^{-1}	The fatigue life of T91 was reduced by 10×; fatigue crack initiation was delayed under combined conditions	[502]

(*continued on next page*)

Table 4.2 (*continued*)

Material	Test	Specimen shape, surface condition	Heat treatment and metallurgical state; irradiated state	Pre-exposure conditions	HLM	C_O in HLM	Temperature (°C)	Loading conditions (Strain rate/loading rate)	Remarks	Refs.
									of high LBE oxygen concentration, small total strain ranges, and slow strain rates, leading to a limited fatigue life reduction by LME	
T91	Low-cycle fatigue	Cylindrical; mechanically polished	normalised: 1050 °C, 15 min & tempered: 770 °C, 45 min	LBE pre-exposure at 400 °C for 20–24 h	LBE	Low-oxygen LBE	160–450	Strain controlled mode; R = -1, $\dot{\varepsilon} \approx 4.5 \times 10^{-3}$ s^{-1}	The temperature dependence of T91 fatigue life in LBE showed a "fatigue life trough"; fractography revealed typical quasi-brittle features after testing in LBE at 160–450 °C, indicating that T91 could be embrittled at all tested temperatures and the "trough" was mainly associated with fatigue crack initiation	[500]
T91	Low-cycle fatigue	Cylindrical; mechanically polished	normalised: 1050 °C, 15 min & tempered: 770 °C, 45 min	LBE pre-exposure at 400 °C for 20–24 h	LBE	Oxygen saturation, moderate-oxygen LBE & low-oxygen LBE	350	Strain controlled mode; R = -1; $\dot{\varepsilon} \approx 4.5 \times 10^{-3}$ s^{-1}	Grain refinement occurred close to the crack tip of specimens tested in vacuum, contrary to the absence of grain refinement in specimens tested in liquid LBE; this indicates that LME reduces plasticity in the vicinity of the crack tip	[53,508]
T91	Low-cycle fatigue	Cylindrical; electropolished	normalised: 1050 °C, 15 min & tempered: 770 °C, 45 min	No pre-exposure	LBE	No oxygen control	350	Strain controlled mode; R = -1, $\dot{\varepsilon} \approx 4.0 \times 10^{-3}$ s^{-1}	Fatigue life in LBE was 2–10 × shorter than that in air; LBE accelerated the formation of long cracks by promoting the extension of the initially formed short cracks	[531]

(*continued on next page*)

Material	Test	Specimen shape, surface condition	metallurgical state; irradiated state	Pre-exposure conditions	HLM	C_O in HLM	Temperature (°C)	Loading conditions (Strain rate/loading rate)	Remarks	Refs.
T91	FCG† based on four-point bending	Notched specimens	normalised: 1050 °C, 1 h & tempered: 750 °C, 1 h; normalised 1050 °C, 1 h & tempered: 500 °C, 1 h	Unknown	LBE	Oxygen saturation	300	Pre-cracking in air; FCG† tests started from 5 MPa·m$^{1/2}$ at f = 5 Hz and R = 0.5 at 300 °C	The FCG† rate in the Paris regime was approximately 10 × higher in LBE than in air; the fracture surface showed mixed transgranular and intergranular cracking characteristics	[527]
T91	FCG†	1/2CT† specimens	austenitised at 1050 °C, hold time: 1 min/mm; annealed at 770 °C, hold time: 3 min/mm	Pre-cracking in air or LBE at 350 °C	LBE	$C_O \approx 2 \times 10^{-11}$–$7 \times 10^{-6}$ wt%	300	Two loading rates: 0.2 mm/min & 0.02 mm/min; extensometer not used to measure the COD†, measurements later corrected; R = 0.1; plane strain; f = 0.25 Hz	FCG† rate showed no obvious differences in oxygen-saturated LBE and air; decreasing the oxygen concentration from saturation to 4 × 10^{-7} wt% accelerated the FCG† rate by a factor of 10, while no changes were observed as oxygen concentration was further reduced; fractography typically showed transgranular cleavage fracture features	[58]
T91	Fracture toughness	CCT; Compact tension (CT), pre-cracking in LBE	normalised: 1050 °C, 1 h & tempered: 750 °C, 1 h	Pre-wetting by chemical flux for CCT† specimens; pre-exposure to low-oxygen LBE at 500 °C for 1000 h	LBE	Low-oxygen LBE (conditioned with flowing Ar + 5 %H_2)	300	7×10^{-8} m/s; 7×10^{-9} m/s	Fracture toughness values strongly depended on wetting conditions; specimens pre-wetted by chemical flux and *in situ* pre-cracked in LBE showed a significant reduction in fracture toughness; LME was more severe under plane-strain conditions than under plane-stress conditions	[470]

Table 4.2 (*continued*)

Material	Test	Specimen shape, surface condition	Heat treatment and metallurgical state; irradiated state	Pre-exposure conditions	HLM	C_O in HLM	Temperature (°C)	Loading conditions (Strain rate/loading rate)	Remarks	Refs.
T91	Fracture toughness	DCT†; pre-crack in air	normalised: 1100 °C, 15 min & tempered: 770 °C, 45 min	No pre-exposure	LBE	Oxygen saturation	200, 300	0.25 mm/min	Plane-strain fracture toughness of T91 reduced by 30% at 200 °C and 16% at 300 °C, sufficient ductility retained; fractography showed both cleavage fracture and dimples (ductile fracture)	[466,479]
T91	Fracture toughness	1/2CT† specimens	normalised: 1050 °C, 1 h & tempered: 770 °C, 45 min	Pre-cracking in air or LBE	LBE	$C_O \approx 10^{-11}$–10^{-8} wt %	350	Plane-strain conditions; 0.2 mm/min	Pre-cracking in LBE resulted in a much more severe reduction in fracture toughness (J_{IC}) as compared to that in air	[467]
T91	Fracture toughness	1/2CT specimens	normalised: 1050 °C & tempered: 770 °C, 45 min	LBE pre-exposure at 450 °C for 20 h	LBE	$C_O \approx 5 \times 10^{-12}$–$1.6 \times 10^{-4}$ wt%	355	0.2 mm/min	Fracture toughness reduced by 30% compared to that in air; it was suggested that fracture toughness of T91 steels tested in liquid LBE should be calculated as a J integral using the maximum load	[468]
T91	Fracture toughness	1/2CT† specimens	normalised: 1100 °C, 15 min & tempered: 770 °C, 45 min	Pre-cracking in LBE at 350 °C	LBE	Pre-cracking: $C_O \approx 10^{-11}$–10^{-7} wt%; testing: $C_O \approx 10^{-11}$–10^{-8} wt%	350, 200	0.0002–2 mm/min	The reduction of fracture toughness in LBE was larger at 350 °C than at 200 °C; the slower the loading rate, the smaller the fracture toughness; fractography showed a mixture of quasi-cleavage and dimples	[532]

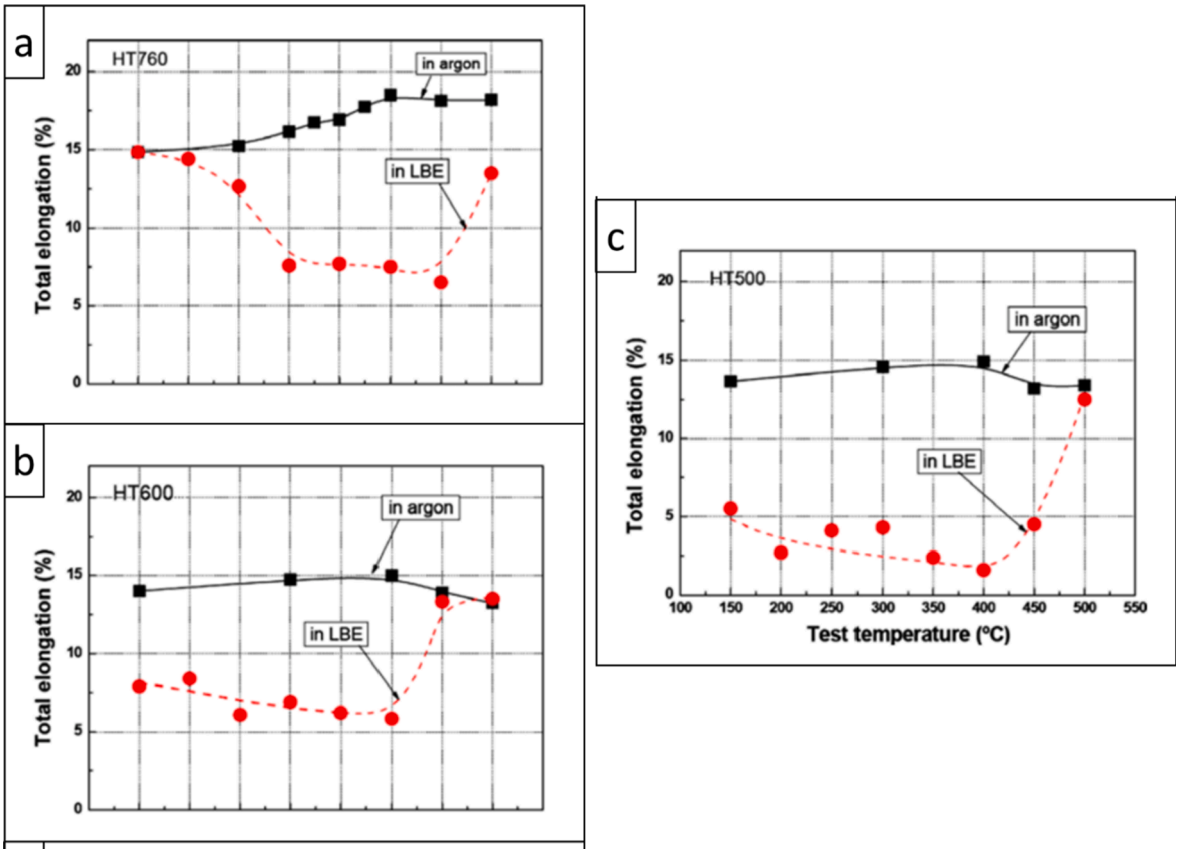

Fig. 4.15. Total elongation *vs.* testing temperature for (a) HT760, (b) HT600, and (c) HT500 (T91) F/M steels tested in Ar and liquid LBE (HT: tempering temperature). Adapted from [458].

metallurgical state, the determined "trough" varies from one study to another.

For a T91/Pb couple (T91 F/M steels in the hardened state), Nicaise et al. [457] discovered a "ductility trough" in the 350–500 °C range, based on tensile tests. The steel showed a strong LME sensitivity at 350 °C, while its ductility was fully recovered at 500 °C. Dai and Long et al. [447,458,471] have studied the LME susceptibility of T91 F/M steels as a function of the steel tempering temperature in the 160–500 °C range and in contact with oxygen-saturated liquid LBE, using slow strain rate tensile (SSRT) tests. Their results showed a clear "ductility trough", the shape of which depended on the steel tempering temperature (Fig. 4.15). For steels tempered at 760 °C (HT760), the LME susceptibility was severe in the 300–450 °C range, while more severe LME effects were observed when the tempering heat treatment was performed at 600 °C (HT600) and 500 °C (HT500), as evidenced by the existence of both wider and deeper "ductility troughs". A similar "ductility trough" was also observed in Si-enriched ferritic steels [251,501]. This also bears similarity with the findings of Abramov et al. regarding an Fe-12Cr-Mo ferritic steel in contact with liquid Pb [360]. T91 F/M steels with a higher strength obtained by steel tempering at relatively low temperatures were more susceptible to LME. This could be attributed to the mechanical effect of hardening on LME-induced crack propagation. Another possible effect of low-temperature tempering that favours LME, at least in T91 F/M steels, is the fact that it leads to intragranular carbide precipitation [458]. This would leave the GBs or martensite lath interfaces free of carbides, a potential crack arrester, an assumption supported by the TEM examination on an electron-transparent sample prepared by FIB lift-out technique [533]).

Hadjem-Hamouche et al. [306] observed in T91 F/M steels tempered at the standard temperature of 760 °C that the lower boundary of the "ductility trough" in liquid LBE was shifted from 300 °C (as reported in Ref. [458]) to 160 °C, based on crack propagation rate tests using CCT† specimens. This indicates that the lower boundary of the "ductility trough" is very close to the melting point of LBE ($T_m \approx 125$ °C). They also found that the stress-assisted dissolution model and thermally-activated ductility recovery mechanism failed to explain the temperature dependence of the maximum crack propagation rate, while a surface desorption process at high temperatures could be more suitable, as the activation energy of the latter was in agreement with *ab initio* calculation results [519].

Gong et al. [500] performed low-cycle fatigue tests of standard T91 F/M steels in the 160–450 °C range in low-oxygen LBE, and observed a "fatigue endurance trough" (Fig. 4.16), the lower and upper boundaries of which were similar to those reported for tensile tests in Refs. [447,458,471]. However, fractographic examinations showed that the fatigue fracture surfaces of the steel specimens tested at each temperature were covered by typical quasi-brittle fracture features (Fig. 4.17). No plasticity-induced grain refinement

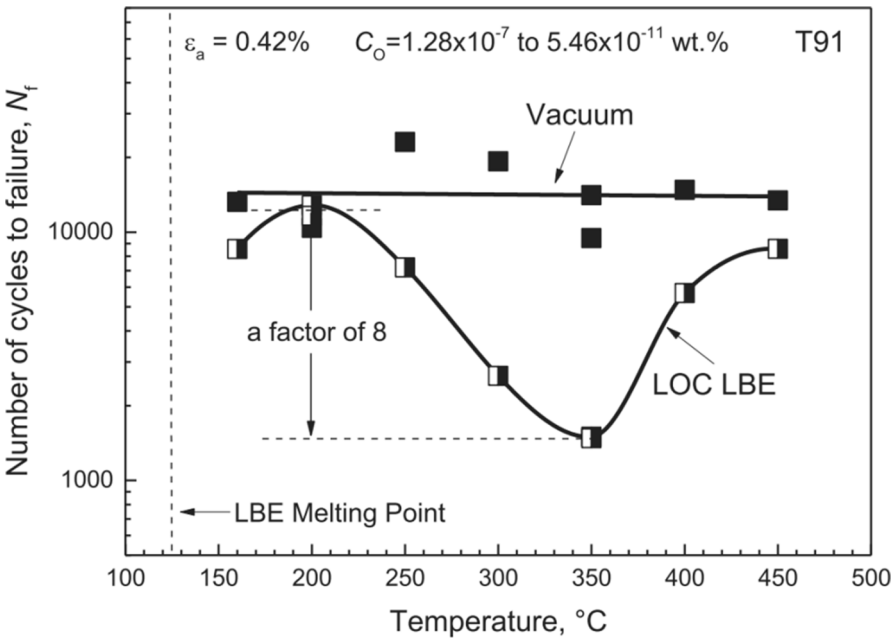

Fig. 4.16. Temperature dependence of the fatigue life of T91 F/M steels in vacuum and in liquid LBE with low-oxygen concentration (LOC) [500].

was observed around crack tips (Fig. 4.18), contrary to the presence of prevalent dimples and massive grain refinement in the specimens tested in vacuum. This interesting phenomenon has been recently confirmed at 350 °C by Vogt et al. [531]. These findings suggested that T91 F/M steels could be embrittled at any temperature in the 160–450 °C range during fatigue crack propagation. In other words, fatigue crack propagation in contact with liquid LBE did not depend strongly on the test temperature. The formation of a "fatigue endurance trough" is most likely associated with the fatigue crack initiation stage that is affected by LMC, wettability, and cyclic plastic deformation. It is worthwhile noticing that the temperature range of LME sensitivity for fatigue crack propagation in T91 F/M steels does not coincide with the temperature range of dynamic strain ageing (DSA) [534] that is often used to tentatively account for the "ductility trough" determined by tensile elongation data.

As far as the low-temperature side of the "ductility trough" or "fatigue endurance trough" is concerned, it is generally thought that the limited transport rate of liquid metal atoms to the crack tip may contribute to the much less affected elongation and fatigue life, as the liquid metal atoms cannot be rapidly supplied to the crack tip due to limited kinetics at low temperatures [282]. If this is the case, ductile features should prevail on the fracture surfaces of the specimens tested in liquid LBE at low temperatures. Apparently, this contradicts the observation of quasi-brittle features on the fracture surface of a specimen tested in low-oxygen liquid LBE at 160 °C (Fig. 4.17c and d). Therefore, the mechanism responsible for the low-temperature side of the "trough" is still unclear. It is also likely that the variation in the LME onset temperature is related to the different pre-exposure procedures from study to study. For the high-temperature side of the "trough", the ductility recovery induced by the onset of a significant mechanical softening may be principally responsible. Dissolution-induced crack blunting may also play a non-negligible role at high temperatures. Moreover, according to the work conducted by Hadjem-Hamouche et al. [306], the right side of the "trough" may be linked to the temperature dependence of desorption activity at crack tips. In other words, increasing the temperature facilitates the desorption of the liquid metal species, so that LME is inhibited. Weisenburger et al. [530] also observed weak changes in the fatigue life of T91 F/M steels in oxygen-saturated liquid LBE at 550 °C. This effect was attributed to ductility recovery at this high test temperature. Di Gabriele et al. [499] ascribed the absence of LME in T91 F/M steels tested at 500 °C to the severe oxidation of crack walls, which is promoted at high temperatures.

Ye et al. [504] studied the temperature effect on the LME susceptibility of T91 F/M steels exposed to liquid LBE using SPT† (Fig. 4.19a), and recorded the load *vs.* displacement curves to show the LBE effect (Fig. 4.19b). Their findings showed that, as the temperature increased, the fracture energy (represented by the area under the load–displacement curve) decreased linearly and, therefore, a "ductility trough" was not observed (Fig. 4.19c). Interestingly, brittle failure features were present on the fracture surfaces at every test temperature (Fig. 4.19d shows a specimen tested at 300 °C), indicating that LME could happen at any temperature in the 200–400 °C range under the SPT loading conditions. This finding is in agreement with the statement made by Gong et al. [500]. Particularly, LME seems to be promoted at higher temperatures, as a stronger reduction in fracture energy was observed at 400 °C when compared with lower test temperatures. This indicates that the LME susceptibility depends also on the loading conditions, since T91 F/M steels are more susceptible to LME under biaxial SPT loading conditions when compared to uniaxial tensile loading.

4.6.2. The role of strain rate

The strain rate is a key factor affecting the occurrence of LME, as the wetting of the steel surface or crack tip by the liquid LBE is, in general, time-dependent, when fresh surfaces are either exposed or created (e.g., upon crack propagation) during plastic deformation.

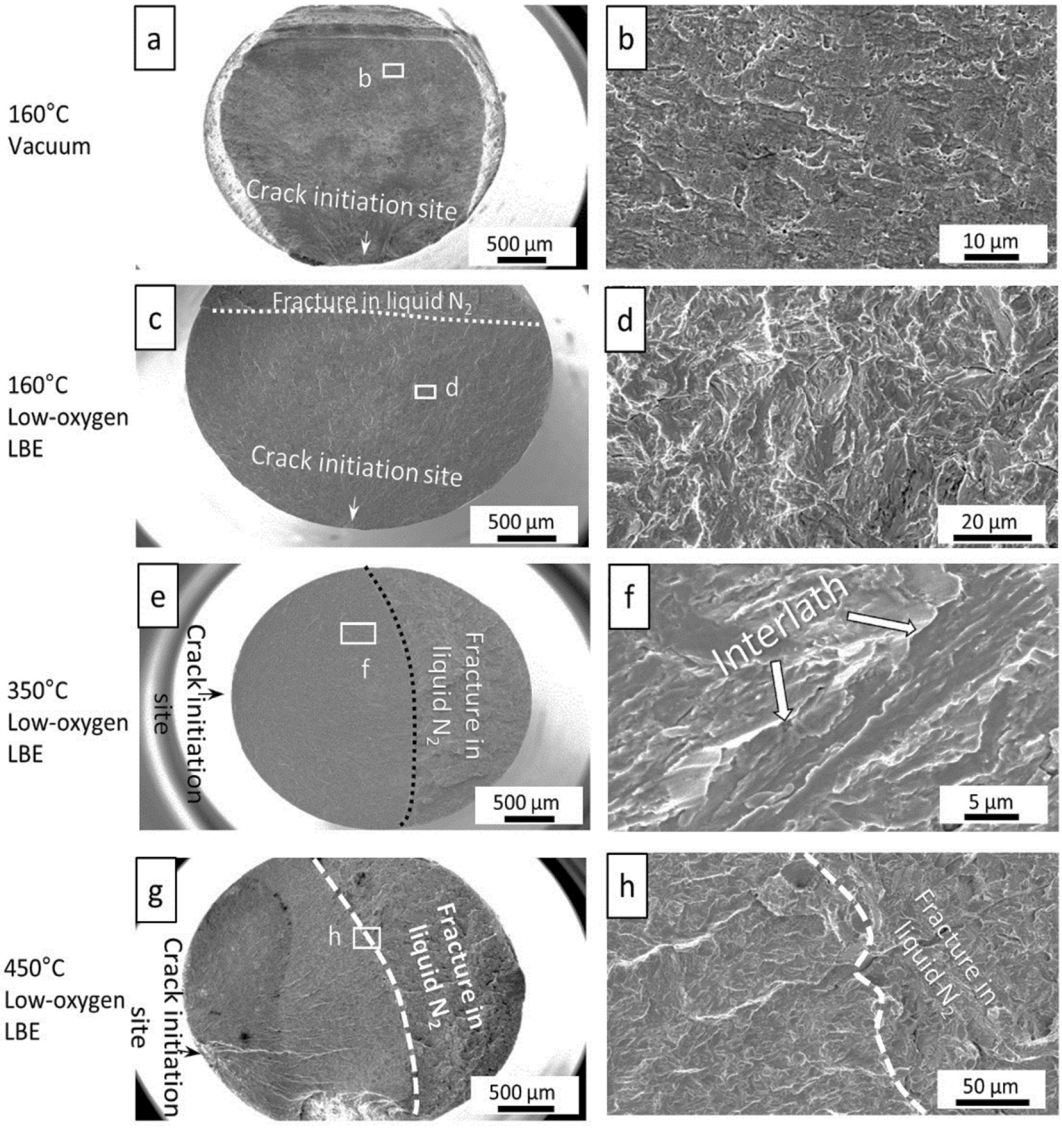

Fig. 4.17. SEM† images of T91 F/M steels tested in vacuum and low-oxygen liquid LBE: (a,b) vacuum, 160 °C, strain amplitude $\varepsilon_a = 0.40\%$; (c-d) low-oxygen LBE, 160 °C, $C_O \approx 3.8 \times 10^{-9}$ wt%, $\varepsilon_a = 0.43\%$; (e-f) low-oxygen LBE, 350 °C, $C_O \approx 3.26 \times 10^{-9}$ wt%, $\varepsilon_a = 0.42\%$; (g-h) low-oxygen LBE, 450 °C, $C_O \approx 3.8 \times 10^{-8}$ wt%, $\varepsilon_a = 0.43\%$. "Fracture in liquid N_2" means that the specimen was broken into two parts in liquid nitrogen (N_2) to enable SEM fractographic examination. Adapted from [500].

Slow strain rates provide more time for steel surfaces and crack tips to interact with liquid LBE, thereby promoting LME. On the other hand, the stability of the oxide scales is also affected by the applied strain rate, considering that minor oxide scale damage could potentially self-heal when sufficient time is provided for oxygen diffusion to the damaged areas. In addition, stress relaxation could also benefit from slow strain rates, which, in turn, may inhibit crack initiation. Under these circumstances, the occurrence of LME is decelerated. Therefore, the applied strain rate may have competing effects on the LME susceptibility of T91 F/M steels.

Hamouche-Hadjem et al. [478] have studied LME of T91 F/M steels exposed to liquid LBE at 160 °C under different strain (displacement) rates, using thin CCT† specimens to create plane-stress conditions. In order to improve wetting, a soft Zn soldering flux consisting of zinc chloride, ammonium chloride, and hydrochloric acid was used to remove the native oxides from the specimen surface, and the notch was pre-filled with liquid LBE. After testing, it was found that the T91 F/M steel was susceptible to LME in a wide range of displacement rates: low strain rates promoted the occurrence of LME and the formation of fracture features characteristic of brittle failure on the fracture surfaces. In contrast, at high displacement rates, ductile fracture started to prevail. The recovery of ductility at higher displacement rates was linked to sub-critical crack growth rate maxima competing with ductile fracture modes characterised by void nucleation, growth, and coalescence. Di Gabriele et al. [499] observed that at a higher strain rate ($\dot{\varepsilon} \approx 10^{-4}\ s^{-1}$), T91 F/M steels were more sensitive to crack nucleation, forming a larger number of brittle cracks on the fracture surface when compared to specimens of the same steels tested at a lower strain rate ($\dot{\varepsilon} \approx 10^{-6}\ s^{-1}$). However, at the lower applied strain rate, the steel

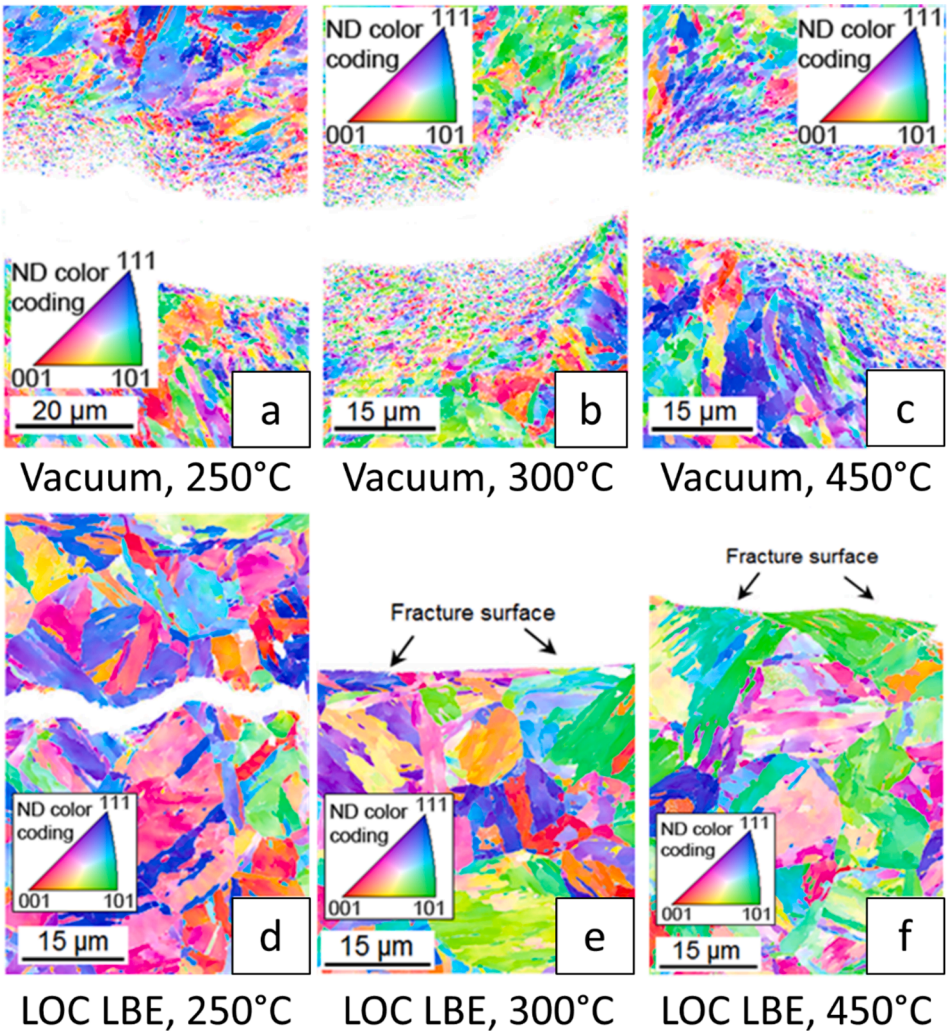

Fig. 4.18. EBSD† grain orientation maps in T91 F/M steels tested in vacuum at 250 °C, 300 °C, and 450 °C showing grain refinement along the crack wake, as opposed to testing in low-oxygen (LOC) liquid LBE at the same temperatures. Adapted from [500].

elongation to rupture was shorter, indicating a comparatively faster crack propagation process.

Ye et al. [504] found that regardless of the LBE oxygen concentration, the fracture energy of T91 F/M steels exposed to liquid LBE at 300 °C upon SPT† conditions was reduced with the displacement speed, which decreased in their study from 0.05 to 0.0005 mm/min, indicating an enhanced LME effect at the low strain rate. This may be attributed to the more extensive interactions between the liquid LBE and the steel surface at the slower strain rate. They also observed that both in oxygen-saturated and oxygen-poor liquid LBE, T91 F/M steels remained ductile at the highest displacement speed corresponding to a strain rate of $\dot{\varepsilon} \approx 5 \times 10^{-3}\ s^{-1}$. This led the authors to state that the most effective factor promoting LME was the applied strain rate.

The shape of the "ductility trough" was also reported to depend on the applied strain rate [501,535]. It was found by Liu et al. [501] that a slower strain rate resulted in a wider "trough" in a Si-enriched F/M steel. The lower and upper boundaries of the "trough" shifted towards the lower and higher temperatures, respectively. Gavrilov et al. [535] reported that at 350 °C and regardless of the environment (Ar + 5 %H_2 *vs.* liquid LBE), the total elongation of T91 F/M steels first decreased with increasing the strain rate from $\dot{\varepsilon} \approx 5 \times 10^{-7}\ s^{-1}$ to $\dot{\varepsilon} \approx 5 \times 10^{-5}\ s^{-1}$, and then increased with increasing the strain rate from $\dot{\varepsilon} \approx 5 \times 10^{-5}\ s^{-1}$ to $\dot{\varepsilon} \approx 5 \times 10^{-4}\ s^{-1}$ (Fig. 4.20). Fig. 4.20 also shows that increasing the applied strain rate shifted the bottom of "ductility trough" to the high-temperature domain. For instance, at $\dot{\varepsilon} \approx 5 \times 10^{-5}\ s^{-1}$, the strongest LME effect occurred at around 350 °C, while this temperature shifted to 400 °C when the applied strain rate increased to $\dot{\varepsilon} \approx 5 \times 10^{-4}\ s^{-1}$. While a clear explanation for this interesting phenomenon is still under debate, it should be mentioned that some features of the "ductility trough" obtained by tensile tests in liquid LBE bear similarity with the temperature dependence of DSA†. DSA is a phenomenon involving dislocation pinning/unpinning interactions with interstitial atoms (e.g., carbon, nitrogen, etc.) or substitutional steel alloying elements (possibly, Cr for Fe-Cr alloys [536]). DSA can occur in T91 F/M steels under certain applied strain rate and temperature ranges, causing reduction in steel ductility and increase in steel strength [534,536]. It is possible, therefore, that DSA is partly responsible for the minimum in the "ductility trough". At high applied strain

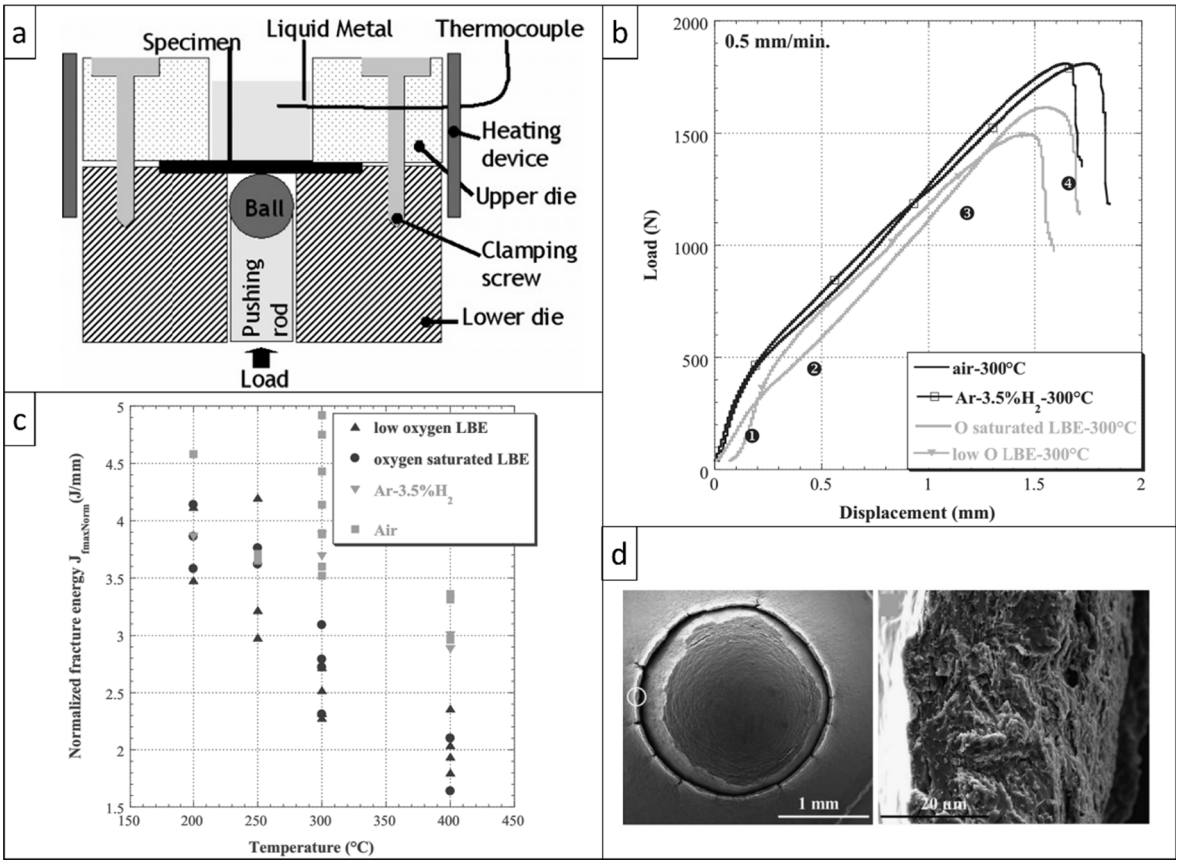

Fig. 4.19. (a) Schematic of an SPT† device. (b) Load *vs.* displacement curves obtained by SPT tests. (c) Fracture energy as a function of test temperature. (d) A typical fracture surface of a disc specimen fractured at 300 °C in liquid LBE upon SPT. Adapted from [504].

rates, the diffusion rates of the impurity atoms are not comparable with the dislocation motion rate, so they cannot catch up with the fast-moving dislocations. Under such conditions, higher temperatures activate diffusion of interstitial atoms, so that they can diffuse faster to the dislocation cores and trigger dislocation pinning/unpinning (i.e., DSA effect). The interplay of DSA with LME may explain why the bottom of the "ductility trough" moves to higher temperatures when the applied strain rate increases.

Fracture toughness tests on 1/2CT specimens of T91 F/M steels exposed to liquid LBE also showed a very strong displacement rate dependence of the LME effect, as reported by Ersoy et al. [532]. In this work, the authors showed that the fracture toughness (J_Q) changed from 42 to 116 KJ/m^2 when the displacement rate increased from 0.0002 to 2 mm/min. This suggests that a lower displacement rate allows the liquid LBE to wet better the crack tip, thereby promoting the LME effect.

In addition, the applied strain rate interplays with other factors, such as the applied strain and LBE oxygen concentration (Fig. 4.21). Gong et al. [502,537] performed strain-controlled fatigue tests under different LBE oxygen concentrations, strain rates, and total strain ranges. They found that at relatively high total strain ranges (i.e., $\Delta\varepsilon_t \approx 1.5$–$1.6\%$), the fatigue life did not depend strongly on the amount of dissolved oxygen in liquid LBE, while a significant effect of the LBE oxygen concentration was observed at relatively low total strain ranges (i.e., $\Delta\varepsilon_t \approx 0.80$–$0.85\%$). In particular, under the combined conditions of slow applied strain rate, low total strain range, and high LBE oxygen concentration, the fatigue specimen was not broken and its fatigue life was comparable to that in vacuum (Fig. 4.21a). SEM† and EDS† analyses showed that the almost unaffected fatigue life was attributed to the formation of thin, dense and presumably defect-free oxide scales that were not broken under the combined test conditions, thus protecting the steel surface from crack initiation (Fig. 4.21b). It was suggested that the formation of protective oxide scales was favoured by the specific employed test conditions: first, the low imposed total strain range was unable to damage or destroy the oxide scales as the stresses applied on the oxide scales were insufficient to impart oxide scale damage. Second, assuming the oxide scales were locally damaged, the other two test conditions (i.e., high LBE oxygen concentration and slow strain rate) could enable self-healing of the local oxide scale damage by providing sufficient oxygen and diffusion time. Hojná et al. [503] also found that the threshold stress necessary to initiate a crack in T91 F/M steels exposed to liquid LBE was strain rate-dependent, and it decreased as the strain rate increased.

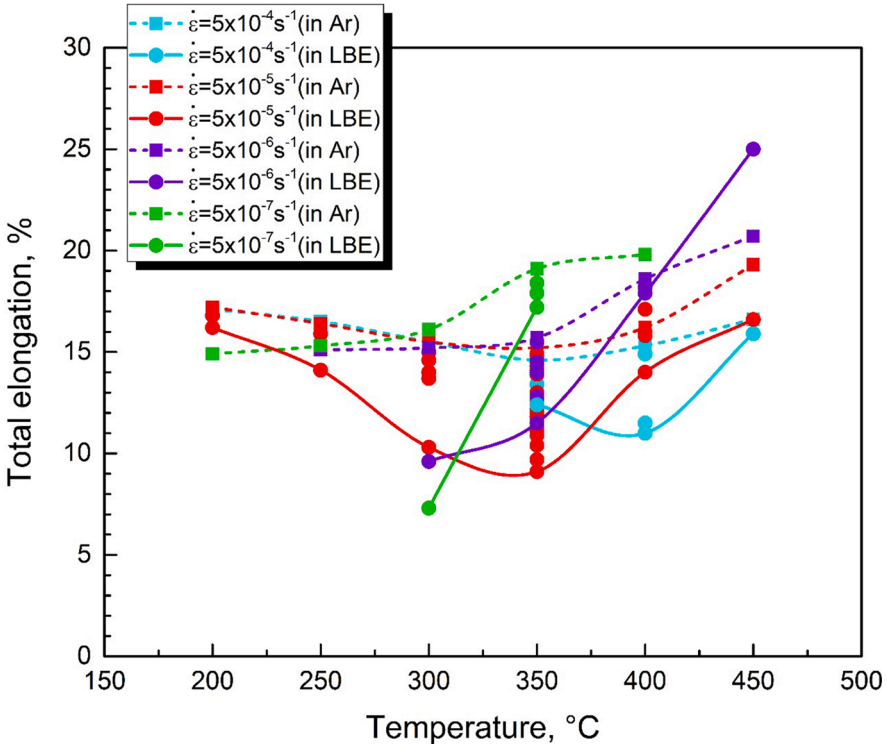

Fig. 4.20. Effect of the applied strain rate on the "ductility trough" of T91 F/M steels tested in liquid LBE; $\dot{\varepsilon}$ is the applied strain rate. Data from Ref. [535].

4.6.3. The role of mechanical constraint

The mechanical constraint affects greatly the LME intensity of T91 F/M steels. A plane-stress loading condition, achieved by testing a thin-sheet CCT† specimen geometry (1.5 mm-thick) resulted in a maximum reduction of the order of 30–50% in the determined J-R curve (Fig. 4.22) [470]. On the other hand, the effect of a plane-strain loading condition on the crack growth in T91 F/M steels exposed to liquid LBE was studied by Ersoy et al. [467], who used a 1/2CT† specimen geometry. That particular LME study demonstrated the need for a precise pre-cracking procedure of T91 F/M steels in low-oxygen liquid LBE. This pre-cracking procedure resulted in a dramatic decrease of the crack growth resistance at 350 °C (up to 87% drop), as can be seen in Fig. 4.23. Such a change can be explained by the higher triaxiality of the 1/2CT test, as compared to a CCT specimen geometry (plane-stress conditions). This indicates that the fracture mechanism is sensitive to the stress state (mechanical constraint).

4.6.4. The role of LBE oxygen concentration

As mentioned in Chapter 3, the LBE oxygen concentration must be closely controlled and maintained within a specific range to avoid steel dissolution corrosion at low concentrations and precipitation of solid PbO at high concentrations. Whether active oxygen control can also mitigate LME is an interesting question. It was reported in several studies that the impact of the dissolved oxygen concentration in liquid LBE/Pb on the LME sensitivity of T91 F/M steels was associated with the formation of oxide scales either during mechanical testing [493,502,504,517], or upon steel pre-oxidation before mechanical testing [538]. In oxygen-rich liquid LBE, the steel could form *in situ* typical double-layer oxide scales, composed of outer magnetite (Fe_3O_4) and inner FeCr-spinel. These oxides can prevent crack initiation as long as they remain intact, thereby preventing the intimate contact of liquid LBE with the base steel, which implies that preventing the wetting of the steel by the HLM is key. For example, Van den Bosch et al. [493] performed tensile tests on polished T91 F/M steel specimens in liquid LBE at different temperatures and applied strain rates. Their results did not show LME at any test condition, even for neutron-irradiated steel specimens. This was later attributed to the unsuccessful control of the LBE oxygen content, i.e., the liquid LBE was saturated in oxygen, forming protective oxide scales on the steel surface that prevented LME.

On the other hand, the protection disappears once the oxide scales are damaged as a result of the application of high stresses/strains on the steel surface. A strong LBE oxygen effect was observed by Ye et al. [504], who used SPT† to test T91 F/M steels (Fig. 4.24). Testing was done in oxygen-poor and oxygen-saturated liquid LBE at 300 °C. Their results showed that at all the imposed displacement speeds, the fracture energy of T91 F/M steels was higher in oxygen-saturated liquid LBE than in oxygen-poor liquid LBE, indicating a stronger LME effect when the LBE oxygen concentration decreased.

The conclusion that high LBE oxygen concentrations tend to mitigate LME is also supported by the studies of Verleene et al. [509] and Gong et al. [502], as shown in Fig. 4.25. Both works reported that in oxygen-saturated liquid LBE, the fatigue life at high total strain ranges (twice the strain amplitude) was up to ten times shorter than that in air or vacuum. As the total strain range decreased, the

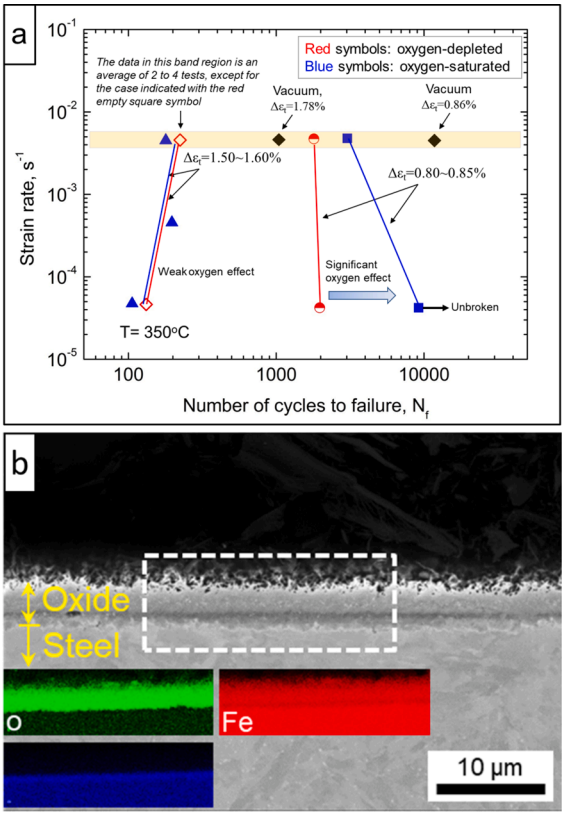

Fig. 4.21. (a) Influence of LBE oxygen concentration, applied strain rate, and total strain range on the fatigue life of T91 F/M steels tested in vacuum and liquid LBE, showing a strong effect of the LBE oxygen concentration at the relatively low total strain ranges. In particular, the fatigue life was comparable to that in vacuum under the combined test conditions of oxygen saturation, slow strain rate (i.e., $\dot{\varepsilon} \approx 4.5 \times 10^{-5}\ s^{-1}$), and low total strain range (i.e., $\Delta\varepsilon_t \approx 0.84\%$). (b) SEM† micrograph and EDS† mapping showing typical duplex oxide scales made of inner FeCr-spinel and outer magnetite (Fe_3O_4) on the surface of the unbroken specimen in (a). Adapted from [502,537].

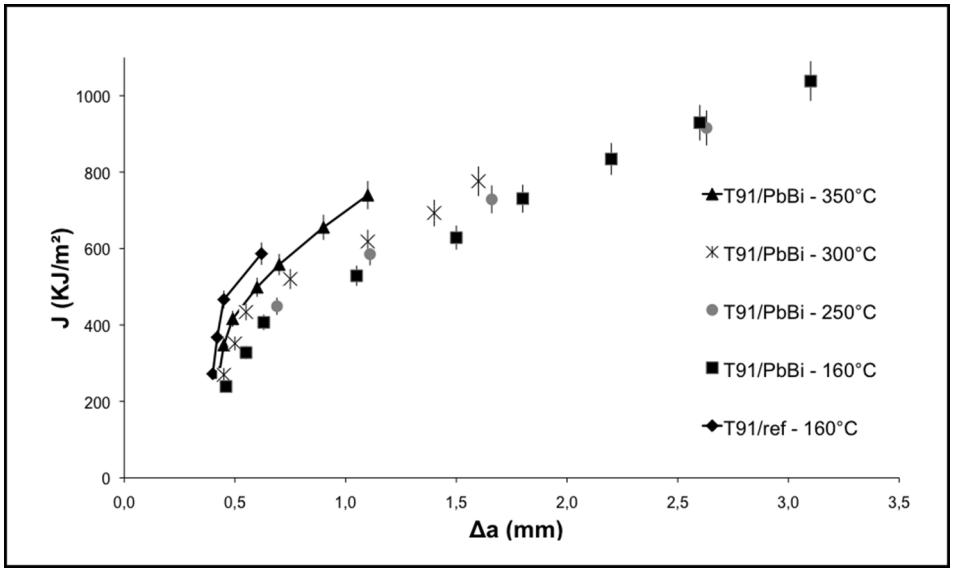

Fig. 4.22. J-R curves for T91 F/M steels exposed to liquid LBE under plane-stress loading conditions, using a CCT† specimen geometry [470].

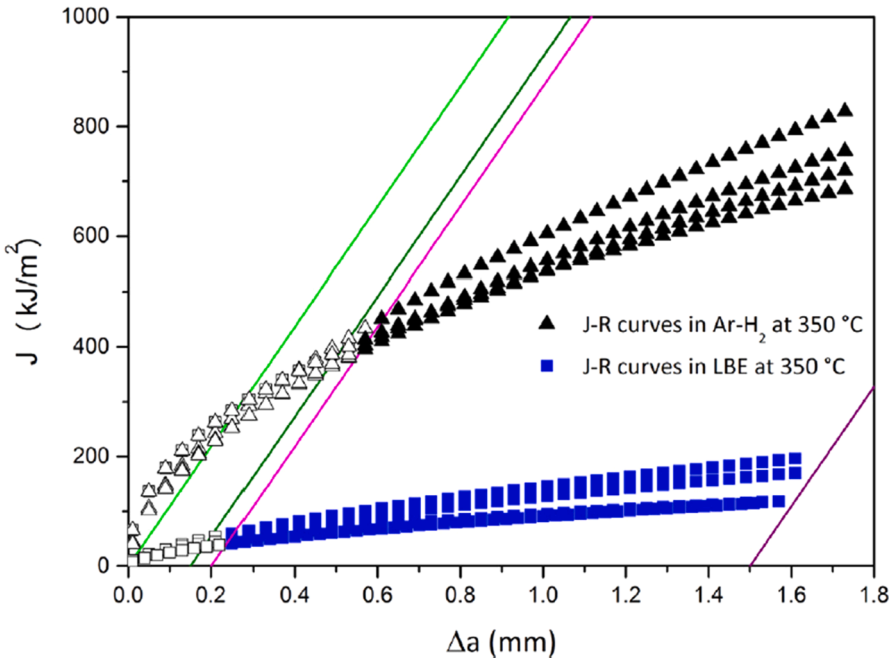

Fig. 4.23. J-R curves for T91 F/M steels in contact with liquid LBE loaded under plane-strain loading conditions, using a 1/2CT† specimen geometry [467].

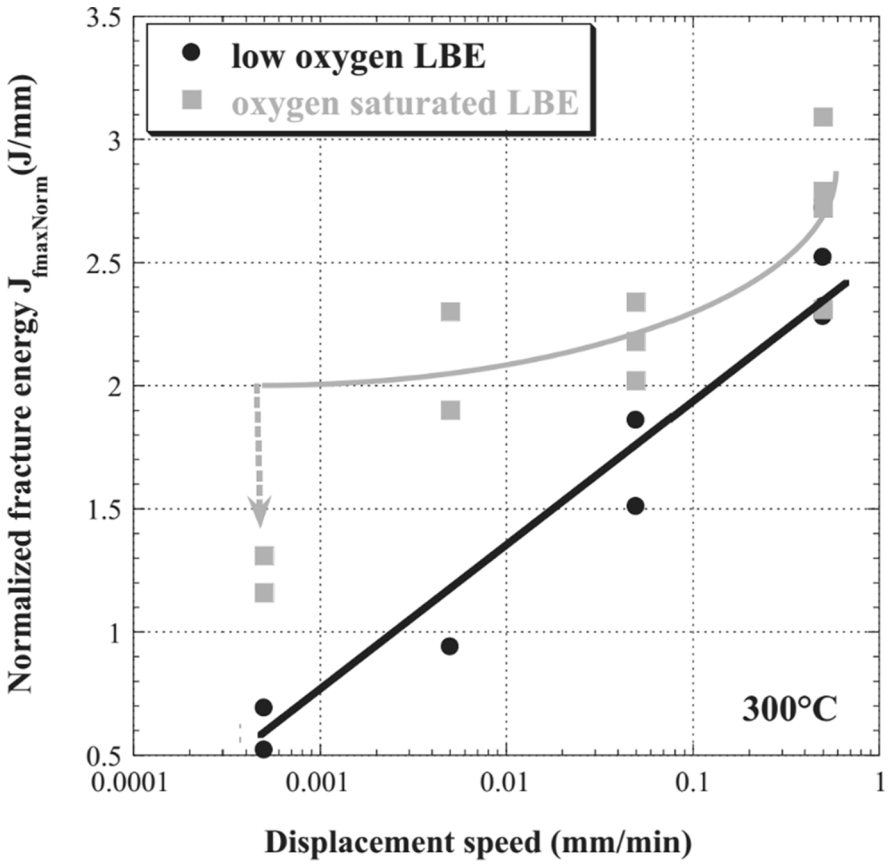

Fig. 4.24. Normalised fracture energy at F_{max} as a function of the displacement speed and the LBE environment in terms of the dissolved oxygen concentration (SPT† at 300 °C) [504].

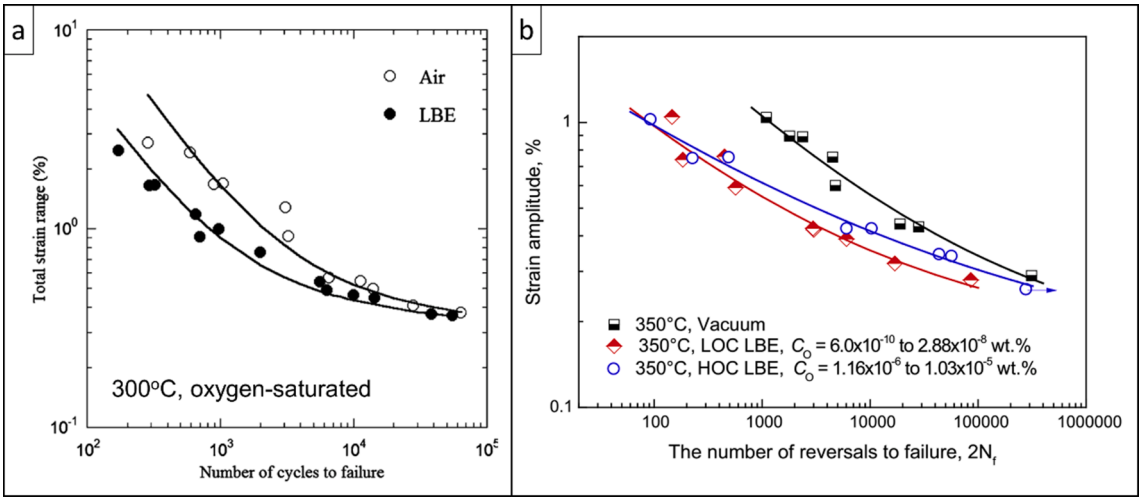

Fig. 4.25. Fatigue life of T91 F/M steels *vs.* strain range or strain amplitude. Adapted from [502,509].

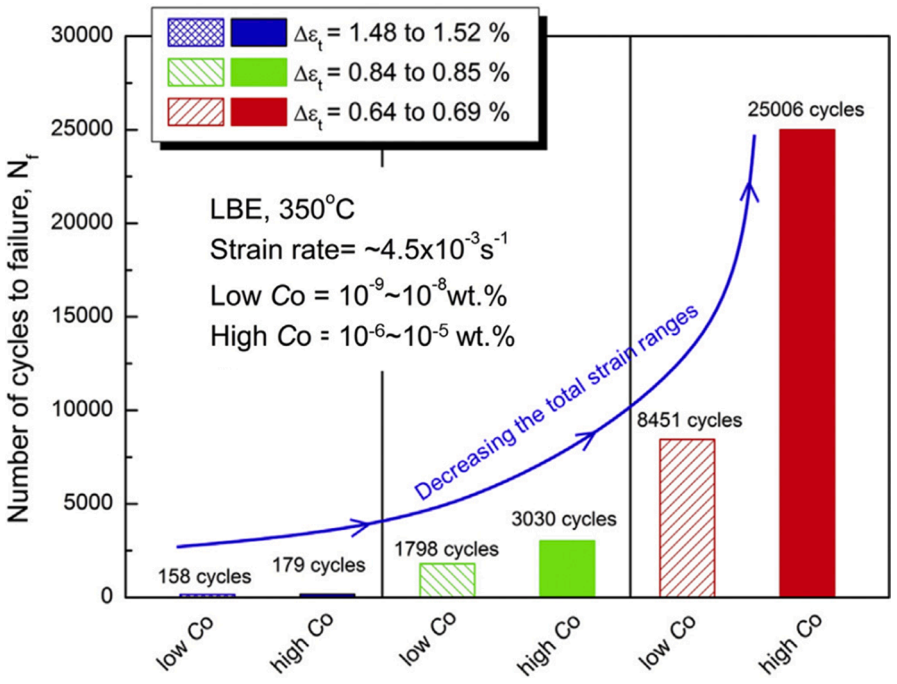

Fig. 4.26. Effect of LBE dissolved oxygen concentration on the fatigue life of T91 F/M steels tested in oxygen-rich ($C_O \approx 10^{-6}$–10^{-5} wt%) and oxygen-poor ($C_O \approx 10^{-9}$–10^{-8} wt%) liquid LBE at 350 °C, showing that the fatigue life was longer in high-oxygen liquid LBE than in low-oxygen liquid LBE, esp. at relatively low total strain ranges, e.g., $\Delta\varepsilon_t \approx 0.64$–$0.69\%$ [537].

fatigue life was reduced accordingly, and finally there were no obvious differences for both environments. However, in oxygen-poor liquid LBE, even at low total strain ranges, the fatigue life remained shorter than that in air. Fig. 4.26 shows the combined effect of the total strain range and the LBE oxygen concentration on the fatigue life of T91 F/M steels. These results indicate that at low total strain ranges, high LBE oxygen contents could inhibit LME. Since the low-cycle fatigue lifetime represents mainly the lifetime of the crack initiation stage, the effect of the LBE oxygen concentration at low total strain ranges might be associated with the presence of oxide scales that could delay fatigue crack initiation. On the other hand, during the crack propagation stage, the LBE oxygen concentration was found to have no obvious impact on the crack propagation rate that was determined from the spacing of fatigue striations on the fracture surface (Fig. 4.27), assuming there was no crack-closure effect during crack propagation. This may be due to the fact that crack propagation is too fast to allow the formation of protective oxide scales at the crack tip. Even if oxide scales could form, they would be easily broken due to the enhanced stress concentration at the crack tip.

A more recent work performed by Gong et al. [537] reported that the oxygen content did not change the basic trend of the

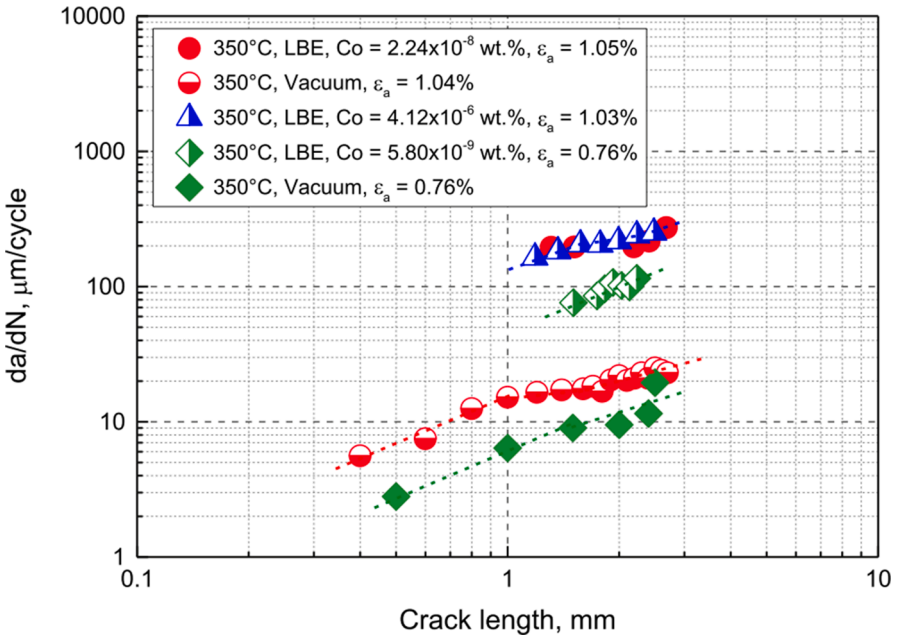

Fig. 4.27. Low-cycle fatigue crack propagation rates (da/dN) for T91 F/M steels in vacuum, oxygen-rich ($C_O \approx 4.12 \times 10^{-6}$ wt%) and oxygen-poor ($C_O \approx 5.80 \times 10^{-9}$–$2.24 \times 10^{-8}$ wt%) liquid LBE at 350 °C. The da/dN data were obtained from the fractographic examination of fatigue striations, where the space between two neighbouring striations corresponds to one cycle, assuming that there is no crack-closure effect [508].

temperature dependence of the fatigue life of T91 F/M steels exposed to liquid LBE, but an oxygen-rich condition increased, to a certain extent, the fatigue life as compared to an oxygen-poor condition. In particular, the authors found that there were no obvious differences observed during the fractography of specimens fractured under high-oxygen and low-oxygen LBE conditions. This suggests that the concentration of dissolved oxygen in liquid LBE may have no strong impact on fatigue crack propagation, while it affects significantly fatigue crack nucleation.

It is also possible to have an inhomogeneous oxygen distribution in liquid LBE, which accounts partly for the observed scatter in fatigue test data. Vogt et al. [539] have attributed the observed scatter in fatigue results to an uneven oxygen distribution at intrusion and crack tips.

4.6.5. The role of pre-exposure

The aim of steel pre-exposure in liquid LBE/Pb (static or dynamic conditions) is to mimic the potential evolution of the protective native oxide scale in the HLM environment. Since the environmental degradation of the unprotected steel by native oxides depends on the LMC resistance of the steel bulk (as defined by the steel chemical composition, microstructure and thermomechanical state) during the pre-exposure treatment, one may consider the pre-exposure as a particular type II factor affecting LME. Pre-exposing a steel specimen to liquid Pb/LBE at high temperatures can have two possible outcomes: when the pre-exposure is performed in low-oxygen LBE, the native oxides are likely to be damaged by dissolution/reduction and mild corrosion effects (depending on the pre-exposure duration) may occur on the steel surface. In this case, wettability is greatly improved and the LME effect is promoted. As liquid LBE is more corrosive than liquid Pb due to higher solubility of most elements in Bi, a pre-exposure duration of a few hours (depending on the exposure temperature) in contact with liquid LBE is considered enough to deoxidise the surface. On the other hand, pre-exposure to oxygen-rich LBE might form thick oxide layers on the steel surface that prevent wetting. Identifying the appropriate pre-exposure conditions, in terms of HLM oxygen concentration, temperature and duration, is imperative prior to mechanical testing (tensile, fatigue, or fracture toughness) that aims at assessing LME sensitivity, so as to conduct directly comparable tests that are capable of producing reproducible results.

Pre-exposure of steel samples in flowing liquid LBE, employing forced convection loops equipped with tensile testing capabilities was initially employed [216,462,463]. The tested steels included Manet II (a 10Cr-0.5Mo steel) and T91 F/M steels, all in normal tempering conditions. A sensitivity to LME in liquid LBE at 300 °C after 2 h of pre-exposure was found for Manet II in unmonitored oxygen concentration conditions [462] and for T91 F/M steels after 1500 h of pre-exposure to low-oxygen LBE ($C_O \approx 10^{-10}$–10^{-8} wt% was achieved by adding 10 wppm of magnesium, Mg) [216]. The required test facilities were quite large, but reproduced true operational conditions; unfortunately, they were dismantled, hampering further work.

Vogt et al. [231,482,495,540] studied the effect of pre-exposure on the low-cycle fatigue life of T91 F/M steels in contact with liquid LBE with two different oxygen contents at 300 °C. Their results showed that the steel fatigue life was significantly decreased by its pre-exposure to reducing liquid LBE ($C_O < 10^{-10}$ wt%) at 600 °C for 613 h, while the fatigue life was almost unchanged when the pre-exposure was performed in oxygen-saturated liquid LBE at 470 °C for 502 h (Fig. 4.28). This difference can be attributed to the

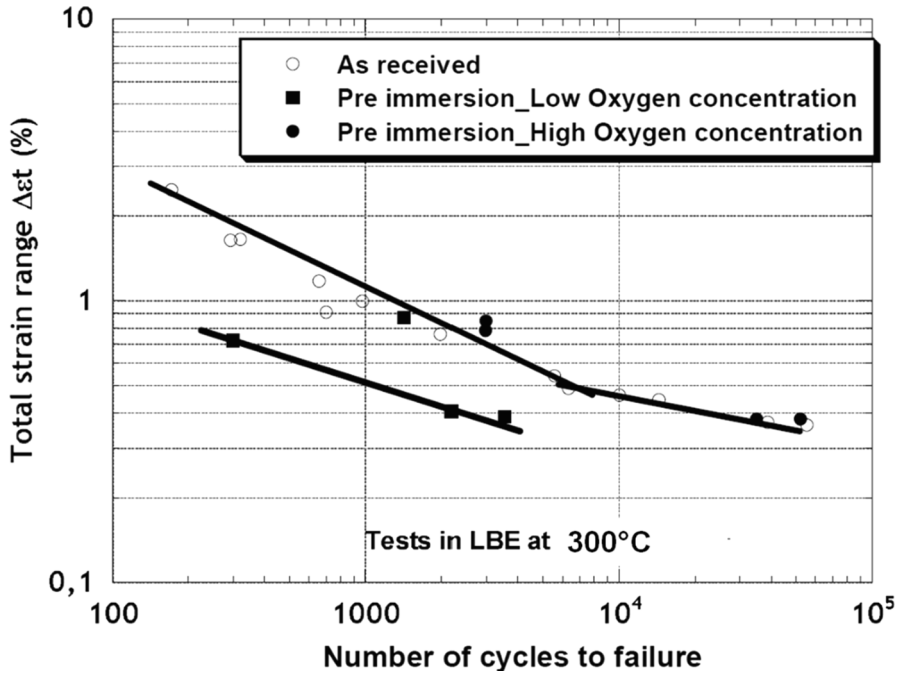

Fig. 4.28. Effect of pre-exposure to liquid LBE, under reducing or oxidising conditions, on the fatigue life of T91 F/M steels tested in liquid LBE and air at 300 °C [231,482,495,540].

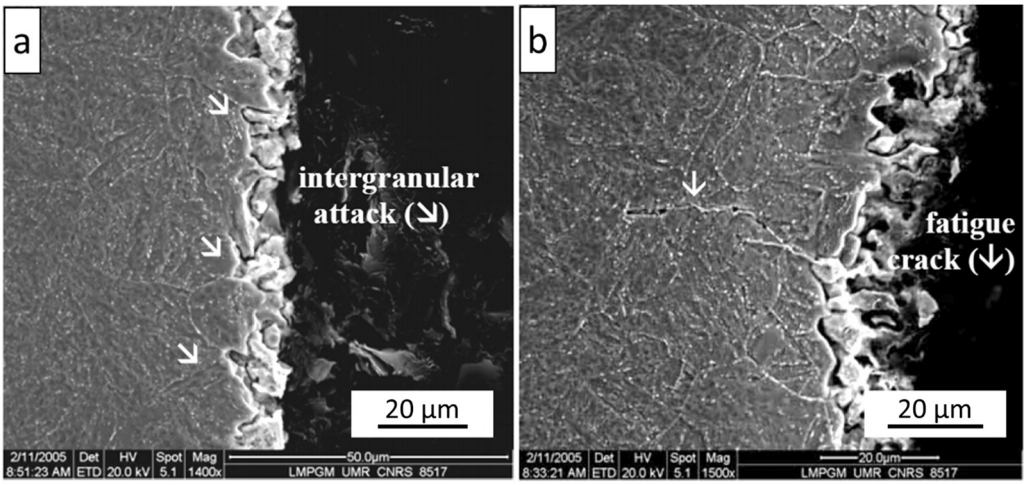

Fig. 4.29. SEM† images of T91 F/M steels after pre-exposure to oxygen-poor ($C_O < 10^{-10}$ wt%) liquid LBE at 600 °C for 613 h: (a) before fatigue testing, (b) after fatigue rupture in liquid LBE at 300 °C and $\Delta\varepsilon_t = 2.2\%$. Adapted from [231,495,540].

different consequences of the steel pre-exposure. In the case of pre-exposure to low-oxygen liquid LBE, intergranular dissolution corrosion occurred; in fact, intergranular LBE penetration allowed short cracks to form at the GBs, which actually shortened or eliminated the crack nucleation stage (Fig. 4.29). By contrast, the pre-exposure to the oxygen-saturated liquid LBE led to the formation of protective oxide films that delayed the fatigue crack nucleation (Fig. 4.30).

Gamaoun et al. [541] reported that the long-term (1 month) pre-exposure of T91 F/M steels to liquid Pb (with an oxygen activity between $\log(a_0) = -13$ and $\log(a_0) = -16$) at 525 °C led to the formation of vacancies and small cavities close to the steel surface, a mechanism favouring crack nucleation.

Pre-exposure was also observed to strongly affect the crack propagation rate in T91 F/M steels exposed to liquid LBE. Hojná et al. [520] pre-exposed steel specimens to flowing liquid LBE at 500 °C for 1000 h. The LBE oxygen concentration was $C_O < 10^{-6}$ wt% and the flow rate was $v \approx 1$ cm/s. After the pre-exposure treatment, the specimens were first pre-cracked in liquid LBE, followed by tensile testing. Their results showed that the crack propagation rate of the specimens that were pre-exposed to liquid LBE was 30 times higher than that in air. They attributed this strong LME effect to the localised failure and lack of self-healing of the oxide scales under the

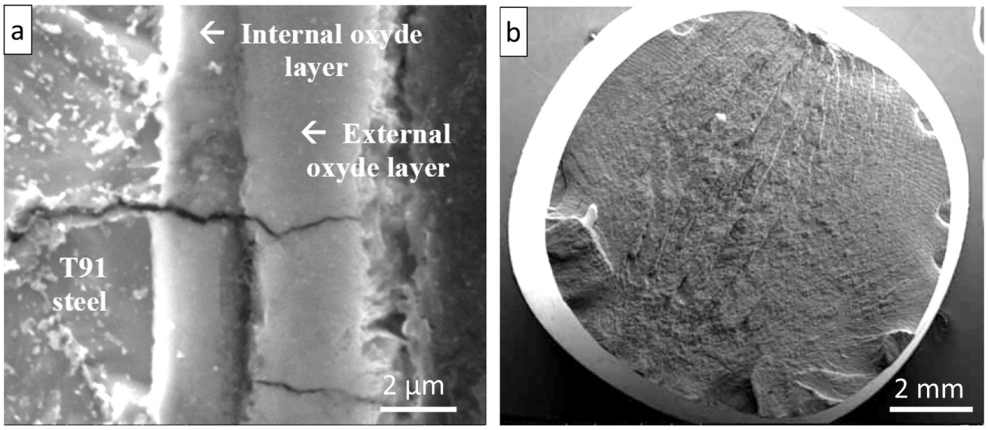

Fig. 4.30. SEM† images of T91 F/M steels after pre-exposure to oxygen-saturated liquid LBE at 470 °C for 502 h and fatigue testing in liquid LBE at 300 °C and $\Delta\varepsilon_t = 0.4\%$. Cross-section (a) and fracture surface (b). Adapted from [231,495,540].

specific exposure conditions.

4.6.6. The role of the steel metallurgical state

Increasing the hardness of T91 F/M steels by tempering at relatively low temperatures, e.g., 500 °C or 600 °C, instead of the standard tempering at ~760 °C, has been shown to strongly promote the steel LME susceptibility to liquid Pb/LBE, particularly in the presence of stress concentrators, such as notches [456,457,471,506,519,526,527]. During steel tempering, interstitial atoms, such as carbon, precipitate from the supersaturated matrix to form carbides at the martensitic lath boundaries. With the decrease of the tempering temperature, the quantity of C atoms that can precipitate at GBs decreases. Indeed, after a sufficiently low-temperature tempering heat treatment, dislocations that formed during the martensitic transformation serve as nucleation sites to nanoscale intragranular carbide precipitates instead of forming interlath carbides [458,459]. The dislocations are pinned at the carbides and annealing does not decrease the steel hardness very efficiently. This leads to the purification of carbides at GBs or martensite lath interfaces and, thus, the amount of carbides serving as a potential crack arrester decreases [533]. In other words, the lower the tempering temperature, the fewer the interlath boundaries decorated with $M_{23}C_6$ carbides. As a result, it might be easier to initiate interlath cracks in steel specimens tempered at lower temperatures. This microstructural change, combined with the large increase in steel hardness and the enhanced difficulty to activate the competing ductile fracture mechanism, favours the occurrence of LME.

In addition, similar T91/T91 joining or dissimilar T91/316L joining by TIG (tungsten inert gas) or EB (electron beam) modified the steel chemical composition and microstructure at the welds. In particular, an increased weld hardness was invariably reported. This resulted in severe embrittlement of the welds when they were mechanically tested in liquid LBE [521,528].

Significant research remains to be carried out in this area; for example, one could study the effect of varying the average size of the prior-austenite grains, which is typically 20–25 µm for thin steel sheets subjected to a standard heat treatment, 50–100 µm for thick components, and up to several hundred microns for high austenitisation temperatures combined with ausforming [542]. The effect of grain size refinement on LME has not been thoroughly investigated; such a study would require the reduction of the block/lath average size by means of an appropriate thermomechanical treatment [543].

4.6.7. The role of irradiation

In the context of Gen-IV LFRs or spallation neutron sources, the structural materials will be irradiated either by fast neutrons or by a mixed spectrum of fast proton/neutrons, notably for the beam window. Materials exposed to neutrons are subjected to displacement damage, leading to the formation of copious amounts of defects, such as vacancies, interstitial atoms, dislocation loops, etc. [544]. These defects can act as effective obstacles to dislocation motion, thereby limiting plastic flow. The main effect of irradiation at temperatures <400 °C on the steel mechanical properties is a rapid (within a few dpa) hardening combined with a large increase in yield stress for most conventional steels [545]. This is associated with a significant decrease in tensile elongation. The small-scale plasticity of irradiated steels is also profoundly modified with plastic shear localisation at the mesoscopic scale, such as the development of surface steps induced by spatially well-separated slip bands on the surface and slip channelling in the bulk. With further irradiation, concerns about embrittlement, swelling, or creep arise [544]. Moreover, proton irradiation at sufficient energies produces spallation impurities (H, He, Mn, Ti, V, Ca) from steel alloying elements that can be a major source of microstructural changes by impurity segregation [546]. Irradiation is, therefore, a major cause of steel bulk property modification that might drastically change the steel susceptibility to LME. As these changes affect the steel bulk, this is another type II factor (effect of microstructural change on LME).

While the LME of standard and heat-treated T91 F/M steels has been established (see Section 4.4), it has been reported in several studies [45,493,496–498,535,547,548] that LME can be greatly intensified by irradiation, resulting in a much more severe reduction in tensile elongation and fracture toughness as compared to the non-irradiated condition. Working with irradiated materials introduces

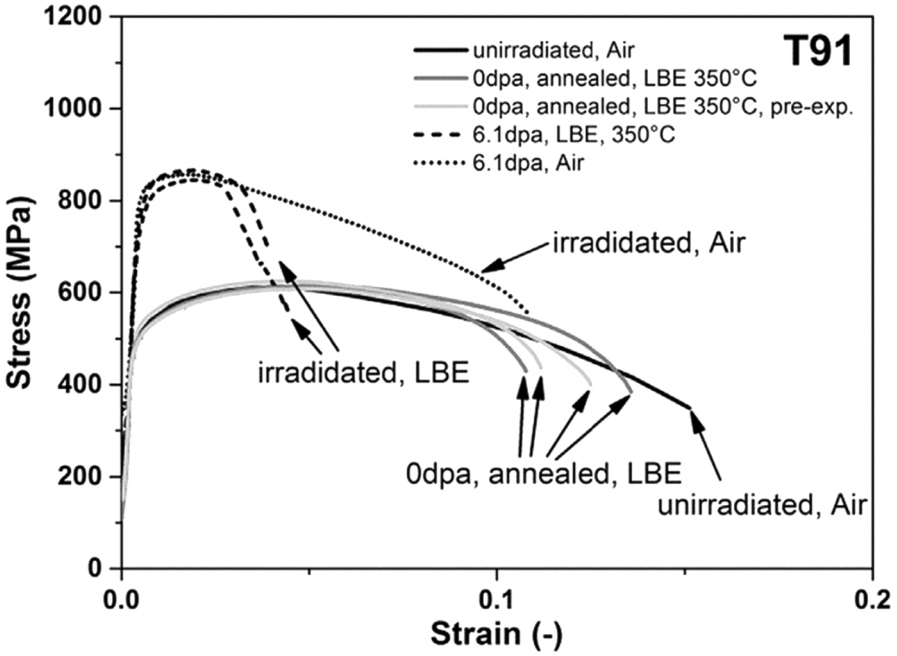

Fig. 4.31. Comparison of stress–strain curves of irradiated and non-irradiated T91 F/M steels tested in tension in both air and liquid LBE [45].

a high level of experimental complexity, making the correct accomplishment of various key tasks a "tour de force". The main challenge is to ensure good wetting of the steel by the HLM, as this review demonstrated that wetting of the metal surface is the strongest factor affecting LME. For practical purposes, surface preparation techniques (e.g., pre-tinning) are excluded, however, steel pre-exposure in well-controlled conditions can be performed in hot cells, on the condition that adequate shielding is provided and radioactive contamination is contained. For instance, Stergar et al. [45] exposed T91 F/M steel specimens to fast neutrons up to 6.1 dpa, and then tested specimens in air and liquid LBE at 350 °C. They observed a much more pronounced reduction in total elongation as compared to non-irradiated specimens tested in liquid LBE, indicating an intensified LME effect (Fig. 4.31). In addition, irradiation appeared to improve wetting, thereby enhancing LME, as stated by Van den Bosch et al. [498].

4.7. Crack initiation/propagation in T91 F/M steels in liquid Pb/LBE

The parametric studies reviewed in Section 4.6 demonstrate that T91 and similar F/M steels are susceptible to liquid Pb/LBE-induced embrittlement. The magnitude of LME susceptibility is crack initiation-controlled, considering that once cracks are initiated, they will propagate into the steel bulk as fast as several tens of micrometres per second [473,520,527]. However, crack initiation takes place at a microscopic length, making it difficult to properly understand the LME mechanism. By contrast, the history of crack propagation is often possible to read on the fracture surface, while its detailed study might demand the use of many characterisation techniques (e.g., LOM†, SEM†, EBSD†, etc.). Therefore, crack propagation in the presence of LME has been better understood than crack initiation to date. In this section, the mechanism regarding the influence of LME on the crack initiation and propagation in T91 F/M steels exposed to liquid Pb/LBE is reviewed.

4.7.1. Crack initiation stage

In an inert environment, crack initiation in ductile materials, such as T91 F/M steels, could preferentially take place at pre-existing imperfections on the steel surface. These imperfections include surface roughness, notches, microcracks, etc., which act as stress raisers resulting in inhomogeneous and localised plastic deformation [549]. This is especially true for low-cycle fatigue tests. On the other hand, crack initiation could also occur inside the steel bulk via void nucleation and coalescence. This is an important failure mechanism under tensile loading.

When exposed to a corrosive environment, such as liquid Pb or LBE, the crack initiation mechanism could be altered by the effects of the liquid metal on the steel surface. For tensile testing, HLM-induced crack initiation at the steel surface competes with void nucleation and coalescence that cause crack nucleation in the steel bulk. If the protective oxide scales are damaged in service, thereby allowing the atomic-scale intimate contact between HLM and steel, crack initiation starting at the steel surface will likely occur before the ductile crack nucleation processes start in the steel bulk. As a consequence, LME can start at a relatively early stage of a tensile test, and steel failure could even occur when the yield point is just barely reached [473]. Luo et al. [550] reported that oxide scales that formed on T91 F/M steels exposed to liquid LBE ($C_O \approx 10^{-6}$ wt%) at 550 °C had different resistance to cracking under tensile loading, and that the magnetite (Fe_3O_4) outer layer was much more fragile than the inner FeCr-spinel layer. In this regard, the inner FeCr-spinel

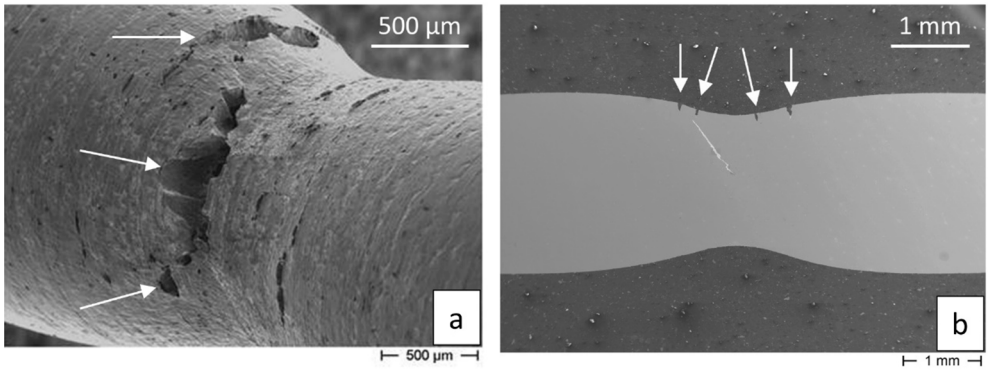

Fig. 4.32. SEM† images of the localisation of LME-induced microcracks (arrows) in the 'neck' area of T91 F/M steel specimens tested in tension in static liquid LBE. Test conditions: 350 °C, $\dot{\varepsilon} \approx 5 \times 10^{-5}$ s^{-1}, $C_O \approx 10^{-10}$–10^{-9} wt%. (Unpublished data produced by the authors).

layer plays a more important role in LME prevention than the outer magnetite layer. Methods that are used to remove or break the native oxides include ion sputtering [444,445] and chemical solder flux [444,464]; steel pre-exposure to reducing (i.e., low-oxygen) liquid LBE at high temperatures [231,482,495,540]; introducing stress raisers, such as notches or surface flaws, to damage the oxide scales [216,444–447,473]; loading the steel specimens at relatively slow strain rates to allow the liquid LBE to attack the surface under the combined effects of stress and corrosion; etc. On the other hand, when the intimate HLM/steel contact is prevented by the oxide scales, LME is generally observed after necking (Fig. 4.32). During necking, the voids start to nucleate and as the loading continues, they grow and coalesce together to form cracks in the steel bulk. Meanwhile, due to the highly localised stresses/strains in the necking area, the superficial oxide scales could be broken to enable intimate HLM/steel contact, thereby promoting crack formation in the 'neck' area. Serre et al. [551] discovered that Pb and Bi penetrated only in plastically-deformed surfaces. This indicates the important role of plastic deformation to promote crack initiation in the presence of liquid LBE. Moreover, Hojná et al. [503] found that most of the cracks initiated in the plastically-strained regions, proving that LME crack initiation occurs in areas where steel plastic deformation has caused the failure of native oxides. The cracks originating on the surface of the 'neck' area propagate inwards and finally merge with the ones coming from the steel bulk. Consequently, the tensile fracture surface is characterised by a mixture of brittle-like and ductile (dimple-rich) zones (Fig. 4.33). The fraction of the fracture surface corresponding to LME-induced brittle failure is determined by the time LME cracks form on the steel surface: the earlier they form, the larger the zones of brittle (quasi-cleavage) fracture. This explains the greater LME susceptibility of specimens subjected to a pre-exposure treatment or specimens with notches and surface flaws, as compared to those with a smooth surface. In oxygen-rich liquid LBE, failure of the oxide scales also competes with oxide self-healing [460,474,475,502]. Steel tempering at relatively low temperatures can retain more interstitial atoms in the steel matrix, which act as barriers to uniform plastic flow, thereby easing crack initiation in areas of plasticity localisation, and in turn, satisfying the stress threshold criterion mentioned earlier. Such a mechanism operates in neutron-irradiated materials as well, where abundant irradiation-induced defects tend to localise plastic deformation, thus favouring crack initiation. Both cases promote the occurrence of LME [45,457,471,493,496–498,519,527].

Despite the similarities between uniaxial creep and tensile tests, the load applied during a creep test is much smaller than that during a tensile test, as a creep specimen is generally subjected to a load well below the steel UTS†. This makes it difficult to fulfil the critical stress or stress intensity factor criterion for LME. Moreover, the strain rate during a creep test is lower, possibly favouring

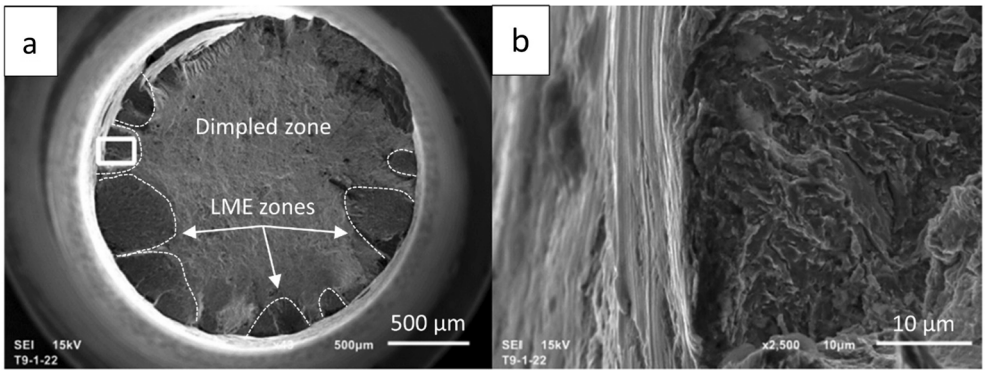

Fig. 4.33. SEM† images of the fracture surface of T91 F/M steels exposed to static liquid LBE: (a) dimpled zones are observed in the specimen centre and LME-affected zones in its periphery (outlined by white dashed curves), and (b) quasi-cleavage fracture appearance. Test conditions: 350 °C, oxygen-saturated LBE, $\dot{\varepsilon} \approx 5 \times 10^{-5}$ s^{-1}. Adapted from [45].

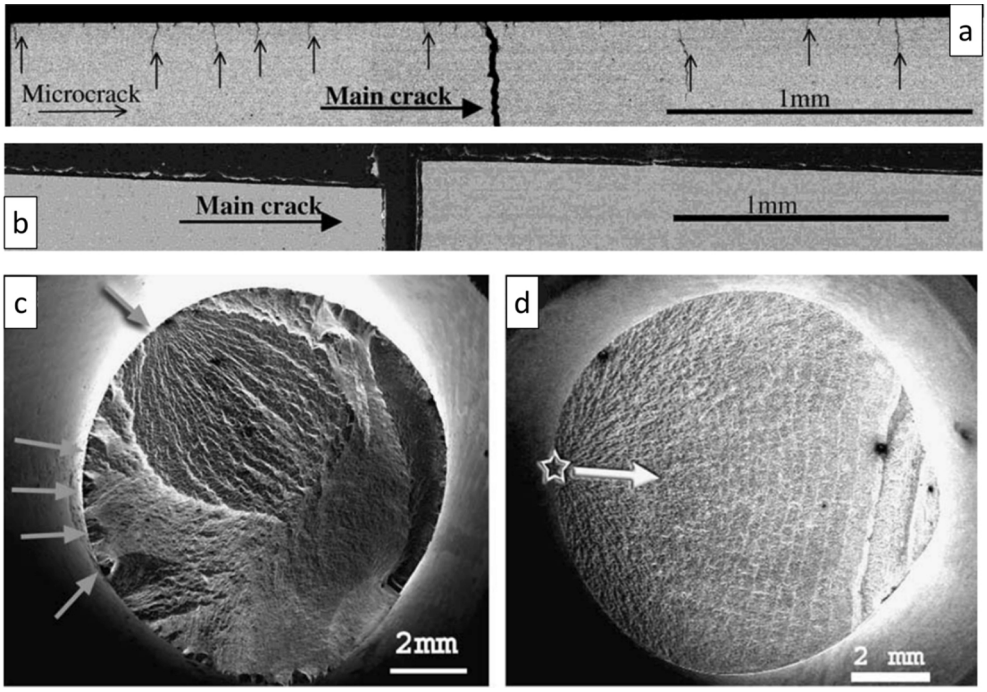

Fig. 4.34. SEM† images showing (a) multiple cracks on the surface of a T91 F/M steel specimen tested in low-cycle fatigue in air, as opposed to a single crack on a specimen tested in liquid LBE at 300 °C (b). (c,d) Fractography shows multiple crack initiation sites for the specimen tested in air, but a single crack initiation site for the specimen tested in liquid LBE. Adapted from [509,529].

material recovery by means of stress relaxation and self-healing of the oxide scales. This is a factor limiting crack initiation at the steel surface. On the other hand, the duration of a creep test is much longer, and, sometimes, it is conducted at a higher temperature. The latter increases the ductility of the steel bulk, which might also limit crack initiation. All these aspects contribute to the determination of the creep properties of T91 F/M steels exposed to liquid Pb/LBE, and it should be considered that, in general, the interplay of LMC effects and stresses promotes crack initiation on the steel surface. Due to the greater corrosiveness of liquid LBE when compared to liquid Pb, it was found that T91 F/M steels underwent severe degradation of their creep properties in contact with liquid LBE at 550 °C, in contrast with the weak effect observed in liquid Pb at 650 °C for various ferritic steels, including T91 and ODS steels [511–515]. Therefore, it is safe to conclude that the degradation of the creep resistance of such steels at elevated temperatures that are beyond the LME-sensitive temperature domain (i.e., around 350 °C) is associated primarily with the LMC effects.

For a low-cycle fatigue test, the situation is much different than in air or vacuum. The crack initiation occurs usually at persistent slip bands (PSBs) that are induced by extrusion/intrusion cycles [549,552]. The extension of microscopic cracks may be impeded by GBs, and thus new cracks can nucleate at the other locations of the steel surface. Consequently, numerous cracks form on the whole surface of specimens subjected to low-cycle fatigue in air and/or vacuum. On the other hand, the formation of a microscopic crack eliminates the GB resistance due to the LME effect in contact with liquid LBE. In this case, the applied stress/strain is concentrated mostly at the crack tip of the first-formed crack, causing fast crack propagation and leaving little chance for new cracks to form on the rest of the steel surface due to the limited stress level. As a result, the specimen surface has a limited number of cracks [509,529,531] (Fig. 4.34). Such an interesting phenomenon was also observed by Kalkhof et al. [477] and Gong et al. [502]. Moreover, Gong et al. [502] found that the number of crack initiation sites on the fatigue fracture surface seemed to be related to the oxygen content in liquid LBE. In oxygen-rich LBE, multiple crack initiation sites were observed, while only one crack initiation site was found in the specimens tested in oxygen-poor LBE. Another important difference with uniaxial tension is that under low-cycle fatigue, crack initiation tends to start on the steel surface, and due to the limited plastic strain involved in each cycle, the void nucleation/coalescence process in the steel bulk is limited. Consequently, the whole fracture surface of a fatigue specimen is covered by the typical LME-induced brittle failure features (Fig. 4.17c–h), instead of the mixed brittle and dimple-like fracture features observed on the fracture surface of a tensile specimen (Fig. 4.33).

Since the crack initiation stage is critical in determining the LME susceptibility of T91 F/M steels exposed to liquid Pb/LBE, it would be useful to draw an LME occurrence map, whereby one may identify the appropriate boundary conditions, so as to minimise the LME risk. Such maps have been drawn by Hojná et al. [524,553], based on extensive tensile tests on T91 F/M steel specimens with different geometries and surface conditions. According to the maps presented in Fig. 4.35, LME may occur in T91 F/M steels when loaded in liquid Pb with $C_O \approx 10^{-7}$ wt% at 350–400 °C, on the condition that the applied stresses are higher than 680 MPa, the corresponding plastic strain exceeds 5%, and the applied strain rate is in the 10^{-6}–10^{-4} s^{-1} range. In addition to the T91/Pb couple, they also identified that LME crack initiation would take place in T91 F/M steels exposed to liquid LBE ($C_O \approx 3 \times 10^{-7}$–$6 \times 10^{-6}$ wt%) at 300 °C,

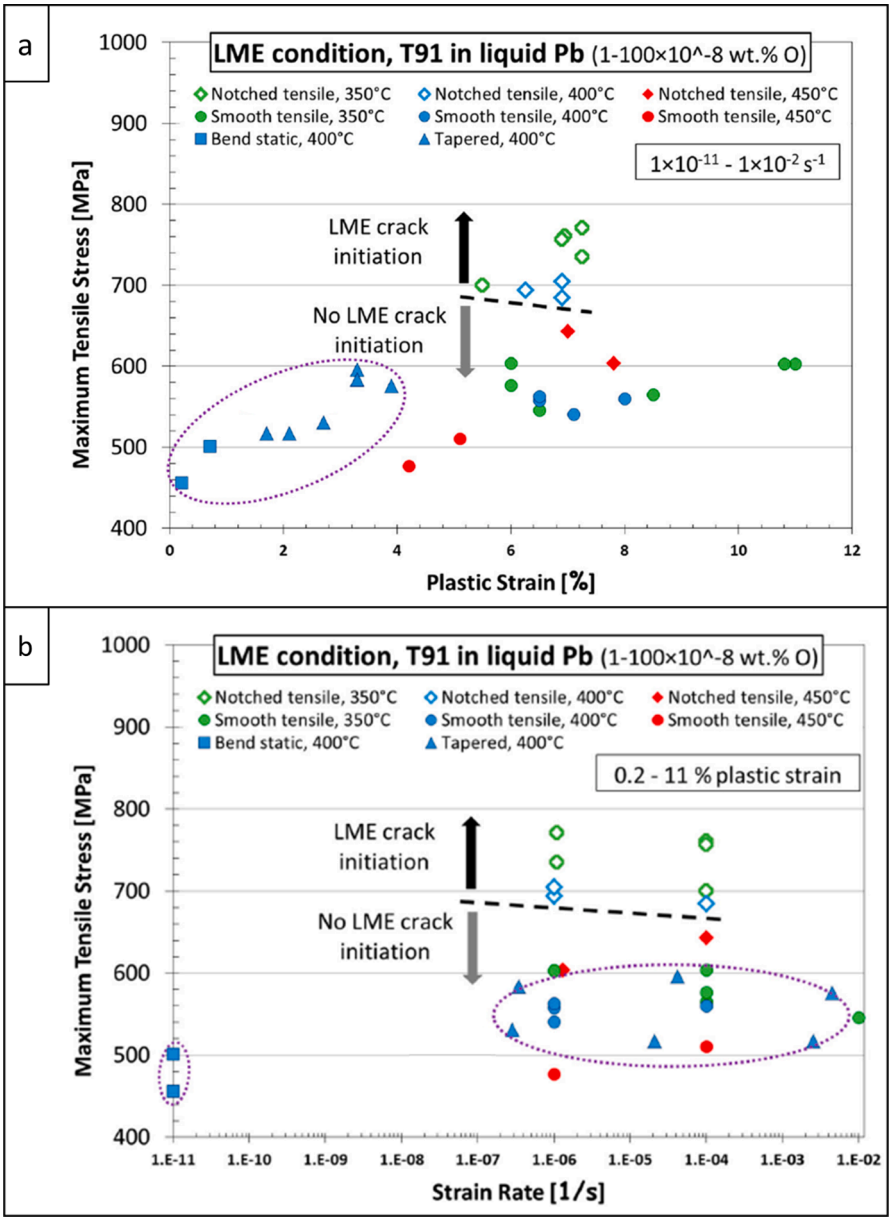

Fig. 4.35. LME occurrence map for T91 F/M steels exposed to liquid Pb under different test conditions. Adapted from [448,464,524].

when the plastic strain and stress were higher than 1.3% and 645 MPa, respectively [503].

4.7.2. Crack propagation stage

4.7.2.1. Interpretation of LME-induced fracture morphology. The main focus of understanding LME crack propagation has been placed on the correct interpretation of the LME-induced fracture morphology. The microstructural complexity of T91 F/M steels (see typical microstructural features in Fig. 2.3), however, triggered long-standing debates on various aspects, such as the nature of LME cracking (e.g., intergranular/interlath *vs.* transgranular) and whether LME crack propagation involves plasticity or not.

In principle, the boundaries of prior-austenite grains and martensitic laths in T91 F/M steels are expected to be the preferential LME cracking paths when compared to the steel bulk, given that these microstructural boundaries provide an additional driving force for HLM ingress. In other words, the surface energy reduction resulting from crack propagation along these internal boundaries is thermodynamically more favourable than that resulting from crack propagation in the steel bulk. In addition, the adsorption-induced reduction in surface energy mechanism predicts that the number of the microstructural boundary decohesion cases should be overwhelmingly high as compared to the translath or transgranular cracking ones. Based on TEM examinations of crack tips, Martin et al.

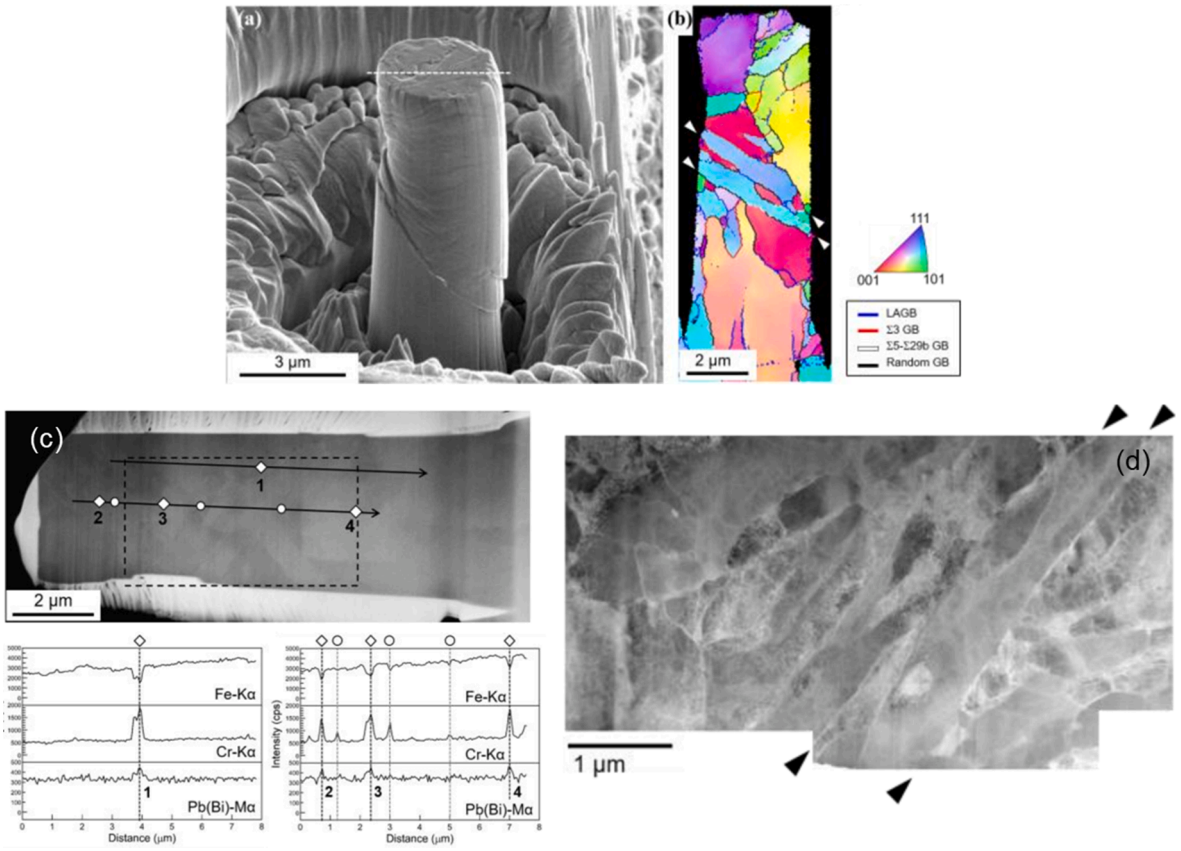

Fig. 4.36. (a) SEM† image of a T91 F/M steel micropillar deformed to 9.4% strain, and (b) the corresponding EBSD† orientation map with inverse pole figure colour map showing the shear deformation along high-angle GBs marked with arrowheads; (c) EDS† point analyses indicating the segregation of LBE segregates at GBs; (d) STEM-HAADF† image of the presence of an LBE film at high-angle GBs marked with arrowheads. Adapted from [554].

[533] and Hémery et al. [438] discovered that the cracks originating from fracture surfaces of T91 F/M steels tested in three different liquid metals (i.e., LBE, In, and Na) were intergranular. They stated that the typical LME-induced fracture features should not be described as "cleavage" or "quasi-cleavage" failure, but as interfacial failure instead. Indeed, intergranular cracking was also observed to dominate the failure mechanism in many other solid metal/liquid metal couples, such as Al/Ga [309,310,391,433], Ni/Bi [426,555], Cu/Bi [556], Fe/Zn [422] and AuSS/Na [440,441,443]. In addition, Kaede et al. [554] found that a thin LBE layer/film was present at high-angle GBs in a T91 F/M steel specimen subjected to corrosion testing; the LBE film led to shear deformation along these GBs during subsequent micropillar compression (Fig. 4.36). Recently, Ma and Zhang [557] reported that α-Fe (ferrite) was attacked by liquid LBE at 900 °C via GB grooving. All these results demonstrate the important role of GBs in LME failure.

However, Gong et al. [53,508] and Halodová et al. [558] found that intergranular or interlath cracking was not the only type of crack propagation in T91 F/M steels fractured either under low-cycle fatigue in liquid LBE at 350 °C, or under monotonic tensile loading in liquid LBE at 300 °C. Instead, they observed cracking either along or across grain/lath boundaries (Fig. 4.37a and b). In their work, intergranular cracking was found to rely on the relative orientation between the GBs and the stress axis. When the orientation favoured the development of a sufficiently high tensile stress perpendicular to the GB surfaces, cracking along boundaries (i.e., intergranular crack propagation) was favoured. Serre et al. [551] used time-of-flight secondary ion mass spectrometry (TOF-SIMS) and observed that lath boundaries or GBs were not the preferred sites for the adsorption of Pb/Bi atoms. This may be another piece of evidence to support the viewpoint that LME cracks do not necessarily follow microstructural boundaries as their preferred propagation paths.

Furthermore, Gong et al. [53] discovered that the preferred LME cracking plane was $\{\bar{1}\ 1\ \bar{1}\}$ (Fig. 4.37c). This contradicts the *ab initio* calculation results on the pure Fe/LBE couple [519], which showed that the maximum surface energy reduction (35%) caused by LBE adsorption occurred on the $\{0\ 1\ 1\}$ plane of Fe, followed by 22% reduction on the $\{0\ 0\ 1\}$ plane, and 16% reduction on the $\{1\ 1\ 1\}$ plane. The discrepancy between the theoretically predicted preferred crystallographic plane (i.e., $\{0\ 1\ 1\}$) for LME cracking and the experimentally observed one (i.e., $\{\bar{1}\ 1\ \bar{1}\}$) indicates that the surface energy reduction mechanism cannot fully explain the LME characteristics in the T91/LBE system.

Considering that transgranular or translath decohesion is also an important LME cracking mode, the two mechanisms based on GB

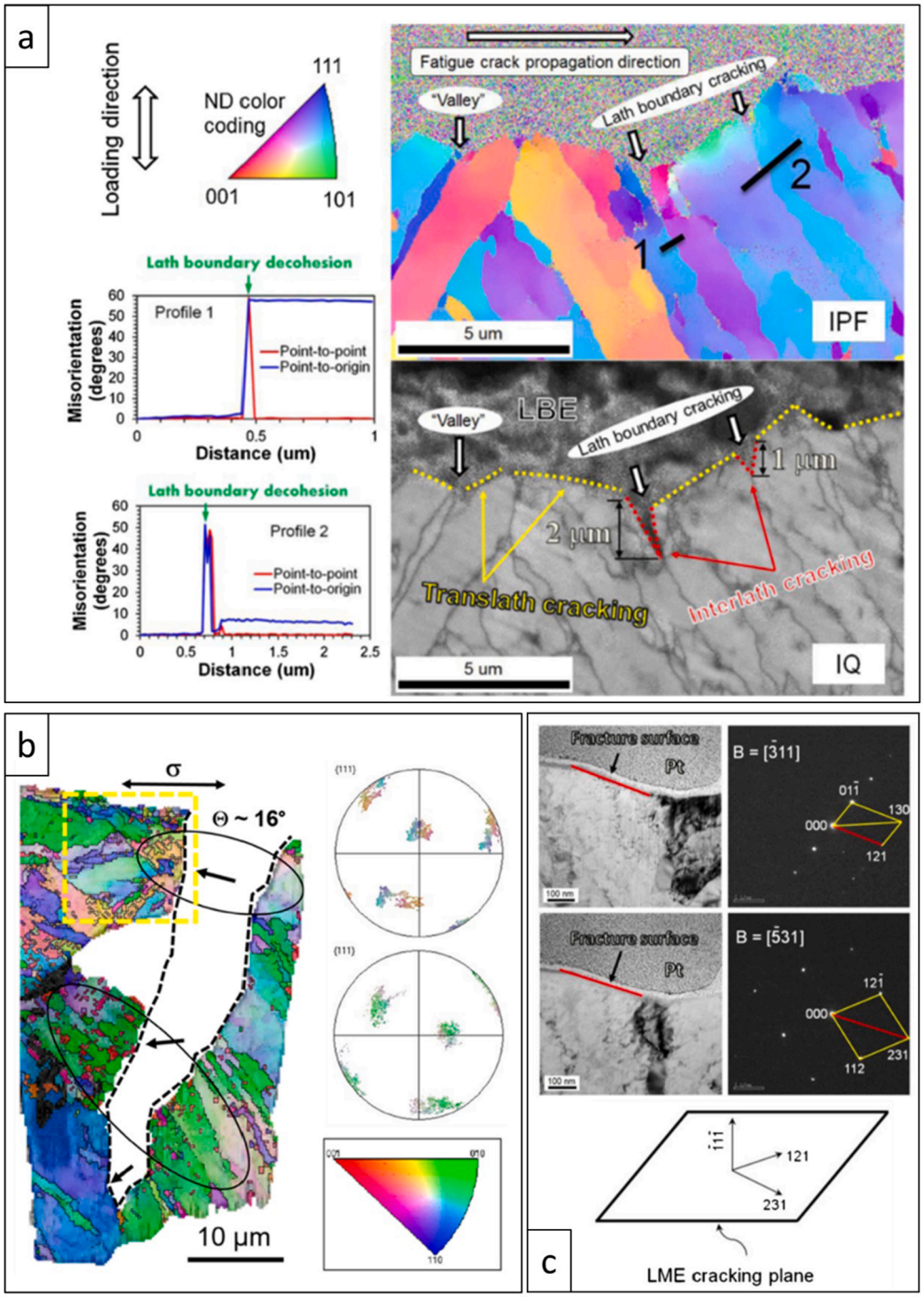

Fig. 4.37. (a) EBSD† examinations of the microstructure underneath the fracture surface of a T91 F/M steel tested in liquid LBE, showing that the LME crack propagated mainly through martensitic laths, accompanied by a few short cracks along lath boundaries with misorientations of 50–60°. (b) EBSD† grain orientation map showing that LME crack propagation occurred either in a translath/transgranular or in an intergranular manner. (c) The preferred crystallographic plane for LME crack propagation was $\{\bar{1}\ 1\ \bar{1}\}$. Adapted from [53,558].

penetration [298,366] cannot fully account for the LME-induced fracture features in the T91/LBE couple. Particularly, both mechanisms claim that GB diffusion determines directly the crack growth rate. This obviously cannot explain the fast crack propagation of several tens of micrometres per second reported in Ref. [527] and shown in Fig. 4.38, as diffusion is a quite time-consuming process. Particularly, both Gong et al. [53] and Martin et al. [533] did not observe any evident LBE penetration zone in the immediate vicinity of the crack tips, which implies that liquid LBE was not present ahead of the crack tips. This is another evidence that rules out the

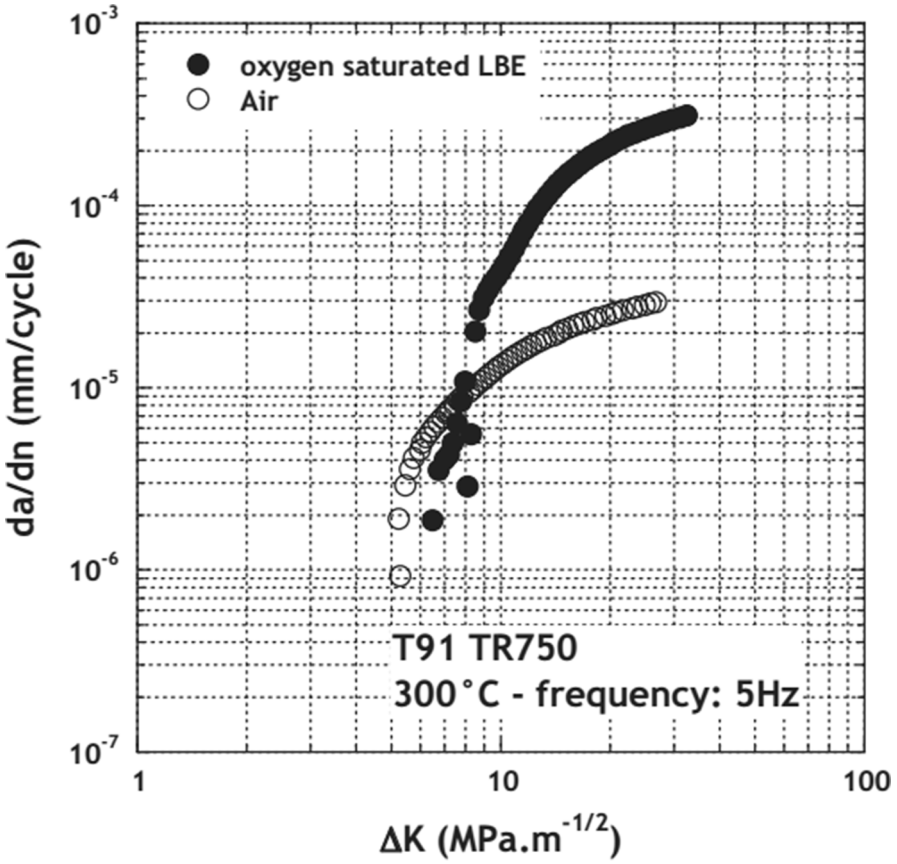

Fig. 4.38. Fatigue crack propagation rate (da/dN) *vs*. stress intensity factor range (ΔK) for T91 F/M steels tested in oxygen-saturated liquid LBE and air at 300 °C; one cycle was 0.2 s [527].

dominant role of atomic diffusion at the crack tips during the fast crack propagation process characterising LME.

The stress-assisted dissolution model is not appropriate to explain the LME features of the T91/LBE system, taking into account that the solubility limits of the two main alloying elements of T91 F/M steels (i.e., Fe and Cr) are quite low in liquid LBE (e.g., C_S(Fe) = 9.8 ppm and C_S(Cr) = 23.4 ppm at 600 °C [559]). Furthermore, Gong et al. [53] calculated the crack growth rate using Eq. (4-12), which is the mathematical formulation of this model, and concluded that, if the stress-assisted dissolution model described accurately LME crack propagation, the crack propagation rate would only be 2.4×10^{-4} μm/s. This value is far smaller than the experimentally observed crack propagation rates, which can actually reach values as high as 100 μm/s [473,520,527]. Ersoy et al. [532] reached a similar conclusion based on 1/2CT fracture toughness tests on T91 F/M steels in oxygen-poor liquid LBE ($C_O \approx 10^{-11}$–10^{-7} wt%) at 200 °C and 350 °C.

The cyclic stress response under low-cycle fatigue showed a predominant cyclic softening behaviour for T91 F/M steels [500,502,509]. This may suggest that strain softening rather than strain hardening occurs at the crack tip. In this regard, the adsorption-enhanced work hardening mechanism [369] may not be applicable for the T91/LBE system. In addition, this mechanism cannot straightforwardly predict whether the fracture occurs intergranularly or transgranularly.

In addition to the presence of both intergranular and transgranular cracking modes in the T91/LBE couple, microdimple-like features were also observed using various characterisation techniques (Fig. 4.39), such as SEM†, TEM†, and AFM† [53]. The presence of the dimples seems to strongly support the adsorption-induced dislocation emission mechanism [285,363–365]. However, the emission of dislocations should result in crack-tip blunting along most crystallographic orientations, therefore, crack propagation should be inhibited according to this mechanism. It is not straightforward, therefore, to comprehend how dislocation emission at crack tips can lead to the fast crack extension. Furthermore, the adsorption-induced dislocation emission mechanism should predict fracture preferentially along shear planes, which are inclined at a specific angle (~45°) to the loading axis, and where the dislocation emission is the strongest. This is in contradiction with the fact that the fatigue fracture surfaces of specimens tested in liquid LBE were nearly vertical to the loading axis, which is the direction of maximum normal stress [509].

Gong et al. [53,500,508] also found that the martensitic lath boundaries in T91 F/M steels were refined into very small equiaxed grains after low-cycle fatigue testing in vacuum, whereas such grain refinement was not observed in the specimens tested in liquid LBE (Fig. 4.18). This is an important piece of evidence of LME occurrence and proves that crack tip plasticity is reduced. In this regard, the adsorption-induced reduction in cohesion model [361,362] is supported by this finding. Indeed, the adsorption-induced reduction in

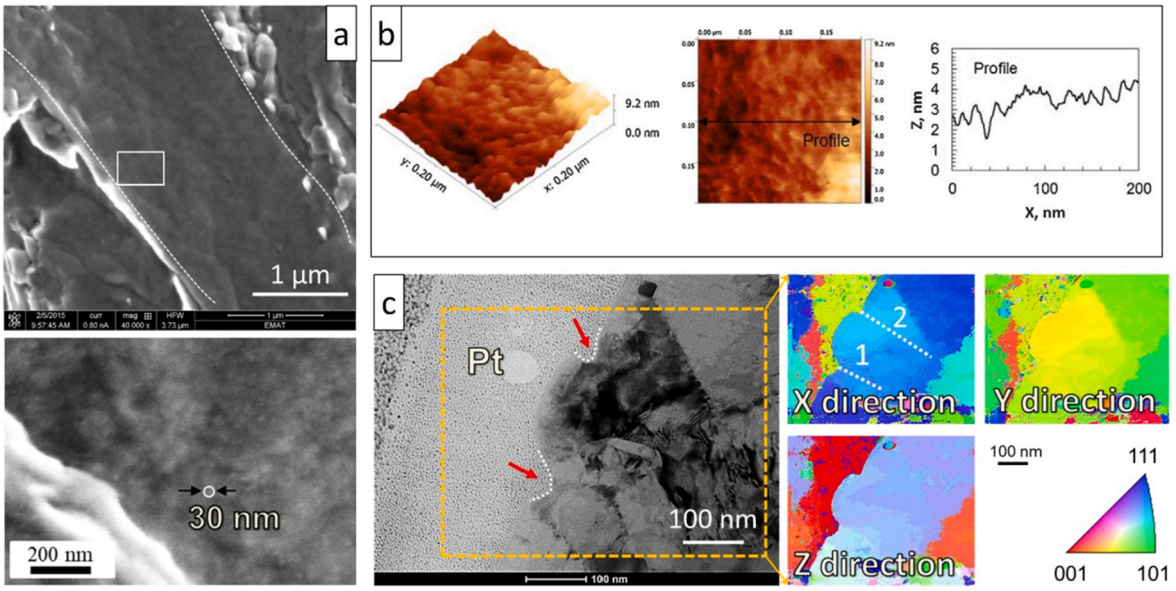

Fig. 4.39. (a) High-resolution SEM†, (b) AFM†, and (c) TEM† BF† images showing the presence of dimple-like structures on the micro/nanometre scales during translath crack propagation in T91 F/M steels. Adapted from [53].

cohesion model is mostly used in literature to explain the LME effect in a wide variety of solid metal/liquid metal systems, as mentioned before. However, this model predicts a featureless and cleavage-like fracture surface, which contradicts the numerous observations of submicron dimples, such as those shown in Fig. 4.39.

Microstructural examinations showed that multiple fracture features were observed in the T91/LBE couple. It appears that each LME mechanism or model could account for only part of the diverse LME features and none could cover all experimental observations. Specifically, cracking at lath boundaries may result from an adsorption-induced reduction in surface energy, since the GB energy makes the LBE attack of any type of boundary thermodynamically more favourable; the adsorption-induced dislocation emission mechanism could explain the observed dimples on the nanometre/micrometre scale, given that the formation of dimples is typically a sign of strong dislocation activity; moreover, the fact that the fracture surfaces tend to be flat and "featureless" may be explained by the adsorption-induced reduction in cohesion model, since this model predicts preferential cracking along crystallographic planes that are subjected to a maximum normal stress, which is often parallel with the loading direction. It is reasonable, therefore, to assume that multiple mechanisms operate simultaneously during the LME cracking process of the T91/LBE system.

Based on the above considerations, Gong et al. [53,502] proposed a qualitative hybrid mechanism (Fig. 4.40) that combined part of the basic ideas of the adsorption-induced reduction in cohesion model, the enhanced work hardening mechanism, and the adsorption-enhanced dislocation emission mechanism to explain the formation of the diverse LME fracture characteristics observed in the T91/LBE couple. This mechanism defined four parameters: (a) the critical normal stress (σ_c) required to break the A-A1 pair of atoms in the absence of liquid LBE, (b) the critical resolved shear stress (τ_c) required to activate dislocation glide at a given slip plane in the absence of liquid LBE, (c) the actual normal stress (σ_y) acting on the A-A1 pair of atoms when LBE is adsorbed at the crack tip, and (d) the actual shear stress at the slip plane (τ) when LBE is adsorbed at the crack tip. It was hypothesised that the adsorption of Pb and Bi atoms at the crack tip in T91 F/M steels leads to a moderate reduction in interatomic cohesion, so that dislocations can still be activated before the interatomic bonds are broken by the normal stress in a brittle manner. The dislocation activity (nucleation and mobility) is assumed to cause local strain hardening around the crack tip, even if cyclic strain softening is the main response of the T91 F/M steel bulk during low-cycle fatigue, as previously mentioned. Meanwhile, microvoids nucleate and grow inside the plastic zone. As the local strain hardening reaches a critical level, dislocation motion becomes difficult. When the continuously increasing load overcomes the weakened interatomic bond strength, crack propagation cuts through the voids, forming micro-dimples on the fracture surface. The size of the voids or dimples depends on the magnitude of the dislocation activity and the bond weakening effect. The stronger the bond weakening, the smaller and less the voids/dimples. For the T91/LBE couple, the bond weakening effect is believed to be moderate rather than catastrophic, thereby leading to a small amount of plasticity around the crack tip. As a result, a limited number of small dimples can only be created on the fracture surface (Fig. 4.39). This mechanism was also used to account for the occurrence of both translath/transgranular and interlath/intergranular cracking. Gong et al. [53,502] stated that only GBs and martensitic lath boundaries with orientations favouring the development of sufficiently high tensile stresses perpendicular to them would undergo boundary decohesion (intergranular/interlath decohesion), otherwise, translath/transgranular cracking would occur instead. In other words, the difference in the severity of the weakening effect between grain and/or lath boundaries and steel bulk may be insignificant, so that the occurrence of boundary cracking depends on the orientation of boundary surfaces relative to the loading axis.

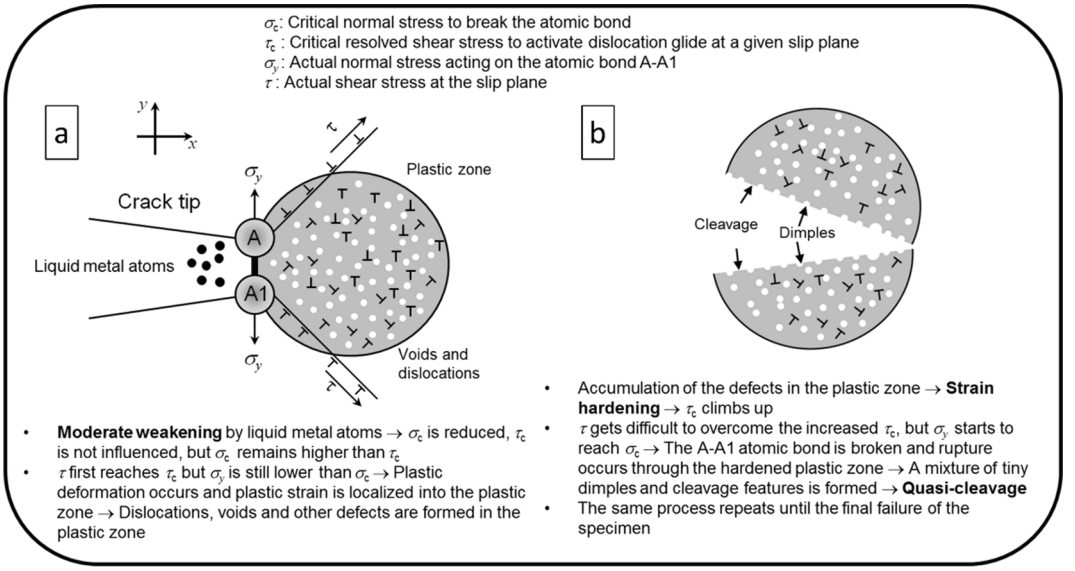

Fig. 4.40. Schematic illustration of an LME crack propagation mechanism proposed for the T91/LBE couple. Adapted from [502].

4.7.2.2. Cracking instability and concentric fracture markings. Cracking instability is a remarkable but not well understood phenomenon, which has been occasionally observed during tensile testing of T91 F/M steels in liquid LBE, leading to the formation of a pattern of concentric markings on the fracture surface, as shown in Fig. 4.41. The formation of these regularly spaced markings on the fracture surface (Fig. 4.41b) coincides with the appearance of a similar quantity of small steps in the final part of the tensile curve (Fig. 4.41a). The fracture surface had two distinct parts, i.e., the dimpled zone, and the area covered by the concentric markings (Fig. 4.41c). Typical brittle failure features characteristic of LME were observed between two successive markings (Fig. 4.41d). This interesting

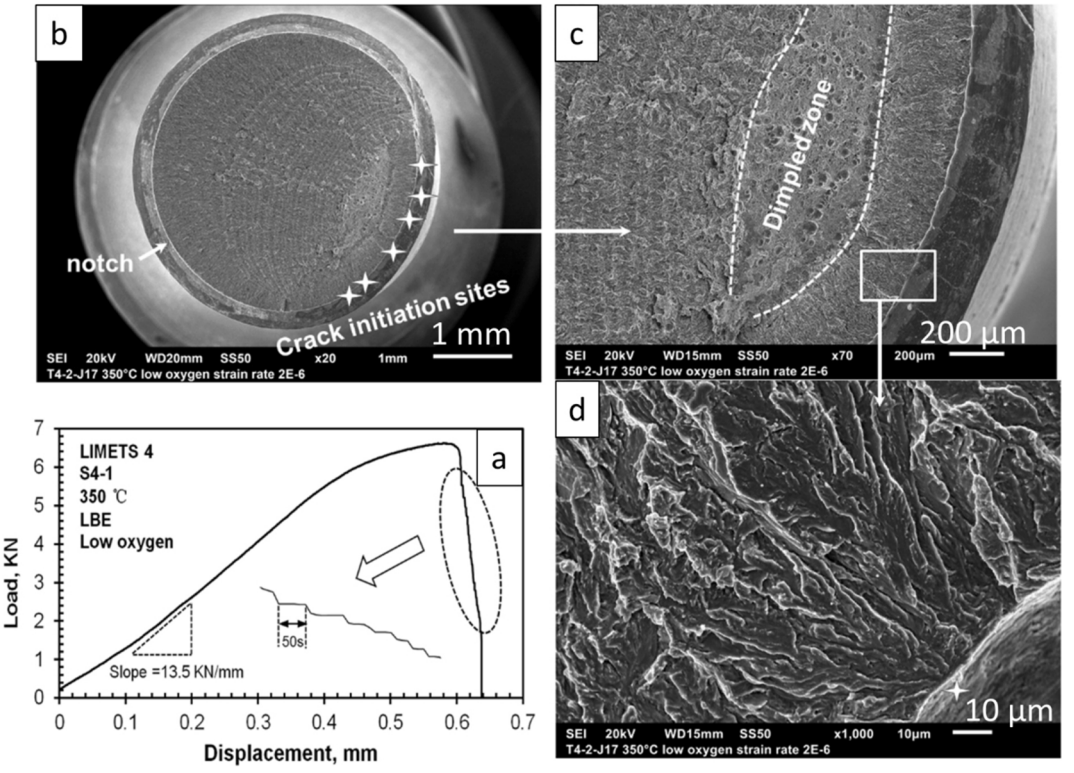

Fig. 4.41. SEM† images of T91 F/M steel fracture surfaces showing a mixture of LME-induced brittle fracture and ductile, dimple-rich fracture tested in low-oxygen liquid LBE at 350 °C. Adapted from [473].

phenomenon was also observed in Si-enriched T91 and EP823 F/M steels exposed to liquid LBE [251], in a T91/Pb couple [507], and other solid metal/liquid metal couples [560].

However, this interesting phenomenon is still not fully understood and there is an ongoing debate to explain it. Klecka et al. [507] attributed it to the DSA† effect, as the small steps on the tensile stress–strain curve were very similar to the stress serrations induced by DSA. Lynch [560] proposed a mechanism based on the emission of dislocations from crack tips to account for this phenomenon. He also suggested that the loss of intimate contact between the liquid metal and the crack tip might be another cause. Gong et al. [473] found that the cause of this phenomenon was linked to the combined effects of LME and the compliance of the tensile machines, as the regularly spaced markings were prone to disappear when the tensile machines became stiffer. They argued that the formation of markings was the result of oscillations of elastic energy in the load line of the tensile machines.

4.8. Open issues for LME

It is puzzling that AuSS are not strongly sensitive to embrittlement by liquid Pb and LBE, while T91 and similar F/M steels are, even though both are Fe-based alloys. Fully figuring out this issue is crucial, not only for Gen-IV LFR materials selection and qualification, but also in order to guide the design of new nuclear materials resistant to LME.

Assuming that the adsorption of Pb and LBE atoms causes a comparable weakening of the steel atomic bonds, the different LME susceptibilities of these two steel families might be associated with their different plasticity around crack tips. The higher the plasticity, the weaker the LME susceptibility, as the threshold stress criterion at crack tips becomes more difficult to fulfil in the case of greater plasticity. If this is a valid assumption, twinning is another important factor promoting plasticity and, thus, inhibiting LME. Nevertheless, excellent ductility may not be exclusively responsible for the weak LME effect in AuSS, as many other solid metals with good ductility can be embrittled by certain liquid metals, such as Al/Ga [388–392], Cu/Bi [425], Ni/Bi [426], AA6262 Al alloy/Pb [561] couples, etc.

Note that wetting AuSS with liquid Pb/LBE is very difficult, requiring special measures, such as chemical processes, long-term exposures to a low-oxygen liquid metal environment, and steel pre-cracking in the liquid metal environment [440,484,490]. The cause for the poor AuSS wettability might be due to their higher Cr content (16–17 wt% for 316L AuSS *vs.* 9 wt% for T91 F/M steels), as it enables the formation of oxide scales even under rather low oxygen partial pressures. This may be part of the reason accounting for the comparatively mild LME of AuSS as compared to the severe LME susceptibility of T91 F/M steels.

Another interesting, but not well understood phenomenon, is the effect of two steel alloying elements, i.e., Si and Al, on the LME susceptibility of ferritic steels. As described previously, Si and Al are utilised to improve LMC properties, due to the formation of passivating silica (SiO_2) and alumina (Al_2O_3) scales (more details in Chapter 5). However, adding these two elements can drastically enhance LME [251,562]. This was attributed to the more brittle nature of Si- and Al-rich oxides, or to the solid-solution strengthening effect of these two elements. It is still unclear, however, whether these two elements have an impact on the intrinsic brittleness of the steels that are doped with Al and/or Si.

Atomic-scale studies of steel/Pb and/or steel/LBE couples are lacking, most likely due to the complexity of the steel composition and microstructure, esp. for T91 F/M steels. To simplify this challenge, it is suggested to use simpler model systems, e.g., α-Fe/Pb, α-Fe/Bi, and α-Fe/LBE. Then, atomic-scale modelling and *in situ* experiments could be utilised to examine in-depth the embrittlement mechanism of pure Fe by these HLMs. The results based on these relatively simple systems will be a good starting point to improve the understanding of LME mechanisms in the more complex steel/HLM systems.

This section may be concluded by highlighting the fact that F/M steels, such as the T91 F/M grade, are embrittled only under service conditions that are damaging to the oxide scales. Therefore, irrevocably removing this class of steels from the list of candidate structural materials for Gen-IV LFRs can only be decided in the future, taking into account all technical advances in fields requiring the use of HLM coolants. Dedicated tests under representative reactor environments should also be done in the future to define the envelop of safe reactor operating conditions that can prevent or suppress the LME effect in T91 and similar F/M steels.

4.9. Chapter summary

This chapter has established that many F/M steels, including the T91 grade, are inherently susceptible to LME under a specific set of service conditions likely to be found in Gen-IV LFRs. Suppressing the occurrence of LME by means of appropriate nuclear system design (e.g., eliminating steels with high LME susceptibility from load-bearing applications) and/or finding new solutions to this materials degradation effect is an important technical challenge for the deployment of Gen-IV LFRs.

Even though the mechanisms described in Chapter 4 summarise the current understanding of this particular materials degradation effect, they cannot account for the empirically observed, LME-induced crack propagation rates in all F/M steels, including the extensively studied T91 grade. This calls for a systematic investigation of LME by combining modelling/simulation and experimentation in different test conditions, thereby mapping the (material- and HLM-specific) service conditions that induce LME. The difficulty in this undertaking lies in the fact that during actual reactor operation, one can expect unforeseen excursions between conditions that favour LME and conditions that suppress it. Moreover, the incomplete understanding of the atomistic mechanisms involved in LME warrants the further in-depth investigation of LME in the highly susceptible F/M steels.

In contrast with the LME-susceptible F/M steels, AuSS do not exhibit a similar inherent susceptibility to LME. The embrittling effects that result from short-term exposures of AuSS to liquid LBE are weak, but long-term exposures (e.g., during creep and fatigue testing) might have a significant impact due to stress-enhanced dissolution corrosion, which in combination with an insufficient supply of oxygen to the crack tip might lead to severe degradation of mechanical properties. Moreover, special attention should be paid to the

possible occurrence of LME in AuSS due to the formation of ferrite induced by selective leaching of Ni and plastic straining. Last, but not least, one should not disregard the possible synergy of ferritisation (either plastic strain- or dissolution corrosion-induced) with LME and irradiation embrittlement.

5. LMC and LME mitigation approaches

There are several measures that could be currently employed to mitigate undesirable LMC effects, such as tailoring the reactor system design based on the LMC behaviour of the candidate steels, active oxygen control, and materials innovation. Since temperature is the key factor determining the extent of LMC damage, it is often considered to lower the nominal operation temperature range of the reactor system so as to avoid very severe LMC effects (both oxidation and dissolution), even if the reduced temperature may increase the LME risk in ferritic and F/M steels. However, this goes directly against NPP economics, both in terms of thermodynamic efficiency and exploring new markets (e.g., hydrogen production with direct use of the heat released by fission reactions), both of which become economically viable only above a certain temperature threshold. Moreover, the nuclear reactor system design must also be optimised to minimise turbulent flow (turbulent flow does not ensure optimal surface heat convection) and eliminate unnecessary flow diversion sites. On the other hand, the objective of active oxygen control is to maintain the HLM dissolved oxygen concentration within a specific domain, which ensures the steel passivation by the formation of stable, protective oxide scales without oxidising the HLM itself. Another appealing solution is the development of innovative materials that are able to survive the harsh service environment of Gen-IV LFRs within much wider domains of allowable temperatures and HLM oxygen concentrations, a prospect that is favourable for many reasons (i.e., NPP economics, simplification of reactor system design, enlarging operational safety margins). The strategy for materials innovation includes steel elemental alloying and surface engineering by coatings and diverse surface treatments, as well as the development of new structural materials (including ceramics) that can address the property requirements of very specific applications (e.g., pump impellers, bearings, bushings). Unfortunately, the measures to mitigate LME contradict LMC prevention methods to some extent. For instance, operating a reactor at relatively high temperatures is beneficial to reduce the LME risk in ferritic and F/M steels, but this will promote LMC in all candidate structural steels. Moreover, the mitigation of LME relies on the presence of (defect-free) protective oxide scales, however, all oxides are inherently brittle materials that are prone to cracking under tension; therefore, it is very difficult to prevent LME in load-bearing components, even when they are initially covered by oxide scales that prohibit the intimate steel/HLM contact. This chapter reviews the efforts already made to mitigate LMC and LME in Gen-IV LFRs and discusses their advantages/disadvantages.

5.1. Optimization of the reactor system design

As mentioned in Chapter 3, the solubility limits of the main steel alloying elements, such as Ni, Cr, and Fe, in liquid Pb/LBE increase remarkably with temperature, while the stability of oxide scales on the steel surfaces is also temperature-dependent. This shows that temperature is arguably the most important reactor system parameter that must be controlled so as to mitigate undesirable LMC effects. Indeed, both steel oxidation and dissolution kinetics are substantially reduced when the reactor operation temperature does not exceed 400–450 °C [29,31]. It should be pointed out, however, that reduced reactor operation temperatures will compromise the thermal efficiency of fast neutron reactors built with the aim of power generation. Moreover, the melting point of LBE is ~125 °C, thus the reactor operating temperature 'window' that stems from keeping the operation temperature below 400–450 °C is quite narrow, entailing the risk of coolant freezing at the reactor 'cold leg', e.g., as result of a loss-of-flow accident (LOFA). This is more challenging for Pb-cooled fast reactors, as Pb has a higher melting point (327 °C) than LBE, even though liquid Pb is less corrosive than liquid LBE. Moreover, opting for lower operation temperatures renders F/M steels more susceptible to LME, as these steels are more susceptible to brittle failure at relatively low temperatures (see Figs. 4.15 and 4.16). Moreover, system design should also take into account local HLM flow patterns, trying to minimise flow instabilities (e.g., 'eddies') and turbulent flow, which have been recognised as important factors that promote the occurrence of both erosion/corrosion and locally enhanced dissolution corrosion [172,189,191]. Acquiring an in-depth understanding of the behaviour of any candidate structural steel to both LMC and LME in contact with a HLM coolant (Pb/LBE) is necessary before consolidating the design of a HLM-cooled fast reactor. For example, if a specific structural steel grade (e.g., the T91 F/M steel) exhibits a strong susceptibility to LME that cannot be addressed by any of the currently available LME mitigation approaches, this steel should be excluded from the reactor design, esp. with respect to its possible use for building structural components. Moreover, knowing the LMC behaviour of any candidate structural steel in contact with a HLM coolant is of paramount importance for defining the detailed design of the HLM-cooled reactor system. In fact, the collection of reliable LMC data under extremely conservative conditions (e.g., very low HLM oxygen concentrations) is key to the assessment of the maximum possible steel loss rates (e.g., due to dissolution corrosion including dissolution 'pitting', erosion/corrosion, etc.) under specific conditions (e.g., temperature, HLM flow rate). Steel testing under the most conservative conditions can allow the designers of a Gen-IV LFR system to confidently define 'corrosion allowances', i.e., the dimensional safety margins for a particular reactor component, so that the component will not fail during its intended lifetime due to LMC-induced material losses. Such 'corrosion allowances' are typically provided by nuclear reactor component design codes, such as ASME, RCC-MRx, etc., however, these codes typically provide tentative values that cannot be fully relied upon for the design of an advanced reactor system. Knowing the required 'corrosion allowance' for a nuclear reactor component that is planned to be built from a specific structural steel defines not only the dimensions of that particular component, but also the size of the whole reactor system. For example, knowing the LMC behaviour of the structural steel that will be used for the construction of an irreplaceable component, such as the reactor vessel, one can decide the maximum temperature that the vessel should see during its lifetime under nominal operation (also making some provisions for short-term high-temperature transients)

so as to maintain the corrosion losses within the desired range. This can determine the distance between the vessel and the reactor core (assuming a maximum allowable temperature in the reactor core that is defined by both the desired efficiency of the reactor system and the LMC behaviour of the candidate fuel cladding steel) and, hence, the size of the reactor system itself. By the same token, devising strategies (e.g., surface engineering methods such as coating deposition, surface modification, etc.) that can expand the envelop of conditions of reliable operation for the chosen structural steels provides some flexibility to the reactor system designers, allowing them to opt for the most cost-efficient design alternatives.

5.2. Active oxygen control

Theoretically, it is possible to build protective oxide scales, while preventing the oxidation of the HLM and the ensuing blockage of HLM flow paths in the reactor, by maintaining the dissolved oxygen concentration in the HLM (Pb/LBE) in a specific range. The lower boundary of this range indicates the HLM oxygen concentration, above which oxide scale formation is promoted on the steel surface. On the other hand, the upper boundary of this range indicates the HLM oxygen concentration, below which the precipitation of Pb and/or Bi oxides is inhibited. The existence of such HLM oxygen concentration range can be attributed to the fact that nearly all the main steel alloying elements form thermodynamically stable oxide scales at smaller oxygen partial pressures as compared to both Pb and Bi [29,31,563–565]. However, a technical challenge associated with active oxygen control is the difficulty to control the oxygen potential everywhere in the reactor system, as crevices, fouling deposits, or occluded regions filled with static HLM will quickly become more reducing in nature; logically, the structural materials in such regions will be more severely affected by LMC (and possibly also by LME, due to the reduction of oxide scales that would normally inhibit the intimate steel/HLM contact).

The upper boundary of the HLM oxygen concentration range is defined by the oxygen concentration corresponding to the Pb/PbO equilibrium in liquid LBE/Pb [174], as PbO is more stable than Bi_2O_3 (Fig. 3.9). This equilibrium is defined by the following oxidation reaction:

$$Pb_{(LBE)} + O_{(LBE)} \leftrightarrow PbO_{(s)} \tag{5-1}$$

If the above oxidation reaction reaches thermodynamic equilibrium at a given temperature, T, then:

$$\Delta_f G^o_{Pb/PbO} + RT\ln\frac{a_{PbO}}{a_{Pb}a_o} = 0 \tag{5-2}$$

where $\Delta_f G^o_{Pb/PbO}$ is the standard Gibbs free energy of PbO formation, R is the gas constant (8.3145 J/K•mol), T is temperature in K, and a is the activity of PbO, Pb and O in liquid LBE.

Considering the formation of pure PbO, i.e., $a_{PbO} = 1$, then Eq. (5-2) can be rewritten as follows:

$$RT\ln a_o = \Delta_f G^o_{Pb/PbO} - RT\ln a_{Pb} \tag{5-3}$$

According to Henry's law, the activity of the oxygen dissolved in LBE can be described by:

$$a_o = k_H C_o \tag{5-4}$$

where k_H is Henry's constant, and C_O is the oxygen concentration dissolved in liquid LBE. Inserting Eq. (5-4) into Eq. (5-3) yields:

$$RT\ln C_{o,max} = \Delta_f G^o_{Pb/PbO} - RT\ln a_{Pb} - G^{ex}_{o(LBE)} \tag{5-5}$$

where $G^{ex}_{o(LBE)}$ is the standard Gibbs free energy of O dissolution in LBE and is equal to $RT\ln k_H$.

The standard molar Gibbs free energy of PbO formation is given in Ref. [566]:

$$\Delta_f G^o_{Pb/PbO}(J/mol) = -218980 + 99.63T \tag{5-6}$$

The activity of Pb in liquid LBE is given in Ref. [567]:

$$\ln a_{Pb} = -0.8291 - \frac{166.80}{T} \tag{5-7}$$

The standard Gibbs free energy of O dissolution in liquid LBE (with respect to the 1 wt% standard state) is given in Ref. [568]:

$$G^{ex}_{o(LBE)}(kJ/mol) = -127.398 + 0.049272T \tag{5-8}$$

Inserting Eqs. (5-6), (5-7) and (5-8) into Eq. (5-5), the following equation can be obtained to calculate the LBE oxygen concentration corresponding to the Pb/PbO equilibrium, i.e., the maximum allowed oxygen concentration:

$$\log C_{o,max}(wt.\%) = 2.99 - \frac{4711}{T} \tag{5-9}$$

The lower boundary of the HLM oxygen concentration range is defined by the oxygen concentration corresponding to the Fe/Fe_3O_4 equilibrium in liquid LBE [174]. It should be pointed out that NiO is thermodynamically less stable than Fe_3O_4 (Fig. 3.9); however, the Ni/NiO equilibrium is not recommended for the lower boundary, because the HLM oxygen concentration range that would be defined by Ni/NiO and Pb/PbO is too narrow, making it difficult to control the HLM oxygen content in a real non-isothermal reactor system.

Therefore, the following dissolution/precipitation reaction is considered:

$$Fe_3O_{4(s)} \leftrightarrow 3Fe_{(LBE)} + 4O_{(LBE)} \tag{5-10}$$

The equilibrium constant or solubility product for this reaction is given in Ref. [569]:

$$K_{sp} = C^3_{Fe(LBE)} C^4_{O(LBE)} \tag{5-11}$$

where $C_{Fe(LBE)}$ and $C_{O(LBE)}$ are the concentrations of Fe and O dissolved in liquid LBE, respectively. The change of the Gibbs free energy of this dissolution/precipitation reaction is:

$$\Delta G_{Fe_3O_4/diss} = 3G^{ex}_{Fe(LBE)} + 4G^{ex}_{o(LBE)} - \Delta_f G^o_{Fe/Fe_3O_4} \tag{5-12}$$

The solubility of Fe in liquid LBE is given by the following equation [559]:

$$\log C_{Fe,s}(wt.\%) = 2.01 - \frac{4380}{T} \tag{5-13}$$

The excess Gibbs free energy (kJ/mol) for the dissolution of Fe in liquid LBE is calculated from its solubility given in Eq. (5-13), as follows:

$$G^{ex}_{Fe(LBE)}(kJ/mol) = -RT\ln C_{Fe,s} = 83.854 - 0.03848\mathrm{T} \tag{5-14}$$

The standard molar Gibbs free energy for Fe_3O_4 formation is given in HSC Chemistry Database (one can also refer to Table 3.1; different datasources may differ slightly):

$$\Delta_f G^o_{Fe/Fe_3O_4}(kJ/mol) = -1103.9 + 0.3146T \tag{5-15}$$

Inserting Eqs. (5-15), (5-14), and (5-8) into Eq. (5-12) yields the expression below for the calculation of the Gibbs free energy for the dissolution of Fe_3O_4 in liquid LBE:

$$\Delta G_{Fe_3O_4/diss} = 845.87 - 0.233T \tag{5-16}$$

When the chemical reaction (5-10) reaches thermodynamic equilibrium, then:

$$\Delta G_{Fe_3O_4/diss} = -RT\ln K_{sp} \tag{5-17}$$

Combining Eqs. (5-11), (5-16), and (5-17), the corresponding solubility product can be calculated by the following equation:

$$\log K_{sp} = \log[C^3_{Fe(LBE)} C^4_{O(LBE)}] = 12.17 - \frac{44182.8}{T} \tag{5-18}$$

Replacing $C_{\mathrm{Fe(LBE)}}$ with the solubility limit $C_{\mathrm{Fe,s}}$, the lower boundary of the HLM oxygen concentration range can be derived as follows:

$$\log C_{o,min}(wt.\%) = 1.535 - \frac{7760.7}{T} \tag{5-19}$$

Eqs. (5-9) and (5-19) are used to define the theoretical upper and lower boundaries of the HLM oxygen concentration range used during active oxygen control.

In Fig. 5.1, the LMC testing parameters (i.e., HLM oxygen concentration and temperature) collected from literature have been plotted together to show the actual oxidation and dissolution LMC regions for 9Cr, 12Cr F/M steels, and 316-type AuSS exposed to liquid LBE/Pb. The actual LMC regions are compared with thermodynamic predictions based on Eqs. (5-9) and (5-19), indicating that the experimentally determined oxidation and dissolution LMC regions deviate from the theoretically predicted ones. According to the experimental results, there is a high probability for both types of steels to undergo dissolution corrosion above 550 °C, esp. for the AuSS that may suffer dissolution corrosion even under HLM oxygen saturation. Moreover, in the 450–550 °C temperature range, there is a large region indicating the possible occurrence of mixed dissolution/oxidation corrosion modes. It can be concluded, therefore, that the service temperature for these steels should be kept below 450 °C (even below 400 °C, if necessary), and that the corresponding oxygen control boundaries can be defined between $C_O \approx 10^{-7}$ wt% and $C_O \approx 10^{-6}$ wt%, in order to ensure a safe operation for reactors with operating temperatures in the 250–450 °C range. It should be noted, however, that more LMC experiments are required to better identify the lower boundary of the proposed oxygen control 'window', esp. concerning crevices and occluded regions, since the data points resulting from long-term steel exposures to either static or flowing LBE in the low-temperature domain are insufficient. Based on the same idea, one can define appropriate oxygen control boundaries corresponding to different reactor operation temperature 'windows'.

Three methods have so far been invented to achieve precise oxygen control (Fig. 5.2), including automatic control of hydrogenated and oxygenated gases [564,570–572], mass exchangers [573,574], and electrochemical oxygen pumping [575,576]. Automatic control by injecting either hydrogenated or oxygenated gases into the HLM has been successfully used in many experimental facilities worldwide (Fig. 5.2a). The mass exchanger technology controls the HLM oxygen concentration in the main loop by automatically adjusting the temperature and LBE flow rate in bypasses packed with PbO solid spheres, which are subjected to either oxidation or dissolution according to the imposed conditions. A Venturi design (Fig. 5.2b) was used to alleviate the PbO poisoning problem, which

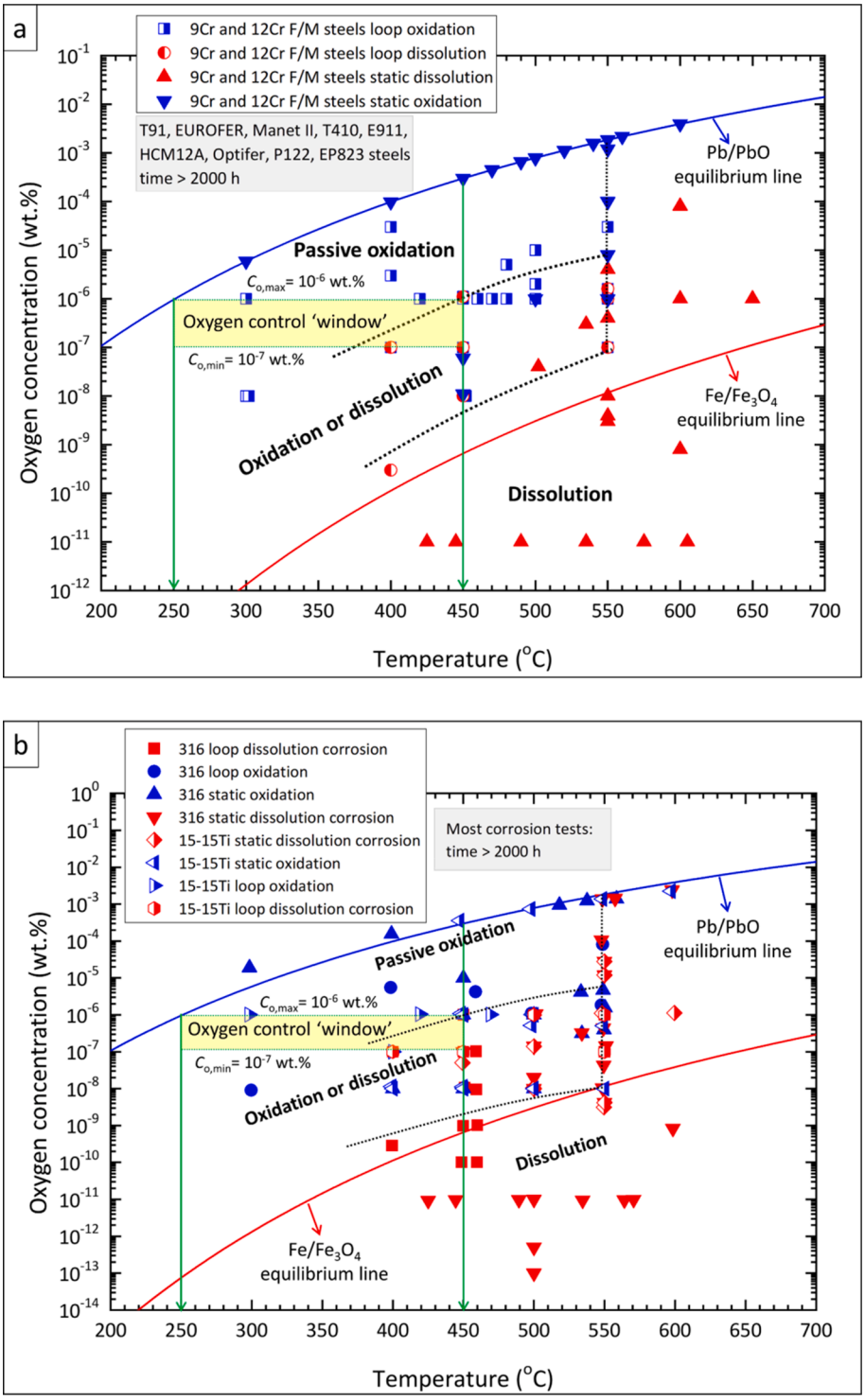

Fig. 5.1. Comparison of the oxygen control 'windows' defined by thermodynamics and LMC experimental data for reactors operating in the 250–450 °C temperature range: (a) 9Cr and 12Cr F/M steels; (b) 316L, 316Ti, and 15-15Ti AuSS. NB: only data from tests with duration >1000–2000 h have been considered, in order to eliminate the effect of incubation of oxidation and/or dissolution. Data collected from Refs. [34,40,42–44,92,95,96,101,104–107,115–118,125,127,133,136,141,167–169,172,176–178,180,181,183,187,192,196–199,202–206,208,210, 212–215,217–222,228,229,232,235,237–240,570,578–582].

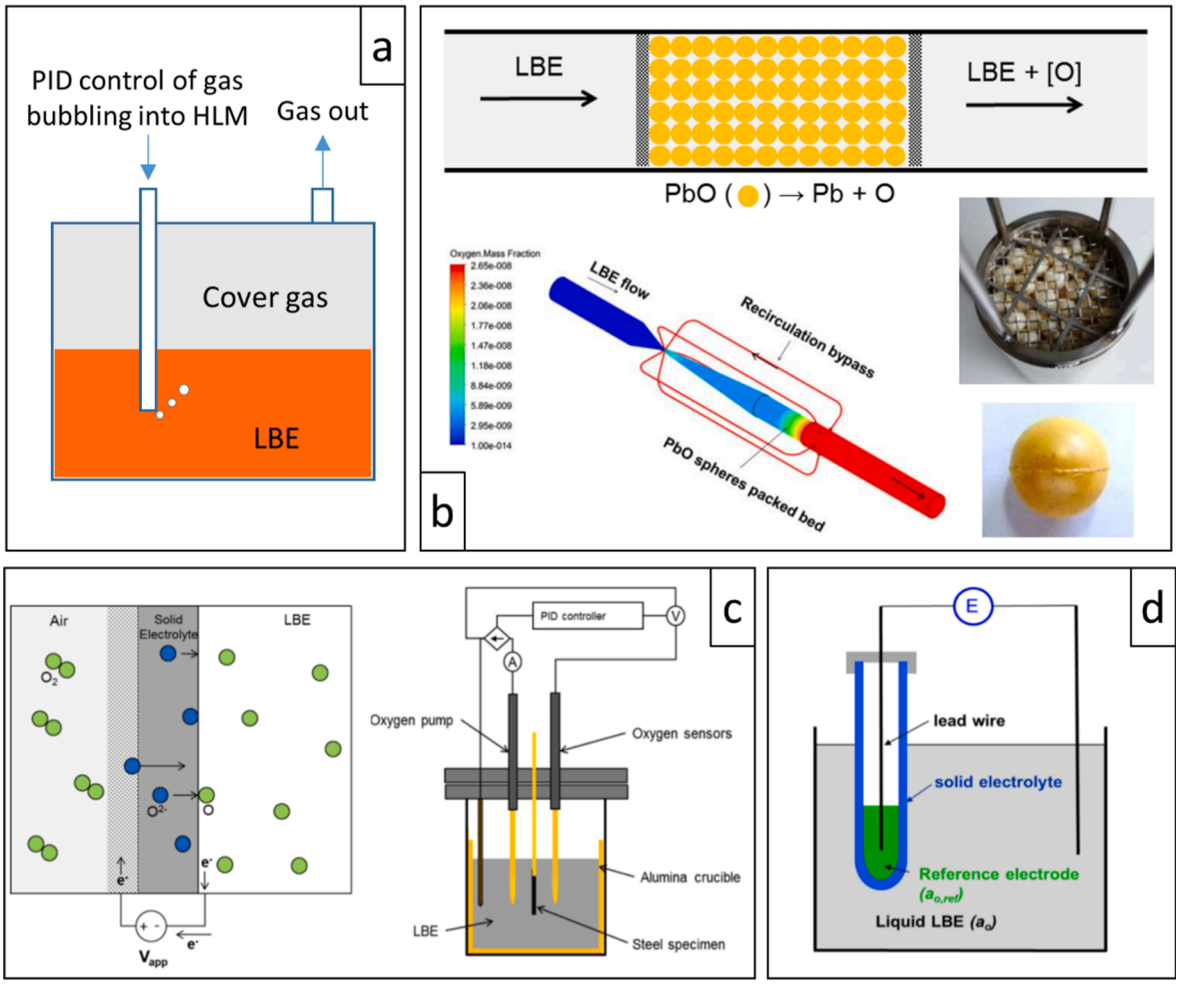

Fig. 5.2. (a) Schematic representation of automatic control by the supply of hydrogenated or oxygenated gases into the HLM bath. (b) A Venturi-type mass exchanger consisting of a packed bed of PbO solid spheres [577]. Working principles of (c) an electrochemical oxygen pump [575], and (d) an electrochemical oxygen sensor, adapted from [583].

is caused by the formation of stable oxides of various elements dissolved in the liquid LBE (e.g., Fe); such oxides tend to deposit on the surfaces of the PbO solid spheres, progressively inhibiting their dissolution process [577]. Electrochemical oxygen pumps (Fig. 5.2c) control the flux of oxygen ions (O^{2-}) through a solid electrolyte (e.g., yttria-stabilised zirconia, YSZ) by regulating an externally applied electrical potential [575,576].

Potentiometric oxygen sensors are essential for active oxygen control. They are employed to closely monitor the oxygen concentration dissolved in liquid Pb/LBE. The sensors are primarily composed of three parts, including the solid electrolyte, the reference electrode, and the lead wire. The key part is the solid electrolyte, often made of a YSZ tube with one end open and the other end closed. The YSZ tube is an oxygen ion conductor, while the reference electrode is usually made of metal/metal oxide powders (e.g., Bi/Bi_2O_3, Cu/Cu_2O, etc.) [568,584–586] or air/catalyst (e.g., Pt, Sr-doped La-manganite, Gd-doped ceria, etc.) [587]. Metallic materials with good compatibility with the reference electrode can be used as lead wires, such as refractory metals and stainless steels. The working principle of oxygen sensors is based on a galvanic cell (Fig. 5.2d). The difference of the oxygen activity between the reference electrode and the working electrode (i.e., liquid Pb or LBE) gives rise to an electromotive force that can be correlated with the two oxygen activities, using the well-known Nernst equation:

$$E = \frac{RT}{2F}\ln\left(\frac{a_{0,ref}}{a_{0,w}}\right) \tag{5-20}$$

where R is the gas constant, T is the absolute temperature (K), F is the Faraday constant, $a_{o,ref}$ is the oxygen activity at the reference electrode, and $a_{o,w}$ is the oxygen activity at the working electrode (i.e., liquid LBE). $a_{o,ref}$ is known from thermodynamics, thus $a_{o,w}$ can be calculated after E is measured by a high-impedance voltmeter. The concentration of dissolved oxygen in the HLM (C_O) can be derived from the oxygen activity ($a_{o,w}$) based on thermodynamics, and the equations correlating E and C_O for various reference

electrodes are described in detail in Ref. [109].

Ballinger and Lim pointed out [31] that relying on the iron oxide (Fe_3O_4) film for LMC mitigation could be discounted in a real system, due to the following reasons: first, the actual HLM oxygen concentration could be distributed inhomogeneously, as, for example, at places where mass transfer is inhibited due to flow blockage. In this case, oxygen may be anomalously low, resulting to a shift of the specified oxygen control 'window' to the domain of dissolution corrosion. In addition, at 570 °C, Fe_3O_4 could be subjected to phase transformation into wüstite (FeO), which has a negative effect on the oxide scale protectiveness, as previously discussed. More importantly, at temperatures >500 °C, elemental solubility and corrosion kinetics are enhanced, making LMC mitigation by means of active oxygen control more difficult. Under these conditions, more stable oxides, such as Al_2O_3 and SiO_2, should be adopted to ensure corrosion resistance at higher temperatures (>500 °C) and within a wider oxygen concentration 'window' [31]. Attention should be paid to the long-term stability of these oxide scales, as they might lose their structural integrity due to stresses induced by a thermal expansion coefficient mismatch between oxides and steel bulk, as well as due to internal oxidation [588].

5.3. Design of innovative structural materials

Even though the present review focuses mainly on commercial AuSS and F/M steels as candidate materials for the construction of near-term Gen-IV LFRs, it would be incomplete if it did not provide an overview of the currently proposed approaches towards the development of more suitable structural materials, i.e., materials that perform reliably in wider ranges of operating conditions (i.e., temperature, HLM oxygen concentration and flow rate). As explained in Chapters 3 and 4, the Gen-IV LFR operational paradigms striving to control LMC and LME have partly contradicting requirements; for example, both LMC and LME are promoted by low HLM oxygen concentrations, as these reduce the protective oxide scales covering the steel surface; on the other hand, high temperatures (>500 °C) favour LMC (esp. dissolution corrosion in 316L and similar AuSS) and limit LME (the upper limit of the "ductility trough" in T91 F/M and similar steels is typically around 500 °C); moreover, low tensile stresses and slow-flowing HLMs allow a better control of both LMC and LME, as they are less damaging to the oxide scales covering the steel surface. Therefore, steels forming dense, protective and adherent oxide scales, or low-solubility near-surface enrichment layers that are stable at higher tensile stresses could expand the currently narrow envelopes of safe operating conditions into economically viable operating regimes for Gen-IV LFRs. Section 5.3 provides an overview of the most important approaches towards the development of innovative structural materials; these involve (a) steel doping with specific alloying elements that improve the steel resistance to both LMC and LME by forming *in situ* protective oxide scales, (b) surface coatings that protect the substrate steel from LMC and LME, and (c) modifications of both the bulk and local (i.e., sub-surface and/or GBs) steel structure to improve oxidation resistance and/or limit the nucleation of undesirable LMC features, such as dissolution 'pits'.

5.3.1. Elemental alloying of steels

Elemental alloying refers to adding strong oxide-forming elements (e.g., Al and Si) to either the bulk or the surface of structural materials [93,132,133,207,245,246,578,589–594]. In addition, adding corrosion inhibitors, such as zirconium (Zr) and Ti, to the HLM coolant has also been demonstrated to be an effective LMC mitigation method [31,175]. The addition of Zr or Ti into the HLM could promote formation of nitrides and carbides that are insoluble in liquid Pb/LBE. These nitride and carbide layers act as protective films for carbon steels and low-alloy steels, while the protection is not effective for stainless steels [30,31].

The addition of Al and Si alloying elements develops thin and stable oxide scales that can effectively inhibit the interdiffusion of cations and anions through their thickness. This leads to slow oxidation kinetics, thereby greatly improving long-term corrosion resistance. Moreover, oxides containing Al and Si were reported to have a self-healing capacity, which might increase the oxide scale tolerance to scratches or local mechanical damage that might occur during long-term service in a nuclear reactor. The role of Al or Si also depends on the content of Cr [31,595], as a higher Cr content leads to formation of protective alumina at lower Al contents [596].

The excellent LMC resistance of Al/Si-containing Fe-Cr ferritic steels and Fe-Cr-Ni AuSS has been demonstrated in many studies [111,132,207,214,236,238,245,246,248,250,592–595,597–609]. In particular, AFA stainless steels with a suggested nominal composition of Fe-(20–29)Ni-(15.2–16.5)Cr-(2.3–4.3)Al (all in wt%) might exhibit good resistance to both LMC and LME, since these steels are effectively passivated by the formation of Cr_2O_3 and Cr_2O_3-Al_2O_3 oxide scales, and they show little susceptibility to LME due to their *fcc* crystal structure [593,610]. High Mn-alloyed AFA steels also showed good LMC resistance in liquid LBE at 450 °C [611].

Al-enriched HEAs (e.g., the $Al_xCrFeNi$ series) are also promising materials for use in liquid Pb/LBE, since protective oxide scales, such as Al_2O_3 and Cr_2O_3, have formed after an exposure of 1000 h at 600 °C to liquid Pb with $C_O \approx 10^{-6}$ wt% [612]. On the other hand, Al-free HEA (e.g., $Fe_{40}Mn_{10}Ni_{10}Co_{20}Cr_{20}$, all in at.%) exhibited a poor resistance to dissolution corrosion in contact with oxygen-poor ($C_O \approx 10^{-13}$–10^{-12} wt%), liquid LBE at 450 °C due to the selective leaching of Ni and Mn [613]. In addition, Gong et al. [614] reported a strong LME effect of a dual-phase (ferrite-like *bcc*/B2 phase & austenite-like *fcc* phase) $Al_{0.7}CoCrFeNi$ HEA in contact with oxygen-saturated liquid LBE. These authors attributed the LME of this HEA to adsorption-induced interatomic cohesion of the *bcc*/B2 phase at 350 °C and *bcc/fcc* interphase boundary wetting at 500 °C, despite the Al enrichment that should have normally promoted the formation of an LME-inhibiting, protective Al_2O_3 oxide scale. These results suggest that future designs of Al-enriched and/or other HEAs for use in liquid LBE should consider minimising dissimilar (*bcc/fcc*) phase boundaries and the fraction of ferrite-like *bcc* phases, so as to reduce the risk of high-temperature boundary wetting, on one hand, and the occurrence of LME in the ferrite-like *bcc* phases, on the other.

Even though doping the bulk steel with Al or Si improved its LMC resistance, the steel mechanical properties were reported to deteriorate. For instance, Si-enriched F/M steels showed poorer impact properties when the Si content exceeded 0.4 wt%, due to formation of δ-ferrite [615,616]. In particular, Si-enriched steels were much more susceptible to LBE-induced LME in comparison to

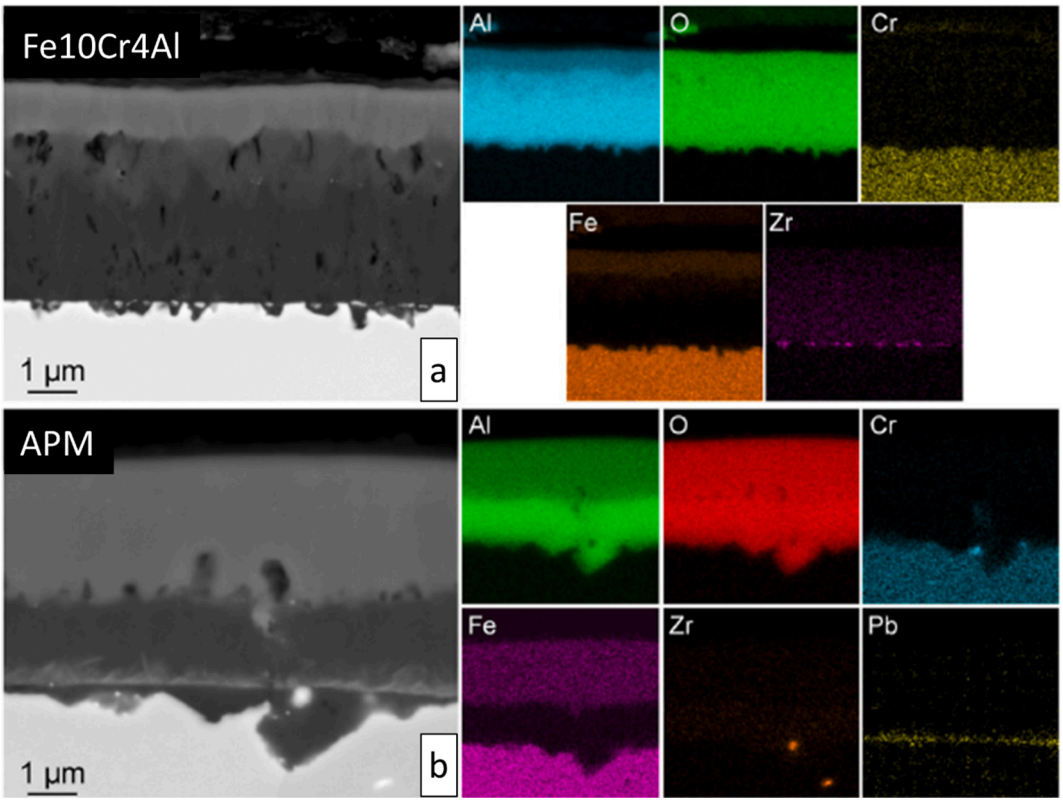

Fig. 5.3. EDS[†] elemental maps of (a) Fe10Cr4Al and (b) APM (Fe21Cr5.8Al) alloys after exposure to liquid Pb at 800 °C, showing the formation of an Fe-enriched Al_2O_3 scale. Adapted from [618]. In this case, Fe10Cr4Al was proposed as a candidate structural material for concentrated solar power (CSP) systems, which require high operation temperatures for better thermal efficiency.

their low-Si or Si-free counterparts [251]. Moreover, Si deteriorated weldability when its content exceeded 0.6 wt% [616], while Al had similar advantages and disadvantages. For instance, commercial FeCrAl alloys containing around 15–20 wt% Cr were reported to be embrittled due to α-α' phase separation in the 400–600 °C range [617], which is the targeted temperature 'window' for Gen-IV LFRs cooled by liquid Pb. Cr can facilitate Al_2O_3 formation, but a high Cr content has a detrimental effect on the alloy fracture toughness, due to the α-α' phase separation. For this reason, ductile FeCrAl alloys with low Cr and Al contents (e.g., Fe-10Cr-4Al) are being developed. Low-alloyed FeCrAl alloys can form protective Al_2O_3 scales at very high temperatures ($\leq$900 °C), when the addition of reactive elements (e.g., rare-earth elements, RE, such as Y; Zr and Ti) and the RE/C ratio are optimised [51,113,590,596,618], see Fig. 5.3. The addition of REs improves oxidation resistance at high temperatures and interfacial adherence of the oxide scales by suppressing Cr-carbide formation. However, the negative effect of the formation of α' clusters in low-Cr FeCrAl alloys (e.g., Fe-10Cr-5Al) under neutron irradiation is a concern [619,620]. Similar to other ferritic steels (e.g., T91), Fe10Cr4Al was extremely susceptible to LME in contact with liquid LBE at ~350 °C, as evidenced by completely cleaved fracture surfaces (Fig. 5.4), irrespective of the HLM oxygen concentration and applied strain rate during testing [562]. An increase in Al content can make FeCrAl more susceptible to LME than an increase in Cr content [621]. The strong LME effect in FeCrAl alloys was attributed to Al-induced solid solution strengthening and the probably more brittle nature of the Al-enriched oxides, while the ductility of the Fe10Cr4Al alloy in LBE recovered fully at 500 °C [622]. These results indicate that Al-rich oxide scales cannot sustain high tensile stresses so as to fully prevent LME in FeCrAl alloys [562], which is unfortunate as these materials possess an excellent LMC resistance.

The fact that the bulk steel mechanical properties are negatively affected by the addition of Al or Si could be overcome by doping only a surface steel layer, thereby leaving the bulk steel properties unaltered. Surface alloying could be realised by the GESA (Gepulste ElektronStrahl Anlage) surface modification process [133,192,598,623,624], various diffusion processes [95,104,578,591], or the deposition of functionally graded coatings [601].

The GESA process employs an intense pulsed electron beam as a strong heat source to melt pure Al or Al-containing alloy (e.g., FeCrAl and FeCrAlY) coatings deposited on the steel surface, so that the chemically modified, Al-enriched surface layer can form *in situ* Al-based oxide scales when exposed to the oxygen-containing HLM [133,192,598,623,624]. The chemically modified surface layers produced by the GESA process are marked by fine-grained or amorphous microstructures with excellent adhesion to the steel substrate. In particular, the GESA process can be scaled up to allow for surface alloying of full-length fuel cladding tubes, making this technique very promising for industrial-scale production. It is recommended that the Al concentration in the surface layer is kept in the 4–6 wt% range, in order to ensure formation of a thin, protective Al_2O_3 scales without affecting the mechanical properties of the chemically

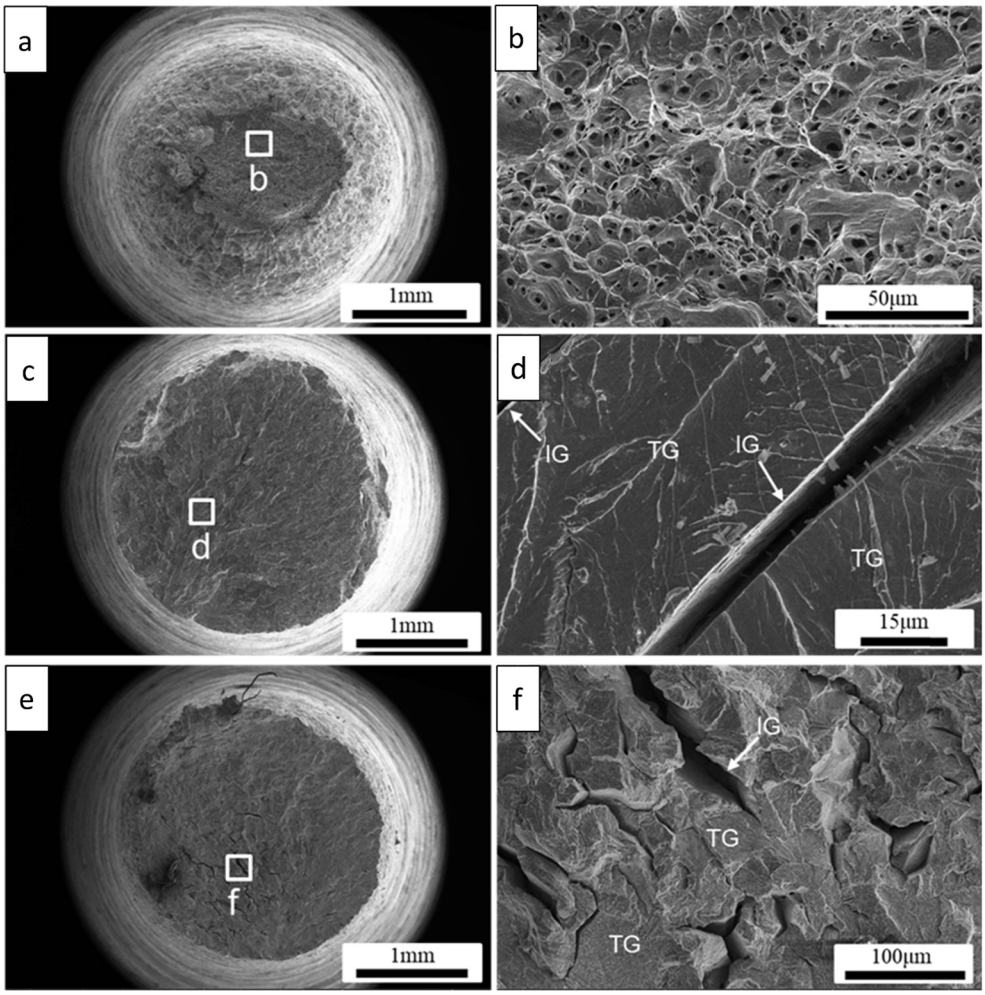

Fig. 5.4. SEM† images of fracture surfaces of an Fe10Cr4Al alloy tested in tension in Ar (a,b), oxygen-poor (c,d) and oxygen-saturated (e,f) liquid LBE at 350 °C, under an applied strain rate of $\dot{\varepsilon} \approx 5 \times 10^{-4}$ s^{-1}. "IG" denotes intergranular cracking; "TG" denotes transgranular cracking. Adapted from [562].

modified surface layer. Al concentrations>24 wt% would make the surface layer vulnerable to dissolution corrosion, due to the high solubility of Al in liquid Pb/LBE. Moreover, high Al contents could result in easy cracking of the surface layer, even during the coating deposition process.

Diffusion processes, such as hot dipping, melting of an Al foil, gas diffusion, and pack cementation, could also be used to form an aluminised layer on the steel surface via atomic interdiffusion [95,104,578,591,625]. Aluminised surfaces using FeAl pack cementation were found to be LMC-resistant in contact with liquid LBE up to 600 °C, when the LBE oxygen concentration was higher than $C_O \approx 10^{-8}$ wt%, even though local damage possibly caused by turbulent flow was observed [578]. Müller et al. [95,104] found that the formation of FeAl on a steel surface treated by either melting of an Al foil or by hot dipping in an Al-12 at.% Si melt was needed for the formation of protective scales, otherwise, dissolution corrosion occurred. Kurata et al. [591] compared two different surface-aluminizing methods: one was gas diffusion of Al_2O_3, $FeAl_2$, and $AlCr_2$, while the other was hot dipping in an Al melt. Corrosion tests on steels treated by these two methods showed that the aluminised layer prepared by the first method protected successfully the steel exposed to liquid LBE at 450 °C and 550 °C for 3000 h; on the other hand, the dipping method produced a surface layer that suffered severe Al dissolution. The industrial process of the surface-aluminizing treatment is available for 316L AuSS. When these methods are applied to T91 F/M steels, the processing temperature must be kept below the standard tempering temperature for these steels (i.e., ~760 °C), in order to avoid modifying the steel microstructure and prevent the formation of intermetallics.

5.3.2. Coating deposition & surface modification of steels

Candidate coating materials that aim primarily at limiting and/or preventing undesirable LMC effects include refractory metals [180,243,626], Al- or Si-containing metallic alloys [192,525,596,626–632], and certain ceramic materials [243,626,632–635].

Refractory metals, such as W, Mo, and Ta, and their alloys have very low solubilities in liquid Pb/LBE, therefore, coatings made of

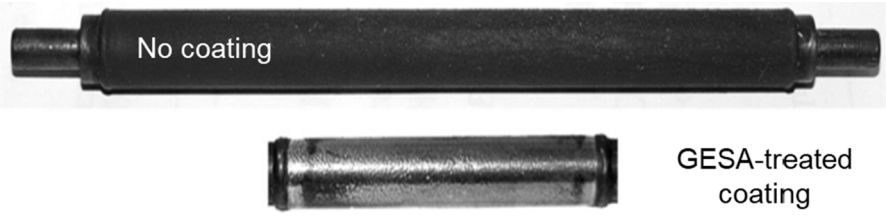

Fig. 5.5. Visual comparison of the surface appearance of T91 F/M steel fuel cladding tubes with and without GESA-treated FeCrAlY coatings after exposure to flowing ($v \approx 1$–1.2 m/s) liquid LBE at 550 °C for 2000 h. The surface of the fuel cladding tube without surface modification is dark, while the surface of the modified tube is shiny, showing the superior LMC resistance of the latter [192].

refractory metals can increase the steel resistance to HLM dissolution attack [216,260]. On the other hand, refractory metals are very susceptible to oxidation, forming unstable and even volatile oxides, such as the formation of gaseous MoO_3 at temperatures >800 °C. In oxygen-saturated liquid LBE at 600 °C, thick, multi-layered oxide scales consisting of MoO_2, $PbMoO_4$ and Pb_2MoO_5 were observed after a short-term exposure of 100 h [244]. Successful application of these coatings requires very low oxygen concentrations in the liquid Pb/LBE to prevent in-service metal oxidation [260]. Due to their high susceptibility to oxidation, preparation of refractory metal coatings is a challenging task, as coating deposition must be performed in an atmosphere with strictly controlled (i.e., ultra-low) oxygen content. Otherwise, the coatings can be embrittled due to oxygen contamination during processing. In addition, refractory metals and alloys, for instance Mo, are generally very vulnerable to neutron irradiation-induced embrittlement for irradiations below 800 °C [636]. This is another drawback against their use in a nuclear environment, esp. for applications close to the reactor core.

Al- or Si-containing coatings require a certain amount of oxygen to slowly develop dense, thin, and self-healing oxide scales on the steel surface. These oxides act as effective barriers against ion diffusion, so that, on one hand, oxidation is very slow and, on the other hand, dissolution corrosion can be effectively prevented. Regarding Al-containing coatings, FeAl compounds have been deposited on T91 F/M steels, showing an excellent LMC resistance in contact with liquid Pb/LBE up to 700 °C [626]. However, FeAl coatings showed a susceptibility to cracking under external loads, resulting in HLM dissolution attack at the crack locations [629]. FeCrAlY compounds are another class of strong alumina formers, but their deposition demands attention to the quality of the coating structure and its adhesion to the substrate steel. These coatings, prepared by a low-pressure plasma spraying process, showed porosity and weak adhesion to the steel substrate, i.e., characteristics that discourage their potential use in contact with a HLM coolant. To optimise the coating quality, the GESA process is employed to re-melt the coating, thereby eliminating coating porosity and greatly improving its adhesion to the steel substrate [637]. FeCrAlY-coated specimens of both T91 F/M steels and 316L AuSS, as well as compositionally similar steels, exhibited improved LMC resistance in a wider range of exposure conditions due to the formation of thin, passivating Al_2O_3 scales that adhered well to the steel substrates (Fig. 5.5). Moreover, mechanical tests (e.g., internally pressurised creep-to-rupture tests, fatigue tests) on fuel cladding tubes and cylindrical solid samples in contact with liquid Pb/LBE at high temperatures showed that the GESA-treated FeCrAlY coatings prevented LME-induced brittle failure in the surface-modified T91 F/M steels, without any detectable changes in tensile, creep, and fatigue properties, as opposed to the significant property degradation of the same steels without surface modification [513,515,530,596]. Moreover, the resistance of steels to fretting wear, an important failure mechanism for fuel assemblies, was significantly improved by the GESA surface modification [37–39]. *In situ* irradiation/corrosion tests on FeCrAlY-coated T91 F/M steels performed with 72 MeV protons to a damage dose of 2.5 dpa in contact with flowing ($v \approx 1$ m/s) liquid LBE, with unknown concentration of dissolved oxygen, at ~400 °C for 900 h showed no evident steel surface damage associated with LBE corrosion attack [548]. This indicates the protectiveness of the GESA-treated FeCrAlY coating against the coupled effects of irradiation and LBE corrosion. Nevertheless, a recent study [525] showed that the GESA surface treatment did not successfully suppress the LME of 9Cr-, 12Cr- and 14Cr-ODS F/M steels in contact with liquid LBE; on the contrary, it even promoted the occurrence of LME under tensile loading. An FeCrAl coating first deposited on 316L AuSS by E-beam PVD and then subjected to the GESA treatment cracked during tensile loading up to 233 MPa at 550 °C in contact with oxygen-containing ($C_O \approx 10^{-7}$ wt%) liquid LBE. Cracking of the GESA-treated FeCrAl coating resulted in local LBE dissolution attack of the 316L AuSS substrate [596], despite the fact that most of the coating remained adherent to the steel substrate and no delamination was observed. Susceptibility to coating cracking is expected to be exacerbated due to irradiation embrittlement combined with LME below 400 °C [548]. Similar to the role of Al, Si can also react with O to form protective Si-rich oxide scales, as mentioned in Chapter 3. In particular, an Fe-12Cr-2Si functionally-graded coating increased the cracking resistance of P92 fuel cladding tubes [111,601,638]. Tubes of this functionally graded composite fuel cladding material have been successfully processed on the semi-industrial scale, from billet fabrication to co-extrusion tube drawing.

Ceramic candidate coating materials include oxides, carbides, nitrides, etc. [243,596,626,633,634,640–644]. Oxides, such as ZrO_2, Y_2O_3, and Al_2O_3, have been used as coating materials for LMC prevention, showing excellent LMC resistance in contact with liquid Pb/LBE, due to their very low solubilities in HLMs. Similar LMC properties have also been achieved with other ceramic coating materials, such as TiZrC, AlTiN, TiSiN, SiC, Si_3N_4, TiN, and CrN, which react *in situ* with the dissolved oxygen in liquid LBE to form passivating oxide scales based on Ti (TiO_2), Al (Al_2O_3), Si (SiO_2), and/or Cr (Cr_2O_3).

The main problem of ceramic coatings is the lack of damage self-healing in service. Moreover, most of the ceramic coatings are generally brittle, leading to easy cracking and spallation under externally applied loads. These inherent weaknesses bear the risk of undesirable LMC and/or LME effects on the steel substrate at the locations where the coating is damaged [645]. For instance, a TiAlN coating deposited by magnetron sputtering showed excellent adherence to a T91 F/M steel substrate in the absence of an externally

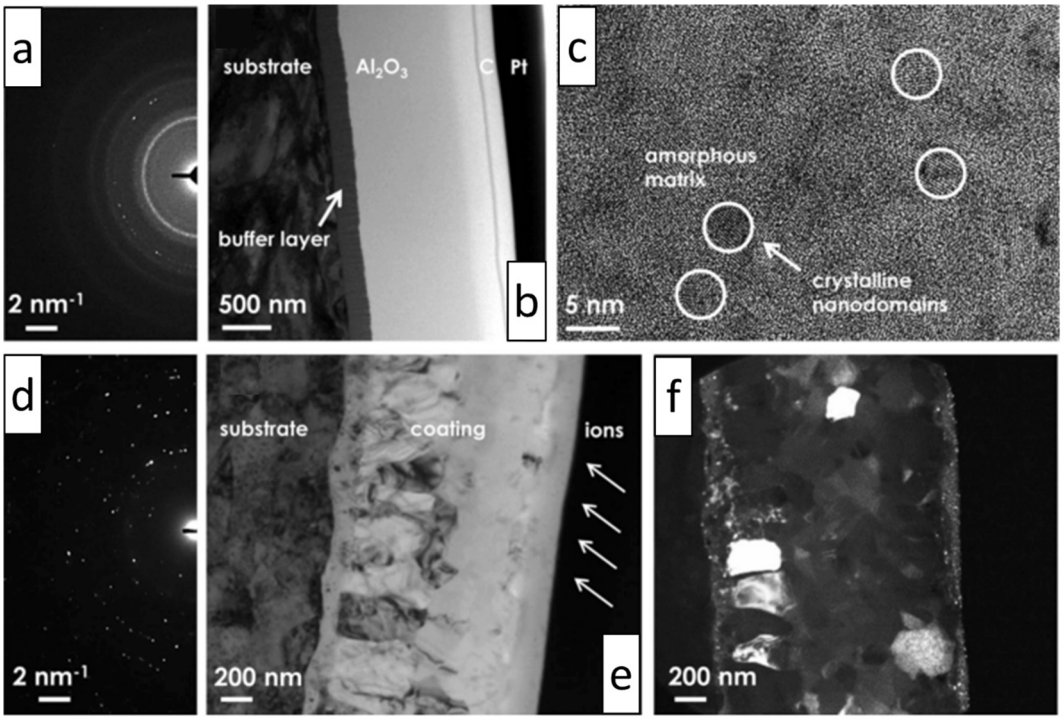

Fig. 5.6. TEM† investigation of as-deposited (a-c) and irradiated (d-f) Al_2O_3 coatings deposited by PLD†. The as-deposited Al_2O_3 coating is fully dense and consists of crystalline Al_2O_3 nanodomains that are homogeneously distributed in an amorphous Al_2O_3 matrix. Upon ion irradiation, the coating crystallinity increased and the nano-sized Al_2O_3 grains coarsened. Adapted from [639].

applied load, but numerous cracks formed in this coating under tensile loading up to the steel UTS†, with particularly severe damage at the notch (notched tensile specimen), due to the high stress intensity in the vicinity of the notch [596]. It should be pointed out, however, that the coating mechanical stability must be checked under conservative external loads that are more representative for the actual reactor operation conditions.

Recently, a nanocrystalline Al_2O_3 coating deposited by pulsed laser deposition (PLD) has shown great potential to overcome the drawbacks of conventional ceramic coatings [639,646]. These nanocrystalline (or amorphous) coatings demonstrated excellent resistance to cracking under different mechanical tests, including nanoindentation, cyclic nano-impact, scratch, and thermal cycling tests. In order to minimise stresses caused by irradiation-induced differential swelling of coating and steel substrate, an FeCrAlY buffer layer was introduced between the 15-15Ti AuSS substrate and the nanocrystalline Al_2O_3 coating. It was found that this buffer layer could withstand ion irradiation with 12 MeV Au^{5+} and 18 MeV W^{8+} up to 150 dpa at the coating/buffer layer interface, and up to 200–450 dpa at the steel/buffer layer interface, even though grain coarsening in the coating was observed after ion irradiation (Fig. 5.6). Corrosion tests in static liquid Pb with $C_O \approx 10^{-8}$ wt% at 550 °C for up to 4000 h demonstrated the excellent protectiveness of these Al_2O_3 coatings against LMC, both in the unirradiated and ion irradiated states (Fig. 5.7). Other coating techniques were also used for the deposition of Al_2O_3 coatings. For example, radio frequency magnetron sputtering was recently demonstrated to be a promising technique for the deposition of dense, adherent Al-O (Al_2O_3) coatings on T91 F/M steels; these coatings showed good LMC resistance in contact with liquid Pb [596,647]. In addition, Al_2O_3 coatings deposited by detonation spraying were found to be very resistant to cracking under tensile loading in contact with liquid LBE [596].

The MAX ($M_{n+1}AX_n$) phases have also exhibited very promising resistance to LMC and/or erosion in contact with liquid Pb/LBE, therefore, they can be considered as candidate materials for anticorrosion coatings on fuel cladding tubes or as structural materials (in monolithic form) for particular applications that demand resistance to erosion/corrosion (e.g., pump impellers) or crevice corrosion (bearings, bushings). Rivai and Takahashi [82] reported that Ti_3SiC_2 exhibited good compatibility with liquid LBE ($C_O \approx 5 \times 10^{-6}$ wt %) at 700 °C for up to 1000 h. Barnes et al. [78] exposed Ti_3SiC_2 to liquid Pb circulating by natural convection at 650 °C and 800 °C for 1000 h; they did not observe any LMC damage except from local interactions at pre-existing surface defects. Utili et al. [80] did not find any evidence of LMC attack on Ti_3SiC_2 exposed at 500 °C for 2000 h to flowing ($v \approx 1$ m/s) liquid Pb with $C_O \approx 10^{-6}$ wt%. Heinzel et al. [79] exposed Ti_3SiC_2 to static liquid Pb/LBE containing $C_O \approx 10^{-8}$ wt% and $C_O \approx 10^{-6}$ wt% at 550–750 °C for up to 4000 h, invariably observing the formation of thin (1–7 μm) rutile (TiO_2) oxide scales on the surface of the exposed MAX phase ceramics. In a later study, Heinzel et al. [81] subjected both Ti_3SiC_2 and Ti_2AlC to long-term (up to 10,000 h) exposures to static liquid LBE containing $C_O \approx 10^{-8}$ wt% and $C_O \approx 10^{-6}$ wt% at 550–700 °C. They reported that the Ti_3SiC_2 MAX phase formed thin TiO_2 oxide scales at 550 °C and $C_O \approx 10^{-6}$ wt%, complex oxide scales (single-layer TiO_2 outer scale, duplex SiO_2/TiO_2 inner scale) at 650/700 °C and $C_O \approx 10^{-6}$ wt%, and non-uniform TiO_2 scales with concurrent oxidation of the secondary phases (mixture of TiC, SiC, and Ti silicides) at 700 °C and $C_O \approx$

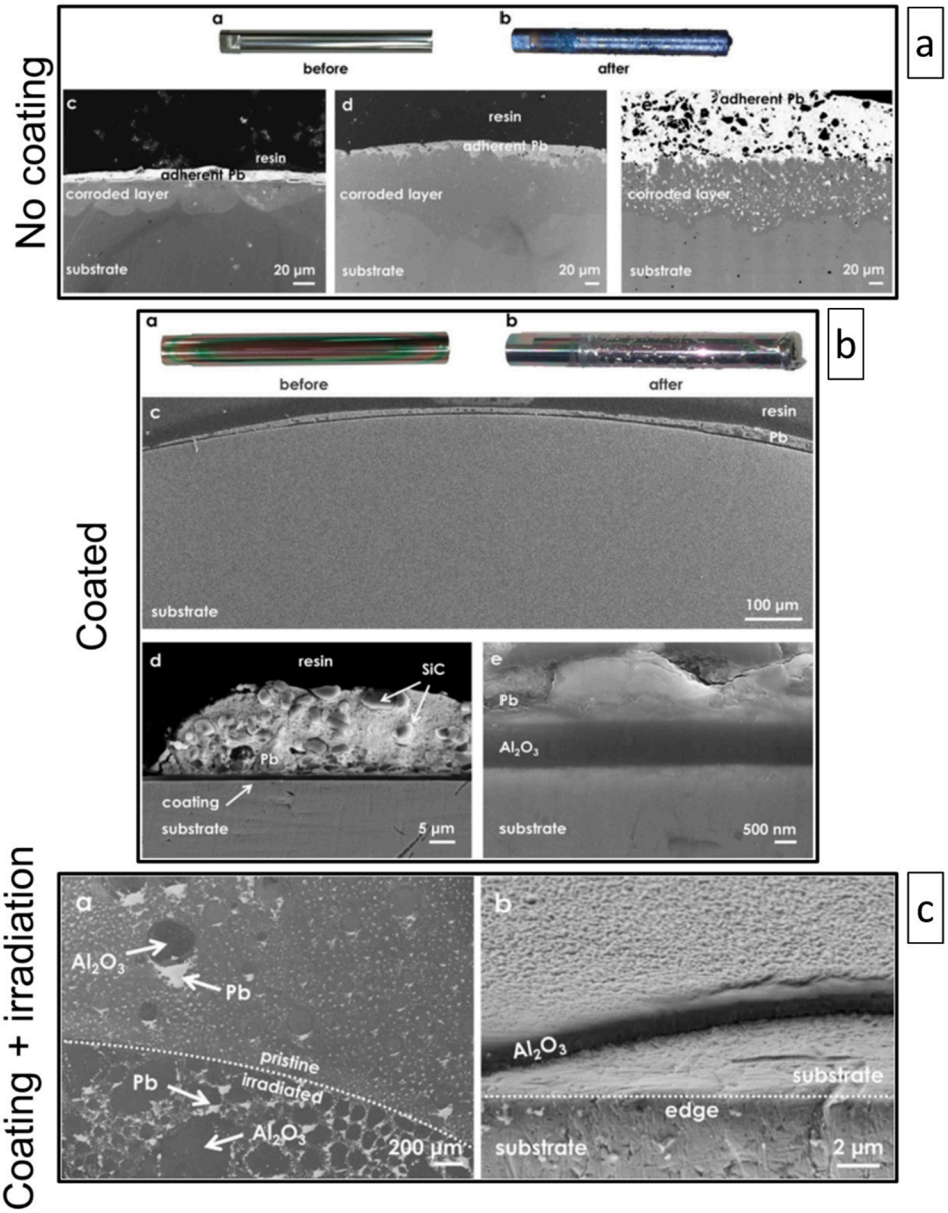

Fig. 5.7. Comparison of the LMC effects in 15-15Ti AuSS with and without PLD†-deposited nanocrystalline Al_2O_3 coatings in contact with liquid Pb ($C_O \approx 10^{-8}$ wt%) at 550 °C for 4000 h. Uncoated 15-15Ti AuSS suffered dissolution corrosion and Pb penetration into the steel bulk (a), while Al_2O_3-coated 15-15Ti AuSS was well protected from liquid Pb dissolution attack, both in the unirradiated (b) and irradiated (c) states. Adapted from [639].

10^{-8} wt% (Fig. 5.8a–c). On the other hand, the Ti_2AlC MAX phase formed (rather protective) mixed TiO_2/Al_2O_3 scales at 550–700 °C and $C_O \approx 10^{-6}$ wt%, and (less protective, susceptible to LBE penetration) TiO_2 scales at 550 °C and $C_O \approx 10^{-8}$ wt%; on the other hand, dissolution corrosion of the secondary phases in Ti_2AlC (TiC, Al_5Ti_2, and $Ti_4Al_2C_2$) occurred after its LBE exposure at 650–700 °C and $C_O \approx 10^{-8}$ wt% (Fig. 5.8d). In contact with low-oxygen ($C_O \approx 10^{-8}$ wt%) liquid LBE at 550–700 °C, protective oxide scales could not form on Ti_3SiC_2, and only secondary (parasitic) phases close to the sample surface underwent oxidation (Fig. 5.8c). All early studies dedicated to the LMC behaviour of MAX phase-based ceramics demonstrated that their LMC resistance depended on the stoichiometries of both the principal MAX phase compound and the parasitic phases (esp. binary intermetallics), and the exact exposure conditions (temperature, HLM C_O, possibly also exposure duration). For applications close to the reactor core (e.g., fuel cladding tube coatings), one should strive for phase-pure MAX phase ceramics, not only for the observed vulnerability of secondary phases to LMC (Fig. 5.8c and d), but also due to the fact that materials consisting of multiple phases are expected to be susceptible to irradiation-induced differential swelling.

In a more recent work, Lapauw et al. [83] assessed the resistance of different MAX phase ceramics to dissolution corrosion and

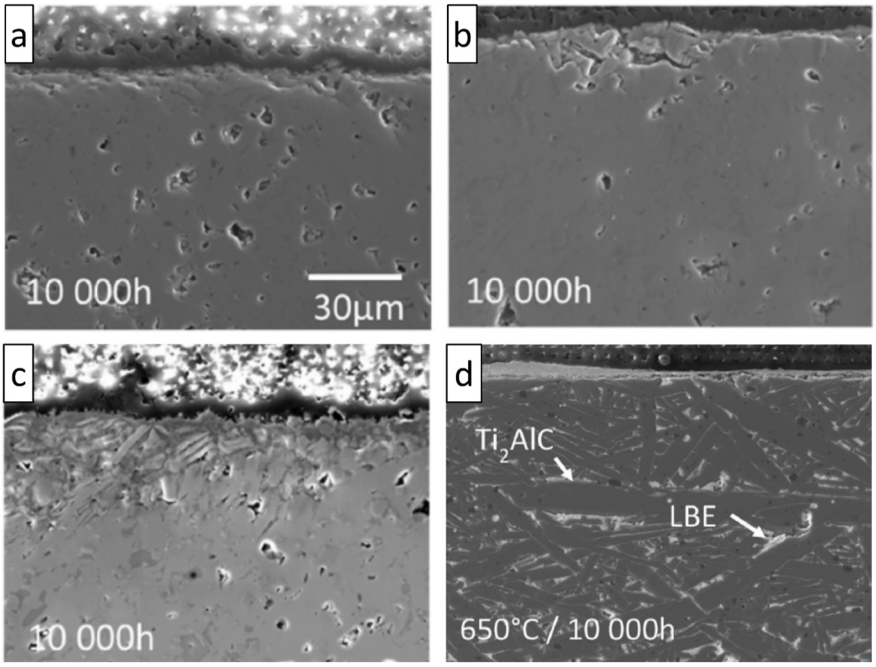

Fig. 5.8. Ti_3SiC_2 exposed to static liquid LBE ($C_O \approx 10^{-8}$ wt%) for 10,000 h at (a) 550 °C, (b) 650 °C, and (c) 700 °C. (d) Ti_2AlC exposed to static liquid LBE with $C_O \approx 10^{-8}$ wt% for 10,000 h at 650 °C. Adapted from [81].

erosion/corrosion in contact with static and fast-flowing liquid LBE, respectively. More specifically, the resistance of Maxthal® 312 (Ti_3SiC_2), Maxthal® 211 (Ti_2AlC & Ti_3AlC_2), $(Ti,Nb)_2AlC$, Ti_3AlC_2, Nb_2AlC, Nb_4AlC_3, $(Nb_{0.85},Zr_{0.15})_4AlC_3$, Zr_2AlC, Zr_3AlC_2, Ti_2SnC, and $(Zr_{0.8},Ti_{0.2})_2AlC$ & $(Zr_{0.8},Ti_{0.2})_3AlC_2$ to dissolution corrosion was assessed in contact with oxygen-poor ($C_O \leq 2.2 \times 10^{-10}$ wt%), static liquid LBE at 500 °C for 1000–3500 h. Moreover, the resistance of Zr_2AlC, Zr_3AlC_2, and $(Nb_{0.85},Zr_{0.15})_4AlC_3$ to erosion/corrosion was assessed in contact with oxygen-poor ($C_O \approx 5 \times 10^{-9}$ wt%), fast-flowing ($v \approx 8$ m/s) liquid LBE at 500 °C for 1000 h. The tested MAX phase-based ceramics maintained their structural integrity at all exposure conditions, while their overall performance was greatly affected by the presence of parasitic phases, such as intermetallic compounds and low melting point inclusions (e.g., Sn). Fig. 5.9 shows the complete lack of interaction for most of the MAX phase ceramics (i.e., Maxthal® 211 & 312, $(Ti,Nb)_2AlC$, Ti_3AlC_2, Nb_2AlC, Nb_4AlC_3, and $(Nb_{0.85},Zr_{0.15})_4AlC_3$) tested under static LBE conditions; moreover, Ti_2SnC remained essentially unaffected, except from the LBE dissolution attack of intergranular Sn-rich areas.

In contrast with the rest of the MAX phase ceramics exposed by Lapauw et al. [83] to static LBE, all Zr-based MAX phase ceramics (i.e., Zr_2AlC, Zr_3AlC_2, and $(Zr_{0.8},Ti_{0.2})_{n+1}AlC_n$) showed local interaction, which, however, did not lead to specimen disintegration or surface recession (Fig. 5.9). Fig. 5.10 shows SEM/EDS data on the local Zr_2AlC/LBE interaction, which resulted in the *in situ* formation of a $Zr_2(Al,Pb,Bi)C$ MAX phase solid solution, due to the partial substitution of Al on the A-site by Pb and Bi [648]. Similarly, the static LBE exposure of the $(Zr_{0.8},Ti_{0.2})_{n+1}AlC_n$ MAX phase ceramic formed *in situ* a $(Zr,Ti)_{n+1}(Al,Pb,Bi)C_n$ solid solution due to the operation of a similar substitution mechanism [83]. Tunca et al. [648] performed a systematic study to unveil the mechanism responsible for the local interaction between liquid LBE and the Zr_2AlC MAX phase-based ceramic, consisting of 67 wt% Zr_2AlC and 33 wt% parasitic ZrC. The proposed four-step Zr_2AlC/LBE interaction mechanism is shown in Fig. 5.11: first, Bi/Pb atoms attack GBs, prior to penetrating into the Zr_2AlC MAX phase laths. The initial penetration of Bi preferentially along stacking faults (SFs) and dislocation pileups lead to the outward diffusion of Al from the bulk of Zr_2AlC laths into GBs. Following the outward Al diffusion into GBs, Bi/Pb atoms penetrate into the Zr_2AlC laths, both along basal SFs and out-of-plane, leading to the *in situ* formation of the $Zr_2(Al,Bi,Pb)C$ MAX phase solid solution. This new MAX phase solid solution tends to exhibit an out-of-plane ordered structure.

Lapauw et al. [83] exposed simultaneously Zr_2AlC, Zr_3AlC_2, and $(Nb_{0.85},Zr_{0.15})_4AlC_3$ (for simplicity, referred to as $(Nb,Zr)_4AlC_3$) MAX phase ceramics and SA 316L AuSS (reference steel) to oxygen-poor ($C_O \approx 5 \times 10^{-9}$ wt%), fast-flowing ($v \approx 8$ m/s) liquid LBE at 500 °C for 1000 h. The fast-flowing LBE tests aimed at comparing the erosion/corrosion resistance of MAX phase ceramics to that of a candidate structural steel (i.e., SA 316L AuSS) for the pump impeller application. These tests showed that the $(Nb,Zr)_4AlC_3$ MAX phase solid solution exhibited the best resistance to erosion/corrosion (Fig. 5.12), making that material a promising candidate material for Gen-IV LFR pump impellers (or parts thereof), under high-temperature, low-oxygen, fast-flowing LBE (i.e., very aggressive) service conditions.

Lapauw et al. [83] demonstrated that MAX phase-based ceramics are usually characterised by better resistance to dissolution corrosion and erosion/corrosion in contact with oxygen-poor, static and fast-flowing liquid LBE, respectively, as compared to a very promising candidate structural steel, i.e., the 316L AuSS. Fig. 5.12 shows the superior resistance of a $(Nb,Zr)_4AlC_3$ MAX phase ceramic to erosion/corrosion as compared to a 316L AuSS exposed simultaneously to oxygen-poor, fast-flowing LBE. The same authors [83]

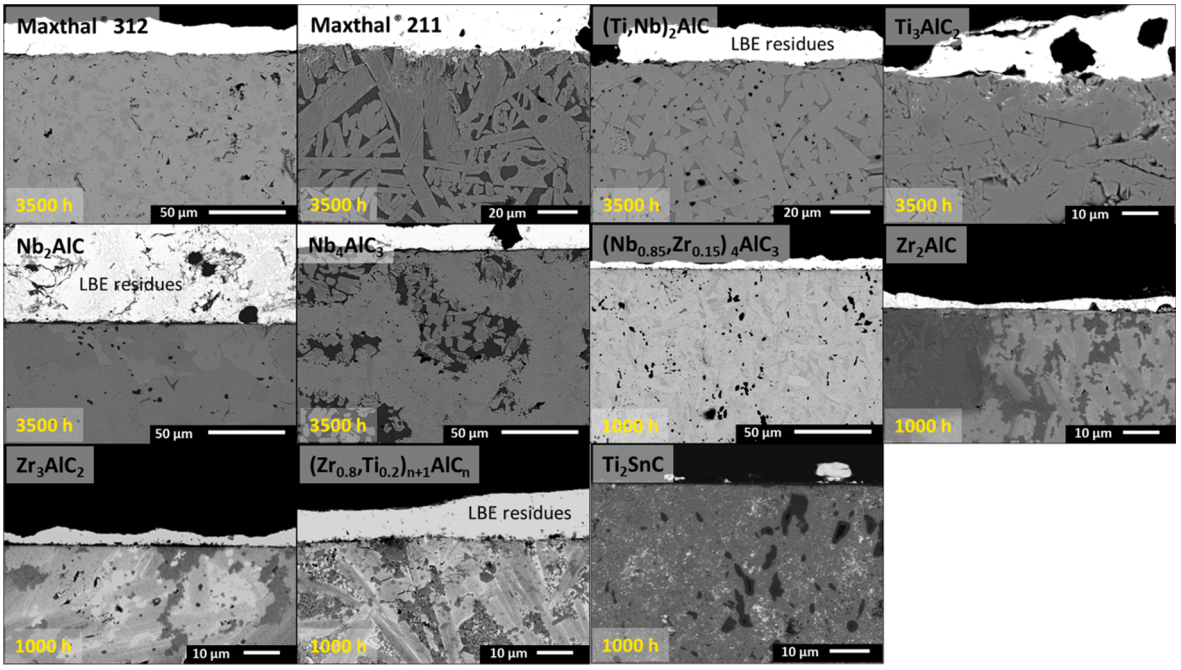

Fig. 5.9. SEM† images of the interaction between various MAX phase ceramics and static liquid LBE; exposure conditions: 500 °C, 1000–3500 h, $C_O \leq 2.2 \times 10^{-10}$ wt% [83].

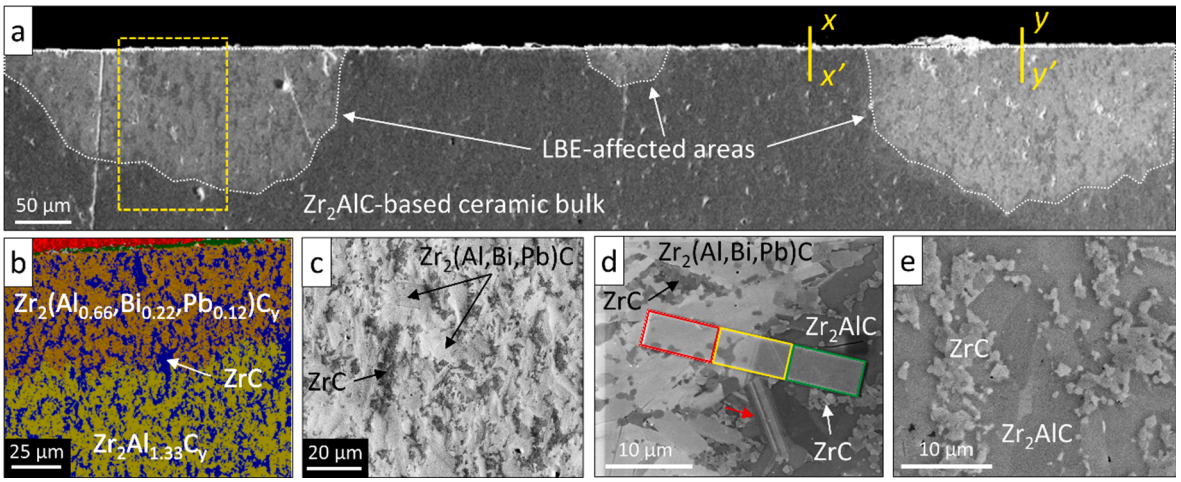

Fig. 5.10. (a) SEM† image of the local Zr_2AlC/LBE interaction, and (b) EDS† map of the framed area in (a), showing the formation of a $Zr_2(Al,Pb,Bi)C$ MAX phase solid solution in the LBE-affected zone. Images of the Zr_2AlC/LBE interaction: (c) fully affected zone, (d) transition zone, and (e) unaffected sample bulk. Adapted from [648]. Test conditions: 500 °C, 1000 h, $C_O \leq 2.2 \times 10^{-10}$ wt%.

compared the dissolution corrosion resistance of MAX phase ceramics with that of (SA & CW) 316L AuSS exposed to similar conditions (i.e., 500 °C, 1000–3282 h, $C_O < 10^{-8}$ wt%) in a previous study [40]. They pointed out that the 316L AuSS suffered severe dissolution corrosion damage, including the formation of deep dissolution 'pits' up to ~350 µm in CW 316L AuSS steels, while the MAX phase-based ceramics remained practically unaffected (Fig. 5.9). Most importantly, the dissolution-affected zones in 316L AuSS lost their load-bearing capacity [40], while this does not seem to happen in areas showing an interaction between liquid LBE and MAX phases (e.g., the Zr_2AlC/LBE interaction resulted in the *in situ* formation of the $Zr_2(Al,Bi,Pb)C$ MAX phase solid solution, the load-bearing capacity of which is expected to be comparable to that of the unaffected Zr_2AlC MAX phase).

5.3.3. Steel surface nanocrystallisation

Lu et al. [649] used a surface mechanical rolling treatment (SMRT) to produce a graded nanocrystalline layer on the surface a 9Cr2WVTa F/M steel, and then tested the steel oxidation properties in air at 600 °C and oxygen-saturated liquid LBE at 550 °C. Their

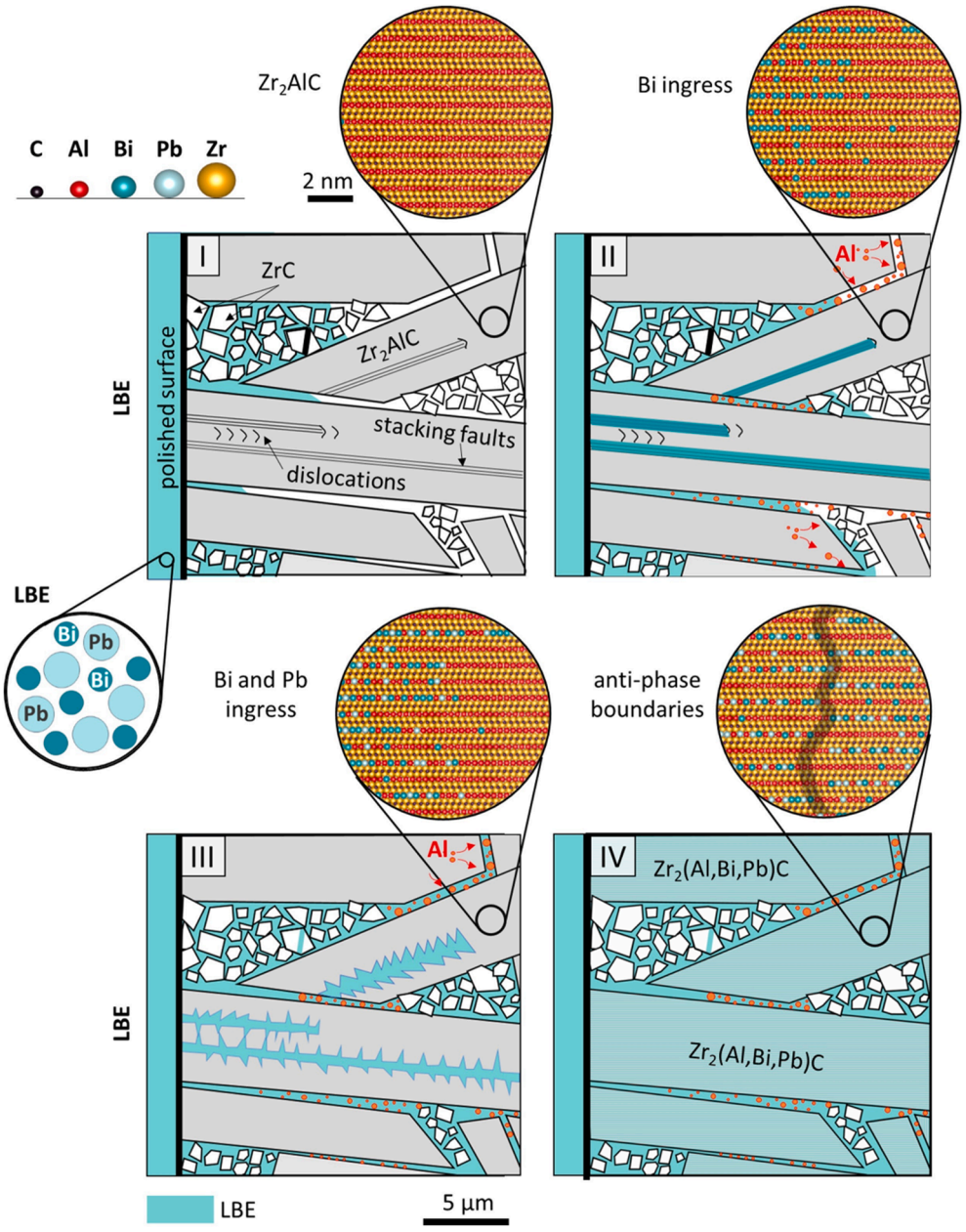

Fig. 5.11. Proposed Zr_2AlC/LBE interaction mechanism [648]. Step-I: Bi/Pb atoms attack GBs in the Zr_2AlC MAX phase-based ceramic. Step-II: Bi atoms penetrate preferentially along SFs† and dislocation pileups, and Al diffuses from the Zr_2AlC bulk into GBs. Step-III: Bi/Pb atoms occupy basal SFs and further diffuse away from the Zr_2AlC basal planes. The Pb/Bi atoms in the Zr_2AlC A-layers form alternating Al-rich and Bi/Pb-rich layers. Step-IV: *in situ* formation of nano-domains of the $Zr_2(Al,Bi,Pb)C$ MAX phase solid solution.

results showed that the surface-nanocrystallised steel had much better oxidation resistance both in air and in liquid LBE after an exposure of ~500 h, whereas a thick (8–50 μm) oxide scale was observed on the surface of the same steel in a coarser-grained counterpart. The enhanced oxidation resistance was ascribed to the accelerated formation of a dense spinel oxide scale, due to greater diffusivity of Al, Si, and Cr in the nanocrystalline surface layer [650,651]. However, the thermal stability of this layer is a concern, as long-term steel exposures at elevated temperatures resulted in grain growth and loss of nanocrystallinity, as expected for a nanocrystalline alloy [652].

5.3.4. Steel GB engineering

Murty and Charit [48] pointed out that GB treatments might be an effective way to mitigate localised LMC effects. Such GB treatments require suitable annealing and thermomechanical processing to produce certain coincident site lattice GBs (e.g., with $\sum$

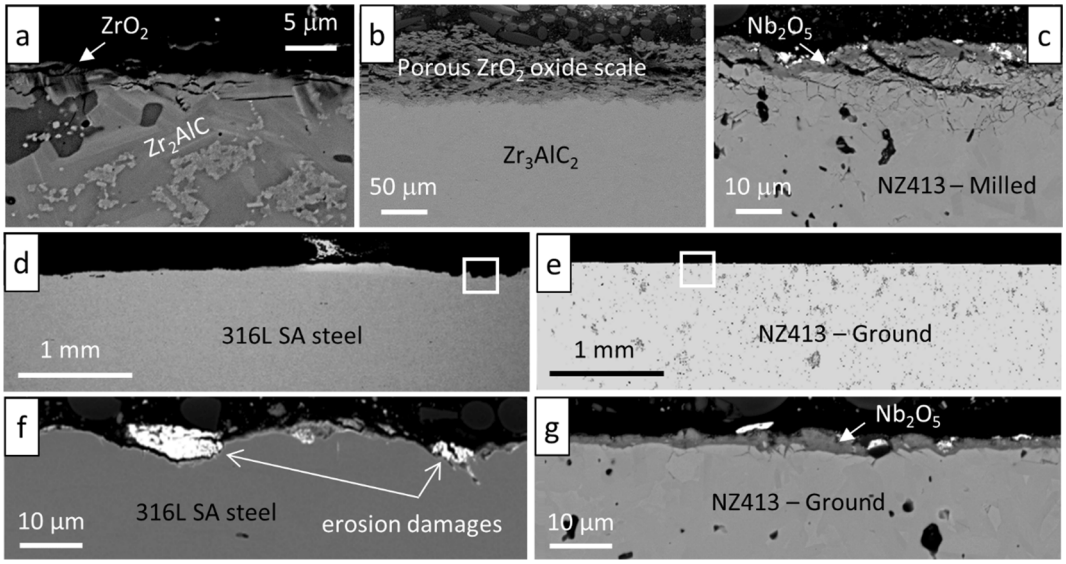

Fig. 5.12. SEM[†] images of materials exposed to fast-flowing ($v \approx 8$ m/s), oxygen-poor ($C_O \approx 5 \times 10^{-9}$ wt%) liquid LBE at 500 °C for 1000 h: (a) Zr_2AlC, (b) Zr_3AlC_2, (c) $(Nb,Zr)_4AlC_3$ with milled surface finish, (d,f) SA 316L AuSS – overview & detail, (e,g) $(Nb,Zr)_4AlC_3$ with ground surface finish – overview & detail. Adapted from [83].

values ≤ 29) with unique properties, such as decreased impurity segregation, lower diffusivity, reduced GB sliding, etc. The presence of such GBs resulted in a greatly improved resistance to intergranular fracture, localised corrosion, thermal creep, and irradiation damage.

To mitigate the GB penetration of liquid LBE in 316 AuSS due to erosion/corrosion, Saito et al. [221] have tried the GB engineering method. The GB engineered material (GBEM) was produced by cold rolling and subsequent annealing of the base steel at 967 °C for 72 h. The cold rolling treatment introduced 3% pre-strain in the base steel and the produced GBEM showed 86% of its GBs to be CSL boundaries. Both the base steel and GBEM were exposed to oxygen-poor ($C_O \approx 10^{-9}$–10^{-8} wt%), flowing liquid LBE ($v \approx 0.7$ m/s) for 3600 h at 450 °C. The corrosion results showed that the GB engineering treatment affected significantly the steel LMC behaviour, since the metal recession was much larger in the base steel (~390 μm) than in the GBEM steel (190–270 μm). The authors attributed the less severe LBE penetration observed in the GBEM steel to the high density of low-energy CSL GBs. It remains to be seen whether GB engineering can be carried out and/or maintained on welds and their heat-affected zones (HAZ).

5.4. Chapter summary

This chapter provides an overview of the existing LMC and LME mitigation approaches, which range from adjusting the reactor system design based on the knowledge of the behaviour of the selected structural and fuel cladding steels under very conservative service conditions, to active oxygen control, and to materials innovation (i.e., elemental alloying, coating or surface modification of steels, steel GB engineering, etc.). Active oxygen control relies on the rather precise control of the HLM oxygen concentration within the operational temperature range of the reactor system, so as to achieve the passivation of the structural and fuel cladding steels by the *in situ* formation of protective oxide scales without saturating the oxygen concentration dissolved in HLM, as the latter would lead to the blockage of flow paths due to the oxidation of the HLM itself. The existing data that resulted from the exposure of 'nuclear grade' AuSS and F/M steels to liquid Pb/LBE have shown that the mitigation of severe LMC effects in unprotected (i.e., not coated, surface alloyed or otherwise engineered) steels requires nuclear reactor operation temperatures below 450 °C, esp. in contact with flowing HLMs; however, caution must be exercised with the low-temperature use of F/M steels, due to their severe susceptibility to LME around 350 °C. Assuming that the operation of Gen-IV LFRs takes place in the 250–450 °C temperature range, the recommended 'window' of the HLM oxygen concentration that can suppress undesirable LMC effects in both 9Cr and 12Cr F/M steels as well as 316L and 15-15Ti AuSS is: $C_O \approx 10^{-7}$–10^{-6} wt%. It is also recommended to limit the maximum HLM flow velocity to $v \approx 2$ m/s, so as to suppress flow-assisted LMC effects, such as erosion and erosion/corrosion, and to also design the nuclear reactor system carefully, so as to minimise disturbances in the HLM flow pattern that are often accountable for locally enhanced material losses due to LMC.

Moving beyond this relatively narrow envelope of nominal operation conditions for Gen-IV LFRs will require continuous materials innovation; such innovation is unavoidable and the envisaged way forward, esp. when the safe, efficient and profitable operation of Gen-IV LFR NPPs is targeted. The current trends towards materials innovation include: steel alloying that allows the *in situ* formation of highly protective oxide scales (e.g., Al_2O_3), deposition of anticorrosion coatings (both simple and functionally graded), steel surface alloying, steel GB engineering, and steel surface nanocrystallisation. The aforementioned strategies of materials innovation have exhibited a considerable promise at limiting or preventing both LMC and LME in liquid Pb/LBE, hence, they must be further explored so as to help the deployment of Gen-IV LFRs. However, all considered strategies for structural materials innovation demand further

optimization, not only in terms of demonstrating reliable performance under reactor-relevant conditions, but also in terms of industrial scalability prior to their eventual transfer to market.

6. Summary & future outlook

The main conclusions of this detailed review of environmental degradation effects in structural materials considered for use in liquid Pb/LBE-cooled reactors may be summarised as follows:

(1) For T91 and compositionally similar F/M† steels, exposure to liquid Pb/LBE typically leads to the formation of duplex oxide scales consisting of an outer, porous magnetite (Fe_3O_4) layer and an inner, dense FeCr-spinel layer. An IOZ† has been observed below the inner FeCr-spinel layer at elevated temperatures (>500 °C) after short-term (1000–3000 h) exposures. Dissolution corrosion is the predominant LMC† mechanism in HLMs with lower oxygen concentrations ($C_O < 5 \times 10^{-6}$ wt%), while oxidation prevails in oxygen-richer HLMs. In general, the passivation of F/M steels by oxide scale formation happens below 500–550 °C. In flowing liquid LBE, the porous outer Fe_3O_4 scale is eroded at high HLM flow velocities ($v > 2$ m/s), whereas the inner FeCr-spinel scale tends to remain intact, protecting the steel bulk from further LMC damage. The LMC behaviour of 316L and compositionally similar AuSS† differs: exposure to HLMs leads to the formation of thin Cr-based (Cr_2O_3 or FeCr-spinel) oxide scales below 450 °C and duplex oxide scales above 450 °C. The passivation of AuSS by oxide scale formation requires temperatures below 450 °C and moderate HLM oxygen concentrations ($C_O \approx 10^{-7}$–10^{-6} wt%). Above 450 °C and/or at lower HLM oxygen concentrations (esp. $C_O < 10^{-8}$ wt%), selective leaching of the steel alloying elements (Ni, Mn, Cr) that are highly soluble in the HLM is accompanied by HLM penetration into the steel bulk and ferritisation (*fcc*-to-*bcc* phase transformation) of the dissolution-affected zones. It has been observed that the HLM penetrates into the steel bulk along preferred ingress paths in the steel microstructure, such as GBs, annealing/deformation twin boundaries, and interfaces between the steel matrix and secondary inclusions (e.g., MnS, oxides, δ-ferrite). Liquid metal corrosion damage can be either uniform or localised, while one of the most detrimental forms of LMC is the locally enhanced dissolution corrosion (also known as dissolution 'pitting'). Dissolution 'pitting' cannot be avoided even in contact with adequately oxygenated, flowing HLMs. Deep 'pits' have been observed underneath the oxide scales covering the steel surface. The current understanding of dissolution 'pitting' suggests that the formation of 'pits' can either be attributed to localised HLM flow instabilities (e.g., eddies) or to specific steel microstructural features (e.g., twin boundaries, non-oxidising inclusions) with direct access to the steel surface. Limiting dissolution corrosion damage in both F/M and AuSS requires low operation temperatures (<400 °C). The synergy of LMC with neutron irradiation has not yet been sufficiently addressed. Apart from collecting additional reliable experimental data, it is necessary to develop accurate predictive models of the steel-specific oxidation/dissolution corrosion effects in contact with liquid Pb/LBE, and to use such models to predict the in-service evolution of LMC damage in Gen-IV LFR† components.

(2) T91 F/M steels are inherently susceptible to LME † in contact with liquid Pb/LBE within the temperature 'window' between the LBE melting point (~125 °C) and approximately 450 °C, while the ductility of these steels starts to recover above 450 °C. An important prerequisite for the occurrence of LME in T91 F/M steels is the establishment of intimate contact between the steel and the HLM, which essentially implies the (local) absence of protective oxide scales. The severity of LME is affected by both (steel) metallurgical and "kinetic" factors, reflecting the interplay between crack initiation and crack propagation processes and the resistance of the steel to these processes. The LME susceptibility of T91 F/M steels is mainly controlled by the stability of the oxide scales and the crack initiation process. Crack initiation after the failure or loss of protectiveness of the oxide scales covering the steel surface is followed by rapid crack propagation, resulting in complex fractures that show interlath/intergranular cracking as well as translath/transgranular cracking and nano/submicron-dimples upon fatigue testing. Research in the past two decades has shown that despite its complexity, the LME phenomenology in T91 F/M steels exposed to liquid LBE exhibits similar traits with other LME model systems. However, the precise atomic-scale LME mechanism remains elusive, and fundamental work is still required to explain both the intrinsic LME sensitivity of a certain alloy, as well as the effect of all relevant metallurgical and "kinetic" factors. In practical terms, service conditions that help to maintain the integrity and protectiveness of oxide scales can delay crack initiation; for example, the combination of slow applied strain rates, low imposed strains, and high HLM oxygen concentrations is known to significantly delay crack nucleation under cyclic loading. Therefore, the use of T91 F/M steels could, in principle, be envisaged under nominal operation conditions provided that the above recommendations were taken into account. Unfortunately, what might appear as theoretically feasible is rarely possible in practice, as the oxide scales can be destabilised under transient/accidental conditions and/or can be damaged under certain conditions (e.g., in zones of static, oxygen-poor HLM; in crevices; due to fretting wear or HLM flow instabilities; at uneven corrosion sites which can cause significant stress concentration; etc.). This implies that the safe operation of Gen-IV LFRs dictates the exclusion of F/M steels from the list of candidate structural materials and recommends the use of structural materials that are less susceptible to LME, such as AuSS. Indeed, AuSS are much less affected by LME, but they could still become vulnerable to LME, in case of plastic strain- or dissolution corrosion-induced ferritisation especially under neutron irradiation. It is also worthwhile noting that the underlying mechanisms that are responsible for the observed differences in the LME susceptibilities of F/M steels and AuSS in contact with liquid Pb/LBE are still unclear. Further investigations combining experimental and computational work are needed to improve the elucidation of these issues, especially on the atomic scale.

(3) Below 450 °C, severe LMC damage on both T91 F/M steels and AuSS can be avoided by means of active oxygen control, i.e., by employing techniques that maintain the HLM oxygen concentration within a specific 'window' that prevents the reduction of the protective oxide scales, on one hand, and the precipitation of PbO, on the other hand. For Gen-IV LFRs cooled by liquid Pb/

LBE and with nominal operation temperatures in the 250–450 °C range, the existing (rather extensive) population of LMC data suggests to maintain the HLM oxygen concentration in the $C_O \approx 10^{-7}$–10^{-6} wt% range. Above 500 °C, the oxide scales lose their protectiveness, therefore, active oxygen control cannot prevent steel dissolution corrosion damage anymore. Under such conditions, steel alloying with elements that are strong oxide formers (e.g., Al or Si) enables the *in situ* formation of passivating oxide scales (e.g., Al_2O_3 or SiO_2) that remain stable in very low HLM oxygen potentials. In general, alloying the steel bulk with these elements is not preferred, as the bulk mechanical properties are significantly changed and the steel propensity to irradiation embrittlement might increase (esp. by the addition of Si). The deposition of Al/Si-based oxide coatings or the use of Al/Si-alloyed surface layers can solve this issue, without compromising the steel bulk properties. Coatings with a ferritic (*bcc*) structure, however, are not recommended, due to their expected susceptibility to LME, analogously to T91 F/M steels. Several MAX phases exhibit strong resistance to dissolution corrosion and erosion/corrosion in oxygen-poor, static and fast-flowing liquid Pb/LBE, which makes them promising candidate materials for fuel cladding tube coatings, bearings, bushings, as well as pump impellers (or parts thereof). AFAs[†] and *fcc* Al-enriched HEAs[†] are also promising structural materials, which can potentially exhibit good resistance to both LMC and LME, depending on their composition, microstructure, and crystal structure (*fcc* alloys are preferred over *bcc* alloys, due to their better resistance to LME). Before their actual use in-reactor, however, all these promising innovative materials still require an extensive testing campaign under reactor-relevant conditions to demonstrate their suitability in Gen-IV LFRs.

Declaration of Competing Interest

The authors declare that they have no known competing financial interests or personal relationships that could have appeared to influence the work reported in this paper.

Acknowledgements

X. Gong gratefully acknowledges the support of National Natural Science Foundation of China, China (Grant no. 51801129 and U21B2066). M.P. Short gratefully acknowledges the support of the U.S. Department of Energy's Nuclear Energy University Program (NEUP), under Grant No. DE-NE0008871, United States. K. Lambrinou and E. Charalampopoulou gratefully acknowledge the support of the MYRRHA project that is currently ongoing at SCK CEN, Belgium. This review is in direct alignment with the interests of the EERA (European Energy Research Alliance) Joint Programme on Nuclear Materials (JPNM).

References

[1] BP. p.l.c. Statistical Review of World Energy; 2020. https://www.bp.com/content/dam/bp/business-sites/en/global/corporate/pdfs/energy-economics/statistical-review/bp-stats-review-2020-full-report.pdf.
[2] Enerdata. Global Energy Statistical Yearbook; 2020, https://yearbook.enerdata.net/.
[3] Chu S, Majumdar A. Opportunities and challenges for a sustainable energy future. Nature 2012;488:294–303.
[4] Olivier JGJ, Peters JAHW. Trends in global CO_2 and total greenhouse gas emissions – 2019 Report. The Hague: PBL Netherlands Environmental Assessment Agency; 2020.
[5] Conca, J. Is Nuclear Power A Renewable Or A Sustainable Energy Source? Forbes; 2016. https://www.forbes.com/sites/jamesconca/2016/03/24/is-nuclear-power-a-renewable-or-a-sustainable-energy-source/#54dfb1cb656e.
[6] Sen S, Ganguly S. Opportunities, barriers and issues with renewable energy development – A discussion. Renew Sustain Energy Rev 2017;69:1170–81.
[7] Mohtasham J. Review Article - Renewable energies. Energy Procedia 2015;74:1289–97.
[8] Sinn HW. Buffering volatility: A study on the limits of Germany's energy revolution. Eur Econ Rev 2017;99:130–50.
[9] IEA. Nuclear Power in a Clean Energy System; 2019. https://www.eenews.net/assets/2019/05/28/document_ew_01.pdf.
[10] Abderrahim HA. Multi-purpose hYbrid Research Reactor for High-tech Applications a multipurpose fast spectrum research reactor. Int J Energy Res 2012;36:1331–7.
[11] OECD/NEA. Actinide and Fission Product Partitioning and Transmutation, Nuclear Science and Nuclear Development, ISBN 978-92-64-99174-3. In Eleventh Information Exchange Meeting. November 1–4, 2010, San Francisco, California, USA; 2010.
[12] IAEA. Status and Trends in Spent Fuel and Radioactive Waste Management. IAEA Nuclear Energy Series, No. NW-T-1.14; 2018.
[13] Trauth KM, Hora SC, Guzowski RV. Expert Judgment on Markers to Deter Inadvertent Human Intrusion into the Waste Isolation Pilot Plant, SAND92–1382•UC–721. USA: Sandia National Laboratories; 1993.
[14] Humphrey UE, Khandaker MU. Viability of thorium-based nuclear fuel cycle for the next generation nuclear reactor: Issues and prospects. Renew Sustain Energy Rev 2018;97:259–75.
[15] IAEA. Waste from Innovative Types of Reactors and Fuel Cycles - A Preliminary Study. IAEA Nuclear Energy Series No. NW-T-1.14; 2019.
[16] Hwang IS, Jeong SH, Park BG, Yang WS, Suh KY, Kim CH. The concept of proliferation-resistant, environment-friendly, accident-tolerant, continual and economical reactor (PEACER). Prog Nucl Energy 2000;37:217–22.
[17] Bourg S, Hill C, Caravaca C, Rhodes C, Ekberg C, Taylor R, et al. ACSEPT-Partitioning technologies and actinide science: Towards pilot facilities in Europe. Nucl Eng Des 2011;241:3427–35.
[18] OECD/NEA. Handbook on lead-bismuth eutectic alloy and lead properties, materials compatibility. Therm-Hydraul Technol 2015.
[19] Alemberti A, Smirnov V, Smith CF, Takahashi M. Overview of lead-cooled fast reactor activities. Prog Nucl Energy 2014;77:300–7.
[20] Alemberti A. The lead fast reactor: an opportunity for the future? Engineering 2016;2:59–62.
[21] Lorusso P, Bassini S, Del Nevo A, Di Piazza I, Giannetti F, Tarantino M, et al. GEN-IV LFR development: status & perspectives. Prog Nucl Energy 2018;105:318–31.
[22] Fazio C, Groschel F, Wagner W, Thomsen K, Smith BL, Stieglitz R, et al. The MEGAPIE-TEST project: Supporting research and lessons learned in first-of-a-kind spallation target technology. Nucl Eng Des 2008;238:1471–95.
[23] US DOE & GIF. Technology Roadmap Update for Generation IV. Nucl Energy Syst 2014.
[24] IAEA. Liquid Metal Coolants for Fast Reactors Cooled By Sodium, Lead, and Lead-Bismuth Eutectic. IAEA Nuclear Energy Series No. NF-T-1.6; 2012.
[25] Zrodnikov AV, Toshinsky GI, Komlev OG, Stepanov VS, Klimov NN. SVBR-100 module-type fast reactor of the IV generation for regional power industry. J Nucl Mater 2011;415:237–44.
[26] Smith CF, Halsey WG, Brown NW, Sienicki JJ, Moisseytsev A, Wade DC. SSTAR: The US lead-cooled fast reactor (LFR). J Nucl Mater 2008;376:255–9.

[27] Choi S, Cho JH, Bae MH, Lim J, Puspitarini D, Jeun JH, et al. PASCAR: Long burning small modular reactor based on natural circulation. Nucl Eng Des 2011; 241:1486–99.
[28] Todreas NE, MacDonald PE, Hejzlar P, Buongiorno J, Loewen EP. Medium-power lead-alloy reactors: Missions for this reactor technology. Nucl Technol 2004; 147:305–20.
[29] Zhang JS, Li N. Review of the studies on fundamental issues in LBE corrosion. J Nucl Mater 2008;373:351–77.
[30] Zhang JS. A review of steel corrosion by liquid lead and lead–bismuth. Corros Sci 2009;51:1207–27.
[31] Ballinger RG, Lim J. An overview of corrosion issues for the design and operation of high-temperature lead-and lead-bismuth-cooled reactor systems. Nucl Technol 2004;147:418–35.
[32] Balbaud F, Martinelli L. Corrosion issues in lead-cooled fast reactor (LFR) and accelerator driven systems (ADS). in Nuclear Corrosion Science and Engineering, Féron D (editor). Woodhead Publishing Series. Energy 2012:807–41.
[33] Gnanasekaran T, Dayal RK, Raj B. Liquid metal corrosion in nuclear reactor and accelerator driven systems. In: Féron D, editor. Nuclear Corrosion Science and Engineering. Woodhead Publishing Series in Energy; 2012. p. 301–28.
[34] Kikuchi K. Material Performance in Lead and Lead-Bismuth Alloy. in Comprehensive Nuclear Materials, Konings RJM (editor). Woodhead Publishing 2012: 207–19.
[35] Fazio C, Balbaud F. In: Corrosion phenomena induced by liquid metals in Generation IV reactors. in Structural Materials for Generation IV Nuclear Reactors. Woodhead Publishing; 2017. p. 23–74.
[36] Gorse D, Auger T, Vogt JB, Serre I, Weisenburger A, Gessi A, et al. Influence of liquid lead and lead–bismuth eutectic on tensile, fatigue and creep properties of ferritic/martensitic and austenitic steels for transmutation system. J Nucl Mater 2011;415:284–92.
[37] Del Giacco M, Weisenburger A, Müller G. Fretting corrosion in liquid lead of structural steels for lead-cooled nuclear systems: Preliminary study of the influence of temperature and time. J Nucl Mater 2012;423:79–86.
[38] Del Giacco M, Weisenburger A, Müller G. Fretting corrosion of steels for lead alloys cooled ADS. J Nucl Mater 2014;450:225–36.
[39] Del Giacco M, Weisenburger A, Müller G. Fretting of fuel cladding materials for Pb cooled fast reactors–Approach to long term prediction using fretting maps. Nucl Eng Des 2014;280:697–703.
[40] Lambrinou K, Charalampopoulou E, Van der Donck T, Delville R, Schryvers D. Dissolution corrosion of 316L austenitic stainless steels in contact with static liquid lead-bismuth eutectic (LBE) at 500°C. J Nucl Mater 2017;490:9–27.
[41] Hosemann P, Frazer D, Stergar E, Lambrinou K. Twin boundary-accelerated ferritization of austenitic stainless steels in liquid lead–bismuth eutectic. Scr Mater 2016;118:37–40.
[42] Klok O, Lambrinou K, Gavrilov S, Stergar E, Lim J, Van der Donck T, et al. Effect of deformation twinning on dissolution corrosion of 316L stainless steels in contact with static liquid lead-bismuth eutectic (LBE) at 500°C. J Nucl Mater 2018;510:556–67.
[43] Tsisar V, Schroer C, Wedemeyer O, Skrypnik A, Konys J. Corrosion behaviour of austenitic steels 1.4970, 316L and 1.4571 in flowing LBE at 450 and 550°C with 10^{-7} mass% dissolved oxygen. J Nucl Mater 2014;454:332–42.
[44] Tsisar V, Schroer C, Wedemeyer O, Skrypnik A, Konys J. Long-term corrosion of austenitic steels in flowing LBE at 400°C and 10^{-7} mass% dissolved oxygen in comparison with 450 and 550°C. J Nucl Mater 2016;468:305–12.
[45] Stergar E, Eremin SG, Gavrilov S, Lambrecht M, Makarov O, Lakovlev V. Influence of LBE long term exposure and simultaneous fast neutron irradiation on the mechanical properties of T91 and 316L. J Nucl Mater 2016;473:28–34.
[46] Yvon P, Carré F. Structural materials challenges for advanced reactor systems. J Nucl Mater 2009;385:217–22.
[47] Gong X, Li R, Sun MZ, Ren QS, Liu T, Short MP. Opportunities for the LWR ATF materials development program to contribute to the LBE-cooled ADS materials qualification program. J Nucl Mater 2016;482:218–28.
[48] Murty KL, Charit I. Structural materials for Gen-IV nuclear reactors: Challenges and opportunities. J Nucl Mater 2008;383:189–95.
[49] Zinkle SJ, Was GS. Materials challenges in nuclear energy. Acta Mater 2013;61:735–58.
[50] Kohyama A, Hishinuma A, Gelles DS, Klueh RL, Dietz W, Ehrlich K. Low-activation ferritic and martensitic steels for fusion application. J Nucl Mater 1996; 233–237:138–47.
[51] Ejenstam J, Thuvander M, Olsson P, Rave F, Szakalos P. Microstructural stability of Fe–Cr–Al alloys at 450–550°C. J Nucl Mater 2015;457:291–7.
[52] Tan L, Kim BK, Yang Y, Field KG, Gray S, Li M. Microstructural evolution of neutron-irradiated T91 and NF616 to ~4.3 dpa at 469°C. J Nucl Mater 2017;493: 12–20.
[53] Gong X, Marmy P, Volodin A, Amin-Ahmadi B, Qin L, Schryvers D, et al. Multiscale investigation of quasi-brittle fracture characteristics in a 9Cr–1Mo ferritic–martensitic steel embrittled by liquid lead–bismuth under low cycle fatigue. Corros Sci 2016;102:137–52.
[54] Anderoglu O, Byun TS, Toloczko M, Maloy SA. Mechanical performance of ferritic martensitic steels for high dose applications in advanced nuclear reactors. Metall Mater Trans A 2013;44:70–83.
[55] Alamo A, Bertin JL, Shamardin VK, Widент P. Mechanical properties of 9Cr martensitic steels and ODS-FeCr alloys after neutron irradiation at 325°C up to 42 dpa. J Nucl Mater 2007;367:54–9.
[56] IAEA. Structural Materials for Liquid Metal Cooled Fast Reactor Fuel Assemblies-Operational Behaviour. IAEA Nuclear Energy Series No. NF-T-4.3; 2012.
[57] Bain EC, Paxton HW. Alloying Elements in Steel, 2nd ed. Metals Park (Ohio): ASM; 1966, p. 123–62 [p. 243–7].
[58] Chocholousek M, Stergar E, Gong X, Marmy P, Gavrilov S, Ersoy F, et al. Mechanical/microstructural characteristics of environmentally-assisted degradation effects of steels in lead alloys and assessment of environmental degradation effects on performance of structural and functional components of MYRRHA ADS & LFR. MatISSE – D5.42; 2017.
[59] Ukai S, Ohtsuka S, Kaito T, De Carlan Y, Ribis J, Malaplate J. Oxide dispersion-strengthened/ferrite-martensite steels as core materials for generation IV nuclear reactors. Struct Mater Gen IV Nucl React 2017:357–414.
[60] Lu CY, Lu Z, Wang X, Xie R, Li ZY, Higgins M, et al. Enhanced Radiation-tolerant Oxide Dispersion Strengthened Steel and its Microstructure Evolution under Helium-implantation and Heavy-ion Irradiation. Sci Rep 2017;7:40343.
[61] Xu HJ, Lu Z, Wang DM, Liu CM. Microstructure Refinement and Strengthening Mechanisms of a 9Cr Oxide Dispersion Strengthened Steel by Zirconium Addition. Nucl Eng Technol 2017;49:178–88.
[62] Dryepondt S, Unocic KA, Hoelzer DT, Massey CP, Pint BA. Development of low-Cr ODS FeCrAl alloys for accident-tolerant fuel cladding. J Nucl Mater 2018; 501:59–71.
[63] Yu ZZ, Feng ZL, Hoelzer D, Tan LZ, Sokolov MA. Friction Stir Welding of ODS and RAFM Steels. Metall Mater Trans E 2015;2:164–72.
[64] Cheng B, Kim YJ, Chou P. Improving accident tolerance of nuclear fuel with coated Mo-alloy cladding. Nucl Eng Technol 2016;48:16–25.
[65] Snead LL, Katoh Y, Nozawa T. Radiation Effects in SiC and SiC-SiC. Comprehens Nucl Mater 2012;4:215–40.
[66] Deck CP, Jacobsen GM, Sheeder J, Gutierrez O, Zhang J, Stone J, et al. Characterization of SiC–SiC composites for accident tolerant fuel cladding. J Nucl Mater 2015;466:667–81.
[67] Sauder C. Chapter 22 - Ceramic Matrix Composites: Nuclear Applications. In Ceramic Matrix Composites: Materials, Modeling and Technology. Wiley-American Ceramic Society; 2015.
[68] Kaur S, Cutler RA, Shetty DK. Short-Crack Fracture Toughness of Silicon Carbide. J Am Ceram Soc 2009;92:179–85.
[69] Hoffman EN, Vinson DW, Sindelar RL, Tallman DJ, Kohse G, Barsoum MW. MAX phase carbides and nitrides: Properties for future nuclear power plant in-core applications and neutron transmutation analysis. Nucl Eng Des 2012;244:17–24.
[70] Barsoum MW. The $M_{N+1}AX_N$ phases: A new class of solids: Thermodynamically stable nanolaminates. Prog Solid State Chem 2000;28:201–81.
[71] Barsoum MW. MAX Phases: Properties of Machinable Ternary Carbides and Nitrides. Wiley-VCH Verlag GmbH & Co. KGaA; 2013.
[72] Barosum MW, Radovic M. Elastic and mechanical properties of the MAX phases. Ann Rev Mater Res 2011;41:195–227.
[73] Lapauw T, Tunca B, Potashnikov D, Pesach A, Ozeri O, Vleugels J, et al. The double solid solution $(Zr, Nb)_2(Al, Sn)C$ MAX phase: a steric stability approach. Sci Rep 2018;8:12801.

[74] Lapauw T, Tytko D, Vanmeensel K, Huang S, Choi P, Raabe D, et al. $(Nb_x, Zr_{1-x})_4AlC_3$ MAX phase solid solutions: processing, mechanical properties and density functional theory calculations. Inorg Chem 2016;55:5445–52.
[75] Tunca B, Lapauw T, Karakulina OM, Batuk M, Cabioc'h T, Hadermann J, et al. Synthesis of MAX phases in the Zr-Ti-Al-C system. Inorg Chem 2017;56:3489–98.
[76] Tunca B, Lapauw T, Delville R, Neuville D, Hennet L, Thiaudière D, et al. Synthesis and characterisation of double solid solution $(Zr, Ti)_2(Al, Sn)C$ MAX phase ceramics. Inorg Chem 2019;58:6669–83.
[77] Griseri M, Tunca B, Huang S, Dahlqvist M, Rosén J, Lu J, et al. Ta-based 413 and 211 MAX phase solid solutions with Hf and Nb. J Eur Ceram Soc 2020;40:1829–38.
[78] Barnes LA, Rago NLD, Leibowitz L. Corrosion of ternary carbides by molten lead. J Nucl Mater 2008;373:424–8.
[79] Heinzel A, Müller G, Weisenburger A. Compatibility of Ti_3SiC_2 with liquid Pb and PbBi containing oxygen. J Nucl Mater 2009;392:255–8.
[80] Utili M, Agostini M, Coccoluto G, Lorenzini E. Ti_3SiC_2 as a candidate material for lead cooled fast reactor. Nucl Eng Des 2011;241:1295–300.
[81] Heinzel A, Weisenburger A, Müller G. Long-term corrosion tests of Ti_3SiC_2 and Ti_2AlC in oxygen containing LBE at temperatures up to 700°C. J Nucl Mater 2016;482:114–23.
[82] Rivai AK, Takahashi M. Compatibility of surface-coated steels, refractory metals and ceramics to high temperature lead–bismuth eutectic. Prog Nucl Energy 2008;50:560–6.
[83] Lapauw T, Tunca B, Joris J, Jianu A, Fetzer R, Weisenburger A, et al. Interaction of $M_{n+1}AX_n$ phases with oxygen-poor, static and fast-flowing liquid lead-bismuth eutectic. J Nucl Mater 2019;520:258–72.
[84] Hu CF, Sakka Y, Grasso S, Nishimura T, Guo SQ, Tanaka H. Shell-like nanolayered Nb_4AlC_3 ceramic with high strength and toughness. Scr Mater 2011;64:765–8.
[85] Tallman DJ, Hoffman EN, Caspi EN, Garcia-Diaz BL, Kohse G, Sindelar RL, et al. Effect of neutron irradiation on select MAX phases. Acta Mater 2015;85:132–43.
[86] Tallman DJ, He L, Garcia-Diaz BL, Hoffman EN, Kohse G, Sindelar RL, et al. Effect of neutron irradiation on defect evolution in Ti_3SiC_2 and Ti_2AlC. J Nucl Mater 2016;468:1–13.
[87] Tallman DJ, He L, Gan J, Caspi EN, Hoffman EN, Barsoum MW. Effects of neutron irradiation of Ti_3SiC_2 and Ti_3AlC_2 in the 121–1085°C temperature range. J Nucl Mater 2017;484:120–34.
[88] Ang C, Silva S, Shih C, Koyanagi T, Katoh Y, Zinkle SJ. Anisotropic swelling and microcracking of neutron irradiated Ti_3AlC_2-$Ti_5Al_2C_3$ materials. Scr Mater 2016;114:74–8.
[89] Ang C, Parish CM, Shih C, Katoh Y. Microstructure and mechanical properties of titanium aluminum carbides neutron irradiated at 400–700°C. J Eur Ceram Soc 2017;37:2353–63.
[90] Amy C, Budenstein D, Bagepalli M, England D, DeAngelis F, Wilk G, et al. Pumping liquid metal at high temperatures up to 1,673 kelvin. Nature 2017;550:199–203.
[91] Zhang J, Hosemann P, Maloy S. Models of liquid metal corrosion. J Nucl Mater 2010;404:82–96.
[92] Lambrinou K, Koch V, Coen G, Van den Bosch J, Schroer C. Corrosion scales on various steels after exposure to liquid lead–bismuth eutectic. J Nucl Mater 2014;450:244–55.
[93] Roy M, Martinelli L, Ginestar K, Favergeon J, Moulin G. Dissolution and oxidation behaviour of various austenitic steels and Ni rich alloys in lead-bismuth eutectic at 520°C. J Nucl Mater 2016;468:153–63.
[94] Zrodnikov AV, Chitaykin VI, Gromov BF, Grigoryv OG, Dedoul AV, Toshinsky GI, et al. Use of Russian Technology of ship reactors with lead-bismuth coolant in nuclear power. No. IAEA-TECDOC-1172; 2000.
[95] Müller G, Heinzel A, Konys J, Schumacher G, Weisenburger A, Zimmermann F, et al. Behaviour of steels in flowing liquid PbBi eutectic alloy at 420–600°C after 4000–7200 h. J Nucl Mater 2004;335:163–8.
[96] Schroer C, Wedemeyer O, Novotny J, Skrypnik A, Konys J. Selective leaching of nickel and chromium from Type 316 austenitic steel in oxygen-containing lead-bismuth eutectic (LBE). Corros Sci 2014;84:113–24.
[97] Farrell K, Byun TS. Tensile properties of candidate SNS target container materials after proton and neutron irradiation in the LANSCE accelerator. J Nucl Mater 2001;296:129–38.
[98] Maloy SA, James MR, Johnson WR, Byun TS, Farrell K, Toloczko MB. Comparison of fission neutron and proton/spallation neutron irradiation effects on the tensile behavior of type 316 and 304 stainless steel. J Nucl Mater 2003;318:283–91.
[99] Pokor C, Brechet Y, Dubuisson P, Massoud J-P, Averty X. Irradiation damage in 304 and 316 stainless steels: experimental investigation and modelling. Part II: irradiation induced hardening. J Nucl Mater 2004;326:30–7.
[100] Elen JD, Fenici P. Fast neutron irradiation hardening of austenitic stainless steel at 250°C. J Nucl Mater 1992;191–194:766–70.
[101] Tsisar V, Schroer C, Wedemeyer O, Skrypnik A, Konys J. Characterization of corrosion phenomena and kinetics on T91 ferritic/martensitic steel exposed at 450 and 550°C to flowing Pb-Bi eutectic with 10^{-7} mass% dissolved oxygen. J Nucl Mater 2017;494:422–38.
[102] Schroer C, Nold E, Konys J. Micro-analysis of 316L stainless-steel after long-term exposure to lead-bismuth eutectic at 550°C. In Proceedings of EUROCORR, Nice at France; 2009.
[103] Balbaud-Célérier F, Barbier F. Investigation of models to predict the corrosion of steels in flowing liquid lead alloys. J Nucl Mater 2001;289:227–42.
[104] Müller G, Heinzel A, Konys J, Schumacher G, Weisenburger A, Zimmermann F, et al. Results of steel corrosion tests in flowing liquid Pb/Bi at 420–600°C after 2000 h. J Nucl Mater 2002;301:40–6.
[105] Gorynin IV, Karzov GP, Markov VG, Yakovlev VA. Structural materials for atomic reactors with liquid metal heat-transfer agents in the form of lead or lead-Bismuth alloy. Met Sci Heat Treat 1999;41:384–8.
[106] Gorynin IV, Karzov GP, Markov VG, Lavrukhin VS, Yakovlev VA. Structural materials for power plants with heavy liquid metals as coolants. In Heavy Liquid Metal Coolants in Nuclear Technology (HLMC-98). Obninsk, Russian Federation; 1999.
[107] Klok O, Lambrinou K, Gavrilov S, Lim J, De Graeve I. Effect of Lead-Bismuth Eutectic Oxygen Concentration on the Onset of Dissolution Corrosion in 316 L Austenitic Stainless Steel at 450 °C. J Nucl Eng Radiat Sci 2018;4:031019.
[108] Giuranno D, Novakovic R, Tomasi C, Ricci E. Evaluation of corrosion phenomena of T91 steel in stagnant liquid lead at high operational temperatures. Corrosion 2020;76(11):1–11.
[109] Schroer C, Konys J. Physical chemistry of corrosion and oxygen control in liquid lead and lead bismuth eutectic. FZKA 7364, Karlsruhe, Germany; 2007.
[110] Xiao J, Gong X, Xiang CY, Yu ZY, Wang H, Zhao K, et al. A refined oxidation mechanism proposed for ferritic-martensitic steels exposed to oxygen-saturated liquid lead-bismuth eutectic at 400°C for 500 h. J Nucl Mater 2021;549:152852.
[111] Short MP. The design of Functionally Graded Composite for Service in High Temperature Lead and Lead-Bismuth Cooled Nuclear Reactors. Massachusetts Institute of Technology, PhD dissertation; 2010.
[112] Polekhina NA, Litovchenko IY, Almaeva KV, Pinzhin YP, Akkuzin SA, Tyumentsev AN, et al. Behavior of 12% Cr low-activation ferritic-martensitic steel EK-181 after holding in a static lead melt at 600°C for 3000 hours. J Nucl Mater 2021;545:152754.
[113] Dömstedt P, Lundberg M, Szakalos P. Corrosion Studies of Low-Alloyed FeCrAl Steels in Liquid Lead at 750°C. Oxid Met 2019;91:511–24.
[114] Lee SG, Shin YH, Park J, Hwang IS. High-Temperature Corrosion Behaviors of Structural Materials for Lead-Alloy-Cooled Fast Reactor Application. Appl Sci 2021;11:2349.
[115] Schroer C, Konys J. Quantification of the long-term performance of steels T91 and 316L in oxygen-containing flowing lead-bismuth eutectic at 550°C. J Eng Gas Turbines Power 2010;132:082901.
[116] Gnecco F, Ricci E, Bottino C, Passerone A. Corrosion behaviour of steels in lead-bismuth at 823 K. J Nucl Mater 2004;335:185–8.
[117] Schroer C, Voß Z, Wedemeyer O, Novotny J, Konys J. Oxidation of steel T91 in flowing lead–bismuth eutectic (LBE) at 550 °C. J Nucl Mater 2006;356:189–97.
[118] Zhang J, Li N, Chen Y, Rusanov AE. Corrosion behaviours of US steels in flowing lead-bismuth eutectic (LBE). J Nucl Mater 2005;336:1–10.

[119] Tan L, Machut MT, Sridharan K, Allen TR. Corrosion behaviour of a ferritic/martensitic steel HCM12A exposed to harsh environments. J Nucl Mater 2007;371:161–70.
[120] Frazer D, Qvist S, Parker S, Krumwiede DL, Caro M, Tesmer J, et al. Degradation of HT9 under simultaneous ion beam irradiation and liquid metal corrosion. J Nucl Mater 2016;479:382–9.
[121] Hosemann P, Swadener J, Welch J, Li N. Nano-indentation measurement of oxide layers formed in LBE on F/M steels. J Nucl Mater 2008;377:201–5.
[122] Tsisar V, Yeliseyeva O. Oxidation of Armco-Fe and steels in oxygen-saturated liquid lead. Mater High Temp 2007;24:93–101.
[123] Eliseeva OI, Tsisar VP. Effect of temperature on the interaction of ÉP823 steel with lead melts saturated with oxygen. Mater Sci 2007;43:230–7.
[124] Yeliseyeva O, Tsisar V. Comparison of oxidation of ferritic-martensitic steel EP-823 and armco-Fe in Pb melt saturated by oxygen. J Corros Sci Eng 2004;7.
[125] Yeliseyeva O, Tsisar V, Benamati G. Influence of temperature on the interaction mode of T91 and AISI 316L steels with Pb-Bi melt saturated by oxygen. Corros Sci 2008;50:1672–83.
[126] Ye ZF, Wang P, Dong H, Li DZ, Zhang YT, Li YY. Oxidation mechanism of T91 in liquid lead-bismuth eutectic: with consideration of internal oxidation. Sci Rep 2016;6:35268.
[127] Hosemann P, Hawley ME, Koury D, Welch J, Johnson AL, Mori G, et al. Nanoscale characterization of HT-9 exposed to lead bismuth eutectic at 550 °C for 3000 h. J Nucl Mater 2008;381:211–5.
[128] Yeliseyeva O, Tsisar V, Zhou Z. Corrosion behaviour of Fe-14Cr-2W and Fe-9Cr-2W ODS steels in stagnant liquid Pb with different oxygen concentration at 550 and 650 °C. J Nucl Mater 2013;442:434–43.
[129] Tsisar VP. Oxidation of ferritic steels dispersion strengthened with TiO_2 and Y_2O_3 oxides in lead melt. Mater Sci 2008;44:630–7.
[130] Di Gabriele F, Amore S, Scaiola C, Arato E, Giuranno D, Novakovic R, et al. Corrosion behaviour of 12Cr-ODS steel in molten lead. Nucl Eng Des 2014;280:69–75.
[131] Yaskiv OI, Fedirko VM. Oxidation/Corrosion Behaviour of ODS Ferritic/Martensitic Steels in Pb Melt at Elevated Temperature. Int J Nucl Energy 2014:657689.
[132] Hosemann P, Thau HT, Johnson AL, Maloy SA, Li N. Corrosion of ODS steels in lead-bismuth eutectic. J Nucl Mater 2008;373:246–53.
[133] Müller G, Schumacher G, Zimmermann F. Investigation on oxygen controlled liquid lead corrosion of surface treated steels. J Nucl Mater 2000;278:85–95.
[134] Zhang J, Li N. Oxidation mechanism of steels in liquid-lead alloys. Oxid Met 2005;63:353–81.
[135] Berthon J, Revcolevschi A, Morikawa H, Touzelin B. Growth of wüstite ($Fe_{1-x}O$) crystals of various stoichiometries. J Cryst Growth 1979;47:736–8.
[136] Martin F, Soler L, Hernández F, Gómez-Briceño D. Oxide layer stability in lead–bismuth at high temperature. J Nucl Mater 2004;335:194–8.
[137] Steiner H, Konys J. Stresses in oxidized claddings and mechanical stability of oxide scales, FZKA 7191. Forschungszentrum Karlsruhe; 2006.
[138] Hosemann P, Dickerson R, Dickerson P, Li N, Maloy S. Transmission electron microscopy (TEM) on oxide layers formed on D9 stainless steel in lead bismuth eutectic (LBE). Corros Sci 2013;66:196–202.
[139] Hosemann P, Hawley M, Koury D, Swadener JG, Welch J, Johnson AL, et al. Characterization of oxide layers grown on D9 austenitic stainless steel in lead bismuth eutectic. J Nucl Mater 2008;375:323–30.
[140] Hosemann P, Hawley M, Mori G, Li N, Maloy SA. AFM and MFM characterization of oxide layers grown on stainless steels in lead bismuth eutectic. J Nucl Mater 2008;376:289–92.
[141] Hosemann P, Hofer C, Hlawacek G, Li N, Maloy SA, Teichert C. Structural, electrical and magnetic measurements on oxide layers grown on 316L exposed to liquid lead-bismuth eutectic. J Nucl Mater 2012;421:140–6.
[142] Charalampopoulou E, Delville R, Verwerft M, Lambrinou K, Schryvers D. Transmission electron microscopy study of complex oxide scales on DIN 1.4970 steel exposed to liquid Pb-Bi eutectic. Corros Sci 2019;147:22–31.
[143] Steiner H, Schroer C, Voß Z, Wedemeyer O, Konys J. Modelling of oxidation of structural materials in LBE systems. J Nucl Mater 2008;374:211–9.
[144] Tomlinson L, Cory N. Hydrogen emission during the steam oxidation of ferritic steels: kinetics and mechanism. Corros Sci 1989;29:939–65.
[145] Cory N, Herrington T. Kinetics of oxidation of ferrous alloys by super-heated steam. Oxid Met 1987;28:237–58.
[146] Cory N, Herrington T. The location of hydrogen in the kinetics of oxidation of ferrous alloys by superheated steam. Oxid Met 1988;29:135–52.
[147] Robertson J. The mechanism of high temperature aqueous corrosion of stainless steels. Corros Sci 1991;32:443–65.
[148] Tomlinson L. Mechanism of corrosion of carbon and low alloy ferritic steels by high temperature water. Corrosion 1981;37:591–6.
[149] Gibbs GB. A model for mild steel oxidation in CO_2. Oxid Met 1973;7:173–84.
[150] Cox MGC, McEnaney B, Scott VD. A chemical diffusion model for partitioning of transition elements in oxide scales on alloys. Phil Mag 1972;26:839–51.
[151] Taylor MR, Calvert JM, Lees DG, Meadowcroft DB. The mechanism of corrosion of Fe-9% Cr alloys in carbon dioxide. Oxid Met 1980;14:499–516.
[152] Kofstad P. On the formation of porosity and microchannels in growing scales. Oxid Met 1985;24:265–76.
[153] Brückman A, Romanski J. On the mechanism of sulphide scale formation on iron. Corros Sci 1965;5:185–91.
[154] Brückman A. The mechanism of transport of matter through the scales during oxidation of metals and alloys. Corros Sci 1967;7:51–9.
[155] Brückman A, Emmerich R, Mrowec S. Investigation of the high-temperature oxidation of Fe-Cr alloys by means of the isotope ^{18}O. Oxid Met 1972;5:137–47.
[156] Hales R, Hill AC. The role of metal lattice vacancies in the high temperature oxidation of nickel. Corros Sci 1972;12:843–53.
[157] Gibbs GB, Hales R. The influence of metal lattice vacancies on the oxidation of high temperature materials. Corros Sci 1977;17:487–507.
[158] Atkinson A, Smart DW. Transport of nickel and oxygen during the oxidation of nickel and dilute nickel/chromium alloy. J Electrochem Soc 1988;135:2886–93.
[159] Kyung H, Kim CK. Microstructural evolution of duplex grain structure and interpretation of the mechanism for NiO scales grown on pure Ni-and Cr-doped substrates during high temperature oxidation. Mater Sci Eng, B 2000;76:173–83.
[160] Robertson J, Manning MI. Criteria for formation of single layer, duplex, and breakaway scales on steels. Mater Sci Technol 1988;4:1064–71.
[161] Wagner C. The distribution of cations in metal oxide and metal sulphide solid solutions formed during the oxidation of alloys. Corros Sci 1969;9:91–109.
[162] Tedmon Jr CS. The effect of oxide volatilization on the oxidation kinetics of Cr and Fe-Cr alloys. J Electrochem Soc 1966;113:766–8.
[163] Zhang J. Lead-Bismuth Eutectic (LBE): A Coolant Candidate for Gen. IV Advanced Nuclear Reactor Concepts. Adv Eng Mater 2014;16:349–56.
[164] Zhang J, Li N. Analysis on liquid metal corrosion-oxidation interactions. Corros Sci 2007;49:4154–84.
[165] Zhang J. Long-term behaviours of oxide layer in liquid lead–bismuth eutectic (LBE), Part I: model development and validation. Oxid Met 2013;80:669–85.
[166] Zhang J. Long-Term Behaviours of Oxide Layer in Liquid Lead-Bismuth Eutectic (LBE), Part II: Model Application. Oxid Met 2014;81:597–615.
[167] Martinelli L, Balbaud-Célérier F, Terlain A, Delpech S, Santarini G, Favergeon J, et al. Oxidation mechanism of a Fe-9Cr-1Mo steel by liquid Pb-Bi eutectic alloy (Part I). Corros Sci 2008;50:2523–36.
[168] Martinelli L, Balbaud-Célérier F, Terlain A, Bosonnet S, Picard G, Santarini G. Oxidation mechanism of an Fe-9Cr-1Mo steel by liquid Pb-Bi eutectic alloy at 470 °C (Part II). Corros Sci 2008;50:2537–48.
[169] Martinelli L, Balbaud-Célérier F, Picard G, Santarini G. Oxidation mechanism of a Fe-9Cr-1Mo steel by liquid Pb-Bi eutectic alloy (Part III). Corros Sci 2008;50:2549–59.
[170] Martinelli L, Jean-Louis C, Fanny B. Oxidation of steels in liquid lead bismuth: Oxygen control to achieve efficient corrosion protection. Nucl Eng Des 2011;241:1288–94.
[171] Martinelli L, Dufrenoy T, Jaakou K, Rusanov A, Balbaud-Célérier F. High temperature oxidation of Fe-9Cr-1Mo steel in stagnant liquid lead-bismuth at several temperatures and for different lead contents in the liquid alloy. J Nucl Mater 2008;376:282–8.
[172] Weisenburger A, Schroer C, Jianu A, Heinzel A, Konys J, Steiner H, et al. Long term corrosion on T91 and AISI1 316L steel in flowing lead alloy and corrosion protection barrier development: Experiments and models. J Nucl Mater 2011;415:260–9.
[173] Martinelli L, Balbaud-Célérier F, Picard G, Santarini G. High temperature oxidation of Fe-9Cr-1Mo steel in liquid metal. Mater Sci Forum 2008;595–598:519–28.
[174] Lim J. Thermodynamic Assessment of the Oxygen Control Boundary for the Operation of MYRRHA. SCK·CEN 2011.
[175] Ilinčev G. Research results on the corrosion effects of liquid heavy metals Pb, Bi and Pb-Bi on structural materials with and without corrosion inhibitor. Nucl Eng Des 2002;217:167–77.

[176] Heinzel A, Weisenburger A, Müller G. Corrosion behaviour of austenitic steels in liquid lead bismuth containing 10^{-6} wt.% and 10^{-8} wt.% oxygen at 400–500°C. J Nucl Mater 2014;448:163–71.
[177] Klok O, Lambrinou K, Gavrilov S, Stergar E, Van der Donck T, Huang S, et al. Influence of plastic deformation on dissolution corrosion of type 316L austenitic stainless steel in static, oxygen-poor liquid lead-bismuth eutectic at 500°C. Corrosion 2017;73:1078–90.
[178] Yamaki E, Ginestar K, Martinelli L. Dissolution mechanism of 316L in lead-bismuth eutectic at 500°C. Corros Sci 2011;53:3075–85.
[179] Charalampopoulou E, Cautaerts N, Van der Donck T, Schryvers D, Lambrinou K, Delville R. Orientation relationship of the austenite-to-ferrite transformation in austenitic stainless steels due to dissolution corrosion in contact with liquid Pb-Bi eutectic. Scr Mater 2019;167:66–70.
[180] Benamati G, Gessi A, Scaddozzo G. Corrosion behaviour of steels and refractory metals in flowing Lead-Bismuth Eutectic at low oxygen activity. J Mater Sci 2005;40:2465–70.
[181] Tsisar V, Schroer C, Wedemeyer O, Skrypnik A, Konys J. Corrosion Interaction of 9% Cr Ferritic/Martensitic Steels at 450 and 550 °C With Flowing Pb-Bi Eutectic Containing 10^{-7} Mass% Dissolved Oxygen. J Nucl Eng Radiat Sci 2019;5:031201.
[182] Schroer C, Tsisar V, Durand A, Wedemeyer O, Skrypnik A, Konys J. Corrosion in Iron and Steel T91 Caused by Flowing Lead-Bismuth Eutectic at 400 °C and 10^{-7} Mass% Dissolved Oxygen. J Nucl Eng Radiat Sci 2019;5:011006.
[183] Schroer C, Tsisar V, Wedemeyer O, Skrypnik A, Konys J. Corrosion in Steel T91 Caused by Flowing Lead-Bismuth Eutectic at 400°C and 10^{-7} Mass% Solved Oxygen. In 24th International Conference on Nuclear Engineering, Charlotte, North Carolina; 2016.
[184] Balbaud-Celerier F, Terlain A. Influence of the Pb-Bi hydrodynamics on the corrosion of T91 martensitic steel and pure iron. J Nucl Mater 2004;335:204–9.
[185] Balbaud-Célérier F, Martinelli L. Modelling of Fe–Cr Martensitic Steels Corrosion in Liquid Lead Alloys. J Eng Gas Turbines Power 2010;132:102912.
[186] Martinelli L, Ginestar K, Botton V, Delisle C, Balbaud-Célérier F. Corrosion of T91 and pure iron in flowing and static Pb-Bi alloy between 450°C and 540°C: experiments, modelling and mechanism. Corros Sci 2020;176:108897.
[187] Martín-Muñoz FJ, Soler-Crespo L, Gómez-Briceño D. Corrosion behaviour of martensitic and austenitic steels in flowing lead–bismuth eutectic. J Nucl Mater 2011;416:87–93.
[188] Schroer C, Wedemeyer O, Novotny J, Skrypnik A, Konys J. Long-term service of austenitic steel 1.4571 as a container material for flowing lead-bismuth eutectic. J Nucl Mater 2011;418:8–15.
[189] Balbaud-Célérier F, Deloffre P, Terlain A, Rusanov A. Corrosion of metallic materials in flowing liquid lead-bismuth. Journal de Physique IV (Proceedings) 2002;12:177–90.
[190] Tsisar V, Gavrilov S, Schroer C, Stergar E. Long-term corrosion performance of T91 ferritic/martensitic steel at 400°C in flowing Pb-Bi eutectic with 2×10^{-7}mass% dissolved oxygen. Corros Sci 2020;174:108852.
[191] Kondo M, Takahashi M, Suzuki T, Ishikawa K, Hata K, Qiu S, et al. Metallurgical study on erosion and corrosion behaviours of steels exposed to liquid lead-bismuth flow. J Nucl Mater 2005;343:349–59.
[192] Weisenburger A, Heinzel A, Müller G, Muscher H, Rousanov A. T91 cladding tubes with and without modified FeCrAlY coatings exposed in LBE at different flow, stress and temperature conditions. J Nucl Mater 2008;376:274–81.
[193] Chen G, Ju N, Lei Y, Wang D, Zhu Q, Li T. Corrosion behaviour of 410 stainless steel in flowing lead-bismuth eutectic alloy at 550°C. J Nucl Mater 2019;522:168–83.
[194] Li C, Fang XD, Wang QS, Shen ML, Wang HL, Zeng X, et al. A synergy of different corrosion failure modes pertaining to T91 steel impacted by extreme lead-bismuth eutectic flow pattern. Corros Sci 2021;180:109214.
[195] Li C, Liu YJ, Zhang FF, Fang XD, Liu Z. Erosion-corrosion of 304N austenitic steels in liquid Pb-Bi flow perpendicular to steel surface. Mater Charact 2021;175:111054.
[196] Sapundjiev D, Van Dyck S, Bogaerts W. Liquid metal corrosion of T91 and A316L materials in Pb–Bi eutectic at temperatures 400–600°C. Corros Sci 2006;48:577–94.
[197] Tsisar V, Schroer C, Wedemeyer O, Skrypnik A, Konys J. Influence of Cold Work on Solution-Based Corrosion Attack on 1.4970 (15-15Ti) Austenitic Steel in Static Liquid Lead-Bismuth Eutectic at 550°C and $\leq10^{-8}$ mass% Dissolved Oxygen. In 23rd International Conference on Nuclear Engineering, Chiba, Japan; 2015.
[198] Fazio C, Benamati G, Martini C, Palombarini G. Compatibility tests on steels in molten lead and lead-bismuth. J Nucl Mater 2001;296:243–8.
[199] Benamati G, Fazio C, Piankova H, Rusanov A. Temperature effect on the corrosion mechanism of austenitic and martensitic steels in lead-bismuth. J Nucl Mater 2002;301:23–7.
[200] Kondo M, Takahashi M. Metallurgical analysis of a tube ruptured in the lead bismuth corrosion test facility. J Nucl Sci Technol 2006;43:174–8.
[201] Deloffre P, Terlain A, Barbier F. Corrosion and deposition of ferrous alloys in molten lead-bismuth. J Nucl Mater 2002;301:35–9.
[202] Kurata Y, Saito S. Results of corrosion tests in liquid Pb-Bi at JAEA - temperature and oxygen concentration dependence, and corrosion properties of Si-enriched steels. In Actinide and fission product partitioning and transmutation, Mito, Japan; 2008.
[203] Kurata Y. Corrosion experiments and materials developed for the Japanese HLM systems. J Nucl Mater 2011;415:254–9.
[204] Kurata Y, Futakawa M, Saito S. Comparison of the corrosion behaviour of austenitic and ferritic/martensitic steels exposed to static liquid Pb-Bi at 450 and 550°C. J Nucl Mater 2005;343:333–40.
[205] Kurata Y, Futakawa M, Saito S. Corrosion behaviour of steels in liquid lead-bismuth with low oxygen concentrations. J Nucl Mater 2008;373:164–78.
[206] Furukawa T, Muller G, Schumacher G, Weisenburger A, Heinzel A, Zimmermann F, et al. Corrosion behaviour of FBR candidate materials in stagnant Pb-Bi at elevated temperature. J Nucl Sci Technol 2004;41:265–70.
[207] Kurata Y, Futakawa M. Excellent corrosion resistance of 18Cr-20Ni-5Si steel in liquid Pb-Bi. J Nucl Mater 2004;325:217–22.
[208] Kurata Y, Saito S. Temperature dependence of corrosion of ferritic/martensitic and austenitic steels in liquid lead-bismuth eutectic. Mater Trans 2009;50:2410–7.
[209] Martín-Muñoz FJ, Soler-Crespo L, Gómez-Briceño D. Assessment of the influence of surface finishing and weld joints on the corrosion/oxidation behaviour of stainless steels in lead bismuth eutectic. J Nucl Mater 2011;416:80–6.
[210] Soler L, Martín FJ, Hernández F, Gómez-Briceño D. Corrosion of stainless steels in lead-bismuth eutectic up to 600°C. J Nucl Mater 2004;335:174–9.
[211] Deloffre P, Terlain A. Influence of Zn as a spallation product on the behaviour of martensitic steel T91 and austenitic steel 316L in liquid Pb-Bi. J Nucl Mater 2004;335:244–8.
[212] Bian L, Xia S, Bai Q, Li H, Zhou BX. The effects of cold working on the corrosion behaviour of an austenitic stainless steel in liquid lead-bismuth eutectic under vacuum at 873K. J Nucl Mater 2018;509:591–9.
[213] Kurata Y. Corrosion behaviour of cold-worked austenitic stainless steels in liquid lead–bismuth eutectic. J Nucl Mater 2014;448:239–49.
[214] Barbier F, Benamati G, Fazio C, Rusanov A. Compatibility tests of steels in flowing liquid lead-bismuth. J Nucl Mater 2001;295:149–56.
[215] Long B, Scaddozzo G, Fazio C, Agostini M, Aiello A, Benamati G. Corrosion behaviour of steels and refractory metals in flowing Pb-Bi 2003;6876:199–210.
[216] Fazio C, Ricapito I, Scaddozzo G, Benamati G. Corrosion behaviour of steels and refractory metals and tensile features of steels exposed to flowing PbBi in the LECOR loop. J Nucl Mater 2003;318:325–32.
[217] Aiello A, Azzati M, Benamati G, Gessi A, Long B, Scaddozzo G. Corrosion behaviour of stainless steels in flowing LBE at low and high oxygen concentration. J Nucl Mater 2004;335:169–73.
[218] Benamati G, Gessi A, Zhang PZ. Corrosion experiments in flowing LBE at 450°C. J Nucl Mater 2006;356:198–202.
[219] Gessi A, Benamati G. Corrosion experiments of steels in flowing Pb at 500°C and in flowing LBE at 450°C. J Nucl Mater 2008;376:269–73.
[220] Kikuchi K, Kurata Y, Saito S, Futakawa M, Sasa T, Oigawa H, et al. Corrosion-erosion test of SS316 in flowing Pb-Bi. J Nucl Mater 2003;318:348–54.
[221] Saito S, Kikuchi K, Hamaguchi D, Tezuka M, Miyagi M, Kokawa H, et al. Corrosion-erosion test of SS316L grain boundary engineering material (GBEM) in lead bismuth flowing loop. J Nucl Mater 2012;431:91–6.
[222] Li N, He X, Rusanov A, Demishonkov AP. Corrosion Test of US Steels in Lead-Bismuth Eutectic (LBE) and Kinetic Modelling of Corrosion in LBE Systems, Los Alamos report LA-UR-01-5241; 2001.

[223] Ilincev G, Kárník D, Paulovic M. The impact of the composition of structural steels on their corrosion stability in liquid Pb-Bi at 500 and 400°C with different oxygen concentrations. J Nucl Mater 2004;335:210–6.
[224] Takahashi M, Sekimoto H, Ishikawa K, Sawada N, Suzuki T, Hata K, et al. Experimental study on flow technology and steel corrosion of lead-bismuth. In 10th International Conference on Nuclear Engineering, Arlington, Virginia, USA; 2002.
[225] Kondo M, Takahashi M, Sawada N, Hata K. Corrosion of steels in lead-bismuth flow. J Nucl Sci Technol 2006;43:107–16.
[226] Takahashi M, Kondo M, Sawada N, Hata K. Corrosion of steels in lead-bismuth flow. In 10th International Conference on Nuclear Engineering, Arlington, Virginia, USA; 2002.
[227] Doubková A, Di Gabriele F, Brabec P, Keilova E. Corrosion behaviour of steels in flowing lead–bismuth under abnormal conditions. J Nucl Mater 2008;376:260–4.
[228] Johnson A, Parsons D, Manzerova J, Perry D, Koury D, Hosterman B, et al. Spectroscopic and microscopic investigation of the corrosion of 316/316L stainless steel by lead-bismuth eutectic (LBE) at elevated temperatures: importance of surface preparation. J Nucl Mater 2004;328:88–96.
[229] Tsisar V, Schroer C, Wedemeyer O, Skrypnik A, Konys J. Effect of structural state and surface finishing on corrosion behaviour of 1.4970 austenitic steel at 400 and 500°C in flowing Pb-Bi eutectic with dissolved oxygen. Journal of Nuclear Engineering and Radiation. Science 2018;4:041001.
[230] Tian SJ. Growth and Exfoliation Behaviour of the Oxide Scale on 316L and T91 in Flowing Liquid Lead-Bismuth Eutectic at 480°C. Oxid Met 2020;93:183–94.
[231] OECD/NEA. Handbook on Lead-bismuth Eutectic Alloy and Lead Properties, Materials Compatibility. Thermal-hydraulics and Technologies; 2007.
[232] Schroer C, Wedemeyer O, Novotny J, Skrypnik A, Konys J. Compatibility of Ferritic/Martensitic Steels With Flowing Lead-Bismuth Eutectic at 450-550 °C and 10^{-6} Mass% Dissolved Oxygen. In 20th International Conference on Nuclear Engineering (ICONE20). Anaheim, California, USA: ASME; 2012.
[233] Mikityuk K. Analytical model of the oxide layer build-up in complex lead-cooled systems. Nucl Eng Des 2010;240:3632–7.
[234] Hwang IS, Lim J. Structural developments for lead-bismuth cooled fast reactors PEACER and PASCAR. In 25th KAIF/KNS Annual Conference, Seoul, Korea; 2010.
[235] Kurata Y, Futakawa M, Kikuchi K, Saito S, Osugi T. Corrosion studies in liquid Pb-Bi alloy at JAERI: R&D program and first experimental results. J Nucl Mater 2002;301:28–34.
[236] Shi QQ, Liu J, Luan H, Yang ZG, Wang W, Yan W, et al. Oxidation behaviour of ferritic/martensitic steels in stagnant liquid LBE saturated by oxygen at 600 °C. J Nucl Mater 2015;457:135–41.
[237] Schroer C, Wedemeyer O, Skrypnik A, Novotny J, Konys J. Corrosion kinetics of Steel T91 in flowing oxygen-containing lead-bismuth eutectic at 450 °C. J Nucl Mater 2012;431:105–12.
[238] Barbier F, Rusanov A. Corrosion behaviour of steels in flowing lead-bismuth. J Nucl Mater 2001;296:231–6.
[239] Schroer C, Wedemeyer O, Novotny J, Skrypnik A, Konys J. Performance of 9% Cr steels in flowing lead-bismuth eutectic at 450 and 550 °C, and 10^{-6} mass% dissolved oxygen. Nucl Eng Des 2014;280:661–72.
[240] Tian SJ, Jiang ZZ, Luo L. Oxidation behaviour of T91 in flowing oxygen-containing lead-bismuth eutectic at 500°C. Mater Corros 2016;67:1274–85.
[241] Ricci E, Giuranno D, Canu G, Amore S, Novakovic R. Corrosion behaviour of oxide dispersion strengthened iron-chromium steels in liquid lead at 973 K. Mater Corros 2018;69:1584–96.
[242] Johnson AL, Koury D, Welch J, Ho T, Sidle S, Harland C, et al. Spectroscopic and microscopic investigation of the corrosion of D-9 stainless steel by lead-bismuth eutectic (LBE) at elevated temperatures. Initiation of thick oxide formation. J Nucl Mater 2008;376:265–8.
[243] Asher RC, Davies D, Beetham SA. Some observations on the compatibility of structural materials with molten lead. Corros Sci 1977;17:545–57.
[244] Cairang WD, Ma SQ, Gong X, Zeng Y, Yang HJ, Xue DZ, et al. Oxidation mechanism of refractory Molybdenum exposed to oxygen-saturated lead-bismuth eutectic at 600°C. Corros Sci 2021;179:109132.
[245] Kurata Y. Corrosion behaviour of Si-enriched steels for nuclear applications in liquid lead-bismuth. J Nucl Mater 2013;437:401–8.
[246] Short MP, Ballinger RG, Hänninen HE. Corrosion resistance of alloys F91 and Fe-12Cr-2Si in lead-bismuth eutectic up to 715 °C. J Nucl Mater 2013;434:259–81.
[247] Schroer C, Koch V, Wedemeyer O, Skrypnik A, Konys J. Silicon-containing ferritic/martensitic steel after exposure to oxygen-containing flowing lead-bismuth eutectic at 450 and 550 °C. J Nucl Mater 2016;469:162–76.
[248] Wang J, Lu SP, Rong LJ, Li DZ, Li YY. Effect of silicon on the oxidation resistance of 9 wt% Cr heat resistance steels in 550 °C lead-bismuth eutectic. Corros Sci 2016;111:13–25.
[249] Eliseeva O, Tsisar V, Fedirko V, Matychak Y. Changes in the phase composition of an oxide film on EP-823 steel in contact with stagnant lead melt. Mater Sci 2004;40:260–9.
[250] Kondo M, Takahashi M. Corrosion resistance of Si-and Al-rich steels in flowing lead–bismuth. J Nucl Mater 2006;356:203–12.
[251] Van den Bosch J, Coen G, Hosemann P, Maloy SA. On the LME susceptibility of Si enriched steels. J Nucl Mater 2012;429:105–12.
[252] Porollo SI, Dvoriashin AM, Konobeev YV, Garner FA. Microstructure and mechanical properties of ferritic/martensitic steel EP-823 after neutron irradiation to high doses in BOR-60. J Nucl Mater 2004;329–333:314–8.
[253] Rivai AK, Saito S, Tezuka M, Kato C, Kikuchi K. Effect of cold working on the corrosion resistance of JPCA stainless steel in flowing Pb-Bi at 450 °C. J Nucl Mater 2012;431:97–104.
[254] Tsisar V, Schroer C, Wedemeyer O, Skrypnik A, Konys J. Effect of Structural State of Austenitic 15-15Ti Steel on Initiation and Propagation of Solution-Based Corrosion Attack in Flowing Liquid Pb-Bi Eutectic at 400 and 500°C. In 25th International Conference on Nuclear Engineering, Shanghai, China; 2017.
[255] Dong H, Ye ZF, Wang P, Li DZ, Zhang YT, Li YY. Effect of cold rolling on the oxidation resistance of T91 in oxygen-saturated stagnant liquid lead-bismuth eutectic at 450°C and 550°C. J Nucl Mater 2016;476:213–7.
[256] Dong H, Wang P, Li DZ, Li YY. Effect of pre-deformation on the oxidation resistance of a high Si ferritic/martensitic steel in oxygen-saturated stagnant lead-bismuth eutectic at 550°C. Corros Sci 2017;118:129–42.
[257] Liu J, Jiang ZZ, Tian SJ, Huang QY, Liu YJ. Stress corrosion behaviour of T91 in static lead–bismuth eutectic at 480°C. J Nucl Mater 2016;468:299–304.
[258] Yae Kina A, Souza VM, Tavares SSM, Pardal JM, Souza JA. Microstructure and intergranular corrosion resistance evaluation of AISI 304 steel for high temperature service. Mater Charact 2008;59:651–5.
[259] Kikuchi K, Kamata K, Ono M, Kitano T, Hayashi K, Oigawa H. Corrosion rate of parent and weld materials of F82H and JPCA steels under LBE flow with active oxygen control at 450 and 500°C. J Nucl Mater 2008;377:232–42.
[260] Heinzel A, Müller G, Weisenburger A. Corrosion behaviour of welds and Ta in liquid lead. J Nucl Mater 2016;469:62–71.
[261] Mustari APA, Takahashi M. Study on corrosion of welded steel for LBE-cooled fast reactors. Prog Nucl Energy 2011;53:1073–7.
[262] Mustari APA, Takahashi M. Study on the corrosion properties of welded ferritic-martensitic steels in liquid lead-bismuth at 600°C. J Power Energy Syst 2011;5:69–76.
[263] Wang J, Rong LJ, Li DZ, Lu SP. Effect of welding thermal cycles on the oxidation resistance of 9 wt% Cr heat resistant steels in 550 °C lead-bismuth eutectic. Appl Surf Sci 2016;389:930–41.
[264] Chen G, Lei YC, Zhu Q, Ju N, Li TQ, Wang D. Corrosion behaviour of CLAM steel weld bead in flowing Pb-Bi at 550°C. J Nucl Mater 2019;515:187–98.
[265] Chen G, Lei YC, Zhu Q, Li TQ, Wang D, Ju N, et al. Study on Corrosion Behaviour of Weld Bead by Tungsten Inert Gas Welding China Low Activation Martensitic Steel in Static Oxygen-Saturated Pb-Bi at 500 °C. Corrosion 2019;75:408–16.
[266] Chen G, Ju N, Lei YC, Wang D, Zhu Q, Li TQ. Corrosion behaviour of base metal and weld bead of CLAM steel in flowing Pb-Bi at 550 °C. Prog Nucl Energy 2020;118:103074.
[267] Heinzel A, Müller G, Weisenburger A. Behaviour of welds in liquid lead containing 10^{-6} wt.% and 10^{-8} wt.% oxygen. J Nucl Mater 2013;437:116–21.
[268] Zhou WY, Yang Y, Zheng GQ, Woller KB, Stahle PW, Minor AM, et al. Proton irradiation-decelerated intergranular corrosion of Ni-Cr alloys in molten salt. Nat Commun 2020;11:3430.
[269] Was GS, Jiao Z, Getto E, Sun K, Monterrosa AM, Maloy SA, et al. Emulation of reactor irradiation damage using ion beams. Scr Mater 2014;88:33–6.

[270] Lillard RS, Paciotti M, Tcharnotskaia V. The influence of proton irradiation on the corrosion of HT-9 during immersion in lead bismuth eutectic. J Nucl Mater 2004;335:487–92.
[271] Yao CF, Wang ZG, Zhang HP, Chang HL, Sheng YB, Shen TL, et al. HLMIF, a facility for investigating the synergistic effect of ion-irradiation and LBE corrosion. J Nucl Mater 2019;523:260–7.
[272] Li BS, Sheng YB, Liu HP, Lu XR, Shu XY, Xiong AL, et al. Dissolution corrosion of 4H-SiC in lead-bismuth eutectic at 550°C. Mater Corros 2019;70:1878–83.
[273] Allen TR, Konings RJM, Motta AT. 5.03 - Corrosion of Zirconium Alloys. Comprehens Nucl Mater 2012;5:49–68.
[274] Wang P, Was GS. Oxidation of Zircaloy-4 during in situ proton irradiation and corrosion in PWR primary water. J Mater Res 2015;30:1335–48.
[275] Asher RC, Davies D, Kirstein TBA, McCullen PAJ, White JF. The effects of radiation on the corrosion of some Zr alloys. Corros Sci 1970;10:695–707.
[276] Bakai AS. Combined Effect of Molten Fluoride Salt and Irradiation on Ni-based Alloys. in Materials Issues for Generation IV Systems. Springer 2008:537–57.
[277] Lei GH, Li C, Jiang Z, Huang FF. Irradiation accelerated fluoride molten salt corrosion of nickel-based UNS N10003 alloy revealed by X-ray absorption fine structure. Corros Sci 2020;165:108408.
[278] Ignatiev V, Surenkov A. 5.10 - Material Performance in Molten Salts. Comprehens Nucl Mater 2012;5:221–50.
[279] Zhou WY, Woller KB, Zheng GQ, Stahle PW, Short MP. A simultaneous corrosion/irradiation facility for testing molten salt-facing materials. Nucl Instrum Methods Phys Res, Sect B 2019;440:54–9.
[280] Huntington AK. Discussion on Report to Beilby Prize Committee. J Instit Met 1914;12:108.
[281] Fernandes PJL, Jones DRH. Mechanisms of liquid metal induced embrittlement. Int Mater Rev 1997;42:251–61.
[282] Kamdar MH. Embrittlement by liquid metals. Prog Mater Sci 1973;15:289–374.
[283] Joseph B, Picat M, Barbier F. Liquid metal embrittlement: A state-of-the-art appraisal. Eur Phys J Appl Phys 1999;5:19–31.
[284] Kolman DG. A review of recent advances in the understanding of liquid metal embrittlement. Corrosion 2019;75:42–57.
[285] Lynch SP. Mechanisms and kinetics of environmentally assisted cracking: current status, issues, and suggestions for further work. Metall Mater Trans A 2013; 44:1209–29.
[286] Nicholas MG, Old CF. Liquid metal embrittlement. J Mater Sci 1979;14:1–18.
[287] Beal C, Kleber X, Fabregue D, Bouzekri M. Liquid zinc embrittlement of a high-manganese-content TWIP steel. Philos Mag Lett 2011;91:297–303.
[288] Beal C, Kleber X, Fabregue D, Bouzekri M. Liquid zinc embrittlement of twinning-induced plasticity steel. Scr Mater 2012;66:1030–3.
[289] Beal C, Kleber X, Fabregue D, Bouzekri M. Embrittlement of a zinc coated high manganese TWIP steel. Mater Sci Eng, A 2012;543:76–83.
[290] Lynch SP. A fractographic study of hydrogen-assisted cracking and liquid-metal embrittlement in nickel. J Mater Sci 1986;21:692–704.
[291] Proriol Serre I, Vogt JB. Liquid metal embrittlement sensitivity of the T91 steel in lead, in bismuth and in lead bismuth eutectic. J Nucl Mater 2020;531: 152021.
[292] Kolman DG. Liquid Metal Induced Embrittlement, Corrosion: Fundamentals, Testing, and protection. ASM Handbook ASM Int 2003;13A:381–92.
[293] Kelley MJ, Stoloff NS. Analysis of liquid metal embrittlement from a bond energy viewpoint. Metall Trans A 1975;6:159–66.
[294] Johnston TL, Davies RG, Stoloff NS. Slip character and the ductile to brittle transition of single-phase solids. Phil Mag 1965;12:305–17.
[295] Stoloff NS, Davies RG, Johnston TL. Slip Character and Liquid Metal Embrittlement. Environment-Sensitive Mechanical Behaviour 1966;vol. 35:613–55.
[296] Rostoker W, McCaughey JM, Markus H. Embrittlement by liquid metals. New York: Reinhold Publishing Corporation; 1960.
[297] Shunk FA, Warke WR. Specificity as an aspect of liquid metal embrittlement. Scr Metall 1974;8:519–26.
[298] Gordon P, An HH. The mechanisms of crack initiation and crack propagation in metal-induced embrittlement of metals. Metall Trans A 1982;13:457–72.
[299] Popovich VV, Dmukhovskaya IG. The embrittlement of metals and alloys being deformed in contact with low-melting alloys (a review of foreign literature). Soviet materials science: a transl. of Fiziko-khimicheskaya mekhanika materialov/Academy of Sciences of the. Ukrainian SSR 1987;23:535–44.
[300] Fernandes PJL, Clegg RE, Jones DRH. Failure by liquid metal induced embrittlement. Eng Fail Anal 1994;1:51–63.
[301] Glickman EE. Mechanism of liquid metal embrittlement by simple experiments: from atomistic to life-time. In: Lepinoux J, editor. Multiscale Phenomena in Plasticity. Dordrecht, The Netherlands: Kluwer Academic Publishers; 2000. p. 383–401.
[302] Gorse D, Goryachev S, Auger T. Liquid metal embrittlement. From basic concepts to recent results related to structural materials for liquid metal spallation targets. In JAERI conf 2003–001, 2003..
[303] Ina K, Koizumi H. Penetration of liquid metals into solid metals and liquid metal embrittlement. Mater Sci Eng, A 2004;387–389:390–4.
[304] Wesley-Austin G. The effect of molten solder on some stressed materials. J Inst Metals 1936;58:173–85.
[305] Old CF. Liquid metal embrittlement of nuclear materials. J Nucl Mater 1980;92:2–25.
[306] Hadjem-Hamouche Z, Auger T, Guillot I. Temperature effect in the maximum propagation rate of a liquid metal filled crack: The T91 martensitic steel/ Lead–Bismuth Eutectic system. Corros Sci 2009;51:2580–7.
[307] Old CF, Trevena P. Embrittlement of zinc by liquid metals. Metal Science 1979;13:487–95.
[308] Tsutsui N, Koizumi H. Intergranular/transgranular fracture in the liquid metal embrittlement of polycrystalline zinc. Procedia Struct Integrity 2018;13:849–54.
[309] Senel E, Walmsley JC, Diplas S, Nisancioglu K. Liquid metal embrittlement of aluminium by segregation of trace element gallium. Corros Sci 2014;85:167–73.
[310] Rajagopalan M, Bhatia MA, Tschopp MA, Srolovitz DJ, Solanki KN. Atomic-scale analysis of liquid-gallium embrittlement of aluminium grain boundaries. Acta Mater 2014;73:312–25.
[311] Uan JY, Chang CC. Characterization of gallium-induced intergranular fracture surface and the Auger electron spectroscopic analysis for mg grain boundary segregation in AA6061 T4 Al-Mg-Si alloy. Mater Trans 2004;45:1925–32.
[312] Uan JY, Chang CC. Gallium-induced magnesium enrichment on grain boundary and the gallium effect on degradation of tensile properties of aluminium alloys. Metall Mater Trans A 2006;37:2133–45.
[313] Lu GH, Zhang Y, Deng S, Wang T, Kohyama M, Yamamoto R, et al. Origin of intergranular embrittlement of Al alloys induced by Na and Ca segregation: Grain boundary weakening. Phys Rev B 2006;73:224115.
[314] Lynch SP. Metal-induced embrittlement of materials. Mater Charact 1992;28:279–89.
[315] Gordon P. Metal-induced embrittlement of metals—an evaluation of embrittler transport mechanisms. Metall Trans A 1978;9:267–73.
[316] Lynch SP. Failures of structures and components by metal-induced embrittlement. J Fail Anal Prev 2008;8:259–74.
[317] Kolman DG, Chavarria R. Liquid-metal embrittlement of 7075 aluminium and 4340 steel compact tension specimens by gallium. J Test Eval 2002;30:452–6.
[318] Keller SG, Gordon AP. Experimental study of liquid metal embrittlement for the aluminium 7075–mercury couple. Eng Fract Mech 2012;84:146–60.
[319] Woolman J, Jacques A. Influence of Lead Additions on the Mechanical Properties and Machinability of Some Alloy Steels. J Iron Steel Instit 1950;165:257–67.
[320] Swinden T. Leaded manganese molybdenum steel. J Iron Steel Instit 1943;148:441–7.
[321] Bhattacharya D. Effects of Metal Induced Embrittlement in Free-Machining Steels. Embrittlement by Liquid and Solid Metals. In Kamdar MH, editor, Embrittlement by Liquid and Solid Metals; 1984, p. 367–98.
[322] Potak YM, Shcheglakov IM. Zh. Tek. Fiz. 1955;25:897 [in Russian].
[323] Kishkin ST, Nikolenko VV. Heat resistance and influence of working media. Dokl Akad Nauk SSSR 1956;110:1018–21.
[324] Der RW. interkristalline Angriff von Metallschmelzen auf Stahl. Mater Corros 1973;24:851–9 [in German].
[325] Andreev IV, Gorshkov VF, Dityatkovskii YM. Effect of molten metals on the mechanical properties of steel. Met Sci Heat Treat 1964;6:311–3.
[326] Chaevskii MI, Shatinskii VF, Popovich VV. The role of oxygen in the adsorption-induced reduction of load-carrying capacity of steel specimens in contact with liquid alloys. Sov Mater Sci: a transl of Fiziko-khimicheskaya mekhanika materialov/Acad Sci Ukrainian SSR 1966;1:445–8.
[327] Shatinskii VF. Thermomechanical surface treatment as applied to steel 40Kh. Sov Mater Sci: a transl of Fiziko-khimicheskaya mekhanika materialov/Acad Sci Ukrainian SSR 1967;2:82–7.
[328] Shchukin ED, Yushchenko VS. Selectivity of adsorption-induced reduction in strength under the influence of liquid metals. Sov Mater Sci: a transl of Fiziko-khimicheskaya mekhanika materialov/Acad Sci Ukrainian SSR 1967;2:95–101.
[329] Bichuya AL, Zamora MF, Pikhel'son VF, Chaevskii MI. Effect of molten Pb-Bi eutectic on the fatigue strength of steel. Sov Mater Sci: a transl of Fiziko-khimicheskaya mekhanika materialov/Acad Sci Ukrainian SSR 1969;4:12–4.

[330] Chaevskii MI, Bichuya AL. Eliminating the weakening effect of lead-bismuth eutectic on steel by reducing the strain rate. Sov Mater Sci: a transl of Fiziko-khimicheskaya mekhanika materialov/Acad Sci Ukrainian SSR 1972;5:82–4.
[331] Chaevskii MI, Bichuya AL. The role of oxygen in the formation of cracks in steel deformed in contact with liquid Pb-Bi eutectic. Sov Mater Sci: a transl of Fiziko-khimicheskaya mekhanika materialov/Acad Sci Ukrainian SSR 1973;6:330–2.
[332] Balandin YF, Divisenko IF. Strength and ductility of a type 12 KhM heat-resistant steel in contact with liquid Pb-Bi eutectic. Sov Mater Sci: a transl of Fiziko-khimicheskaya mekhanika materialov/Acad Sci Ukrainian SSR 1973;6:732–5.
[333] Bichuya AL, Popovich VV, Zamora MF, Mizetskii VL, Shil'nikova GK. The fatigue strength, in a Pb-Bi eutectic melt, of steel 15KhS1MFB smelted in the ordinary way and in vacuo. Sov Mater Sci: a transl of Fiziko-khimicheskaya mekhanika materialov/Acad Sci Ukrainian SSR 1973;7:336–9.
[334] Tanaka M, Fukunaga H. On the Embrittlement of Mild Steel in Liquid Metals. J Soc Mat Sci 1969;18:411–7. in Japanese.
[335] Tanaka M, Fukunaga H. Consideration on the Fatigue Behaviour of Low Carbon Steel in Liquid Metal Environment. J Soc Mat Sci 1969;18:714–20.
[336] Tanaka M, Fukunaga H. Fatigue Strength of Low Carbon Steel in Molten Tin, Lead and Zinc (The Case of Notched Specimen). J Soc Mat Sci 1969;18:632–6 [in Japanese].
[337] Tanaka M, Fukunaga H. Fatigue strength of mild steel, 13Cr steel and 18Cr-8Ni steel subjected to elevated temperature and to contact with liquid Pb and Sn. J Soc Mat Sci 1969;18:254–8 [in Japanese].
[338] Mostovoy S, Breyer NN. The effect of lead on the mechanical properties of 4145 steel. ASM Trans Quart 1968;61:219–32.
[339] Zipp RD, Warke WR, Breyer NN. A Comparison of Elevated Temperature Tensile Fractures in Nonleaded and Leaded 4145 Steel. in Electron Microfractography. ASTM. International 1969;453:111–33.
[340] Warke WR, Breyer NN. Effect of steel composition on lead embrittlement. J Iron Steel Inst 1971;209:779–84.
[341] Warke WR, Johnson KL, Breyer NN. Liquid Metal Embrittlement of Steel by Lead and Lead Alloys. In: Draley JE, Weeks JR, editors. Corrosion by Liquid Metals. Boston, MA: Springer; 1970.
[342] Lynn JC, Warke WR, Gordon P. Solid metal-induced embrittlement of steel. Mater Sci Eng 1975;18:51–62.
[343] Dinda S, Warke WR. The effect of grain boundary segregation on liquid metal induced embrittlement of steel. Mater Sci Eng 1976;24:199–208.
[344] Johnson KL, Breyer NN, Dally JW. Environmental Sensitivity of Structural Metals: Some Dynamic Aspects of Liquid Metal Embrittlement. In: Environmental Degradation of Engineering Materials. AIME; 1977. p. 91–103.
[345] Popovich VV. Influence of deformation rate on the ductility of steel samples in contact with a liquid metal medium. Sov Mater Sci: a transl of Fiziko-khimicheskaya mekhanika materialov/Acad Sci Ukrainian SSR 1982;17:392–5.
[346] Landow M, Harsolia A, Breyer NN. Liquid metal embrittlement of 4145 steel by lead alloys. J Mater Energy Syst 1981;2:50–9.
[347] Breyer NN, Johnson KL. Liquid metal embrittlement of 4145 steel by lead-tin and lead-antimony alloys. J Test Eval 1974;2:471–7.
[348] Kamdar MH. Embrittlement of 4340 type steel by liquid lead and antimony and lead-antimony. Embrittlement by liquid and solid metals. The metallurgical society of AIME; 1982.
[349] Popovich VV, Dmukhovskaya IG. Rebinder effect in the fracture of Armco iron in liquid metals. Sov Mater Sci: a transl of Fiziko-khimicheskaya mekhanika materialov/Acad Sci Ukrainian SSR 1978;14:365–70.
[350] Dmukhovskaya IG, Popovich VV. Effect of lead on the fracture of Armco iron. Sov Mater Sci: a transl of Fiziko-khimicheskaya mekhanika materialov/Acad Sci Ukrainian SSR 1980;15:366–9.
[351] Dmukhovskaya IG, Yaremchenko NY, Zima YV, Popovich VV. Influence of temperature on the character of failure of Armco iron in liquid-metal media. Sov Mater Sci: a transl of Fiziko-khimicheskaya mekhanika materialov/Acad Sci Ukrainian SSR 1984;19:431–4.
[352] Dmukhovskaya IG, Popovich VV. Role of grain size in liquid-metal embrittlement of iron. Sov Mater Sci: a transl of Fiziko-khimicheskaya mekhanika materialov/Acad Sci Ukrainian SSR 1981;16:334–7.
[353] Popovich VV, Dmukhovskaya IG. Relationship of liquid-metal embrittlement to the character of interaction of a medium with a metal being deformed. Sov Mater Sci: a transl of Fiziko-khimicheskaya mekhanika materialov/Acad Sci Ukrainian SSR 1984;19:489–92.
[354] Popovich VV, Kalyandruk VI, Dmukhovskaya IG, Peresichanskaya MA. Influence of the residual gases of a vacuum on the liquid metal embrittlement of Armco iron. Sov Mater Sci: a transl of Fiziko-khimicheskaya mekhanika materialov/Acad Sci Ukrainian SSR 1985;20:486–9.
[355] Dmukhovs'ka IH, Popovych VV. Influence of stress concentrators on the temperature dependence of the liquid metal embrittlement of Armco iron. Mater Sci 1993;29:501–6.
[356] Broc M, Sannier J, Santarini G. Experimental studies on the use of liquid lead in a molten salt nuclear reactor. Nucl Technol 1983;63:197–208.
[357] Chaevskii MI, Shatinskii VF. Improving the performance of steels in liquid low-melting metals by thermo-mechanical treatment. Sov Mater Sci: a transl of Fiziko-khimicheskaya mekhanika materialov/Acad Sci Ukrainian SSR 1966;1:453–6.
[358] Bichuya AL. Effect of oxide films on the corrosion-fatigue strength of 1Cr18Ni9Ti steel in liquid Pb-Bi eutectic. Sov Mater Sci: a transl of Fiziko-khimicheskaya mekhanika materialov/Acad Sci Ukrainian SSR 1972;5:352–4.
[359] Bichuya AL, Toropovskaya IN. Estimate of the protective properties of coatings of structural metals in Pb-Bi eutectic. Sov Mater Sci: a transl of Fiziko-khimicheskaya mekhanika materialov/Acad Sci Ukrainian SSR 1974;8:306–9.
[360] Abramov VY, Bozin SN, Eliseeva OI, Kalinin GM, Kalyandruk VI, Lyutyi EM. Influence of a lead melt on plastic deformation of high-alloyed heat-resistant steels. Mater Sci 1995;30:465–9.
[361] Stoloff NS, Johnston TL. Crack propagation in a liquid metal environment. Acta Metall 1963;11:251–6.
[362] Westwood ARC, Kamdar MH. Concerning liquid metal embrittlement, particularly of zinc monocrystals by mercury. Phil Mag 1963;8:787–804.
[363] Lynch SP. Liquid-metal embrittlement in an Al6%Zn3%Mg alloy. Acta Metall 1981;29:325–40.
[364] Lynch SP. Environmentally assisted cracking: overview of evidence for an adsorption-induced localised-slip process. Acta Metall 1988;36:2639–61.
[365] Lynch SP. Metallographic contributions to understanding mechanisms of environmentally assisted cracking. Metallography 1989;23:147–71.
[366] Hancock PC, Ives MB. The role of plastic deformation in liquid metal embrittlement. Can Metall Q 1971;10:207–11.
[367] Robertson WM. Propagation of a crack filled with liquid metal. Trans Met Soc AIME 1966;236:1478–82.
[368] Glickman EE. Dissolution condensation mechanism of stress corrosion cracking in liquid metals: driving force and crack kinetics. Metall Mater Trans A 2011;42:250–66.
[369] Dmukhovskaya IG, Popovich VV. A phenomenological model of embrittlement of metals under conditions of the adsorption action of liquid metal media. Sov Mater Sci: a transl of Fiziko-khimicheskaya mekhanika materialov/Acad Sci Ukrainian SSR 1983;18:461–7.
[370] Rebinder PA. Investigation of the influence of the surface energy of a crystal on its mechanical properties when the surface tension of its faces is lowered by the introduction of surface-active substances into the working medium. Moscow: Gosizdat; 1928.
[371] Gomez-Moreno O, Coudurier L, Eustathopoulos N. Role de l'adsorption dans la mouillabilite du fer solide par le plomb et ses alliages. Acta Metall 1982;30:831–40.
[372] Zaïdi M, Giorgi ML, Guillot JB, Goodwin F. Spreading of liquid lead droplets on metallic iron covered by silicon oxide particles or films. Mater Sci Eng, A 2008;495:90–5.
[373] Roth TA. The surface and grain boundary energies of iron, cobalt and nickel. Materials Science and Engineering 1975;18:183–92.
[374] Monchoux JP, Rabkin E. Microstructure evolution and interfacial properties in the Fe–Pb system. Acta Mater 2002;50:3159–74.
[375] Lynch SP. Stress Corrosion Cracking: Theory and Practice. Cambridge: Woodhead Publishing; 2011.
[376] Nam HS, Srolovitz DJ. Molecular dynamics simulation of Ga penetration along Σ5 symmetric tilt grain boundaries in an Al bicrystal. Phys Rev B 2007;76:184114.
[377] Nam HS, Srolovitz DJ. Effect of material properties on liquid metal embrittlement in the Al–Ga system. Acta Mater 2009;57:1546–53.
[378] Yun K, Nam HS. Molecular dynamics simulation of Ga penetration along Al grain boundaries under a constant strain rate condition. Mater Trans 2014;55:838–41.
[379] Schoeck G. The emission of dislocations from crack tips: A critical assessment. Mater Sci Eng, A 2003;356:93–101.

[380] Rice JR. Dislocation nucleation from a crack tip: an analysis based on the Peierls concept. J Mech Phys Solids 1992;40:239–71.
[381] Andric P, Curtin WA. New theory for Mode I crack-tip dislocation emission. J Mech Phys Solids 2017;106:315–37.
[382] Zhang Y, Lu GH, Wang TM, Deng SH, Shu XL, Kohyama M, et al. First-principles study of the effects of segregated Ga on an Al grain boundary. J Phys: Condens Matter 2006;18:5121–8.
[383] Zhang Y, Lu GH, Kohyama M, Wang T. Investigating the effects of a Ga layer on an Al grain boundary by a first-principles computational tensile test. Modell Simul Mater Sci Eng 2008;17:015003.
[384] Maksimenko VV, Zagaynov VA, Agranovski IE. Localization of electromagnetic field on the "Brouwer-island" and liquid metal embrittlement. Mater Chem Phys 2015;153:145–54.
[385] Nam HS, Srolovitz DJ. Molecular dynamics simulation of Ga penetration along grain boundaries in Al: A dislocation climb mechanism. Phys Rev Lett 2007;99:025501.
[386] Kobayashi M, Toda H, Uesugi K, Ohgaki T, Kobayashi T, Takayama Y, et al. Preferential penetration path of gallium into grain boundary in practical aluminium alloy. Phil Mag 2006;86:4351–66.
[387] Hugo RC, Hoagland RG. The kinetics of gallium penetration into aluminium grain boundaries-in situ TEM observations and atomistic models. Acta Mater 2000;48:1949–57.
[388] Ludwig W, Bellet D. Penetration of liquid gallium into the grain boundaries of aluminium: a synchrotron radiation microtomographic investigation. Mater Sci Eng, A 2000;281:198–203.
[389] Pereiro-Lopez E, Ludwig W, Bellet D. Discontinuous penetration of liquid Ga into grain boundaries of Al polycrystals. Acta Mater 2004;52:321–32.
[390] Pereiro-Lopez E, Ludwig W, Bellet D, Cloetens P, Lemaignan C. Direct evidence of nanometric invasionlike grain boundary penetration in the Al/Ga system. Phys Rev Lett 2005;95:215501.
[391] Ludwig W, Pereiro-López E, Bellet D. In situ investigation of liquid Ga penetration in Al bicrystal grain boundaries: grain boundary wetting or liquid metal embrittlement? Acta Mater 2005;53:151–62.
[392] Pereiro-Lopez E, Ludwig W, Bellet D, Lemaignan C. In situ investigation of Al bicrystal embrittlement by liquid Ga using synchrotron imageing. Acta Mater 2006;54:4307–16.
[393] Luo J. A short review of high-temperature wetting and complexion transitions with a critical assessment of their influence on liquid metal embrittlement and corrosion. Corrosion 2016;72:897–910.
[394] Namilae S, Radhakrishnan B, Morris JR. Atomistic simulation of the effect of Ga on crack tip opening in Al bicrystals. Modell Simul Mater Sci Eng 2008;16:075001.
[395] Bernardini J, Monchoux JP, Chatain D, Rabkin E. Liquid metal penetration in metallic polycrystals: New tools for a challenging unsolved problem of materials science. J Phys IV (Proc) 2002;12:229–37.
[396] Glickman EE. Grain boundary grooving accelerated by local plasticity as a possible mechanism of liquid metal embrittlement. Interface Sci 2003;11:451–9.
[397] Ling ZX, Wang M, Kong L. Liquid metal embrittlement of galvanized steels during industrial processing: A review. In Transactions on Intelligent Welding Manufacturing; 2018, p. 25–42.
[398] Razmpoosh MH, DiGiovanni C, Zhou YN, Biro E. Pathway to Understand Liquid Metal Embrittlement (LME) in Fe-Zn Couple: From Fundamentals toward Application. Prog Mater Sci 2021;121:100798.
[399] Cho L, Kang H, Lee C, De Cooman BC. Microstructure of liquid metal embrittlement cracks on Zn-coated 22MnB5 press-hardened steel. Scr Mater 2014;90–91:25–8.
[400] Frappier R, Paillard P, Le Gall R, Dupuy T. Embrittlement of steels by liquid zinc: crack propagation after grain boundary wetting. Adv Mater Res 2014;922:161–6.
[401] Pańcikiewicz K, Tuz L, Zielińska-Lipiec A. Zinc contamination cracking in stainless steel after welding. Eng Fail Anal 2014;39:149–54.
[402] Seok HH, Mun JC, Kang CG. Micro-crack in zinc coating layer on boron steel sheet in hot deep drawing process. Int J Precis Eng Manuf 2015;16:919–27.
[403] Ashiri R, Shamanian M, Salimijazi HR, Haque MA, Bae JH, Ji CW, et al. Liquid metal embrittlement-free welds of Zn-coated twinning induced plasticity steels. Scr Mater 2016;114:41–7.
[404] Ashiri R, Haque MA, Ji CW, Shamanian M, Salimijazi HR, Park YD. Supercritical area and critical nugget diametre for liquid metal embrittlement of Zn-coated twining induced plasticity steels. Scr Mater 2015;109:6–10.
[405] Luithle A, Pohl M. On the influence of cold deformation on liquid metal embrittlement of a steel in a liquid zinc bath. Mater Corros 2015;66:1491–7.
[406] Ding N, Xu N, Guo WM, Shi JB, Zang QS, Wu CML. Liquid metal induced embrittlement of a nitrided clutch shell of a motorbike. Eng Fail Anal 2016;61:54–61.
[407] Jung G, Woo IS, Suh DW, Kim SJ. Liquid Zn assisted embrittlement of advanced high strength steels with different microstructures. Met Mater Int 2016;22:187–95.
[408] Kang H, Cho L, Lee C, De Cooman BC. Zn penetration in liquid metal embrittled TWIP steel. Metall Mater Trans A 2016;47:2885–905.
[409] Takahashi M, Nakata M, Imai K, Kojima N, Otsuka N. Liquid Metal Embrittlement of Hot Stamped Galvannealed Boron Steel Sheet. ISIJ Int 2017;57:1094–101.
[410] Frei J, Rethmeier M. Susceptibility of electrolytically galvanized dual-phase steel sheets to liquid metal embrittlement during resistance spot welding. Welding in the World 2018;62:1031–7.
[411] Kim D, Kang JH, Kim SJ. Heating rate effect on liquid Zn-assisted embrittlement of high Mn austenitic steel. Surf Coat Technol 2018;347:157–63.
[412] Takahashi M, Nakata M, Kojima N, Otsuka N. Characterization of Liquid Metal Embrittlement for the Hot Stamped Galvannealed Boron Steel Sheets. Tetsu Hagane J Iron Steel Instit Jpn 2018;104:218–26.
[413] Razmpoosh MH, Macwan A, Biro E, Chen DL, Peng Y, Goodwin F, et al. Liquid metal embrittlement in laser beam welding of Zn-coated 22MnB5 steel. Mater Des 2018;155:375–83.
[414] Razmpoosh MH, Biro E, Chen DL, Goodwin F, Zhou Y. Liquid metal embrittlement in laser lap joining of TWIP and medium-manganese TRIP steel: The role of stress and grain boundaries. Mater Charact 2018;145:627–33.
[415] Lee H, Jo MC, Sohn SS, Kim SH, Song T, Kim SK, et al. Microstructural evolution of liquid metal embrittlement in resistance-spot-welded galvanized TWinning-Induced Plasticity (TWIP) steel sheets. Mater Charact 2019;147:233–41.
[416] Kang JH, Kim D, Kim DH, Kim SJ. Fe-Zn reaction and its influence on microcracks during hot tensile deformation of galvanized 22MnB5 steel. Surf Coat Technol 2019;357:1069–75.
[417] Ghatei-Kalashami A, Ghassemali E, DiGiovanni C, Goodwin F, Zhou NY. Occurrence of liquid-metal-embrittlement in a fully ferritic microstructure. Materialia 2021;15:101036.
[418] Bhattacharya D, Cho L, van der Aa E, Pichler A, Pottore N, Ghassemi-Armaki H, et al. Influence of the starting microstructure of an advanced high strength steel on the characteristics of Zn-Assisted liquid metal embrittlement. Mater Sci Eng, A 2021;804:140391.
[419] Razmpoosh MH, Macwan A, Goodwin F, Biro E, Zhou Y. Crystallographic study of liquid-metal-embrittlement crack path. Mater Lett 2020;267:127511.
[420] Razmpoosh MH, Langelier B, Marzbanrad E, Zurob HS, Zhou N, Biro E. Atomic-scale Investigation of Liquid-Metal-Embrittlement Crack-path: Revealing Mechanism and Role of Grain Boundary Chemistry. Acta Mater 2021;204:116519.
[421] Razmpoosh MH, Macwan A, Goodwin F, Biro E, Zhou Y. Suppression of liquid-metal-embrittlement by twin-induced grain boundary engineering approach. Materialia 2020;11:100668.
[422] Bauer KD, Todorova M, Hingerl K, Neugebauer J. A first principles investigation of zinc induced embrittlement at grain boundaries in bcc iron. Acta Mater 2015;90:69–76.
[423] Scheiber D, Prabitz K, Romaner L, Ecker W. The influence of alloying on Zn liquid metal embrittlement in steels. Acta Mater 2020;195:750–60.
[424] Liu WG, Han H, Ren CL, He XJ, Jia YY, Wang S, et al. First-principles study of intergranular embrittlement induced by Te in the Ni $\sum$ 5 grain boundary. Comput Mater Sci 2014;88:22–7.
[425] Kundu A, Asl KM, Luo J, Harmer MP. Identification of a bilayer grain boundary complexion in Bi-doped Cu. Scr Mater 2013;68:146–9.
[426] Luo J, Cheng H, Asl KM, Kiely CJ, Harmer MP. The role of a bilayer interfacial phase on liquid metal embrittlement. Science 2011;333:1730–3.

[427] Wolski K, Laporte V, Marie N, Biscondi M. About the importance of nanometre-thick intergranular penetration in the analysis of liquid metal embrittlement. Interface Sci 2001;9:183–9.
[428] Marie N, Wolski K, Biscondi M. Grain boundary penetration of nickel by liquid bismuth as a film of nanometric thickness. Scr Mater 2000;43:943–9.
[429] Marie N, Wolski K, Biscondi M. Intergranular penetration and embrittlement of solid nickel through bismuth vapour condensation at 700°C. J Nucl Mater 2001;296:282–8.
[430] Duscher G, Chisholm MF, Alber U, Rühle M. Bismuth-induced embrittlement of copper grain boundaries. Nat Mater 2004;3:621–6.
[431] Kang J, Glatzmaier GC, Wei SH. Origin of the bismuth-induced decohesion of nickel and copper grain boundaries. Phys Rev Lett 2013;111:055502.
[432] Thomson DI, Heine V, Payne MC, Marzari N, Finnis MW. Insight into gallium behaviour in aluminium grain boundaries from calculation on Σ=11 (113) boundary. Acta Mater 2000;48:3623–32.
[433] Sigle W, Richter G, Rühle M, Schmidt S. Insight into the atomic-scale mechanism of liquid metal embrittlement. Appl Phys Lett 2006;89:121911.
[434] Klinger L, Rabkin E. The effect of stress on grain boundary interdiffusion in a semi-infinite bicrystal. Acta Mater 2007;55:4689–98.
[435] Schweinfest R, Paxton AT, Finnis MW. Bismuth embrittlement of copper is an atomic size effect. Nature 2004;432:1008–11.
[436] Yu ZY, Cantwell PR, Gao Q, Yin D, Zhang YY, Zhou NX, et al. Science 2017;358:97–101.
[437] Hamdane O, Bouquerel J, Proriol-Serre I, Vogt JB. Effect of heat treatment on liquid sodium embrittlement of T91 martensitic steel. J Mater Process Technol 2011;211:2085–90.
[438] Hémery S, Auger T, Courouau JL, Balbaud-Célérier F. Effect of oxygen on liquid sodium embrittlement of T91 martensitic steel. Corros Sci 2013;76:441–52.
[439] Serre IP, Hamdane O, Vogt JB. Comparative study of the behaviour of different highly alloyed steels in liquid sodium. Nucl Eng Des 2017;320:17–27.
[440] Hémery S, Auger T, Courouau JL, Balbaud-Célérier F. Liquid metal embrittlement of an austenitic stainless steel in liquid sodium. Corros Sci 2014;83:1–5.
[441] Barkia B, Auger T, Courouau JL, Bourgon J. Multiscale investigation of crack path and microstructural changes during liquid metal embrittlement of 304L austenitic steel in liquid sodium. Corros Sci 2017;127:213–21.
[442] Barkia B, Auger T, Courouau JL, Bourgon J. Wetting by liquid sodium and fracture path analysis of sodium induced embrittlement of 304L stainless steel. J Mater Res 2018;33:121–9.
[443] Barkia B, Courouau JL, Perrin E, Lorentz V, Rivollier M, Robin R, et al. Investigation of crack propagation resistance of 304L, 316L and 316L(N) austenitic steels in liquid sodium. J Nucl Mater 2018;507:15–23.
[444] Auger T, Lorang G, Guérin S, Pastol JL, Gorse D. Effect of contact conditions on embrittlement of T91 by lead–bismuth. J Nucl Mater 2004;335:227–31.
[445] Auger T, Lorang G. Liquid metal embrittlement susceptibility of T91 by lead-bismuth. Scr Mater 2005;52:1323–8.
[446] Vogt JB, Nicaise G, Legris A, Foct F. The risk of liquid metal embrittlement of the Z10CDNbV 9–1 martensitic steel. J Phys IV (Proc) 2002;12:217–25.
[447] Dai Y, Long B, Groeschel F. Slow strain rate tensile tests on T91 in static lead-bismuth eutectic. J Nucl Mater 2006;356:222–8.
[448] Di Gabriele F, Hojná A, Chocholousek M, Klecka J. Behaviour of the steel T91 under multi axial loading in contact with liquid and solid Pb. Metals 2017;7:1–14.
[449] Gnecco F, Giuranno D, Ricci E. Wettability of T91 by Pb and Pb-Bi eutectic alloy. Genoa: CNR-IENI report; 2002.
[450] Du XC, Niu F, Zhu HP, Ma TF, Zhao YG, Xiong W, et al. Influence of oxide scale on the wettability of LBE on T91. Fusion Eng Des 2017;125:378–83.
[451] Giuranno D, Gnecco F, Ricci E, Novakovic R. Surface tension and wetting behaviour of molten Bi–Pb alloys. Intermetallics 2003;11:1313–7.
[452] Straumal BB, Mazilkin AA, Baretzky B. Grain boundary complexions and pseudopartial wetting. Curr Opin Solid State Mater Sci 2016;20:247–56.
[453] Lesueur C, Chatain D, Bergman C, Gas P, Baque F. Analysis of the stability of native oxide films at liquid lead/metal interfaces. J Phys IV (Proc) 2002;12:155–62.
[454] Protsenko P, Eustathopoulos N. Surface and grain boundary wetting of Fe based solids by molten Pb and Pb-Bi eutectic. J Mater Sci 2005;40:2383–7.
[455] Diop I, David N, Fiorani JM, Podor R, Vilasi M. Experimental investigations and thermodynamic description of the PbO-Fe_2O_3 system. Thermochim Acta 2010;510:202–12.
[456] Legris A, Nicaise G, Vogt JB, Foct J, Gorse D. Embrittlement of a martensitic steel by liquid lead. Scr Mater 2000;43:997–1001.
[457] Nicaise G, Legris A, Vogt JB, Foct J. Embrittlement of the martensitic steel 91 tested in liquid lead. J Nucl Mater 2001;296:256–64.
[458] Long B, Tong Z, Gröschel F, Dai Y. Liquid Pb-Bi embrittlement effects on the T91 after different heat treatments. J Nucl Mater 2008;377:219–24.
[459] Hamdane O, Serre IP, Vogt JB, Nuns N. ToF-SIMS analyses of brittle crack initiation of T91 by liquid sodium. Mater Chem Phys 2014;145:243–9.
[460] Glasbrenner H, Gröschel F. Bending tests on T91 in Pb-Bi eutectic, Bi and Pb-Li eutectic. J Nucl Mater 2004;335:239–43.
[461] Guerin S, Pastol JL, Leroux C, Gorse D. Synergy effect of LBE and hydrogenated helium on resistance to LME of T91 grade. J Nucl Mater 2003;318:339–47.
[462] Glasbrenner H, Gröschel F, Kirchner T. Tensile tests on MANET II steel in circulating Pb-Bi eutectic. J Nucl Mater 2003;318:333–8.
[463] Aiello A, Agostini M, Benamati G, Long B, Scaddozzo G. Mechanical properties of martensitic steels after exposure to flowing liquid metals. J Nucl Mater 2004;335:217–21.
[464] Hojná A, Di Gabriele F, Klecka J, Burda J. Behaviour of the steel T91 under uniaxial and multiaxial slow loading in contact with liquid lead. J Nucl Mater 2015;466:292–301.
[465] Auger T, Serre I, Lorang G, Hamouche Z, Gorse D, Vogt JB. Role of oxidation on LME of T91 studied by small punch test. J Nucl Mater 2008;376:336–40.
[466] Van den Bosch J, Coen G, Almazouzi A, Degrieck J. Fracture toughness assessment of ferritic-martensitic steel in liquid lead-bismuth eutectic. J Nucl Mater 2009;385:250–7.
[467] Ersoy F, Gavrilov S, Verbeken K. Investigating liquid-metal embrittlement of T91 by fracture toughness tests. J Nucl Mater 2016;472:171–7.
[468] Hojná A, Di Gabriele F, Klecka J. Characteristics and Liquid Metal Embrittlement of the steel T91 in contact with Lead-Bismuth Eutectic. J Nucl Mater 2016;472:163–70.
[469] Auger T, Hamouche Z, Medina-Almazan L, Gorse D. Liquid metal embrittlement of T91 and 316L steels by heavy liquid metals: A fracture mechanics assessment. J Nucl Mater 2008;377:253–60.
[470] Auger T, Gorse D, Hamouche-Hadjem Z, Van den Bosch J, Coen G, Almazouzi A, et al. Fracture mechanics behaviour of the T91 martensitic steel in contact with liquid lead-bismuth eutectic for application in an accelerator driven system. J Nucl Mater 2011;415:293–301.
[471] Long B, Dai Y. Investigation of LBE embrittlement effects on the fracture properties of T91. J Nucl Mater 2008;376:341–5.
[472] Kamdar MH. Embrittlement of high and low strength steel in liquid lead environment. International conference and exposition on fatigue corrosion cracking, fracture mechanics and failure analysis. American Society of Metals; 1985.
[473] Gong X, Stergar E, Marmy P, Gavrilov S. Tensile fracture behaviour of notched 9Cr-1Mo ferritic-martensitic steel specimens in contact with liquid lead-bismuth eutectic at 350°C. Mater Sci Eng, A 2017;692:139–45.
[474] Baker BW, Brewer LN. Evaluation of liquid metal embrittlement susceptibility of oxide dispersion strengthened steel MA956. J Nucl Mater 2014;453:239–46.
[475] Hojná A, Hadraba H, Di Gabriele F, Husak R. Behaviour of pre-stressed T91 and ODS steels exposed to liquid lead-bismuth eutectic. Corros Sci 2018;131:264–77.
[476] Van den Bosch J. ADS Candidate Materials Compatibility with Liquid Metal in a Neutron Irradiation Environment, PhD dissertation. Belgium: Gent University; 2008.
[477] Kalkhof D, Grosse M. Influence of PbBi environment on the low-cycle fatigue behaviour of SNS target container materials. J Nucl Mater 2003;318:143–50.
[478] Hamouche-Hadjem Z, Auger T, Guillot I, Gorse D. Susceptibility to LME of 316L and T91s by LBE: Effect of strain rate. J Nucl Mater 2008;376:317–21.
[479] Coen G, Van den Bosch J, Almazouzi A, Degrieck J. Investigation of the effect of lead-bismuth eutectic on the fracture properties of T91 and 316L. J Nucl Mater 2010;398:122–8.
[480] Hojná A, Di Gabriele F, Chocholousek M, Spirit Z, Rozumova L. Study of crack initiation of 15–15Ti austenitic steel in liquid PbBi. J Nucl Eng Radiat Sci 2019;5:030902.
[481] Yaskiv OI, Fedirko VM, Kukhar IS. Effect of Lead and Lead-Bismuth Eutectic Melts on the Fatigue Life of Steels of the Martensitic and Austenitic Classes. Mater Sci 2014;50:102–8.
[482] Vogt JB, Proriol-Serre I. Fatigue behaviour of a martensitic and an austenitic steel in heavy liquid metals. Procedia Eng 2013;55:812–8.

[483] Gong X, Yang ZB, Deng YB, Xiao J, Wang H, Yu ZY, et al. Creep failure of a solution-annealed 15–15Ti steel exposed to stagnant lead-bismuth eutectic at 550 and 600°C. Mater Sci Eng, A 2020;798:140230.
[484] Kolman DG, Chavarria R. Liquid-metal embrittlement of Type 316L stainless steel by gallium as measured by elastic-plastic fracture mechanics. Corrosion 2004;60:254–61.
[485] Naoe T, Yamaguchi Y, Futakawa M. Quantification of fatigue crack propagation of an austenitic stainless steel in mercury embrittlement. J Nucl Mater 2012; 431:133–9.
[486] Strizak JP, DiStefano JR, Liaw PK, Tian H. The effect of mercury on the fatigue behaviour of 316 LN stainless steel. J Nucl Mater 2001;296:225–30.
[487] Strizak JP, Tian H, Liaw PK, Mansur LK. Fatigue properties of type 316LN stainless steel in air and mercury. J Nucl Mater 2005;343:134–44.
[488] Tian H, Liaw PK, Wang H, Fielden D, Strizak JP, Mansur LK, et al. Influence of mercury environment on the fatigue behaviour of spallation neutron source (SNS) target container materials. Mater Sci Eng, A 2001;314:140–9.
[489] Medina-Almazan L, Rouchaud JC, Auger T, Gorse D. Optimization of contact conditions between iron base alloys and mercury at room temperature. J Nucl Mater 2008;375:102–12.
[490] Medina-Almazan L, Auger T, Gorse D. Liquid metal embrittlement of an austenitic 316L type and a ferritic-martensitic T91 type steel by mercury. J Nucl Mater 2008;376:312–6.
[491] Hojná A, Hadraba H, Di Gabriele F, Husak R, Kuběna I, Rozumová L, et al. Corrosion-Mechanical Behaviour of T91 and 14–19Cr ODS Steels Exposed to flowing Lead-Bismuth. Solid State Phenom 2016;258:627–30.
[492] Liu J, Shi QQ, Luan H, Yan W, Sha W, Wang W, et al. Oxidation and tensile behaviour of ferritic/martensitic steels after exposure to lead-bismuth eutectic. Mater Sci Eng, A 2016;670:97–105.
[493] Van den Bosch J, Bosch RW, Sapundjiev D, Almazouzi A. Liquid metal embrittlement susceptibility of ferritic-martensitic steel in liquid lead alloys. J Nucl Mater 2008;376:322–9.
[494] Van den Bosch J, Sapundjiev D, Almazouzi A. Effects of temperature and strain rate on the mechanical properties of T91 material tested in liquid lead bismuth eutectic. J Nucl Mater 2006;356:237–46.
[495] Vogt JB, Verleene A, Serre I, Balbaud-Célérier F, Terlain A. Coupling effects between corrosion and fatigue in liquid Pb-Bi of T91 martensitic steel. EUROCORR. Lisbon; 2005.
[496] Konstantinović MJ, Stergar E, Lambrecht M, Gavrilov S. Comparison of the mechanical properties of T91 from the MEGAPIE, and TWIN-ASTIR irradiation program. J Nucl Mater 2016;468:228–31.
[497] Long B, Dai Y, Baluc N. Investigation of liquid LBE embrittlement effects on irradiated ferritic/martensitic steels by slow-strain-rate tensile tests. J Nucl Mater 2012;431:85–90.
[498] Van den Bosch J, Coen G, Bosch RW, Almazouzi A. TWIN ASTIR: First tensile results of T91 and 316L steel after neutron irradiation in contact with liquid lead–bismuth eutectic. J Nucl Mater 2010;398:68–72.
[499] Di Gabriele F, Doubková A, Hojná A. Investigation of the sensitivity to EAC of steel T91 in contact with liquid LBE. J Nucl Mater 2008;376:307–11.
[500] Gong X, Marmy P, Qin L, Verlinden B, Wevers M, Seefeldt M. Temperature dependence of liquid metal embrittlement susceptibility of a modified 9Cr-1Mo steel under low cycle fatigue in lead-bismuth eutectic at 160–450°C. J Nucl Mater 2016;468:289–98.
[501] Liu J, Yan W, Sha W, Wang W, Shan YY, Yang K. Effects of temperature and strain rate on the tensile behaviours of SIMP steel in static lead bismuth eutectic. J Nucl Mater 2016;473:189–96.
[502] Gong X, Marmy P, Verlinden B, Wevers M, Seefeldt M. Low cycle fatigue behaviour of a modified 9Cr-1Mo ferritic-martensitic steel in lead-bismuth eutectic at 350°C–effects of oxygen concentration in the liquid metal and strain rate. Corros Sci 2015;94:377–91.
[503] Hojná A, Di Gabriele F, Chocholousek M, Spirit Z, Halodova P, Lorincik J. Initiation of LME crack in ferritic martensitic steel in liquid lead-bismuth. J Nucl Mater 2018;511:459–72.
[504] Ye CQ, Vogt JB, Serre IP. Liquid metal embrittlement of the T91 steel in lead bismuth eutectic: The role of loading rate and of the oxygen content in the liquid metal. Mater Sci Eng, A 2014;608:242–8.
[505] Marmy P, Gong X. LIMETS 3, a novel system for high strain fatigue testing in lead-bismuth eutectic. J Nucl Mater 2014;450:256–61.
[506] Serre I, Vogt JB. Liquid metal embrittlement of T91 martensitic steel evidenced by small punch test. Nucl Eng Des 2007;237:677–85.
[507] Klecka J, Di Gabriele F, Hojná A. Mechanical properties of the steel T91 in contact with lead. Nucl Eng Des 2015;283:131–8.
[508] Gong X, Marmy P, Qin L, Verlinden B, Wevers M, Seefeldt M. Effect of liquid metal embrittlement on low cycle fatigue properties and fatigue crack propagation behaviour of a modified 9Cr-1Mo ferritic-martensitic steel in an oxygen-controlled lead-bismuth eutectic environment at 350°C. Mater Sci Eng, A 2014;618: 406–15.
[509] Verleene A, Vogt JB, Serre I, Legris A. Low cycle fatigue behaviour of T91 martensitic steel at 300°C in air and in liquid lead bismuth eutectic. Int J Fatigue 2006;28:843–51.
[510] Yaskiv OI, Fedirko VM. Mechanical and fatigue properties of martensitic Fe-13Cr steel in contact with lead and lead-bismuth melts. Fusion Eng Des 2014;89: 29–34.
[511] Yurechko M, Schroer C, Skrypnik A, Wedemeyer O, Konys J. Creep-to-rupture of 12Cr-and 14Cr-ODS steels in oxygen-controlled lead and air at 650°C. J Nucl Mater 2014;450:88–98.
[512] Yurechko M, Schroer C, Wedemeyer O, Skrypnik A, Konys J. Creep-to-rupture of 9% Cr steel T91 in air and oxygen-controlled lead at 650°C. J Nucl Mater 2011;419:320–8.
[513] Weisenburger A, Jianu A, An W, Fetzer R, Del Giacco M, Heinzel A, et al. Creep, creep-rupture tests of Al-surface-alloyed T91 steel in liquid lead bismuth at 500 and 550°C. J Nucl Mater 2012;431:77–84.
[514] Yurechko M, Schroer C, Skrypnik A, Wedemeyer O, Konys J. Creep-to-rupture of the steel P92 at 650°C in oxygen-controlled stagnant lead in comparison to air. J Nucl Mater 2013;432:78–86.
[515] Jianu A, Müller G, Weisenburger A, Heinzel A, Fazio C, Markov VG, et al. Creep-to-rupture tests of T91 steel in flowing Pb–Bi eutectic melt at 550°C. J Nucl Mater 2009;394:102–8.
[516] Yurechko M, Schroer C, Wedemeyer O, Skrypnik A, Konys J. Creep-rupture tests on chromium-containing conventional and ODS steels in oxygen-controlled Pb and air at 650°C. Nucl Eng Des 2014;280:686–96.
[517] Yurechko M, Schroer C, Skrypnik A, Wedemeyer O, Tsisar V, Konys J. Steel T91 subjected to static stress in lead-bismuth eutectic at 450–550°C and low oxygen concentration. J Nucl Mater 2018;512:423–39.
[518] Strafella A, Coglitore A, Salernitano E. Creep behaviour of 15–15Ti (Si) austenitic steel in air and in liquid lead at 550°C. Procedia Struct Integrity 2017;3: 484–97.
[519] Legris A, Nicaise G, Vogt JB, Foct J. Liquid metal embrittlement of the martensitic steel 91: influence of the chemical composition of the liquid metal.: Experiments and electronic structure calculations. J Nucl Mater 2002;301:70–6.
[520] Hojná A, Di Gabriele F. On the kinetics of LME for the ferritic–martensitic steel T91 immersed in liquid PbBi eutectic. J Nucl Mater 2011;413:21–9.
[521] Van den Bosch J, Almazouzi A. Compatibility of martensitic/austenitic steel welds with liquid lead bismuth eutectic environment. J Nucl Mater 2009;385: 504–9.
[522] Van den Bosch J, Coen G, Van Renterghem W, Almazouzi A. Compatibility of ferritic–martensitic steel T91 welds with liquid lead-bismuth eutectic: Comparison between TIG and EB welds. J Nucl Mater 2010;396:57–64.
[523] Van den Bosch J, Hosemann P, Almazouzi A, Maloy SA. Liquid metal embrittlement of silicon enriched steel for nuclear applications. J Nucl Mater 2010;398: 116–21.
[524] Hojná A, Di Gabriele F, Chocholoušek M, Rozumová L, Vít J. Effect of applied stress on T91 steel performance in liquid lead at 400 °C. Materials 2018;11:2512.
[525] Heinzel A, W A, Serrano M, Hernandez Pascual R, Ricci E, Ripamonti D, et al. Compatibility assessment of surface modified ODS under relevant FNR environment, MatISSE – Deliverable D4.32; 2017.

[526] Serre I, Vogt JB. Heat treatment effect of T91 martensitic steel on liquid metal embrittlement. J Nucl Mater 2008;376:330–5.
[527] Ye C, Vogt JB, Proriol-Serre I. Brittle fracture of T91 steel in liquid lead–bismuth eutectic alloy. Nucl Eng Des 2014;280:680–5.
[528] Serre I, Vogt JB. Mechanical properties of a 316L/T91 weld joint tested in lead-bismuth liquid. Mater Des 2009;30:3776–83.
[529] Vogt JB, Verleene A, Serre I, Legris A. Mechanical behaviour of the T91 martensitic steel under monotonic and cyclic loadings in liquid metals. J Nucl Mater 2004;335:222–6.
[530] Weisenburger A, Heinzel A, Fazio C, Müller G, Markow VG, Kastanov AD. Low cycle fatigue tests of surface modified T91 steel in 10^{-6} wt.% oxygen containing $Pb_{45}Bi_{55}$ at 550°C. J Nucl Mater 2008;377:261–7.
[531] Vogt JB, Carlé C, Bouquerel J, Proriol Serre I. Behaviour of short and long cracks in air and in liquid metal in T91 steel. In 12th International Fatigue Congress (FATIGUE 2018), MATEC Web of Conferences, vol. 165; 2018, p. 03016.
[532] Ersoy F, Verbeken K, Gavrilov S. Influence of displacement rate and temperature on the severity of liquid metal embrittlement of T91 steel in LBE. Mater Sci Eng, A 2021;800:140259.
[533] Martin ML, Auger T, Johnson DD, Robertson IM. Liquid-metal-induced fracture mode of martensitic T91 steels. J Nucl Mater 2012;426:71–7.
[534] Keller C, Margulies MM, Guillot I. Experimental analysis of the dynamic strain ageing for a modified T91 martensitic steel. Mater Sci Eng, A 2012;536:273–5.
[535] Gavrilov S, Lambrecht M, Coen G, Stergar E, Van den Bosch J. PIE of ASTIR: Report on the full set of results of tests on irradiated and non-irradiated specimens. FP7-212175-GETMAT; 2014.
[536] Keller C, Margulies MM, Hadjem-Hamouche Z, Guillot I. Influence of the temperature on the tensile behaviour of a modified 9Cr-1Mo T91 martensitic steel. Mater Sci Eng, A 2010;527:6758–64.
[537] Gong X, Marmy P, Yin Y. The role of oxide films in preventing liquid metal embrittlement of T91 steel exposed to liquid lead-bismuth eutectic. J Nucl Mater 2018;509:401–7.
[538] Yaskiv OI, Kukhar IS, Fedirko VM. Effect of preliminary diffusion oxidation on mechanical properties of ferritic steel in oxygen-containing lead. Fusion Eng Des 2015;101:134–40.
[539] Vogt JB, Bouquerel J, Carle C, Serre IP. Stability of fatigue cracks at 350°C in air and in liquid metal in T91 martensitic steel. Int J Fatigue 2020;130:105265.
[540] Vogt JB, Verleene A, Serre I, Balbaud-Célérier F, Martinelli L, Terlain A. Understanding the liquid metal assisted damage sources in the T91 martensitic steel for safer use of ADS. Eng Fail Anal 2007;14:1185–93.
[541] Gamaoun F, Dupeux M, Ghetta V, Gorse D. Cavity formation and accelerated plastic strain in T91 steel in contact with liquid lead. Scr Mater 2004;50:619–23.
[542] Vivas J, Capdevila C, Jimenez JA, Benito-Alfonso M, San-Martin D. Effect of ausforming temperature on the microstructure of G91 steel. Metals 2017;7:236–47.
[543] Shigeta T, Takada A, Terasaki H, Komizo Y. The Effects of Ausforming on Variant Selection of Martensite in Cr-Mo Steel. Quart J Jpn Weld Soc 2013;31:178s–82s.
[544] Zhang XH, Hattar K, Chen YX, Shao L, Li J, Sun C, et al. Radiation damage in nanostructured materials. Prog Mater Sci 2018;96:217–321.
[545] Gelles DS, Schäublin RE. Post-irradiation deformation in a Fe-9% Cr alloy. Mater Sci Eng, A 2001;309–310:82–6.
[546] Jin HH, Hwang SS, Choi MJ, Lee GG, Kwon J. Proton irradiation for radiation-induced changes in microstructures and mechanical properties of austenitic stainless steel. J Nucl Mater 2019;513:271–81.
[547] Dai Y, Henry J, Auger T, Vogt JB, Almazouzi A, Glasbrenner H, et al. Assessment of the lifetime of the beam window of MEGAPIE target liquid metal container. J Nucl Mater 2006;356:308–20.
[548] Dai Y, Boutellier V, Gavillet D, Glasbrenner H, Weisenburger A, Wagner W. FeCrAlY and TiN coatings on T91 steel after irradiation with 72 MeV protons in flowing LBE. J Nucl Mater 2012;431:66–76.
[549] Antolovich SD, Armstrong RW. Plastic strain localization in metals: origins and consequences. Prog Mater Sci 2014;59:1–160.
[550] Luo L, Jiang ZZ, Xiao ZQ, Huang QY. Cracking and exfoliation behavior of oxide scale on T91 steel under different tensile stresses in oxygen-controlled lead-bismuth eutectic at 550°C. Corros Sci 2021;183:109324.
[551] Proriol Serre I, Vogt JB, Nuns N. ToF-SIMS investigation of absorption of lead and bismuth in T91 steel deformed in liquid lead bismuth eutectic. Appl Surf Sci 2019;471:36–42.
[552] Seidametova G, Vogt JB, Proriol SI. The early stage of fatigue crack initiation in a 12% Cr martensitic steel. Int J Fatigue 2018;106:38–48.
[553] Hojná A, Halodová P, Chocholoušek M, Špirit Z, Rozumová L. Environmentally assisted cracking of T91 ferritic-martensitic steel in heavy liquid metals. Corros Rev 2020;38:183–94.
[554] Kaede K, Jäger A, Gärtnerová V, Takushima C, Yamamuro T, Tsurekawa S. Measurement of Local Mechanical Properties of T91 Steel Corroded by Molten Lead-Bismuth Eutectic Alloy via Micropillar Compression Test. MRS Adv 2018;3:419–25.
[555] Asl KM, Luo J. Impurity effects on the intergranular liquid bismuth penetration in polycrystalline nickel. Acta Mater 2012;60:149–65.
[556] Wolski K, Laporte V. Grain boundary diffusion and wetting in the analysis of intergranular penetration. Mater Sci Eng, A 2008;495:138–46.
[557] Ma SQ, Zhang JS. Interface morphologies and embrittlement behaviour of α-Fe in liquid lead-bismuth eutectic at elevated temperature. Mater Charact 2019;147:43–9.
[558] Halodová P, Lorinčík J, Hojná A. Microstructural investigation of LME crack initiated in ferritic/martensitic steel T91 loaded in liquid lead-bismuth eutectic at 300°C. Materials 2019;12:38.
[559] Gossé S. Thermodynamic assessment of solubility and activity of iron, chromium, and nickel in lead bismuth eutectic. J Nucl Mater 2014;449:122–31.
[560] Lynch SP. Progression markings, striations, and crack-arrest markings on fracture surface. Mater Sci Eng, A 2007;468–470:74–80.
[561] Wouters O, De Hosson JTM. Lead induced intergranular fracture in aluminium alloy AA6262. Mater Sci Eng, A 2003;361:331–7.
[562] Gong X, Chen JJ, Hu FY, Xiang CY, Yu ZY, Xiao J, et al. Liquid metal embrittlement of an Fe10Cr4Al ferritic alloy exposed to oxygen-depleted and -saturated lead-bismuth eutectic at 350°C. Corros Sci 2020;165:108364.
[563] Zhang J, Li N, Chen Y. Oxygen control technique in molten lead and lead-bismuth eutectic systems. Nucl Sci Eng 2006;154:223–32.
[564] Li N. Active control of oxygen in molten lead–bismuth eutectic systems to prevent steel corrosion and coolant contamination. J Nucl Mater 2002;300:73–81.
[565] Frazer D, Stergar E, Cionea C, Hosemann P. Liquid metal as a heat transport fluid for thermal solar power applications. Energy Procedia 2014;49:627–36.
[566] Ganesan R, Gnanasekaran T, Srinivasa RS. Standard molar Gibbs free energy of formation of PbO(s) over a wide temperature range from EMF measurements. J Nucl Mater 2003;320:258–64.
[567] Gocken NA. The Bi-Pb (Bismuth-Lead) System. J Phase Equilib 1992;13:21–31.
[568] Lim J, Mariën A, Rosseel K, Aerts A, Van den Bosch J. Accuracy of potentiometric oxygen sensors with Bi/Bi_2O_3 reference electrode for use in liquid LBE. J Nucl Mater 2012;429:270–5.
[569] Aerts A, Gavrilov S, Manfredi G, Marino A, Rosseel K, Lim J. Oxygen-iron interaction in liquid lead-bismuth eutectic alloy. PCCP 2016;18:19526–30.
[570] Müller G, Heinzel A, Schumacher G, Weisenburger A. Control of oxygen concentration in liquid lead and lead-bismuth. J Nucl Mater 2003;321:256–62.
[571] Rivai AK, Takahashi M. Investigations of a zirconia solid electrolyte oxygen sensor in liquid lead. J Nucl Mater 2010;398:160–4.
[572] Konys J, Muscher H, Voß Z, Wedemeyer O. Oxygen measurements in stagnant lead-bismuth eutectic using electrochemical sensors. J Nucl Mater 2004;335:249–53.
[573] Lim J, Marino A, Aerts A. Active oxygen control by a PbO mass exchanger in the liquid lead–bismuth eutectic loop: MEXICO. J Nucl Sci Technol 2016;54:131–7.
[574] Legkikh AY, Askhadullin RS, Sadovnichiy RP. Ensuring the corrosion resistance of steels in heavy liquid metal coolants. Nucl Energy Technol 2016;2:136–41.
[575] Lim J, Manfredi G, Gavrilov S, Rosseel K, Aerts A, Van den Bosch J. Control of dissolved oxygen in liquid LBE by electrochemical oxygen pumping. Sens Actuators, B 2014;204:388–92.
[576] Lim J, Manfredi G, Rosseel K, Aerts A. Performance of Electrochemical Oxygen Pump in a Liquid Lead-Bismuth Eutectic Loop. J Electrochem Soc 2019;166:E153–8.

[577] Marino A, Lim J, Keijers S, Van den Bosch J, Deconinck J. Numerical modelling of oxygen mass transfer from PbO spheres packed bed to liquid lead bismuth eutectic: A venturi-type PbO mass exchanger. Nucl Eng Des 2013;265:576–81.
[578] Deloffre P, Balbaud-Célérier F, Terlain A. Corrosion behaviour of aluminized martensitic and austenitic steels in liquid Pb-Bi. J Nucl Mater 2004;335:180–4.
[579] Gómez-Briceño D, Soler-Crespo L, Martín-Muñoz FJ, Hernández-Arroyo F. Influence of temperature on the oxidation/corrosion process of F82Hmod. martensitic steel in lead-bismuth. J Nucl Mater 2002;303:137–46.
[580] Glasbrenner H, Konys J, Müller G, Rusanov A. Corrosion investigations of steels in the flowing lead at 400°C and 550°C. J Nucl Mater 2001;296:237–42.
[581] Schroer C, Voß Z, Novotny J, Konys J. Quantification of the degradation of steels exposed to liquid lead-bismuth eutectic. FZKA 7224, Karlsruhe, Germany.
[582] Schroer C, Konys J, Furukawa T, Aotob K. Oxidation behaviour of P122 and a 9Cr-2W ODS steel at 550°C in oxygen-containing flowing lead-bismuth eutectic. J Nucl Mater 2010;398:109–15.
[583] Lim J. Oxygen control and monitoring, in Heavy Metal Summer School. SCK·CEN Lakehouse, Mol, Belgium; 2015.
[584] Manfredi G, Lim J, Rosseel K, Van den Bosch J, Doneux T, Buess-Herman C, et al. Comparison of solid metal-metal oxide reference electrodes for potentiometric oxygen sensors in liquid lead-bismuth eutectic operating at low temperature ranges. Sens Actuators, B 2015;214:20–8.
[585] Schroer C, Kony J, Verdaguer A, Abellà J, Gessi A, Kobzova A, et al. Design and testing of electrochemical oxygen sensors for service in liquid lead alloys. J Nucl Mater 2011;415:338–47.
[586] Mariën A, Lim J, Rosseel K, Vandermeulen W, Van den Bosch J. Solid electrolytes for use in lead–bismuth eutectic cooled nuclear reactors. J Nucl Mater 2012;427:39–45.
[587] Lim J, Manfredi G, Mariën A, Van den Bosch J. Performance of potentiometric oxygen sensors with LSM-GDC composite electrode in liquid LBE at low temperatures. Sens Actuators, B 2013;188:1048–54.
[588] Popovic MP, Chen K, Shen H, Stan CV, Olmsted DL, Tamura N, et al. A study of deformation and strain induced in bulk by the oxide layers formation on a Fe-Cr-Al alloy in high-temperature liquid Pb-Bi eutectic. Acta Mater 2018;151:301–9.
[589] Ejenstam J, Szakálos P. Long term corrosion resistance of alumina forming austenitic stainless steels in liquid lead. J Nucl Mater 2015;461:164–70.
[590] Ejenstam J, Halvarsson M, Weidow J, Jönsson B, Szakalos P. Oxidation studies of Fe10CrAl-RE alloys exposed to Pb at 550 °C for 10 000h. J Nucl Mater 2013;443:161–70.
[591] Kurata Y, Futakawa M, Saito S. Corrosion behaviour of Al-surface-treated steels in liquid Pb–Bi in a pot. J Nucl Mater 2004;335:501–7.
[592] Song L, Xing Y, Zhao Y, Wang W, Mao X. Si-containing 9Cr ODS steel designed for high temperature application in lead-cooled fast reactor. J Nucl Mater 2019;519:22–9.
[593] Shi H, Jianu A, Weisenburger A, Tang C, Heinzel A, Fetzer R, et al. Corrosion resistance and microstructural stability of austenitic Fe-Cr-Al-Ni model alloys exposed to oxygen-containing molten lead. J Nucl Mater 2019;524:177–90.
[594] Chen L, Wang M, Tsisar V, Schroer C, Zhou Z. Investigation of microstructure and liquid lead corrosion behaviour of a Fe-18Ni-16Cr-4Al base alumina-forming austenitic stainless steel. Mater Res Express 2020;7:026533.
[595] Weisenburger A, Jianu A, Doyle S, Bruns M, Fetzer R, Heinzel A, et al. Oxide scales formed on Fe–Cr–Al-based model alloys exposed to oxygen containing molten lead. J Nucl Mater 2013;437:282–92.
[596] Weisenburger A, Jianu A, Skalaloz P, Utili M, Vassallo E, Ricci E, et al. Summary Report "Functional coatings and modified surface layers". MatISSE – Deliverable D5.21 2017.
[597] Loewen EP. Corrosion studies in support of lead-bismuth cooled FBRs. Prog Nucl Energy 2005;47:561–8.
[598] Takaya S, Furukawa T, Müller G, Heinzel A, Jianu A, Weisenburger A, et al. Al-containing ODS steels with improved corrosion resistance to liquid lead-bismuth. J Nucl Mater 2012;428:125–30.
[599] Takaya S, Furukawa T, Aoto K, Müller G, Weisenburger A, Heinzel A, et al. Corrosion behaviour of Al-alloying high Cr-ODS steels in lead-bismuth eutectic. J Nucl Mater 2009;386–388:507–10.
[600] Del Giacco M, Weisenburger A, Jianu A, Müller G. Influence of composition and microstructure on the corrosion behaviour of different Fe-Cr-Al alloys in molten LBE. J Nucl Mater 2012;421:39–46.
[601] Short MP, Ballinger RG. A Functionally Graded Composite for Service in High-Temperature Lead- and Lead-Bismuth–Cooled Nuclear Reactors—I: Design. Nucl Technol 2012;17:366–81.
[602] Chen X, Haasch R, Stubbins JF. Impedance spectroscopy and microstructural characterization of the corrosion behaviour of FeCrAl alloy in lead–bismuth eutectic. J Nucl Mater 2012;431:125–32.
[603] Lim J, Hwang IS, Kim JH. Design of alumina forming FeCrAl steels for lead or lead–bismuth cooled fast reactors. J Nucl Mater 2013;441:650–60.
[604] Jianu A, Fetzer R, Weisenburger A, Doyle S, Bruns M, Heinzel A, et al. Stability domain of alumina thermally grown on Fe–Cr–Al-based model alloys and modified surface layers exposed to oxygen-containing molten Pb. J Nucl Mater 2016;470:68–75.
[605] Takaya S, Furukawa T, Inoue M, Fujisawa T, Okuda T, Abe F, et al. Corrosion resistance of Al-alloying high Cr–ODS steels in stagnant lead–bismuth. J Nucl Mater 2010;398:132–8.
[606] Takahashi M, Sa RY, Pramutadi A, Yamaki-Irisawa E. Overview of recent studies related to lead-alloy-cooled fast reactors. AIP Conference Proceedings. 2012.
[607] Cionea C, Abad MD, Aussat Y, Frazer D, Gubser AJ, Hosemann P. Oxide scale formation on 316L and FeCrAl steels exposed to oxygen controlled static LBE at temperatures up to 800 °C. Sol Energy Mater Sol Cells 2016;144:235–46.
[608] Popovic MP, Yang Y, Bolind AM, Ozdol VB, Olmsted DL, Asta M, et al. Transmission Electron Microscopy (TEM) Study of the Oxide Layers Formed on Fe-12Cr-4Al Ferritic Alloy in an Oxygenated Pb-Bi Environment at 800 °C. JOM 2018;70:1471–7.
[609] Popovic MP, Bolind AM, Aussat Y, Gubser AJ, Hosemann P. Oxidative passivation of Fe–Cr–Al steels in lead-bismuth eutectic under oxygen-controlled static conditions at 700 and 800°C. J Nucl Mater 2019;523:172–81.
[610] Shi H, Fetzer R, Tang CC, Szabó DV, Schlabach S, Heinzel A, et al. The influence of Y and Nb addition on the corrosion resistance of Fe-Cr-Al-Ni model alloys exposed to oxygen-containing molten Pb. Corros Sci 2021;179:109152.
[611] Wang HR, Yu H, Kondo S, Okubo N, Kasada R. Corrosion behaviour of Al-added high Mn austenitic steels in molten lead bismuth eutectic with saturated and low oxygen concentrations at 450°C. Corros Sci 2020;175:108864.
[612] Shi H. Alumina forming alloys (steels, high entropy materials) for the mitigation of compatibility issues with liquid metals and steam in energy related, high-temperature applications. PhD dissertation, KIT; 2020.
[613] Huang X, Gong X, Song M, Chen JJ, Hu FY, Yin Y, et al. Liquid metal embrittlement susceptibility of a high-entropy alloy exposed to oxygen-depleted liquid lead-bismuth eutectic at 250 and 350°C. J Nucl Mater 2020;528:151859.
[614] Gong X, Xiang CY, Auger T, Chen JJ, Liang XC, Yu ZY, et al. Liquid metal embrittlement of a dual-phase $Al_{0.7}$CoCrFeNi high-entropy alloy exposed to oxygen-saturated lead-bismuth eutectic. Scr Mater 2021;194:113652.
[615] Harrelson KJ, Rou SH, Wilcox RC. Impurity element effects on the toughness of 9Cr-1Mo steel. J Nucl Mater 1986;141–143:508–12.
[616] Wang J, Lu SP, Rong LJ, Li DZ. Effect of silicon contents on the microstructures and mechanical properties of heat affected zones for 9Cr2WVTa steels. J Nucl Mater 2016;470:1–12.
[617] Kobayashi S, Takasugi T. Mapping of 475°C embrittlement in ferritic Fe–Cr–Al alloys. Scr Mater 2010;63:1104–7.
[618] Dömstedt P, Lundberg M, Szakalos P. Corrosion studies of a low alloyed Fe-10Cr-4Al steel exposed in liquid Pb at very high temperatures. J Nucl Mater 2020;531:152022.
[619] Field KG, Hu XX, Littrell KC, Yamamoto Y, Snead LL. Radiation tolerance of neutron-irradiated model Fe-Cr-Al alloys. J Nucl Mater 2015;465:746–55.
[620] Edmondson PD, Briggs SA, Yamamoto Y, Howard RH, Sridharan K, Terrani KA, et al. Irradiation-enhanced α′ precipitation in model FeCrAl alloys. Scr Mater 2016;116:112–6.
[621] Gong X, Chen JJ, Xiang CY, Yu ZY, Gong HR, Yin Y. A comparative study on liquid metal embrittlement susceptibility of three FeCrAl ferritic alloys in contact with liquid lead-bismuth eutectic at 350°C. Corros Sci 2021;183:109346.

[622] Gong X, Hu FY, Chen JJ, Wang H, Gong HR, Xiao J, et al. Effect of temperature on liquid metal embrittlement susceptibility of an Fe10Cr4Al ferritic alloy in contact with stagnant lead-bismuth eutectic. J Nucl Mater 2020;537:152196.
[623] Heinzel A, Kondo M, Takahashi M. Corrosion of steels with surface treatment and Al-alloying by GESA exposed in lead-bismuth. J Nucl Mater 2006;350:264–70.
[624] Engelko V, Müller G, Rusanov A, Markov V, Tkachenko K, Weisenburger A, et al. Surface modification/alloying using intense pulsed electron beam as a tool for improving the corrosion resistance of steels exposed to heavy liquid metals. J Nucl Mater 2011;415:270–5.
[625] Majumdar S, Borgohain A, Kain K. Interaction between liquid lead-bismuth eutectic and aluminized Inconel 625 superalloy at 600 and 850 °C. J Nucl Mater 2019;518:54–61.
[626] Rivai AK, Takahashi M. Corrosion investigations of Al-Fe-coated steels, high Cr steels, refractory metals and ceramics in lead alloys at 700 °C. J Nucl Mater 2010;398:146–52.
[627] Kurata Y, Sato H, Yokota H, Suzuki T. Applicability of Al-Powder-Alloy Coating to Corrosion Barriers of 316SS in Liquid Lead-Bismuth Eutectic. Mater Trans 2011;52:1033–40.
[628] Yamaki-Irisawa E, Numata S, Takahashi M. Corrosion behaviour of heat-treated Fe–Al coated steel in lead–bismuth eutectic under loading. Prog Nucl Energy 2011;53:1066–72.
[629] Yamaki E, Takahashi M. Corrosion Resistance of Fe-Al-Alloy-Coated Ferritic/Martensitic Steel under Bending Stress in High-Temperature Lead-Bismuth Eutectic. J Nucl Sci Technol 2011;48:797–804.
[630] Fetzer R, Weisenburger A, Jianu A, Müller G. Oxide scale formation of modified FeCrAl coatings exposed to liquid lead. Corros Sci 2012;55:213–8.
[631] Kurata Y, Yokota H, Suzuki T. Development of aluminium-alloy coating on type 316SS for nuclear systems using liquid lead–bismuth. J Nucl Mater 2012;424:237–46.
[632] Wang H, Xiao J, Wang H, Chen Y, Yin X, Guo N. Corrosion Behavior and Surface Treatment of Cladding Materials Used in High-Temperature Lead-Bismuth Eutectic Alloy: A Review. Coatings 2021;11:364.
[633] Glasbrenner H, Groschel F. Exposure of pre-stressed T91 coated with TiN, CrN and DLC to Pb-55.5Bi. J Nucl Mater 2006;356:213–21.
[634] Takahashi M, Kondo M. Corrosion resistance of ceramics SiC and Si_3N_4 in flowing lead-bismuth eutectic. Prog Nucl Energy 2011;53:1061–5.
[635] Chen Y, Hu LB, Qiu CJ, He B, Zhou LH, Zhao J, et al. Influence of LBE Temperatures on the Microstructure and Properties of Crystalline and Amorphous Multiphase Ceramic Coatings. Coatings 2019;9:1–11.
[636] Cockeram BV, Smith RW, Leonard KJ, Byun TS, Snead LL. Irradiation hardening in unalloyed and ODS molybdenum during low dose neutron irradiation at 300°C and 600°C. J Nucl Mater 2008;382:1–23.
[637] Weisenburger A, Müller G, Heinzel A, Jianu A, Muscher H, Kieser M. Corrosion, Al containing corrosion barriers and mechanical properties of steels foreseen as structural materials in liquid lead alloy cooled nuclear systems. Nucl Eng Des 2011;241:1329–34.
[638] Short MP, Morton S, Ferry SE, Ballinger RG. Diffusional stability of ferritic–martensitic steel composite for service in advanced lead–bismuth cooled nuclear reactors. Int Heat Treatm Surf Eng 2010;4:74–80.
[639] García Ferré F, Mairov A, Iadicicco D, Vanazzi M, Bassini S, Utili M, et al. Corrosion and radiation resistant nanoceramic coatings for lead fast reactors. Corros Sci 2017;124:80–92.
[640] Li HQ, Bai PW, Lin ZW, Zhang J, Tang Q, Pan YY. Corrosion resistance in Pb-Bi alloy of 15–15Ti steel coated with Al_2O_3/SiC bilayer thin films by magnetron sputtering. Fusion Eng Des 2017;125:384–90.
[641] Miorin E, Montagner F, Zin V, Giuranno D, Ricci E, Pedroni M, et al. Al rich PVD protective coatings: A promising approach to prevent T91 steel corrosion in stagnant liquid lead. Surf Coat Technol 2019;377:124890.
[642] Wu ZY, Zhao X, Liu Y, Cai Y, Li JY, Chen H, et al. Lead-bismuth eutectic (LBE) corrosion behaviour of AlTiN coatings at 550 and 600°C. J Nucl Mater 2020;539:152280.
[643] Wan Q, Wu ZY, Liu Y, Yang B, Liu HD, Ren F, et al. Lead-bismuth eutectic (LBE) corrosion mechanism of nano-amorphous composite TiSiN coatings synthesized by cathodic arc ion plating. Corros Sci 2021;183:109264.
[644] Vogt JB, Serre IP. A Review of the Surface Modifications for Corrosion Mitigation of Steels in Lead and LBE. Coatings 2021;11:53.
[645] Proriol Serre I, Diop I, David N, Vilasi M, Vogt JB. Mechanical behaviour of coated T91 steel in contact with lead-bismuth liquid alloy at 300°C. Surf Coat Technol 2011;205:4521–7.
[646] García Ferré F, Ormellese M, Di Fonzo F, Beghi MG. Advanced Al_2O_3 coatings for high temperature operation of steels in heavy liquid metals: a preliminary study. Corros Sci 2013;77:375–8.
[647] Vassallo E, Pedroni M, Spampinato V. Effect of alumina coatings on corrosion protection of steels in molten lead. J Vac Sci Technol, B 2018;36:01A105.
[648] Tunca B, Lapauw T, Callaert C, Hadermann J, Delville R, Caspi EN, et al. Compatibility of Zr_2AlC MAX phase-based ceramics with oxygen-poor, static liquid lead–bismuth eutectic. Corros Sci 2020;171:108704.
[649] Lu YH, Wang ZB, Song YY, Rong LJ. Effects of pre-formed nanostructured surface layer on oxidation behaviour of 9Cr2WVTa steel in air and liquid Pb–Bi eutectic alloy. Corr Sci 2016;102:301–9.
[650] Zhang WH, Wang ZB, Lu K. Enhanced oxidation resistance of a reduced activation ferritic/martensitic steel in liquid Pb-Bi eutectic alloy by preforming a gradient nanostructured surface layer. J Nucl Mater 2018;507:151–7.
[651] Lu YH, Zhang ML, Tang WB, Song YY, Rong LJ. Effect of Nanostructured Surface on the Corrosion Behaviour of RAFM Steels. Oxid Met 2019;91:495–510.
[652] Weissmüller J. Alloy effects in nanostructures. Nanostruct Mater 1993;3:261–72.